Hydrodynamics, Mass Transfer and Mixing induced by Bubble Plumes in Viscous Fluids

David Laupsien

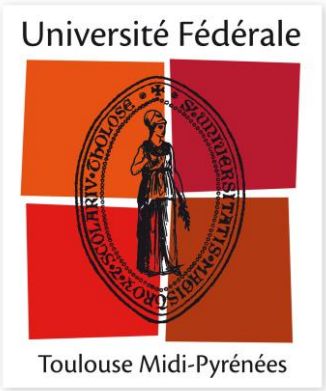

THESIS

submitted for the degree of

Philosophy Doctor

Issued by *Institut National des Sciences Appliquées (INSA) de Toulouse*
Discipline or Specialty: *Fluid Dynamics*

Presented and defended by *David Laupsien*
On December 8, *2017*

Title: *Hydrodynamics, Mass Transfer and Mixing induced by Bubble Plumes in Viscous Fluids*

JURY
Michael Schlüter – Professor, TU Hamburg – External Examiner
Rob Mudde – Professor, TU Delft - External Examiner
Markus Schubert - Res. Ing., HZDR Dresden - Examiner
Véronique Roig – Professor, INP IMFT Toulouse - Examiner
Jamel Chahed – Professor, ENIT Tunis – Examiner
Jerôme Laviéville - Res. Ing., EDF Paris - Visitor
Claude Le Men – *Res. Ing.,* INSA LISBP Toulouse - Visitor
Arnaud Cockx – Professor, INSA LISBP Toulouse - Advisor
Alain Liné – Professor, INSA LISBP Toulouse - Advisor

Doctor school : *Mécanique, Energétique, Génie civil & Procédés (MEGeP)*
Research Unit : *Laboratoire d'Ingénierie des Systèmes Biologiques et des Procédés (LISBP)*
Advisors : *Arnaud Cockx & Alain Liné*

Abstract

This work is an experimental investigation on hydrodynamics, mass transfer and mixing induced by a bubble plume. In chemical engineering, people are often confronted to mixing problems of liquid and gas to create chemical or biochemical reactions. Most of the time, bubble columns of large height compared to their diameter, are used for such kind of processes. But there are also situations using large scale reactors like tanks for methanization or wastewater treatment. In such configurations, spargers must be adapted to reactor dimensions and fluid properties. This is particularly important for methanization reactors since fluid properties are changing continuously during the fermentation. In order to understand hydrodynamics, mass transfer and mixing, it is easier to study bubble swarms, or so called bubble plumes, generated by one single sparger. Different experiments are figured out in two different columns types. First one is a pseudo two dimensional column (6cm * 35 cm * 130cm) situated at the LISBP allowing the application of optical metrological methods. Hence, the gas phase is studied via shadowgraphy and the liquid phase via PIV. Plus, mixing time measurements after dye injection are performed and pressure sensors as well as oxygen probes are used. In this way, one could study the oscillating behavior, the corresponding characteristic frequency, mass transfer and mixing time scales. Furthermore, local information concerning liquid and bubble velocity depending on viscosity, surface tension and injection conditions are presented. Depending on the considered cases, phenomena like bubble plume motion, bubble induced agitation or turbulence contribute differently to column mixing.

In order to analyze fluid properties, a copolymer called Breox is used. Moreover, two different spargers generating different bubble shapes and sizes are applied to estimate their impact. Strong coupling between different parameters could be highlighted.

Additional experiments in a cylindrical bubble column were performed at the HDZR in Germany. The same fluids and the same spargers were used in order to compare results from both geometries. Due to the difficulty to apply optical methods, a Wire-Mesh system recently developed at the HZDR is used to follow the bubble plume motion. Hence, characteristic frequencies as well as void fractions could be investigated.

Finally, first simulations using NEPTUNE CFD code showing encouraging results are presented at the end of the manuscript. Here as well, characteristic time scales and void fraction profiles are used to perform first comparisons.

Résumé

Ce travail est une investigation expérimentale de l'hydrodynamique, du transfert massique et du mélange induit par un panache de bulles dans des mileux de différentes viscosités. Dans l'industrie on est souvent confronté à des problèmes de transfert et de mélange d'une phase liquide et d'une phase gazeuse afin de provoquer des réactions chimiques ou biochimiques. La plupart du temps on utilise des colonnes à bulles, simple à mettre en œuvre, pour ce type de procédé. Mais il existe d'autres situations adaptées aux très grands volumes comme par exemple les bassins d'aération de traitement des eaux ou les méthaniseurs. Dans ce cas de figure, la répartition des injecteurs de gaz doit être adaptée aux dimensions du bassin et contribuer au mélange du liquide. Ceci est autant plus vrai pour le bioréacteur de méthanisation où l'état du liquide change en continu pendant la fermentation. Cependant, il y a un manque d'informations concernant l'hydrodynamique induit par l'injection de gaz en milieu visqueux. Afin de mieux comprendre l'écoulement, le transfert massique et finalement le mélange dans ces situations, il a été décidé d'étudier le cas d'un panache de bulles, généré par un seul injecteur dans des liquides de différentes viscosité. Pour cela des expériences ont été effectuées dans deux types de colonne à bulles avec injection centrale.
La première colonne à bulles qui constitue le cœur de cette étude, est pseudo bidimensionnelle (6cm * 35 cm * 130cm) et permet la visualisation du panache. Celui ci est alors également bidimensionnel ce qui rend plus facile l'application des méthodes métrologiques optiques telles que l'ombroscopie ou la PIV (Particle Image Velocimetry) permettant l'étude de la phase gazeuse et de la phase liquide. L'utilisation de deux cameras distinctes et parfaitement synchronisées a permis l'obtention de champs de vitesse dans le liquide et une caractérisation précise de la taille, de la forme et de la vitesse des bulles de façon simultanée. Pour la mesure de la vitesse des bulles une méthode de traitement de données, appelée BIV (Bubble Image Velocimetry) et inspirée de la PIV, a été développée. L'utilisation de sondes a oxygène a permis d'étudier le transfert massique global gaz-liquide. En changeant le gaz injecté, des suivis temporels de la concentration d'oxygène dissoute dans la phase liquide ont pu être réalisés. Afin de compléter l'analyse hydrodynamique de la colonne à bulles, des mesures de temps de mélange ont été mesurés via des expériences de traçage. Pour cela un colorant a été injecté en zone de paroi. Des mesures d'intensité lumineuse et donc d'absorbance ont servi à suivre la répartition du colorant au cours du temps permettant la caractérisation du mélange.

Le but de notre étude est également la caractérisation du comportement oscillatoire de la trajectoire sinusoïdale du panache de bulles. Afin de mieux comprendre le caractère périodique du mouvement de panache, différentes méthodes d'analyse de séries temporelles ont été appliquées telles que la fonction de corrélation ou la transformée de Fourier. De cette façon différents temps caractéristiques ont pu être identifiés. De plus, les contributions énergétiques résultant de fluctuations à différentes échelles ont pu être déterminées grâce à une décomposition des champs de vitesse dans la phase liquide, appelée POD (Proper Orthongonal Decomposition).

L'influence de la distribution de la taille des bulles, ainsi que l'état du liquide en terme de viscosité et de tension superficielle constituent l'intérêt principal de cette investigation. Pour la réalisation des expériences, deux systèmes d'injection ont été utilisés. Le premier permet d'injecter des bulles ellipsoïdales de l'ordre de quelques millimètres à travers une membrane et le deuxième d'injecter des calottes sphériques de l'ordre de quelques centimètres. Pour la création de calottes, un tube d'un mètre créant des bulles de Taylor, relachées à la base au centre de la colonne, est utilisé. De plus, trois débits d'injection permettant la création d'un large spectre de conditions d'injection ont été choisi (50; 100; 200 $\frac{l}{h}$). Pour l'étude de l'influence des propriétés de la phase liquide, un copolymère appelé Breox, est utilisé. Il permet de modifier la tension superficielle et la viscosité tout en ayant un comportement parfaitement Newtonien. Une base de données complète a ainsi pu être créée.

Une seconde colonne à bulles a été utilisée dans le cadre d'un séjour au HZDR en Allemagne afin d'étendre les expériences aux conditions tridimensionnelles. La colonne est cylindrique et a un diamètre de 39.2cm et une hauteur de 160cm ce qui la rend comparable à la colonne pseudo bidimensionnelle. Du aux difficultés d'appliquer des méthodes métrologiques optiques, un système Wire-Mesh récemment développé au HZDR a été utilisé pour suivre le mouvement du panache. De cette façon, on a pu prouver la présence d'un comportement oscillatoire en conditions tridimensionnelles. Afin de pouvoir comparer ces résultats au cas 2D, les deux mêmes systèmes d'injection, les trois mêmes débits, les trois mêmes vitesses de gaz superficielle et les mêmes fluides ont été utilisés. Ceci a permis de comparer deux géométries distinctes avec des conditions similaires.

Finalement, des simulations CFD transitoire et 3D de nos expériences ont été réalisées sur NEPTUNE CFD. Pour tester la capacité de l'outil à reproduire numériquement le comportement oscillatoire du panache de bulles dans des conditions connues et maitrisées, différents termes de fermeture exprimant le transfert interfacial de la quantité de mouvement ont été testés. La comparaison entre la simulation et l'expérience montre des résultats très encourageants.

Contents

List of Figures

List of Tables

Abbreviation	Definition
2D-BP	Two Dimensional Bubble Plume
3D-BP	Three Dimensional Bubble Plume
ADU	Analogue to Digital Unit
BIV	Bubble Image Velocimetry
COSI	Complex Situations
DCTF	Double Cell Transition Flow
PIV	Particle Image Velocimetry
POD	Proper Orthogonal Decomposition
POTS	Periodic Oscillation Time Scale
RMS	Root Mean Square
VF	Vortical Flow
WIB	Well Identified Bubbles

Symbol	Unit	Definition
A	$[m^2]$	Surface Area of Ellipse Projection on a Bubble
a	$[m^2\ m^{-3}]$	Volumetric Infacial Area
A_{Caps}	$[m^2]$	Projected Surface Area of a Spherical Caps
A_{Circle}	$[m^2]$	Area of an Circle
$a_{Correlation}$	$[m^2]$	Correlation Function Scalar
$A_{Ellipse}$	$[m^2]$	Area of an Ellipse
a_k^n	$[m^2]$	Temporal Scalar of the k-th event and mode n (POD)
$A_{Polygon}$	$[m^2]$	Surface Area of the Smallest Possible Convex Polygon
A_{Raw}	$[m^2]$	Raw Projected Bubble Surface Area
$A_{Section}$	$[m^2]$	Area of the Horizontal Column Cross Section
C	$[mg\ l^{-1}]$	Dissolved Oxygen Concentration
$C^\star$	$[mg\ l^{-1}]$	Dissolved Oxygen Concentration of Saturation
C_0	$[mg\ l^{-1}]$	Initial Dissolved Oxygen Concentration
C_{AM}	[-]	Added Mass Coefficient
C_{Cap}	$[m]$	Contour of a Spherical Cap
C_{Cricle}	$[m]$	Contour of a Circle
C_D	[-]	Drag Coefficient
$C_D^\star$	[-]	Modified Drag Coefficient
C_D^{im}	[-]	Drag Coefficient of a Fully Contaminated Bubble Interface
C_D^m	[-]	Drag Coefficient of a Completely Clean Bubble Interface
C_{D_c}	[-]	Drag Coefficient of a Partially Contaminated Bubble Interface
$C_{Ellipse}$	$[m]$	Contour of an Ellipse
C_{Lift}	[-]	Lift Coefficient
C_{Tchen}	[-]	Tchen Coefficient
D	[ ]	Drift Flux Coefficient
D_E	[m]	Equivalent Diameter
D_H	[m]	Largest Bubble Expansion
Eo	[-]	Eotvos Number
Eo_H	[-]	Modified Eotvos Number
E_V	$[m^5\ s^{-2}\ ]$	Velocity Energy Density Spectrum Vector
f	$[s^{-1}]$	Plume Oscillation Frequency
$\vec{f_{AM}}$	$[kg\ m\ s^{-2}\ ]$	Added Mass Force
$\vec{f_B}$	$[kg\ m\ s^{-2}\ ]$	Body Force
$\vec{f_D}$	$[kg\ m\ s^{-2}\ ]$	Drag Force
$\vec{f_G}$	$[kg\ m\ s^{-2}\ ]$	Gravity Force
$\vec{f_L}$	$[kg\ m\ s^{-2}\ ]$	Lift Force
Fr	[-]	Froude Number
g	$[m\ s^{-2}]$	Gravity Constant
Gr	[-]	Grashof Number
H	$[m]$	Column Height
I	$[kg\ m^{-2}]$	Inertia Moment
J	$[kg\ m^{-2}]$	Inertia Tensor
k	$[m\ s^{-1}]$	Kinetic Energy
K	[-]	Vector Wave Number
K_l	$[m\ s^{-1}]$	Mass Transfer Coefficient
L_i	$[m]$	Inlet Length
$\vec{L_{I,K}}$	$[kg\ m\ s^{-2}\ ]$	Diffusive Momentum Transfer
$\vec{L_g^{AM}}$	$[kg\ m\ s^{-2}\ ]$	Added Mass Force (Momentum Transfer)

Symbol	Unit	Definition
$\vec{L_g^D}$	$[kg\ m\ s^{-2}\ ]$	Drag Force (Momentum Transfer)
$\vec{L_g^L}$	$[kg\ m\ s^{-2}\ ]$	Lift Force (Momentum Transfer)
M	$[m]$	Large Ellipse Axis
m	$[m]$	Small Ellipse Axis
Mo	[-]	Morton Number
N	[-]	Eigenvalue Number
n	[-]	Bubble Number
P_s	$[kg\ m^2\ s^{-2}]$	Relative Energy
P	[-]	Power Spectra
$\overline{P_g}$	$[kg\ m^{-1}\ s^{-2}]$	Averaged Gas Pressure
$\overline{P_l}$	$[kg\ m^{-1}\ s^{-2}]$	Averaged Liquid Pressure
Q_{Inlet}	$[m]$	Inlet Length
r	$[m]$	Sphere Radius
$R_{i,j}$	$[m^4\ s^{-2}]$	Auto-Covariance Tensor
R_{GC}	$[m]$	Radial Distance of Gravity Center
Re	[-]	Reynolds Number
Re_B	[-]	Buoyancy Reynolds Number
S	$[kg\ m^2\ s^{-2}\ K^{-1}]$	Entropy
St	[-]	Strouhal Number
t	$[s]$	Time
t_0	$[s]$	Initial Time
t_{final}	$[s]$	Final Time
T_M	$[s]$	Mixing Time
tks	$[kg\ m^2\ s^{-2}]$	Turbulent Kinetic Energy
U	$[m\ s^{-1}]$	Horizontal Velocity
u	$[m\ s^{-1}]$	Horizontal Velocity Component
$\overline{U^b}$	$[m\ s^{-1}]$	Averaged Bubble Swarm Velocity
u^b	$[m\ s^{-1}]$	Bubble Velocity
U_{b_∞}	$[m\ s^{-1}]$	Terminal Bubble Velocity
$\vec{U_D}$	$[m\ s^{-1}]$	Drift Velocity Vector
$\overline{U^b}$	$[m\ s^{-1}]$	Averaged Gas Velocity
U_g	$[m\ s^{-1}]$	Gas Velocity
$\vec{u_g}$	$[m\ s^{-1}]$	Gas Velocity Vector
u_g'	$[m\ s^{-1}]$	Gas Velocity Fluctuations
U_{GS}	$[m\ s^{-1}]$	Superficial Gas Velocity
$\vec{u_l}$	$[m\ s^{-1}]$	Liquid Velocity Vector
u_l'	$[m\ s^{-1}]$	Liquid Velocity Fluctuations
$\vec{U_r}$	$[m\ s^{-1}]$	Relative Velocity Vector
U_{r_∞}	$[m\ s^{-1}]$	Relative Terminal Velocity
V	$[m\ s^{-1}]$	Vertical Velocity
v	$[m\ s^{-1}]$	Vertical Velocity Component
V_b	$[m^3]$	Volume of a Bubble
$V_{Ellipsoid}$	$[m^3]$	Volume of an Ellipsoid
$\vec{V_k}$	$[m\ s^{-1}]$	Velocity Field Component of the k-th event
V_{Sphere}	$[m^3]$	Volume of a Sphere
$\overline{x}$	$[s^{-1}]$	Any Time Signal
W	$[m]$	Column Width
w	$[rad\ s^{-1}]$	Pulsation
We	[-]	Weber Number

Symbol	Unit	Definition
We_c	[-]	Critical Weber Number
x	$[m]$	Cartesian Coordinate in Horizontal Direction
x_i	$[m]$	Cartesian Coordinate in Horizontal Direction of a Bubble
x_{GC}	$[m]$	Cartesian Coordinate in Horizontal Direction of Gravity Center
y	$[m]$	Cartesian Coordinate in Vertical Direction
y_i	$[m]$	Cartesian Coordinate in Vertical Direction of a Bubble
y_{GC}	$[m]$	Cartesian Coordinate in Vertical Direction of Gravity Center

Symbol	Unit	Definition
α_g	[-]	Void Fraction
α_{gc}	$[rad]$	Azimuth of Gravity Center
α_i	[-]	Local Void Fraction
α_k	[-]	Void Fraction of Phase k
Γ_k	$[m\ s^{-1}]$	Mass Transfer
$\dot{\gamma}$	$[s^{-1}]$	Shear Rate
ϵ	$[m^2\ s^{-1}]$	Energy Dissipation
η	$[kg\ m^{-1}\ s^{-1}]$	Dynamic Viscosity
θ	$[rad]$	Opening Angle of a Spherical Cap
θ_c	$[rad]$	Contamination Angle
θ_s	$[rad]$	Half the Opening Angle of a Spherical Cap
κ	[-]	Scalar Wave Number
λ	[-]	Eigenvalue
λ_w	$[m]$	Wavelength
μ_l	$[m^2\ s^{-1}]$	Kinematic Liquid Viscosity
ν	$[m^2\ s^{-1}]$	Kinematic Viscosity
ν_t	$[m^2\ s^{-1}]$	Turbulent Viscosity
ρ_g	$[kg\ m^{-3}]$	Gas Density
ρ_k	$[kg\ m^{-3}]$	Density of Phase k
ρ_l	$[kg\ m^{-3}]$	Liquid Density
σ	$[kg\ s^{-2}]$	Kinematic Viscosity
τ	$[s]$	Time Lag
τ_c	$[s]$	Characteristic Time Scale
τ_d	$[s]$	Relaxation Time
$\overline{\tau_{k_{i,j}}}$	$[kg\ m^{-1}\ s^{-2}]$	Strain Tensor
τ_t	$[s]$	Turbulence Time Scale
$\vec{\phi^n}$	[-]	Eigenvector of Mode n
χ	[-]	Eccentricity

Introduction

The present manuscript is dealing with multiphase flow appearing in industrial processes in the field of chemical engineering. In all kinds of industrial fields, mixing of gas and liquid is used to transfer species in order to provoke chemical or biochemical reactions. A simple, cheap and efficient way to realise it, is the application of bubble columns where gas bubbles are injected at the column bottom in a stagnant liquid. This kind of reactor is widely used for many different industrial applications, but column dimensions as well as injection conditions must be adapted to process objectives and fluid properties. Besides the simple and cheap construction, bubble columns show other advantages like low operation costs, good mass transfer efficiency and mixing abilities. The present work is focussing on last one. In general, bubble columns are homogeneously aerated, which means that gas is injected at column bottom through a sparger with equally spaced injection holes distributed over the whole horizontal column cross section. Such configurations show high gas hold-up and consequently high values of interfacial area and are therefore used in many different fields like petrochemistry (Fischer-Tropsch process, oxidation of hydrocarbons, oligomerization of ethylene), pharmaceutical, agri-food, cosmetic industries or more recent applications like algae cultivation.

The second configuration where mixing is performed via gas injection in a stagnant liquid is a large tank (of order of several meters in diameter). In such reactors, mixing is the first aim and only afterwards mass transfer. Current applications are aeration in wastewater treatment, mixing in methanization reactors, tank destratification, ice prevention as well as swell destruction along the coasts and many more. Besides, a better understanding of bioreactor mixing can also avoid sedimentation of suspended particles as well as surface rind. Two concrete examples of industrial applications can be seen in figure 1. On the left

side of the figure, the valorization cycle of organic waste by methanization is presented. By mixing such reactors anerobic digestion of organic matter can be improved to increase the production of biogas or more precisely methan. The production of combustibles like methane is still very important because of the dependancy of our society on combustion as energy source. This will not change in the next several decades. Consequently, we must look for new ways of fuel production and for optimizing existing ones.

In the considered case, the biodigestion where the fermentation of green and biodegradable waste producing biogas is taking place, is the most important step. By well mixing such bioreactors, biomass becomes more homogeneous, biochemical reactions are better controled and consequently the whole process becomes more productive. One way to achieve efficient mixing is the injection of recirculated biogas in form of bubbles at the bottom. Hence, detailed knowledge of bubble induced hydrodynamics is needed in order to define adequate sparger distances and characteristics like flow rates and bubble shapes. Plus, during the fermentation process, fluid properties like viscosity or surface tension are changing continuously whatfore injection conditions must be adapted regularly.

On the right side of figure 1, the cycle of a wastewater treatment plant is shown. In the middle of the process an aeration tank is used where bacteria consume nitrogen and carbones. These bacteria need oxygen supply which is ensured by aeration. In the case of such large aeration tanks as well, the understanding of mixing is very important to carry out correct scale-up and define optimal operation conditions. In this way, productivity shall be increased while decreasing energy consumption. Like in other bioreactors, wastewater plants are confronted to complex fluids due to the presence of chemical and biochemical products which makes the understanding of mixing even more difficult.

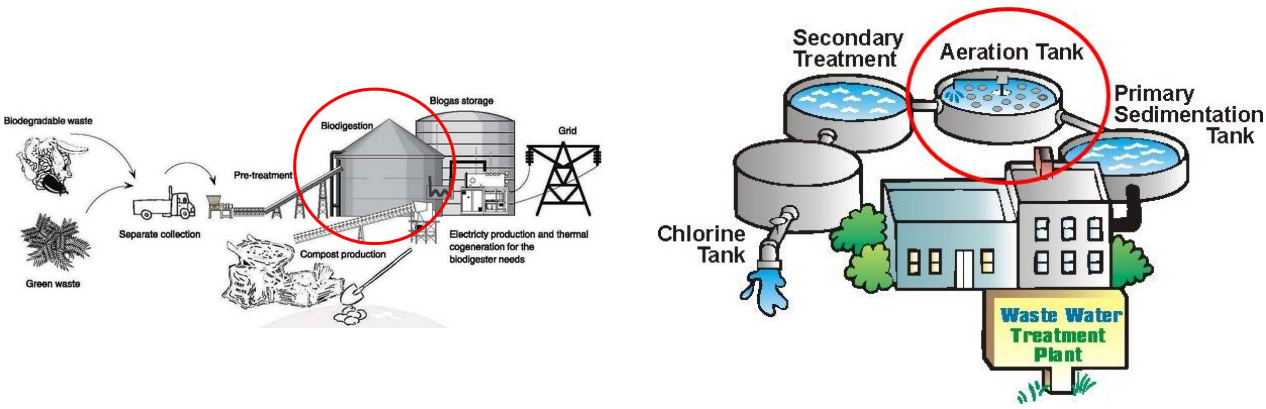

Figure 1: Examples of Bubble Plume Applications

In order to analyse global mixing in such reactors, hydrodynamics induced by a single sparger must be analysed first which brings us back to bubble columns. By modifying injection conditions to a single spot sparger, this kind of experimental facility, which is called heterogeneously aerated bubble column in literature, can be used to study such flow regimes. A more detailted definition is given in the next chapter.

Anyway, spot gas injection in a stagnant liquid generates two phase flow structures which are called bubble swarms or bubble plumes which is the subject of this investigation. These bubble plumes show oscillating behaviour producing large eddies at a so called meso scale. This scale, somewhere in between macro scale corresponding to the size of a whole tank and the microscale, relates local phenomena characterized by liquid properties to local hydrodynamics like vortex cells to macro mixing of bioreactors. Therefore, the current work investigates hydrodynamics of bubble plumes in viscous fluids and its contribution to mixing. The oscillating behaviour and the dispersion depend on several parameters like bubble size and shape, flow rate and liquid properties like surface tension as well as viscosity. Unfortunalty, there is a big gap of knowledge when is comes to bubble size and viscosity influences on bubble plumes. Hence, during the present study, two different sparger types and several liquids characterized by different viscosities are used. Plus, experiments were performed in two different bubble column geometries. First one is a flat pseudo two dimensional column situated at the LISBP in Toulouse while the second one is cylindrical, three dimensional and situated at the HZDR in Dresden. The understanding of such bubble induced flows will help to resolve concrete problems such as correct scale-up and finding optimum operation conditions of large bioreactors with complex fluids enabling CFD simulations, in order to making it predictible. To realize such a big step large databanks have to be aquired which will be mainly the object of the present work. But before, one has to make a step backwards and go to fundamental physics and to isolated single bubbles in order to understand mesoscale mixing phenomena.

After an introduction in bubble dynamics, two chapters are dedicated to the description of experimental setups, data treatment and analysis of physical results. The last chapter show first encouraging results of CFD simulations in water which must be extended to other fluids approaching our goal to develop predictive tools for complex two phase flow situations.

Chapter I

Bubbly Flow

This chapter is an introduction in bubble dynamics with its properties, flow behaviours and definitions. Furthermore, the notion of bubble columns including type characterization and flow structure identification is presented.

I.1 Bubble Dynamics

Bubbles are light particles filled with gaz of density ρ_g and surrounded by a liquid phase of density ρ_l which are separated by an interface. Shapes can differ from one bubble to another depending on its size and fluid properties like surface tension and viscosity. Such carateristics show great importance concerning bubbly flows in nature as well as in industrial processes. Anyway, there is still lack of knowledge when it comes to momentum exchange between the two phases. In literature, a lot of different authors investigated in detail all kind of bubble properties. The book from Clift, Grace and Weber (Clift *et al.*, 1978) is probably the most popular work and the most complete review of its kind.

I.1.1 Size & Shape

In dispersed flows like bubbly flows it is important to characterize present particles of the dispersed phase properly. Clear definitions are needed to describe size and shape in order to compare results with those from literature.

Equivalent Diameter To determine particle or bubble size for all kinds of shapes (spherical, ellipsoidal, etc...) in the same way, an equivalent diameter is generally used. Two different definitions exist and the most suitable one depending on the particle nature (solid or deformable) can be chosen. Most often size measurements, at least visual ones, give two dimensional data. This means that the captured three dimensional particle can only be seen from one side which makes an exact characterization difficult. Nevertheless, the projected two dimensional area can be used to determine the equivalent diameter. It is known that two bodies (here 2D) having same mass (here surface) and inertia ellipsoid (here inertia ellipse) are dynamically equivalent. By calculating eigenvalues and eigenvectors of the inertia tensor of the raw area, small m and large M axis lengths and orientations can be obtained, respectively. Inertia moment calculations are presented in detail in section II.1.3.3.
The first possible equivalent diameter is the one of a circle having the same area than the projected ellipse. In this case no additional assumption is done.

$$A_{Circle} = \pi \frac{D_E^2}{4} \tag{I.1}$$

$$A_{Ellipse} = \pi m M \tag{I.2}$$

$$D_E = \sqrt{4mM} \tag{I.3}$$

where A_{Circle} and $A_{Ellipse}$ correspond to the area of a circle and an ellipse, respectively. The second possibility which is better adapted to deformable bubbles, uses the volume instead of the surface. Therefore, the assumption that bubbles corresponds to ellipsoids with one small axis and two large axis is done. (Moore, 1959) showed that bubbles with small distortion take the shape of an oblate spheroid. The equivalent diameter of a spheroid having the same volume than the ellipsoid can be calculated. In this way, the flattened spherical nature of rising ellipsoidal bubbles can be taken into account.

$$V_{Spheroid} = \pi \frac{D_E^3}{6} \tag{I.4}$$

$$V_{Ellipsoid} = \frac{4}{3}\pi m M^2 \tag{I.5}$$

$$D_E = \sqrt[3]{8mM^2} \tag{I.6}$$

where V_{Circle} and $V_{Ellipse}$ correspond to the volume of a circle and an ellipse, respectively.

Eccentricity The shape of an ascending bubble depends on the equilibrium between surface tension forces which are hindering deformation and ambient hydrostatic as well as dynamic pressure forces which are flattening the bubble. During the ascending motion, the liquid has to get around the bubble and therefore accelerates. This generates a decreasing pressure distribution from the bubble front to its sides. Hence, the surface moves outwards and the local curvature increases (FAN & Tsuchiya, 2013). In other words, bubbles experience a compressive and dilating force in streamwise and transverse direction, respectively, which generates an ellipsoidal shape. For this reason it makes sense to use bubble eccentricity as a second characteristic that can be calculated by taking the ratio of the large axis M and the small one m from the above mentioned ellipse.

$$\chi = \frac{M}{m} \tag{I.7}$$

This ellipse can serve to describe and to distinguish three principal bubble shapes. The first one is the spherical shape where surface tension σ is much higher than the dynamic pressure which can also be expressed by:

$$\frac{\sigma}{D_E} \gg \rho_l U_b^2 \tag{I.8}$$

which is true for undeformable bubbles (low Weber numbers) and where U_b is the bubble velocity and σ the surface tension. Spherical bubbles begin to deform when vicsous forces become more important than inertia (high Morton number):

$$\mu_l D_E U_b \gg \rho_l D_E^2 U_b^2 \tag{I.9}$$

where μ_l is the liquid dynamic viscosity. The Morton number compares viscous and surface tension effects and is well appropriate to express fluid properties influences on bubble shape:

$$Mo = \frac{g\mu_l^4 \Delta\rho}{\rho^2 \sigma^3} \tag{I.10}$$

where g is the gravity constant, $\Delta\rho$ the density difference between gas and liquid. Two other dimensionless numbers which are generally used in bubble dynamics are the Weber and the Reynolds numbers. The above mentioned ratios I.8 and I.9 can be expressed by these numbers:

The Weber Number:

$$We = \frac{\rho_l U_b^2 D_E}{\sigma} \tag{I.11}$$

The Reynolds Number:

$$Re = \frac{\rho_l D_E U_b}{\mu} \tag{I.12}$$

By using the following velocity expression:

$$U_b = \sqrt{\frac{\Delta\rho}{\rho} g D_E} \tag{I.13}$$

the Reynolds number can be extended to the Buoyancy Reynolds Number where the density difference is included:

$$Re_B = \frac{\sqrt{\Delta\rho\rho_l g D_E^3}}{\mu_l} \tag{I.14}$$

In order to complete the short discussion about dimensionless numbers, the last two ones must be given as well:

The Eötvös Number:

$$Eo = \frac{g\Delta\rho D_E^2}{\sigma} \tag{I.15}$$

which compares gravity and surface tension forces.

The Froude Number:

$$Fr = \frac{U_b}{\sqrt{gD_E\frac{\Delta\rho}{\rho}}} \tag{I.16}$$

Three of these dimensionless numbers were used by (Clift *et al.*, 1978) to characterize bubble shapes as illustrated in figure I.1. Depending on Reynolds and Eötvös numbers every bubble type is categorized. Liquid properties like surface tension and viscosity are taken into account as well. In fluid dynamics, as it is also the case in other scientific fields, dimensionless numbers are used to compare same phenomena in different configurations and at different scales. For bubbles and droplets, it is generally admitted to use the above mentioned ones.

The eccentricity can be directly expressed as a function of the Weber number. This was done in theoretical (Moore, 1965) and experimental (Duineveld, 1995) works that can be found in literature. For low Morton numbers, (Moore, 1965) proposed the following analytical solution:

$$\chi = 1 + \frac{9}{64}We \tag{I.17}$$

Besides, (Duineveld, 1995) proposed an empirical solution for ultra pure water:

$$We = 4.41 - 4.39\chi^2 \tag{I.18}$$

suggesting that I.17 is slightly overestimating the deformation. More recently, (Legendre *et al.*, 2012) proposed the following equation depending on both, Weber and Morton number:

$$\chi = \frac{1}{1 - \frac{9}{64}We(1 + K(Mo)We)^{-1}} \tag{I.19}$$

where $K(Mo) = 0.2Mo^{1/10}$. Deformation takes place for $Mo \geq 10^{-10}$. With further increasing Morton number deformation is also increasing and bubbles are getting more and more flattened. The authors also confirm that for low Morton numbers the eccentricity χ depends only on the Weber number. Equation I.19 is valid in the ellipsoidal regime for moderate Weber numbers or in other words for bubbles in water of order of

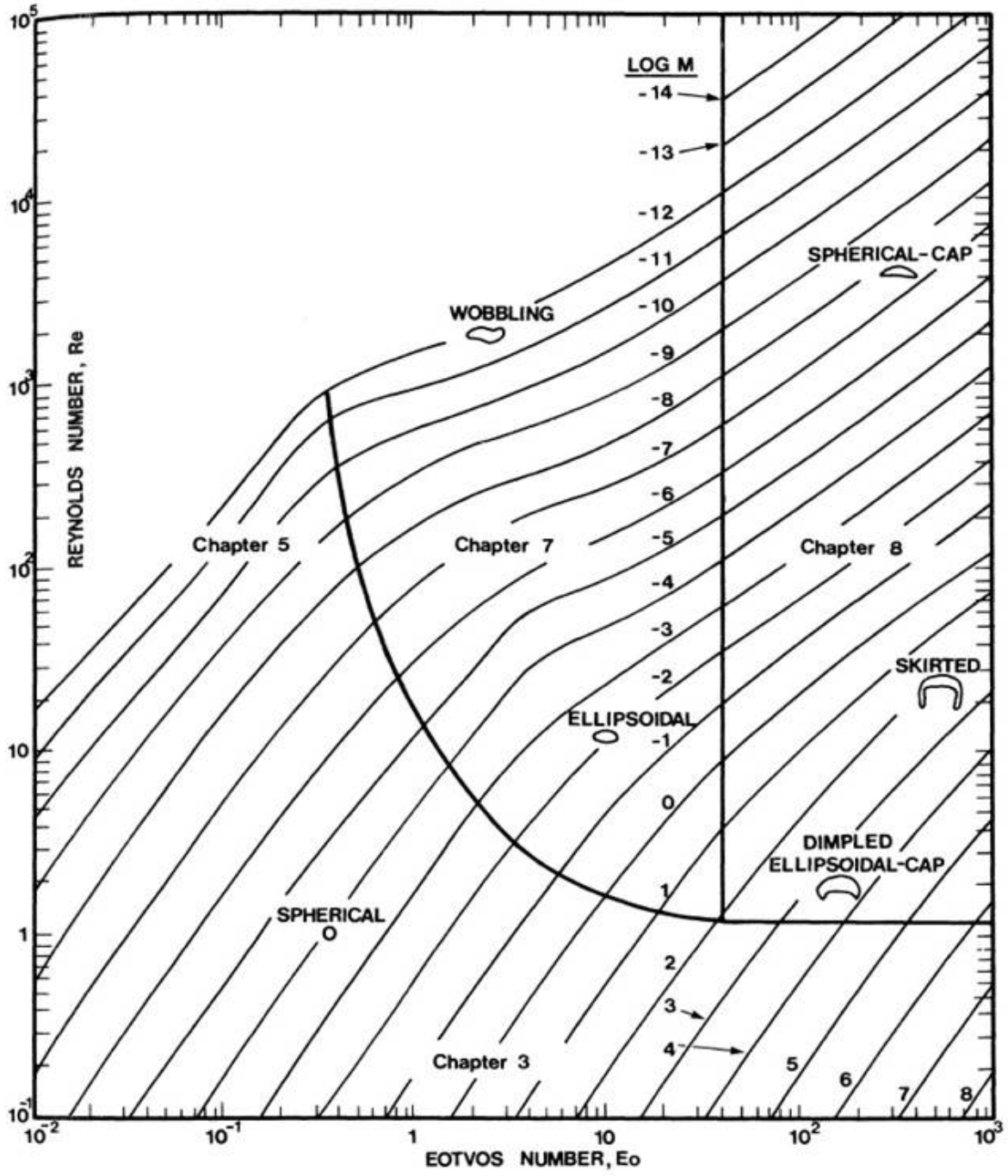

Figure I.1: Bubble Shape in function of Eö and Re by Clift, Grace et Weber

several millimeters.

The second regime, with an eccentricity range between 1 and 2, is the ellipsoidal one showing non-axisymmetric bubble shapes resulting from non-rectilinear trajectories and unsteady wakes. This so called path instability was mentioned by (Ryskin & Leal, 1984b) and already observed for small distortions. There is a strong coupling between interface deformations and the surrounding flow structure. Hence, the interface mobility plays an important role, but depends on the system purity. Further informations about this regime are discussed in section I.1.3.1. For this regime (Wellek *et al.*, 1966) suggested the following correlation:

$$\chi = 1 + 0.185 Eo^{0.8} \tag{I.20}$$

The last regime shows the appearance of large spherical cap bubbles. In literature, only few works dealing with the shape of such large bubbles, can be found and no clear explanation is given. Authors like (Ryskin & Leal, 1984a) and (Batchelor, 1987) investigated for reasons of such shapes via stability analysis. While (Ryskin & Leal, 1984a) defined the cap shape as consequence of flow separation, (Batchelor, 1987) went deeper inside the subject and investigated for maximum bubble size and break-up criteria as well. The authors concluded that over a critical bubble size, no stable solution or stable bubble shape is possible anymore. Anyway, the eccenticity range can be given. For this regime χ varies from values around 2 until values up to 5. The upper limit depends strongly on fluid properties.

I.1.2 Mass Transfer

One important aspect in bubbly flows is the mass transfer between the liquid and the gas phase through the bubble interphase. Independent of involved species, mass transfer is generated by an imbalance of substances between both phases. In industries, all kinds of chemical or biochemical products are brought together to provoke reactions. If they come from separate phases, most of the time bubble columns are used to bring them into

contact. Hence, mass transfer flux is appearing.

In fundamental research, the thermodynamic equilibrium of oxygen and nitrogen is used to evaluate mass transfer. Either by nitrogen injection or by a chemical reaction, the dissolved oxygen concentration in the liquid phase can be decreased close to zero. Then air bubbles are injected where the oxygen tends to the liquid phase in order to balance oxygen concentration between both phases. By following the oxygen concentration in the liquid phase, an overall averaged flux can be determined. This flux is expressed as $k_L a$, composed of an exchange coefficient k_L and the interfacial exchange area a.

In literature, many investigations can be found. Two of the most famous ones are the book written by (Higbie, 1935) or the work from (Danckwerts, 1951).

(Higbie, 1935) investigated laminar flows where fluid elements enter the interface at the front, are transported by interface convection before leaving it at the tail. The authors proposed the following simple expression for a characteristic time scale:

$$\tau_c^{-1} = \frac{U_b}{D_E} \tag{I.21}$$

Unfortunately, the authors neglect effects like bubble deformation or wakes. However, later publications show that flow structures show great influence on mass transfer. (Fortescue, G., Pearson, J., 1967) proposed that mass transfer in isotropic turbulent flow is controled by large eddies. Hence, they concluded that the inverse of the characteristic time scale must be proportional to the ratio of kinetic energy ϵ and dissipation k:

$$\tau_c^{-1} = \frac{\epsilon}{k} \tag{I.22}$$

On the other hand, (Lamont and Scott, 1970) suggested that in highly turbulent flows (like stirring tanks) small eddies exchange surrounding fluid and further interfacial transfer. That is why the authors proposed for the characteristic time scale:

$$\tau_c^{-1} = \frac{\epsilon}{\nu} \tag{I.23}$$

where ν is the liquid viscosity. These influences from the surrounding flow (laminar or turbulent) inducing Reynolds stress close to the interface, interface mobility and therefore its contamination play an important role in mass transfer, but are difficult to estimate. For an exact characterization, information about the interfacial area must

be known as well. Hence, depending on the bubble type (deformable or not) and flow situations, mass transfer can be furthered or not. For these reasons, mass transfer will not be investigated in detail in this work because all these parameters are difficult to control in bubble columns. Further analyzes at the interface scale would be required. Only an averaged $k_L a$ value over the whole column was measured and analyzed.

I.1.3 Bubble Rising Velocity

Bubble's rising movement can be expressed by the balance equation. To calculate the trajectory as well as the terminal velocity of an isolated bubble, one must consider all acting forces described by the following expression:

$$\rho_g V_b \frac{d\vec{U_b}}{dt} = \vec{f} = \vec{f_B} + \vec{f_G} + \vec{f_D} + \vec{f_{AM}} + \vec{f_L} \tag{I.24}$$

where V_b is the bubble volume, $\vec{U_b}$ the bubble veclocity, $\vec{f_B}$ the body force, $\vec{f_G}$ gravity, $\vec{f_D}$ the drag force, $\vec{f_{AM}}$ the added mass force and $\vec{f_L}$ the lift force. Drag, lift, gravity and added mass forces are acting on the bubble interface.

It is well known that bubbles rises through liquids due to buoyancy forces, or in other words because of the density difference between gas and liquid phase, until reaching a free surface. The so called terminal rise velocity, which is a stationary solution, results mainly from the equilibrium between buoyancy (body force) and the drag force which expresses the resistance from the liquid phase on the bubble interface against its flow direction. Three different regimes can be distinguished in the same way than in section I.1.1.

I.1.3.1 Terminal Velocity

In the case of isolated small spherical bubbles without deformation ($Re << 1$), the Stokes solution (Stokes *et al.*, 1880) is of reasonable accuracy. (Hadamard & Hadamard, 1911) and (Rybczyński, 1911) derived the following equation for the terminal velocity:

$$U_\infty = \frac{1}{18} \frac{g D_E^2 (\rho_l - \rho_g)}{\mu_l} \tag{I.25}$$

In the presence of large eddies, drag is becoming more important and bubbles are trapped by liquid circulation. Since these bubbles do not play an important role in swarm dynamics, they are not discussed any further.

With increasing bubble size, velocity calculations are becoming more complicated. Lift forces become important and the bubble begins to zigzag which makes bubble trajectory longer and therefore a damping effect of the rising velocity can be observed. Plus, a strong coupling between bubble deformation and trajectory makes calculations even more difficult. Anyway, (Mendelson, 1967) proposed the following empirical equation for the terminal bubble velocity:

$$U_\infty = \sqrt{\frac{2.14\sigma}{\rho_l D_E} + \frac{\Delta\rho g D_E}{2\rho_l}} \tag{I.26}$$

In the case of isolated large spherical cap bubbles ($D_E > 15mm$), the trajectory is becoming straight again which means that only buoyancy and drag force are acting on the bubble. Hence, (Davies *et al.*, 1950) was able to propose the following rough approximation:

$$U_\infty = 0.707\sqrt{gD_E} \tag{I.27}$$

(Clift *et al.*, 1978) published figure I.2 in order to summarize terminal velocities in function of the equivalent diameter and the Eötvös number. In the range $1mm < D_E < 15mm$ a huge gap between maximum and minimum values can be observed that can be explained by the interface contamination. A more detailed discussion is shown is section I.1.3.3.

I.1.3.2 Drag Coefficient and Dimensionless Numbers

An isolated bubble is mainly driven by the equilibrium between buoyancy and drag forces. Different models can be found in literature for the above mentionned bubble types. They are characterized by different drag coefficients and a certain number of investigations for deformed (ellipsoidal and spherical cap) bubbles were published. Like already mentioned, the drag force is acting on the bubble interface and in opposite direction of the object

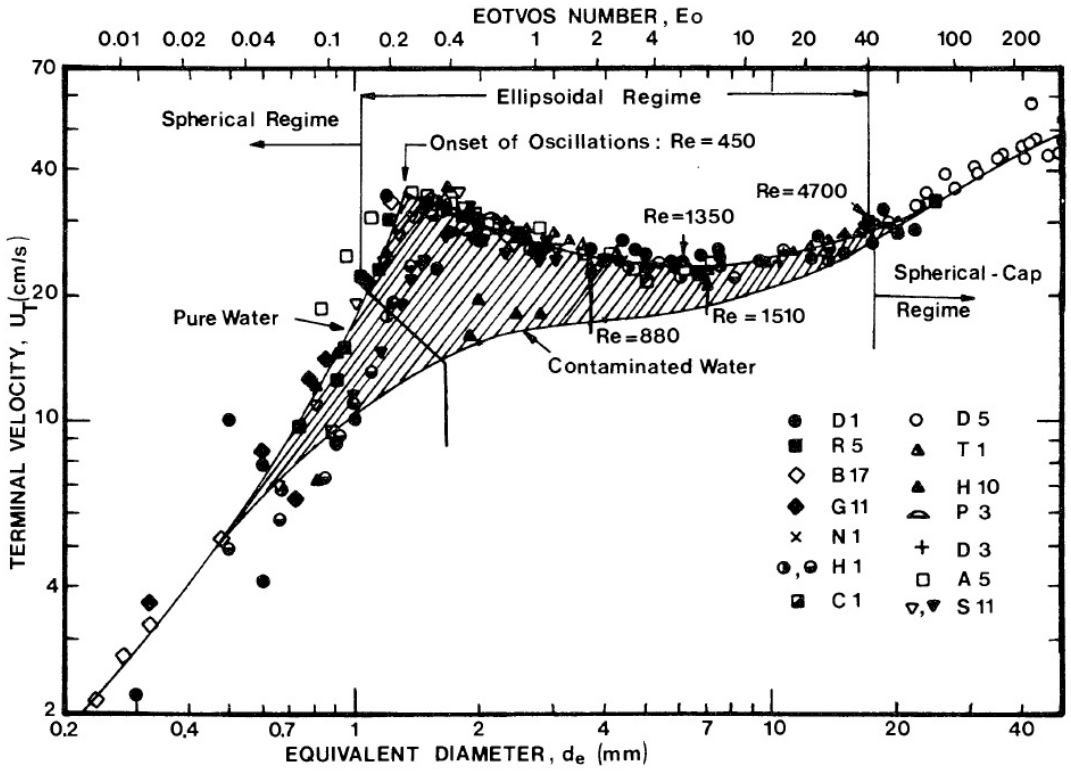

Figure I.2: Terminal Bubble Velocity in function of Eö and Re by Grace, Clift & Weber (1978)

motion. This means that the force is constituting the main flow resistance and plays an important role in bubble terminal velocity. This velocity determines bubble residence times in the liquid phase and therefore the overall void fraction which illustrates its importance for bubble column reactors. In general, the drag coefficient C_D can be expressed via three dimensionless numbers, plus a the so called contamination angle θ_c:

$$C_D(\chi \geq 1) = f(Re_B, Eo, Mo, \theta_c) \tag{I.28}$$

(Maxworthy *et al.*, 1996) showed that the characterization can also be done by using We and Fr which can be written as a combination of the three previous ones.

$$We = Re^2 \left(\frac{Mo}{Eo}\right)^{1/2} \tag{I.29}$$

$$Fr^2 = \frac{Re^2}{Eo}\left(\frac{Mo}{Eo}\right)^{1/2} \tag{I.30}$$

The authors identified different bubble regimes depending on size and velocity from

spherical bubbles to spherical caps in a range of $2.7 \times 10^{-11} < Mo < 5.7 \times 10^{-9}$.

Spherical Regime The drag coefficient for spherical bubbles can be written as follows:

$$C_D = \frac{4}{3}\frac{\Delta\rho}{\rho_l}\frac{gD_E}{U_r^2} \tag{I.31}$$

where $\vec{U_r} = \vec{U_b} - \vec{U_l}$ is the relative bubble velocity. Relation I.31 can also be expressed via dimensionless numbers:

$$C_D = \frac{4}{3}\frac{Eo}{We} \tag{I.32}$$

Bubbles with an equivalent diameter approaching $1mm$, begin to deform while keeping a straight trajectory. This regime can be described by:

$$We \in [1, We_c] \tag{I.33}$$

where We_c is a critical Weber number value which remains the same in the following.

Ellipsoidal Regime The ellipsoidal regime is characterized by trajectory modification from straight to zigzag or helicoidal. As in the previous regime, the ellipsoidal one can also be described via dimensionless numbers. But first, one should distinguish two parts which was proposed by (Maxworthy *et al.*, 1996). The first one is characterized by a constant Weber number ($We_c = cst$) while Reynolds and Eötvös number increase with increasing size. The corresponding drag coefficient I.32 is still valid in the considered range and the critical Weber number value corresponds to:

$$We_c = max(0.517log(Mo) + 7.624; 2.376) \tag{I.34}$$

(Peebles, FN & Garber, HJ, 1953) and (Wallis, 1974) proposed the corresponding values $We_c = 3.65$ and $We_c = 4$, respectively. The borders using the Eötvös number were also defined by (Maxworthy *et al.*, 1996) :

$$Eo_{min} = 72.66Mo^{0.227} \tag{I.35}$$

$$Eo_{max} = \left(\frac{2}{5}We_c\right)^3 \tag{I.36}$$

(Tomiyama *et al.*, 1998) showed the equivalent drag coefficient for equation I.26 in function of the Eötvös number:

$$C_D(Eo) = \frac{8}{3}\frac{Eo}{4+Eo} \tag{I.37}$$

which tends to the solution of (Davies *et al.*, 1950) for spherical cap bubbles:

$$C_D(Eo > 40) = \frac{8}{3} \tag{I.38}$$

In order to give a complet overview, one has to mention that (Comolet, 1979) gave a similar expression:

$$C_D(Eo) = \frac{8}{3}\left(\frac{Eo}{4.28+1.02Eo}\right) \tag{I.39}$$

The beginning of the second part corresponds to the moment where the Weber number begins to evolve again in the following manner:

$$We = 2.5Eo^{1/3} \tag{I.40}$$

where the Eötvös number vary in the range:

$$Eo_{max} \leq Eo < 7.12 \tag{I.41}$$

Finally, the corresponding drag coefficient is given as follows:

$$C_D = \frac{8}{15}Eo^{2/3} \tag{I.42}$$

Spherical Cap Regime Another time, the regime transition can be followed by considering the Eötvös number. The borders for spherical cap bubbles were defined as:

$$7.12 \leq Eo < 40 \tag{I.43}$$

The related Weber number is written as:

$$We = 1.25 + 0.5Eo \tag{I.44}$$

The corresponding drag coefficient is defined as:

$$C_D = \frac{8}{3}\left(\frac{Eo}{2.5 + Eo}\right) \tag{I.45}$$

In conclusion, most of the intermediate ellipsoidal expressions could be derived from the viscous dissipation of a potential flow. This assumption can not be applied to all bubble types since wake instabilities can be involved, which is in contradiction with potentiel flow. Anyway, the drag coefficient for the considered experimental conditions of this work can be given only as a function of the Eötvös and the critical Weber number.

For Eö ≤ 7.12

$$C_D = min\left(\frac{4}{3}\frac{Eo}{We_c}, \frac{8}{15}Eo^{2/3}\right) \tag{I.46}$$

and for Eö > 7.12

$$C_D = \frac{8}{3}\left(\frac{Eo}{2.5 + Eo}\right) \tag{I.47}$$

For Eö $\rightarrow \infty$ equation I.47 tends to I.32. Complementary experimental data was recorded by (Talaia, n.d.) who proposed a global expression for air - glycerol and air - water systems where inertia and dynamic viscosity are the dominant terms. The authors proposed empirical relations between the drag coefficient and the Reynolds number as well as between the terminal velocity and the equivalent diameter for a large bubble size range ($0.1mm < D_E < 10mm$). Their results are in good agreement with I.27 for large bubbles.

I.1.3.3 Contamination

Another parameter which must be considered is the contamination of the system having great impact on bubble interface's mobility. This is the reason for large terminal velocity variations for a given bubble size which is illustrated in figure I.2. The upper limit corresponds to pure water while the down limit corresponds to completely contaminated

water. In the current work, contamination could not be determined and is therefore considered to be constant and was not further investigated. Nevertheless, a short discussion about the subject should be done. First, one must evaluate the contamination degree of the system. (Cuenot *et al.*, 1997) defined the following four situations depending on the adsorption and desorption of impurities on the interface:

- impurities are advected in the bubble wake and do not reach the interface which is still mobile,

- only few impurities are adsorpted on the bubble interface which is still mobile,

- impurities are adsorpted and convected to the bubble bottom on the interface which is partially mobile,

- the interface is completely contaminated and immobile; the bubble can be considered as solid sphere.

(Sadhal & Johnson, 1983) used the angle θ_c to define the degree of contamination and included it in the following drag coefficient expression:

$$C_d^*(\theta_c) = \frac{C_D(\theta_c) - C_D^m}{C_D^{im} - C_D^m} \tag{I.48}$$

where $C_d^{im} = \frac{24}{Re_B}$ and $C_d^m = \frac{16}{Re_B}$ correspond to a completely contaminated and to a completely clean bubble drag coefficient, respectively, in Stokes flow conditions for spherical bubbles. Plus the range could be extended via the correlation of (Schiller & Naumann, 1933) to moderate Reynlods numbers:

$$C_D = \frac{24}{Re_B}(1 + 0.15Re_B^{0.687}) \tag{I.49}$$

Several investigations like (Tomiyama *et al.*, 1998), (FAN & Tsuchiya, 2013) or (Maxworthy *et al.*, 1996) gave drag coefficient correlations for moderate Reynolds numbers which are in agreement with the experimental results from (Gaudin, 1957). All of them described a decreasing drag coefficient evolution with increasing Reynolds number until a local minimum in the range of $200 < Re < 500$. At higher Reynlods numbers, the drag coefficient is increasing again and converging towards a value between 3 and 4. Anyway, the main conclusion on bubble interface contamination is that impurity charged bubbles

show lower rising velocities than clean ones corresponding to higher drag coefficients:

$$C_{D_c} \geq C_D \tag{I.50}$$

I.1.3.4 Swarm Effect

Anyway, the present investigation is not dealing with isolated bubbles, but with bubble swarms. Bubbles interact with eachother and can even coalesce or break-up. This makes it difficult to estimate the rising velocity, especially in the case of polydisperse bubble size distribution. (Batchelor, 1972), (Wijngaarden & Kapteyn, 1990) and (Koch, 1993) investigated dispersed flows with void fraction under 5%. They concluded that for such dilute flows, bubble interactions are mainly binary and induce trajectory modification. (Hallez & Legendre, 2011) studied numerically the interactions between two bubbles ascending side by side in stagnant liquid. The authors gave three possible contribution which are:

- potential effect
- viscous correction (or Moore correction)
- wake effects

The wake effects were already investigated in detail by (Cartellier & Rivière, 2001) and (Cartellier *et al.*, 2009). The authors reported a decreasing probability of the second bubble being in the wake of the first one due to lift force. Last one favors bubble ejection from the wake. However, (Wallis, 1969), (Garnier *et al.*, 2002) and (Riboux *et al.*, 2010) showed a decreasing bubble velocity with increasing void fraction. This result is in agreement with (Legendre *et al.*, 2003) who investigated the infuence of the distance between two bubbles rising side by side via numerical simulations. They defined a critical distance under which the vorticity of the bubbles interact, modifying the pressure distribution and increasing the drag coefficient. This phenomenon is in competition with another one reported by (Bouche *et al.*, 2012) who studied bubble interaction at high Reynolds numbers. They concluded that bubble induced agitation modifies the viscous dissipation behind the first bubble which entrains the following one. This effects the drag coefficient which decreases with increasing void fraction. A wake acceleration effect was also reported by (Krishna *et al.*, 1999). The authors showed an increasement of

the averaged gas velocity by a factor of 3 to 6 for large bubble swarms depending on column dimensions, bubble sizes and void fractions. The highest velocities were recorded in churnflow conditions. It seems that depending on bubble size and shape as well as on the void fraction, the drag coeffcient can increase or decrease which makes it difficult to estimate correct bubble swarm velocities, especially in the case of polydispersed bubble size distribution. All affecting parameters are driven by liquid properties and injection conditions. This is confirmed by (León-Becerril *et al.*, 2002) and (Roghair *et al.*, 2011) who explained the dispersion of results in literature by eccentricity and Eötvös number variations. However, two swarm velocity corrections from literature can be given for dilute bubbly flows.

1) The first one was developped by (Milne Thomson L.N., 1962) who derived via the potential flow assumption, an interesting expression for the drag coefficient for non-isolated ellipsoidal bubbles while taking into account eccentricity:

$$U_r = U_{r_\infty}(1 - P(\chi)\alpha_g) \tag{I.51}$$

with

$$P(\chi) = \frac{1.43(2 + Z(\chi))}{3} \tag{I.52}$$

where

$$Z(\chi) = 2\frac{(\chi^2 - 1)^{1/2} - acos(\chi^{-1})}{acos(\chi^{-1}) - \frac{(\chi^2-1)^{1/2}}{\chi^2}} \tag{I.53}$$

Both equations are plotted in figure I.3 (left). The resulting velocity for a given void fraction of 0.5% and a terminal velocity of $0.25\frac{m}{s}$ for a single bubble, is plotted in figure I.3 (right). In our case P does not exceed the value of 3 which means that the velocity is almost not modified.

2) The second one is the drift flux model introduced by (Zuber & Findlay, 1965) and adapted by (Wallis, 1969) for the drift velocity:

$$U_b = U_\infty(1 - \alpha_g)^n \tag{I.54}$$

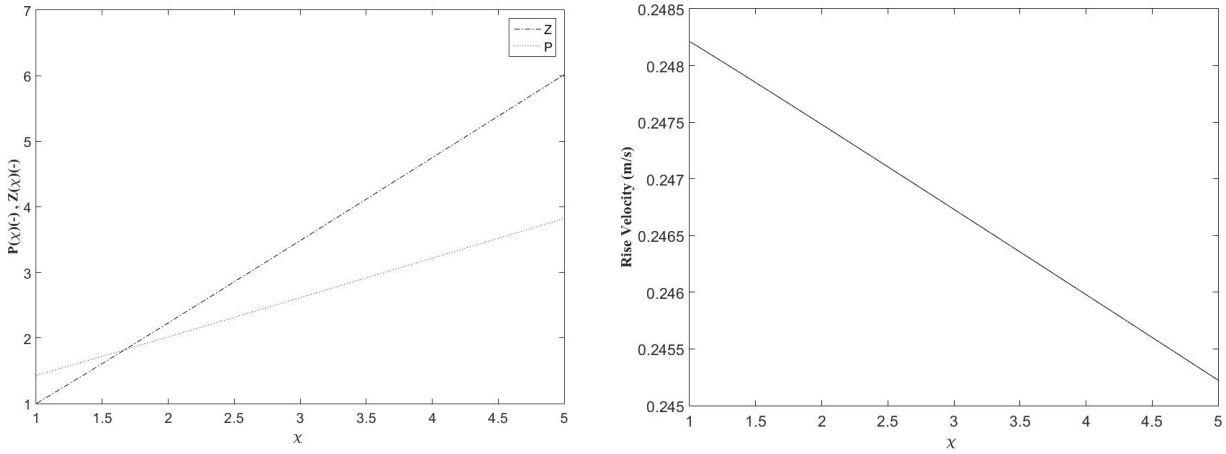

Figure I.3: Left: $Z(\chi)$ and $P(\chi)$ in function of χ; Right: Bubbble Velocity as a function of χ

By applying a first order approximation one obtains:

$$U_b = U_\infty(1 - n\alpha_g) \tag{I.55}$$

where for bubbly flows n was found to be 2 and 2.39 by (Wallis, 1969) and by (F Richardson & N. Zaki, 1954), respectively.

I.2 Bubble Columns

The mixing ability of bubble columns depends mostly on the present flow structure induced by the injected gas bubbles. Depending on liquid properties, column geometry and injection conditions, different flow regimes can be observed. Furthermore, two bubble column categories can be distinguished. In literature, several authors like (Drahoš *et al.*, 1991), (Zahradnik *et al.*, 1997) or (Diaz *et al.*, 2006) illustrated flow regime characterization in terms of gas hold-up depending on the superficial gas velocity which is defined as:

$$U_{GS} = \frac{Q_{inlet}}{A_{section}} \tag{I.56}$$

where Q_{inlet} is the injection flow rate and $A_{section}$ the surface of the horizontal bubble column cross section.

In figure I.4 the above mentionned parameters are used to characterize bubble column types. The solid line indicates qualitatively different flow regimes as a function of the superficial gas velocity in the case of homogeneously aerated bubble columns. At low gas injection, the dispersed bubble regime is characterized by an uniformly rising bubble swarm with almost uniform gas hold-up in the bubble column cross section. With increasing superficial gas velocity heterogeneities in form of large eddies appear indicating the beginning of the transition regime. Finally, with further increasing superficial gas velocity a local minimum in the gas hold-up defines the beginning of the so called turbulent regime (I.4).

The second category, heterogeneously aerated bubble columns, are presented by the dashed line. The flow structure takes the shape of a bubble plume for higher aspect ratios than 2.25. For the whole range of superficial gas velocities, no regime transition characterized by the gas hold-up evolution can be observed. The present flow regime can be recognized by large ascending bubbles in the column middle and small descending bubbles along the column edges.

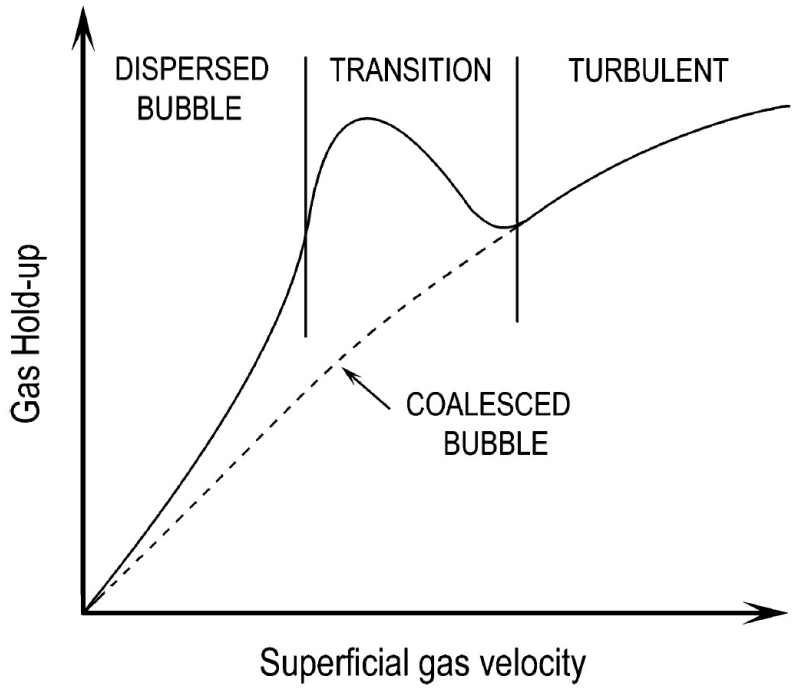

Figure I.4: Identification of flow structures depending on superficial gas velocity by Diaz et al. (2006)

The present contribution focuses only on mixing abilities of bubble plumes generated in heterogeneously aerated bubble columns. The facility is used to study hydrodynamics of an isolated plume in order to better understand meso- and macro-scale mixing of large bioreactors. But even if such bubble columns show lower void fractions, it is still difficult to obtain local time resolved experimental data for both phases. For this reason we have chosen to work mainly with a pseudo two dimensional bubble column allowing the application of visual metrological methods like Particle Image Velocimetry (PIV) and Shadowgraphy. In addition, some complementary experiments were performed in a cylindrical three dimensional bubble column as used in industries.

However, many authors were interested in the characterization of bubble plumes in pseudo two dimensional bubble columns in order to develop predictive tools like CFD simulation. Exact mechanisms and phenomena furthering mixing are still unclear since fluid dynamics depend on complex interactions between phases concerning mass, momentum, and energy transfer. Characteristics length and time scales of macromixing are unpredictible due to the lack of model and the lack of experimental informations. Especially effects of surface tension and viscosity are poorly or not at all investigated. Therefore, models with adequate closure terms have to be tested and compared to experimental data.

A large spectrum of investigations concerning cylindrical bubble columns can also be found in literature. Most authors were interested in the understand of the voidage to superficial gas velocity relation including regime transition and were looking for suitable flow pattern characterization ((Akita & Yoshida, 1973); (Deckwer, 1980); (Hikita *et al.*, 1980); (Maruyama *et al.*, 1981); (Zahradnik *et al.*, 1997); (Vial *et al.*, 2000); (Ruzicka *et al.*, 2001); (Gourich *et al.*, 2006) ; (León-Becerril *et al.*, 2002)). All of them studied homogenously aerated columns showing uniform bubble swarms in most cases. Only few authors like (Simiano *et al.*, 2006) or (Rensen & Roig, 2001) used 3D bubble columns with a small injection area in the column center, which can be considered as single spot injection, to investigate bubble plumes. This configuration can also be modified to so called pseudo two dimensional bubble columns which allows the application of optical metrological methods (Sokolichin *et al.*, 1997). The almost two dimensional column geometry damps three dimensional mesoscale instabilities which generates a quasi two dimensional bubble plume.

I.3 Pseudo-2D Bubble Columns

In the case of pseudo two dimensional bubble columns a sinusoidal trajectory of ascending bubbles predominates the column flow regime while a helical trajectory predominates in the case of cylindrical bubble columns. In both column types, bubble plumes show large ascending bubbles in the column middle and small descending bubbles at the column edges captured by liquid recirculation. All acting mixing mechanisms are the same, which explains the interest of pseudo-2D columns.

Becker et al. (Becker *et al.*, 1994) gave the state of art of modelling of gas-liquid flows in bubble columns and confronted results to experimental observations. They were able to reproduce experimental results with numerical simulations based on a dynamic laminar two-dimensional two-phase Euler-Euler model. A strong influence of the gas distribution system which will be discused later, was also mentionned. (Delnoij *et al.*, 1997) proposed an Eulerian/Lagrangian model for a 2D-BP to model the flow pattern that was confronted to experimental results. Further, the effect of aspect ratio, relation between column height and column width, from 1 to 11 has been studied. First, they observed flow transition for aspect ratios in a range from 1 to 3. Secondly, they revealed that at 7.7 and higher aspect ratios, flow structure was found to consist of two different regions. In the upper part bubbles are dispersed over the entire cross section of the bubble column and vortices do not appear. In the lower part a clear bubble plume was observed. Some years later Diaz et al. (Diaz *et al.*, 2006) also investigated flow transitions for low aspect ratios and proposed figure I.5 to illustrate different flow regimes depending on the superficial gas velocity and aspect ratio. They completed the work of (Delnoij *et al.*, 1997) and defined three different flow regimes which were observed during their work.

For small aspect ratios ($\frac{H}{W} \leq 1.5$) two pseudo steady flow structures can be seen. At low superficial gas velocities a Single Cell Bubbly Flow (SCBF) characterized by convex bubble trajectory and only one vortex cell, appears. The second one is called Double Cell Transition Flow (DCTF) and has the same shape than a vertical vortex dipole, with large upward moving bubbles in the column middle and two vortex cells, one on each side generating downward moving bubbles on the column edges. For aspect ratios larger than $\frac{H}{W} = 2$ an unsteady Vortical Flow (VF) is formed. This regime can be recognized by its sinusoidal trajectory of ascending bubbles. At the column edges and close to the free

surface vortical cells are formed and their number increases with increasing aspect ratio. Plus, bubble plumes (or vortical flows) show a low-frequency oscillating behaviour. The focus of the present investigation will be on this phenomenon in aim to better understand its contribution to column mixing.

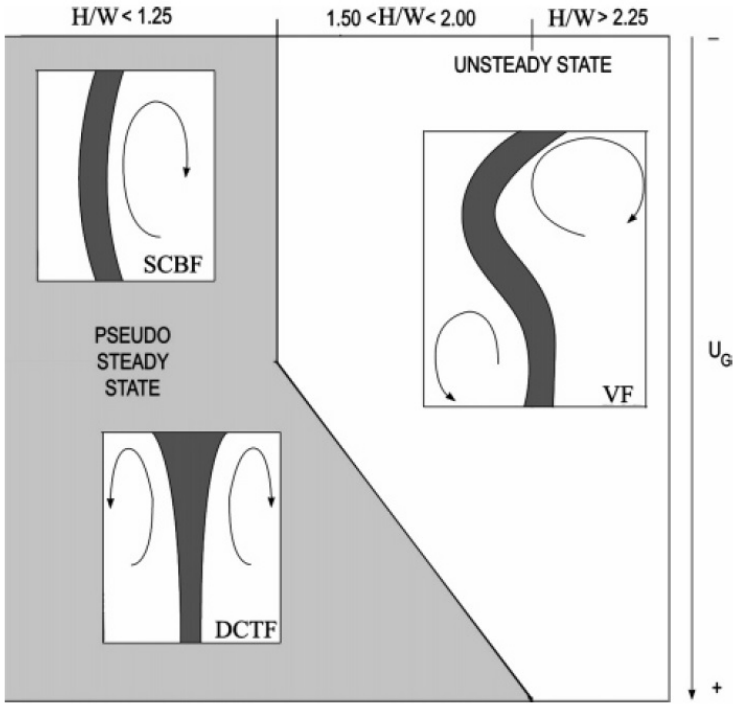

Figure I.5: Identification of flow structures depending on aspect ratio by Delnoij et al. (Delnoij *et al.*, 1997)

I.4 Oscillating Bubble Plume

Several authors like (Delnoij *et al.*, 1997), (Rensen & Roig, 2001), (Buwa & Ranade, 2003) and (Diaz *et al.*, 2006) took a closer look to the low frequency of the wandering bubble plume. For example (Mudde & Simonin, 1999) were able to reproduce bubble plume oscillations numerically. Their results showed comparable time scales than experimental data.

Anyway, from this moment we only consider bubble columns for aspect ratios from 3 to 7. In this way one makes sure that the aspect ratio can be left out of consideration. (Delnoij *et al.*, 1997) studied oscillation frequencies for superficial gas velocities in the range from 2 mm/s to 6 mm/s and showed a strong relation between these two parameters.

With increasing superficial gas velocity, plume oscillation frequency increases as well. In our laboratory, periodic plume time scales were already investigated via optical probe measurements by (Aouinet, H., 2016). Rensen & Roig (Rensen & Roig, 2001) found that this frequency is persistent over the whole column height. They concluded that the horizontal density gradient and the velocity profile of the entrained liquid are the driving terms of the unstable bubble plume behavior. One should mention that the ascending bubble plume naturally disperses which, after a certain height, is damped by the confinement of column walls.

However, in the current investigation our focus is on the impact of fluid properties. (Buwa & Ranade, 2003) were the first ones who used other fluids than pure water in pseudo-2D bubble columns. They pointed out that the oscillation period does not change by the addition of saturated NaCl. This is in disagreement with (Cachaza *et al.*, 2011) who used NaCl to modify surface tension in order to analyze their impact on flow patterns. It is probable, that (Buwa & Ranade, 2003) did not notice any differences because of the small superficial gas velocity range (no flow regime modification) and the use of NaCl as tracer to measure mixing times and not no modify fluid properties.

To our knowledge (Cachaza *et al.*, 2011) are the only ones who investigated the influence of surface tension on flow patterns in such pseudo-2D configurations. Figure I.6 shows flow structures for three liquids with different surface tensions, but with almost same density and viscosity (see figure I.1) at two different superficial gas velocities.

Fluid	Name	Density (kg/m^3)	Surface Tension (mN/m)
Ultrapure Water	*UPW*	996.7	71.39
$CaCl_2$ *Solution*	C_3	1041.5	72.95
IBOH Solution	C_{18}	990.1	37.67

TABLEAU I.1: Fluid properties of surfactant solutions by Cachaza et al. (2011)

At low gas injection rate, no significant difference in flow structures can be observed. But at higher gas injection rates flow regime can change from vortical (VF) to double cell transition flow (DCTF) by modifying surface tension. This result could be explained by bubble interactions occuring much more often at high gas flow rates. At low gas hold-up almost no bubble coalescence or breakup appears independently of surface tension, only bubble size changes slightly due to added surfactants. Therefore, the hydrodynamic

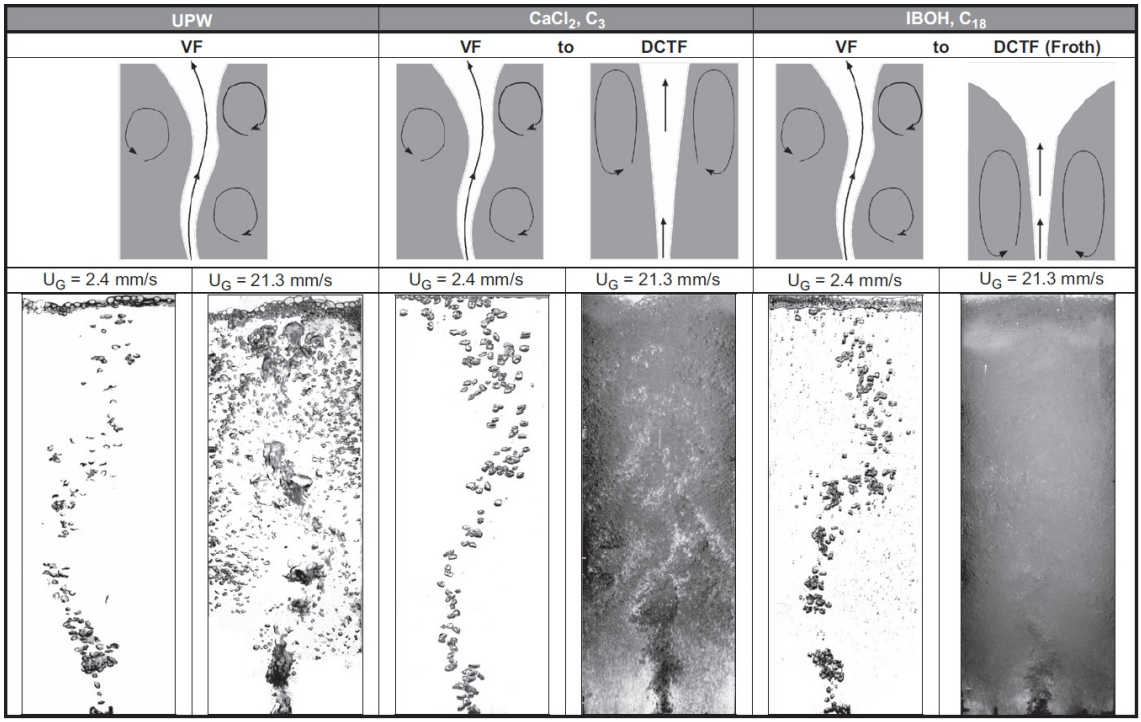

Figure I.6: Influence of surface tension by Cachaza et al. (2011)

structure remains the same. At high gas hold-up, bubble interactions become frequent. Thus, surface tension reduction and the resulting decrease of coalescence (Ruzicka *et al.*, 2008) have a large influence on hydrodynamic structure. Bubble coalescence and breakups also generate a large number of small bubbles. With decreasing bubble size, surface forces like drag or lift became more important compared to body forces like gravity. Hence, bubbles are trapped more easily by liquid recirculation which results in an increasing gas hold-up becoming more and more important in time. (Cachaza *et al.*, 2011) concluded that reduced coalescence and increased aeration destabilize the VF leading to a transition to DCTF. This example shows nicely the impact of liquid properties on flow regimes.

Therefore, effects of fluid properties on bubble plume oscillations must be taken into account. Other properties like viscosity have to be explored because of the information gap in the literature and their crucial role in large bubble column reactor scale-up.

I.5 Conclusion

This chapter gave a short overview of bubble dynamics and bubble columns. The aim is to show the high quantity of work dealing with isolated bubbles. Bubble characteristics like shape, rising velocity, trajectory, etc. were investigated in detail for decades. Furthermore, in the last 30 years a large interest was given to bubble columns because of their importance in industries. But most of the time, only high reactors compared to their width and with a homogeneous injection were studied.

With the increasing importance of energy consumption, large reactors where bubble plumes appear, got in the focus of research and must also be analyzed in detail. If one wants to understand mixing in such large tanks, one has to characterize properly non stationary phenomena like bubble plumes. Such flows show complex bubble interactions which are still not clear, especially when it comes to liquid property influences. They represent also a suitable academic case for the understanding of basic physical phenomena between two phases concerning mass, momentum and energy transfer. Plus, bubble plumes show local, meso- and macroscale phenomena and are therefore perfect test cases to study multiscale mixing.

Chapter II

Experimental Methods & Analyzes

The present investigation is mainly experimental. Therefore, a large number of experiments were performed in two different bubble plume configurations. The first one is a quasi two dimensional one generated in a pseudo two dimensional bubble column situated in Toulouse, whose advantages will be explained in the following section. For a better understanding the abbreviation 2D-BP for two dimensional bubble plume will be used. Additional experiments in a cylindrical three dimensional were performed at the Helmholtz-zentrum in Dresden-Rossendorf in order to study three dimensional bubble plumes. The abbreviation 3D-BP will be used for this case.

II.1 2D Bubble Plume (2D-BP)

II.1.1 Setup

The pseudo two dimensional bubble column used in the present investigation, is $0.06m$ deep, $0.35m$ wide and $2m$ high. Liquid height is fixed to $1.3m$ corresponding to a height to wide ratio of $\frac{H}{W} > 3.5$. In this way one can be sure that this parameter has no influence on flow regime transition for all considered injection gas flow rates (as demonstrated in section I.4). The column is made of $2cm$ thick plexiglass allowing the application of visual metrological methods. Four pressure sensors (PR41X from Keller) are installed, three on the left hand side (at top, middle and bottom of the column) and one on the right hand side (in column middle). Furthermore, on the right hand side two oxygen probes (OX25 from Unisense), one at the top and one at the bottom, are available. A sketch of the bubble column can be seen in figure II.1.

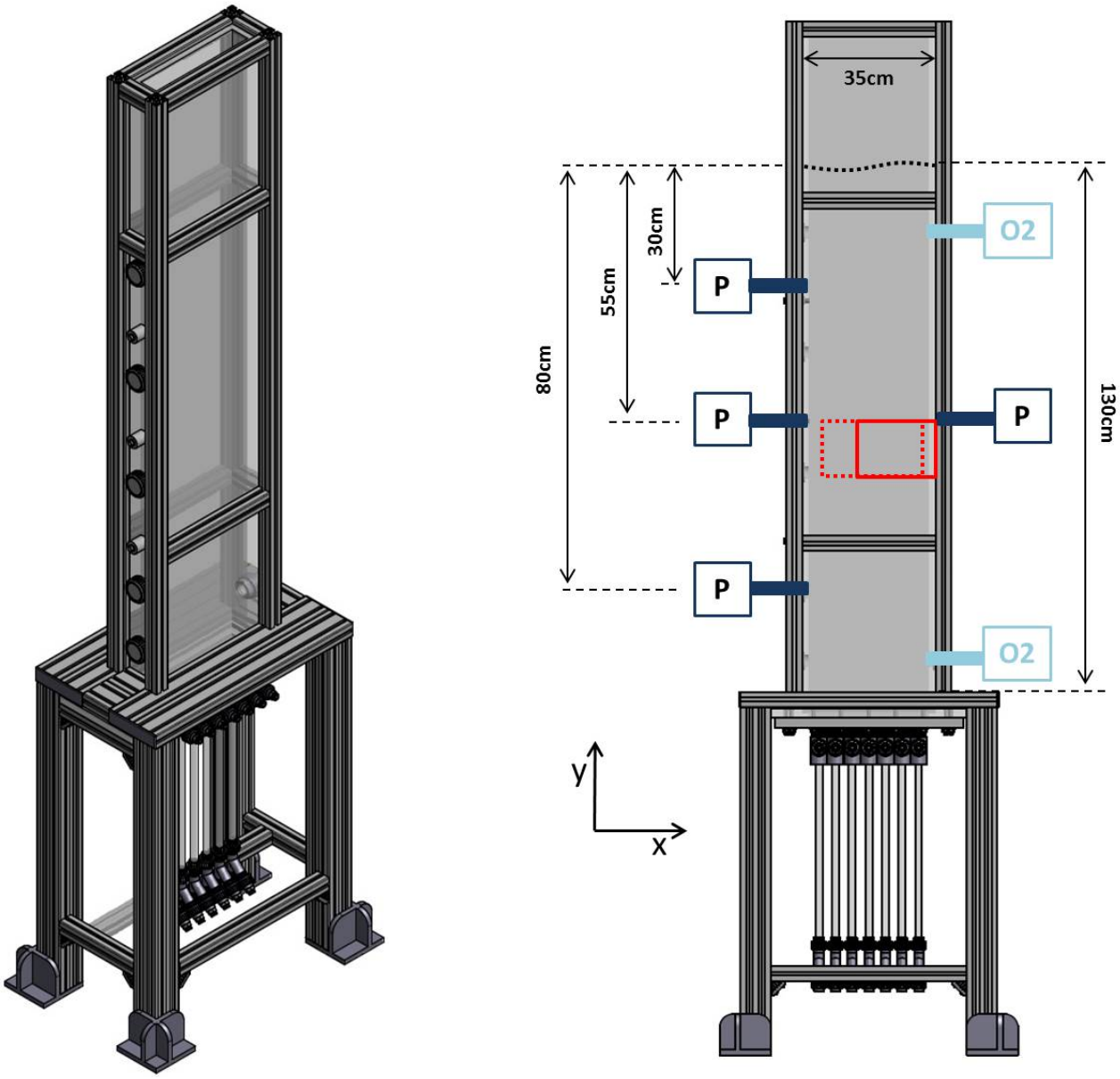

Figure II.1: Experimental Setup at LISBP a) Perspective View b) Sketch

The gas injection sparger consists of seven different injection points, all aligned from left to the right and equally spaced. At each point one can choose between two injection conditions, but in the present work, only central (single spot) injection is used. Either small ellipsoidal bubbles of order of some millimeters can be generated through a membrane sparger with a diameter of $20mm$ or large spherical caps of order of some centimeters (largest distance of the bubble) can be produced via slugflow sparger. To create such a slug flow, $1m$ long tubes with an inner diameter of $16mm$ were used in order to obtain Taylor bubbles. The last 7cm of the tubes show an enlargement to $20mm$

of inner diameter due to construction reasons. The gas injection flow rate is controled by mass flow meter (SLA5850S from Brooks) with an outlet pressure of $3bar$.
In our whole investigation a system of coordinates is admitted where x and the associated velocity U are in horizontal direction and y and the associated velocity V are in vertical direction.

II.1.2 Fluid properties

The focus of the present work is on the impact of fluid properties on bubble plumes. The goal was to simulate experimentally bioreactor fluids. Therefore, a copolymer named Breox 75W55000 from BASF is used. This copolymer shows advantaging properties like stability in shear and time which means that the fluid shows Newtonian behaviour and can be conserved for a long time. Viscosity is measured with the Mars3 Rheometer from Thermofischer and surface tension with the 3S from GIBX. A rheogram showing the dynamic viscosity as a function of the shear rate for the fluids Breox (13.6%), Breox (18.5%) and Breox (24%) can be seen in figure II.2.

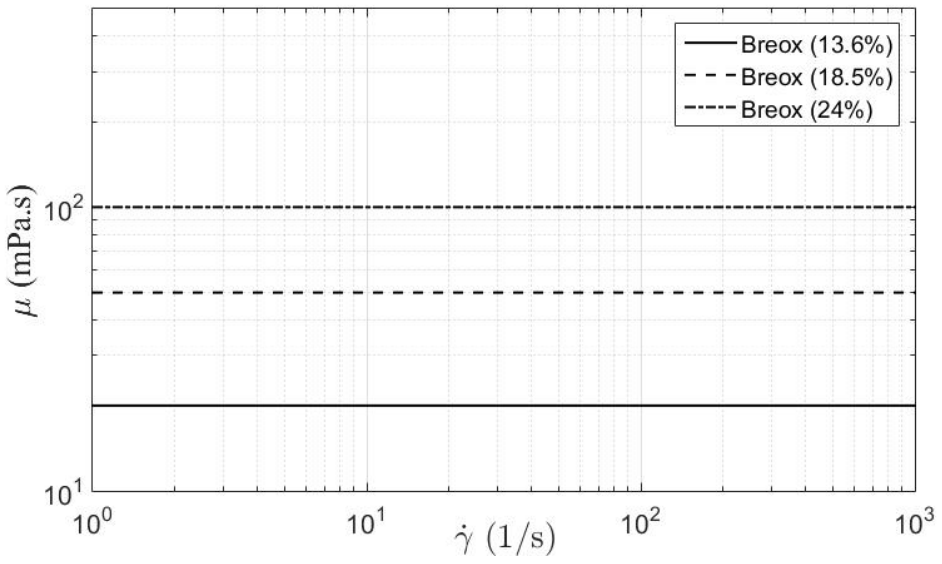

Figure II.2: Dynamic Viscosity as a fucntion of the shear rate in different Fluids: Breox (13.6%) ; Breox (18.5%) ; Breox (24%)

The fluid is also perfectly mixable with water which enables us to create every desired viscosity. Plus, because of its transparency, optical metrological methods can be applied.

All fluid properties depending on copolymer mass concentration are shown in table II.1.

Fluid	Surface Tension (mN/m)	Viscosity (mPa.s)
Water	75.1	1
Breox (0.5%)	56.8	1
Breox (8.7%)	56.0	10
Breox (13.6%)	55.6	20
Breox (18.5%)	55.6	50
Breox (24%)	55.0	100

TABLEAU II.1: Fluid properties

One was able to create a fluid with the same viscosity as water, but with modified surface tension by adding just a small quantity of the copolymer to water. In this way surface tension could be investigated as well. By increasing the copolymer concentration surface tension remains constant, but viscosity increases. The corresponding range of dimensionless numbers are shown in table II.2.

Re_B	[100 - 35000]
Eo	[3.5 - 450]
Mo	[10^{-11} - 10^{-7}]

TABLEAU II.2: Ranges of Dimensionless Numbers

Low values of all three numbers correspond to ellipsoidal bubbles while the higher limits indicate spherical caps which is in agreement with figure I.1.

II.1.3 Metrological Methods

In the case of 2D-BP five different metrological methods are applied in order to study hydrodynamic structures as well as oxygen mass transfer through the bubble interface. Pressure sensors, oxygen probes and PIV measurements are used to analyse the liquid phase. The bubbles or dispersed gas phase is examined by using shadowgraphy. Plus, absorbance measurements were realized to determine mixing times.

II.1.3.1 Particle Image Velocity

The particle image velocity (PIV) measurement technique is an optical method to obtain flow visualizations in form of two dimensional velocity fields.

The idea is as follows: a flat laser sheet illuminates a fluid charged with seeding particles. In orthogonal direction to the acquisition window (or to the laserstheet) a camera takes image pairs with short time-interval depending on fluid velocity. The images are divided in a certain number of submatrix or interrogation areas. Next, spatial intercorrelation is applied to every submatrix of image pairs, giving a velocity vector. Depending on image and submatrix size, resolution can change significantly. For more details of PIV application in multiphase flows, one refers to the article from (Lindken & Merzkirch, 2002). In our case, an adaptive PIV method which is included in the image treatment software DynamicStudio from Dantec, is used. This method iteratively optimize the size and shape of each interrogation area in order to adapt to local flow gradients and seeding densities. In this way, field resolution can be improved. The acquisition window was fixed to $1600 * 840$ $pixels^2$ which corresponds to $167 * 87$ mm^2 covering half of the column width. The right top angle of the interrogation window is just next to the pressure sensor on the right side. The intercorrelation matrix size could be decreased to $16 * 16$ $pixels$, the time between images was fixed to $2ms$ and the acquisition frequency to $15Hz$. Rhodamin-B colored particles with size range from $1\mu m$ to $20\mu m$ are used as seeding particles because of their light spectrum. Indeed, the highest light absorption is in the green range with a peak at $550nm$ while the highest emission is in the orange and red range with peak at $590nm$. Hence, a green ($532nm$) laser (Skylight from Dantec) is used as lightsource for Rhodamin-B particle excitation. Plus, a highpass light filter (over $570nm$) is installed to the camera in order to only register the emitted red light from the particles. In this way, light reflections from bubble interfaces could be avoided on PIV-images. In order to obtain a good statistic of at least 20 oscillation periods, 10000 image pairs are taken during every experiment.

II.1.3.2 Shadowgraphy

A second camera with the exact same interrogation window (as the first one for PIV) is used for shadowgraphy in order to analyze the gas phase. Informations about bubble size, shape, spatial distribution and velocity are extracted. Plus, a second acquisition window over the whole column width is used in order to perform complementary void fraction measurements. The second window is fixed to $2048 * 1280$ $pixels$ corresponding to

$28.7 * 17.9\ cm^2$. One must mention that shadowgraphy is a two dimensional measurement. Because of the high image depth of camera objectives, the whole column depth is taken into account. This is particulary important, when it comes to void fraction calculations. A homogeneous LED-pannel is installed behind the transparent column. The camera registers projected shadows of each bubble on the interrogation window. Bubbles appear as dark shadows because of the light refraction on the interface as illustrated in figure II.3.

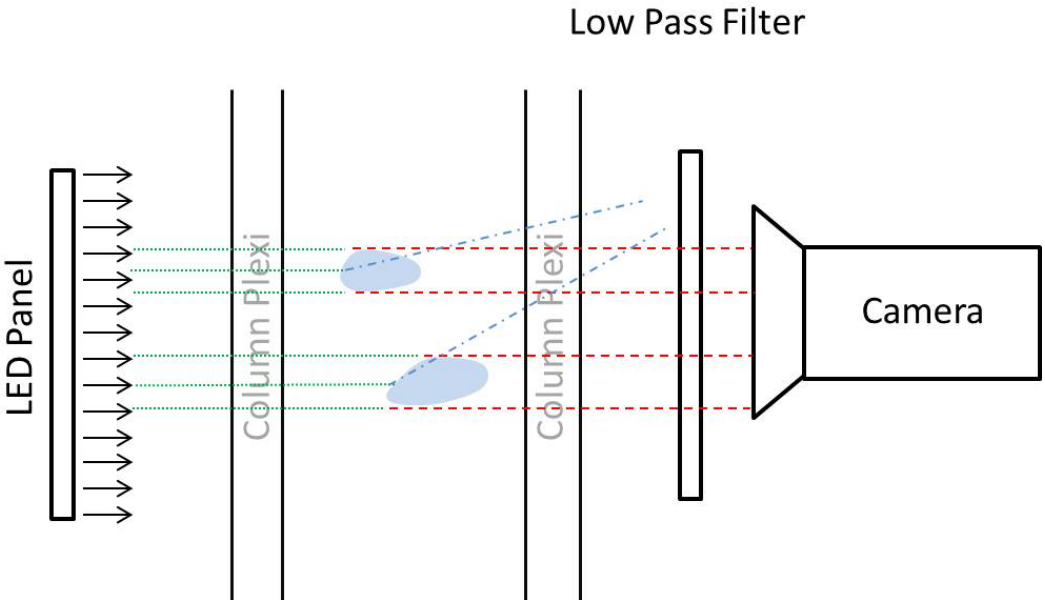

Figure II.3: Shadowgraphy - Experimental Setup

The frequency is the same as for PIV measurements ($15Hz$) and image pairs are taken with a time interval of $2ms$ as well. Both cameras are perfectly synchronized. In our investigation a blue LED-pannel (at $480nm$) and a bandpass light filter (around $480nm$) are used. Hence, the second camera captures only the gas phase without any light perturbation from the PIV laser. In this way, one could make sure to focus on just one fluid at the time per camera in order to consider both phases separately. In case of shadowgraphy 10000 images pairs are taken for the same reason than for PIV.

II.1.3.3 Image processing

Authors like (Ferreira *et al.*, 2012), (Mikaelian *et al.*, 2015) and others used shadowgraphy to characterize bubble morphology in terms of size distribution and shapes in more or

less dense bubbly flows. In most cases, a bubble size based filter is applied that one wanted to avoid here. Our data treatment is supposed to be applicable to all kinds of bubble sizes and shapes, even in bubbly flows with polydispersed size distribution. The idea is to isolate well identified bubbles (WIB) in order to extract informations like bubble eccentricity as a function of bubble size. The second aim is to characterize bubble interactions well enough to calculate void fractions as close as possible to reality. Hence, an algorithm in Matlab was developed to detect all kinds of objects on shadowgraphy images and identify their nature such as overlapping, coalescing, upbreaking and deformed single bubbles. First of all, non homogeneities of the background light are removed by applying a so called flat on every image. The flat is nothing else than a shadowgraphy picture of the same acquisition window without any bubbles. A light filter is used to further intensify object contours as it can be seen in figure II.4.

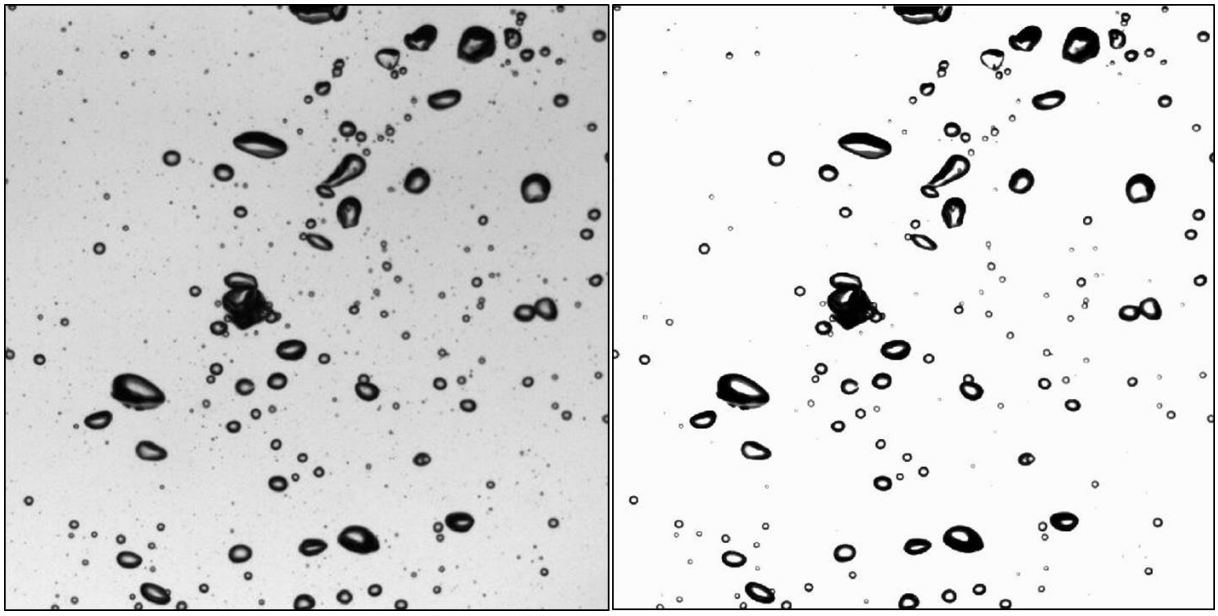

Figure II.4: Left: Raw Image; Right: Flat + Lightfilter

These contours, corresponding to projected interfaces, are then identified by searching the highest light intensity gradients. Images can now get binarized where 0 corresponds to the liquid phase and 1 to the gas phase. Possible holes inside bubbles due to light refraction or uncorrect alignment of the light source, bubbles and the camera, must be filled (see figure II.5).

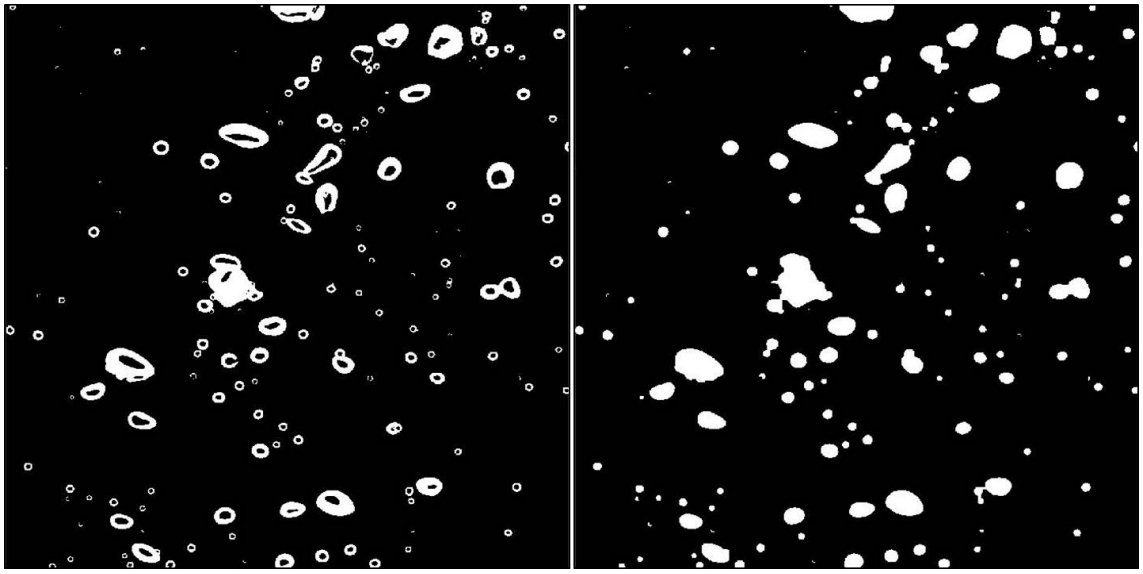

Figure II.5: Left: Binarized Image; Right: Binarization + Hole Filling

Spatial distribution First, bubble position/distribution is used to analyze low frequency oscillations, or in other words to follow the wandering bubble swarm movement. The gravity center and the associated projected surface area of every bubble is calculated. The gravity center of all bubbles is then calculated for every image as follows:

$$(x_{gc}, y_{gc}) = \frac{\sum_{i=1}^{n}(x_i, y_i)A_i}{\sum_{i=1}^{n} A_i} \tag{II.1}$$

where (x_i, y_i) is the gravity center, A_i the projected surface area of each bubble and n the number of bubbles. Figure II.6 shows a raw (left) and a binarized image (right). On both, the gravity center position is indicated. By plotting the horizontal position in time, bubble swarm motion could be followed (see figure II.7).

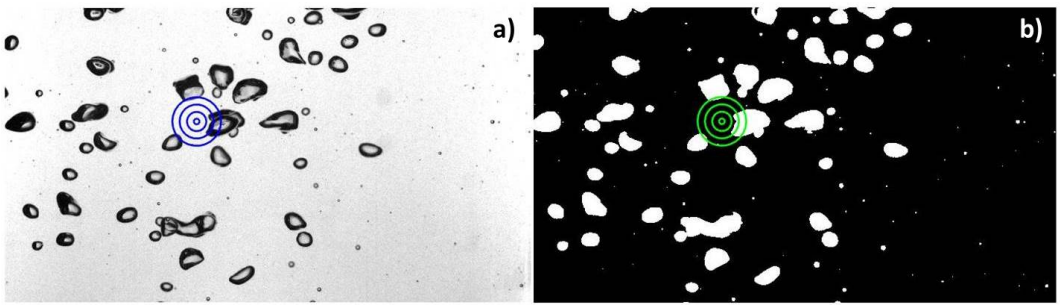

Figure II.6: Image treatment of shadowgraphy with gravity center position of all bubbles; Left: raw image; Right: binarized image

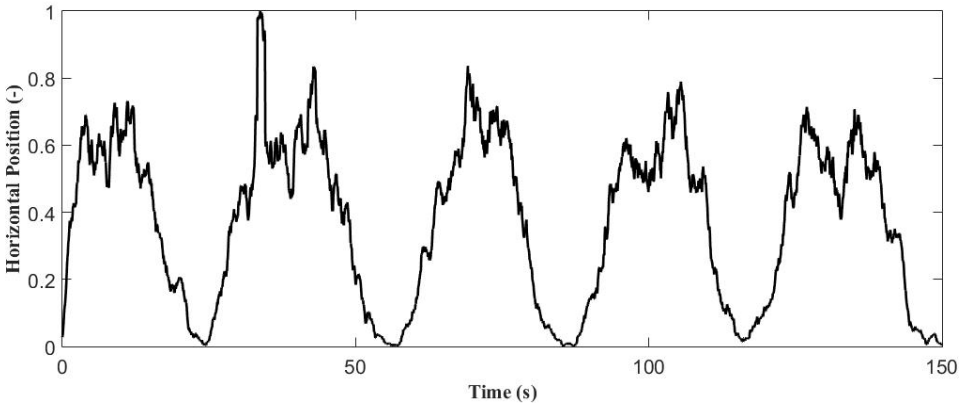

Figure II.7: Bubble Gravity Center Position followed in time

Object Identification Binarized images are also used to identify the nature of objects. For two reasons it is important to separate single, so called "Well Identified Bubbles" (WIB) from all other possible situations like overlapping, coalescence, break-ups which will be named "Complex Situations". First, the WIBs will be used to extract statistical informations concerning size and shape. Second, all detected objects shall be treated correctly in order to calculate in the best manner the corresponding volume enabling us an estimate of the global void fraction as close as possible to reality. Therefore, a series of filters are applied to every single detected object as illustrated in figure II.8.

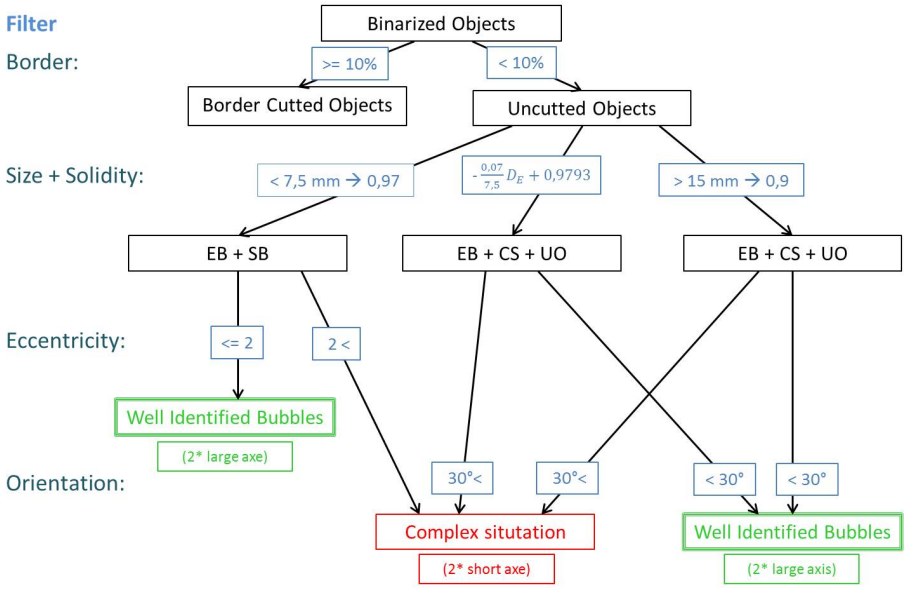

Figure II.8: Scheme of applied filters where: SB = Spherical Bubbles; EB = Ellipsoidal Bubbles; CS = Spherical CAPS; UO = Undefined Objects

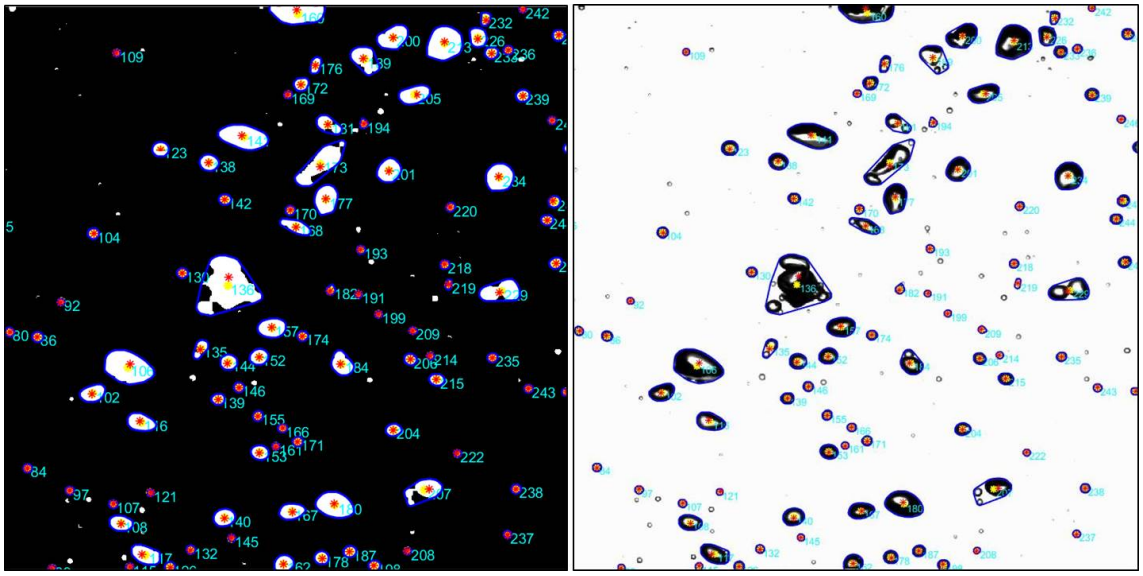

Figure II.9: Smallest Polygon possible projected on Binarized (left) and on Raw Image (right)

All objects having more than 10% of their contours length belonging to the image borders, are rejected. The resting objects are considered as uncutted.
Secondly, solidity, the proportion of pixels in a convex hull (smallest possible polygon illustrated as blue lines in figure II.9) surrounding the considered object and its raw projected area (white area on binarized images), in combinaison with bubble size is checked.

$$Solidity = \frac{A_{Raw}}{A_{Polygon}} \tag{II.2}$$

The threshold of $7.5mm$ of the equivalent diameter is chosen empirically to adapt solidity. For better understanding the polygons are projected on binarized and on raw images as shown in figure II.9. For bubbles smaller than $7.5mm$ a high solidity of 0.97 is defined to make sure that only single bubbles are detected since ellipsoidal bubbles shall be characterized in the best way possible. For large bubbles with an equivalent diameter over $15mm$, a solidity of 0.9 is chosen. Projected shadows of such bubbles can show strong deformation due to interface instabilities which results in lower solidity values. Furthermore, overlapping of a large and a small bubble can fall in this category. This is wanted because the generated potential error is very small. Plus, the distinguishment between these two situations is almost impossible or would require a way more complex

image processing. However, in between the above mentioned points, the following linear function is defined to relate both thresholds:

$$Solidity = -\frac{0.07}{7.5} D_E + 0.9793 \tag{II.3}$$

Under the defined solidity limits, objects are classified as complex situations (COSIs). These objects will not be used for bubble morphology characterization and treated slightly differently for void fraction calculations which will be explained in detail in the following paragraph.

An additional test is applied to WIBs to make sure to exclude every kind of complex situation and take only "real" bubbles. Hence, bubble eccentricity defined as the ratio of the large and small axis of the projected ellipse (see section I.7) is used in the case of ellipsoidal bubbles ($D_E < 7.5mm$). For the considered bubble size range, the limiting value of 2 seems to be reasonable. If eccentricity is larger, the detected object must be constituted of at least two overlapped bubbles and will be rejected. In the case of larger bubbles ($D_E > 7.5mm$) bubble orientation is used to distinguish between single bubbles and COSIs. The bubble orientation can be described by the angle between the large axis (see section I.7) and the horizontal line. Once again to make sure to extract only WIBs, the limiting angle was fixed to 30°. Over this value, objects are considered to correspond to COSIs and are not taken into account for bubble eccentricity identification.

Volume Calculation

The volume calculation of an ellipsodial bubble was already presented in paragraph I.1.1. For ellipsoidal bubble shapes, the ellipse projection on bubble shadows makes necessarily sense since it is almost the exact geometry from the side view. But what is about the volume of spherical caps and complex situations? And how can one calculate a volume, being three dimensional, in a correct way out of images that are only two dimensional? And what are the errors made?

Our image treatment is based on two dimensional measurements of projected shadows. As already presented, bubble volumes are reconstructed to determine the equivalent bubble diameter as good as possible. Hence, our approximation must fit to the two dimensional raw areas. Therefore, the choice was made to keep the inertia moments of the projected

area. In this section the resulting areas are compared to estimate possible errors. For every registered two dimensional shadow area the same moments of inertia I_{ij} are calculated following the inertia tensor:

$$J = \begin{vmatrix} I_{xx} & I_{xy} \\ I_{xy} & I_{yy} \end{vmatrix}.$$

where $I_{xy} = 0$, $I_{xx} = \int y^2 dxdy$ and $I_{yy} = \int x^2 dxdy$ which becomes in the case of an ellipse:

$$I_{xx} = \frac{\pi a b^3}{4} \tag{II.4}$$

$$I_{yy} = \frac{\pi a^3 b}{4} \tag{II.5}$$

To estimate the errors for different bubble-like geometrical shapes two extreme cases, which are a hemisphere and a spherical cap with an opening angle θ, are considered.

Hemisphere

Let us begin with the hemisphere since this geometry is the simpler one. The inertia moment conservation can be expressed by the following equation:

$$I_{xx_{Ellipse}} I_{yy_{Ellipse}} = I_{xx_{Hemisphere}} I_{yy_{Hemisphere}} \tag{II.6}$$

where:

$$I_{xx_{Hemisphere}} = \Big(\frac{\pi}{8} - \frac{8}{9\pi}\Big) r^4 \tag{II.7}$$

$$I_{yy_{Hemisphere}} = \frac{\pi}{8} r^4 \tag{II.8}$$

By using the last three equations, the following relation can be determined:

$$A_{Ellipsoid} = 1.029 A_{Hemisphere} \tag{II.9}$$

This proves that the registered two dimensional area can be considered as not modified by our treatment in the case of an hemisphere. The maximum error made is less than 3%.

Spherical Caps

After the hemispherical shape the spherical cap one is checked. The same strategy is used to conserve the inertia moments of the raw two dimensional area. The inertia moments of spherical caps in the gravity center can be written as:

$$I_{xx}(r,\theta_s) = \frac{r^4}{4}\Big(\frac{2\theta_s + sin(2\theta_s)}{2}\Big) - \frac{r^4}{4}\cos^2(\theta_s)\sin(2\theta_s) - \frac{8}{9}r^4\frac{\sin^6(\theta_s)}{2\theta_s - sin(2\theta_s)} \tag{II.10}$$

$$I_{yy}(r,\theta_s) = \frac{r^4}{4}\Big(\frac{2\theta_s - sin(2\theta_s)}{2}\Big) - \frac{r^4}{12}sin^2(\theta_s)sin(2\theta_s) \tag{II.11}$$

where θ_s correspond to half the opening angle θ.

$$A_{Caps}(r,\theta_s) = \pi r^2\Big(\frac{2\theta_s - sin(2\theta_s)}{2\pi}\Big) \tag{II.12}$$

By using the last expression and the following one:

$$I_{xx_{Ellipse}}I_{yy_{Ellipse}} = I_{xx_{Caps}}I_{yy_{Caps}} \tag{II.13}$$

one obtains:

$$A_{Ellipsoid} = coef(\theta)A_{Caps} \tag{II.14}$$

The last equation illustrates that the error depends on the angle of the spherical cap which is not surprising. Therefore, the coefficient is plotted as a function of θ in figure II.10. The ratio never exceeds the value 1.05. This means that the maximum error made in the case of spherical caps is less than 5%.

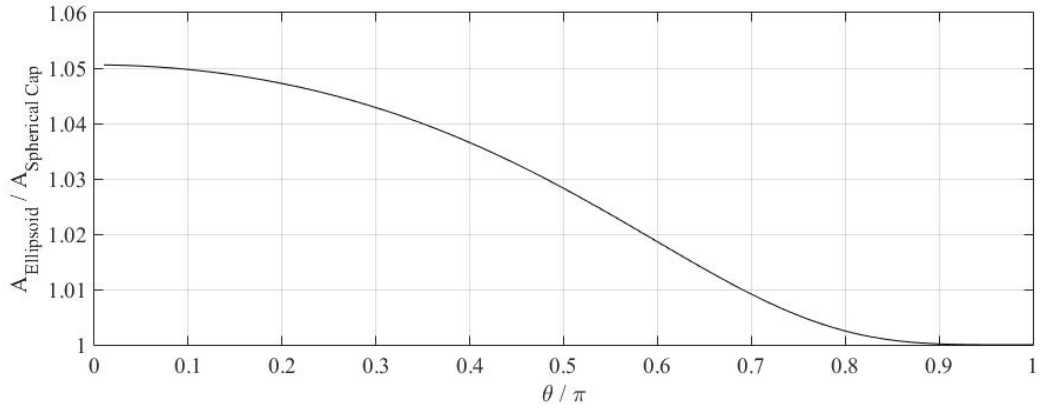

Figure II.10: Ratio of $A_{Ellipsoid}$ and A_{Caps} as a function of θ

Complex Situations

Another error source, and probably the largest one, can derive from the volume calculation of complex situations. In most cases, these situations correspond to bubble overlapping. While in the case of single bubbles a flattened sphere seems to be a good approximation, in case of weakly overlapping bubbles one could overestimate the considered volume. For this raison, the decision is made to take rotation symmetry about the large axis M which can be expressed by the following equation (Treatment 1):

$$V_{Ellipsoid} = \frac{4}{3}\pi m^2 M \tag{II.15}$$

In this way one makes sure not to overestimate the volume of the corresponding object. On the other hand, this choice includes void fraction underestimations that are more or less important depending on the injected gas flow rate. However, one expects that the truth is somewhere in between the two mentioned possibilities of COSI volume calculation (equation I.5 (Treatment 1) and equation II.15 (Treament 2)). From now on only Treatment 1 is considred for the experimental part of this work. An example of ellipse projection on binarized and raw images can be seen in figure II.11. The following discussion will be a comparison between statistical results from WIBs and COSIs. An original way to verify image processing will be presented for two test cases.

Test Case 1: $50\frac{l}{h}$, Water, EB

To validate our image processing two test cases are chosen. For the first one, ellipsoidal bubbles are injected in water through a membrane with a flow rate of $50\frac{l}{h}$ generating an

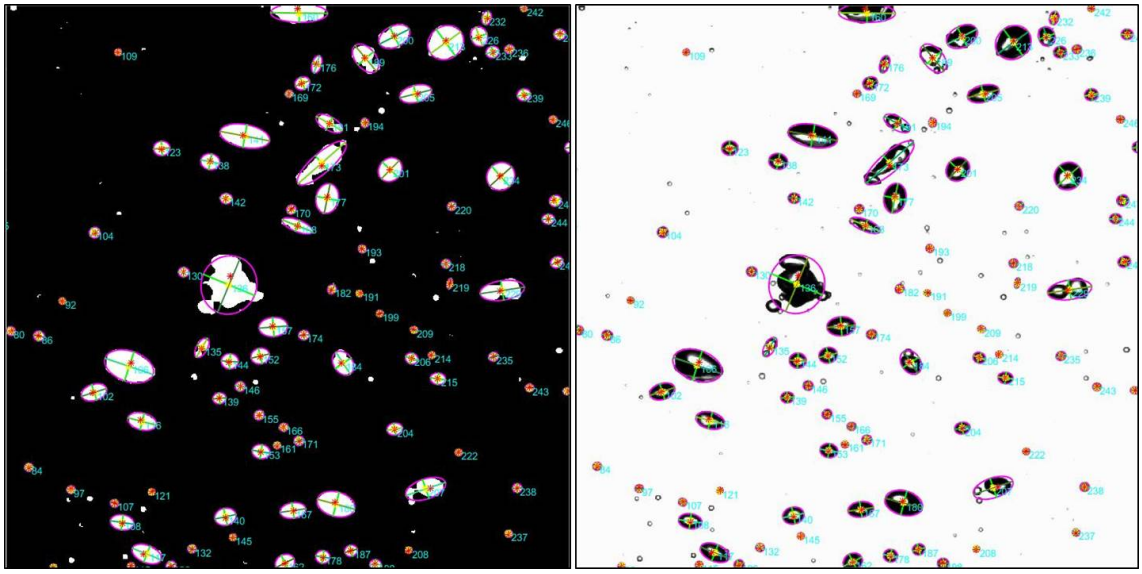

Figure II.11: Ellipse Projection on binarized (left) and raw images (right)

almost monodisperse bubble size distribution. The low gas injection rate induces only a small void fraction making image treatment easier. Figure II.12 shows the bubble size distribution in the form of total gas volume (during the whole experiment) as a function of the equivalent bubble diameter. Stars are indicating the total volume of WIBs while dots represent COSIs. The shape of both curves are quite different. WIBs show an almost symmetric Gaussian distribution centered around $5mm$ and COSIs an asymmetric one that is shifted towards higher values of the equivalent diameter. Since the considered experimental case shows monodisperse size distribution without coalescence or collapse, one concludes that COSIs can only correspond to overlapping bubbles. This result is consistent with manual visual comparisons of raw images suggesting that our image processing is accurate. However, at this point, the statistical volume averaged bubble size corresponding to $5mm$ can already be identified.

To further validate our image treatment figure II.13 is plotted where solidity, orientation and eccentricity are presented as a function of the raw projected area and the raw contour. Every point corresponds to a single bubble and the colorbar indicates the three considered parameters of every subfigure. Three lines corresponding to geometrical relations between area and contour are drawn. The solid line, the dash dotted line and the dashed line represents relations for a circle, an ellipse with $\chi = 2$ and a spherical cap with an opening angle of 100°, respectively. The corresponding equations are written as follows:

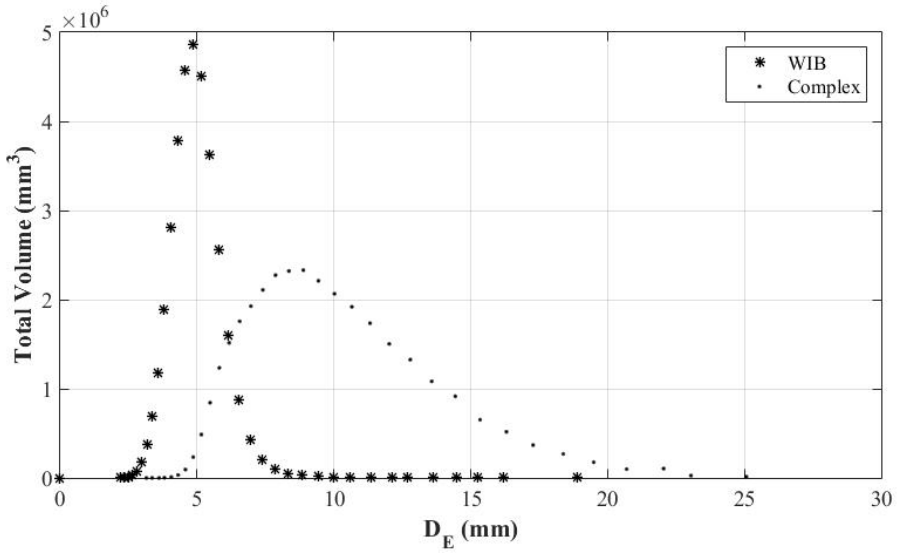

Figure II.12: Total Volume as a function of the Equivalent Diameter for WIBs and COSIs

$$A_{circle} = \frac{1}{4\pi} C_{circle}^2 \qquad with \qquad C_{circle} = 2\pi r \tag{II.16}$$

$$A_{ellipse} = \frac{1}{5\pi} C_{ellipse}^2 \qquad with \qquad C_{ellipse} \approx 2\pi \sqrt{\frac{m^2 + M^2}{2}} = 2\pi m \sqrt{\frac{1 + \chi^2}{2}} \tag{II.17}$$

$$A_{cap}(\theta) = \left(\frac{\theta - sin(\theta)}{2(\theta + 2sin(\frac{\theta}{2}))^2} \right) C_{cap}^2 \qquad with \qquad C_{cap} = \theta r + 2r sin\left(\frac{\theta}{2}\right) \tag{II.18}$$

where $\theta = \left(\frac{100°}{180°}\right)\pi$.

By taking a closer look to figure II.13, one recognizes that most WIBs are situated in the region between the solid and the dash-dotted line, so between a circle and an ellipse corresponding well to the considered bubble size range. Only in the region of very small bubbles, data points are located under the solid line indicating small error generation in our data processing. To understand where this uncertainty comes from, one shall keep in mind that lines are compared to surfaces ($\frac{Contour}{Surface} = \frac{\pi D_E}{\pi\left(\frac{D_E}{2}\right)^2} = \frac{4}{D_E} \propto \frac{1}{D_E}$). By deriving this relation the uncertainty can be obtained ($\propto \frac{1}{D_E^2}$). Last one decreases with increasing size, which partially explains the continuous decrease of the exceeding

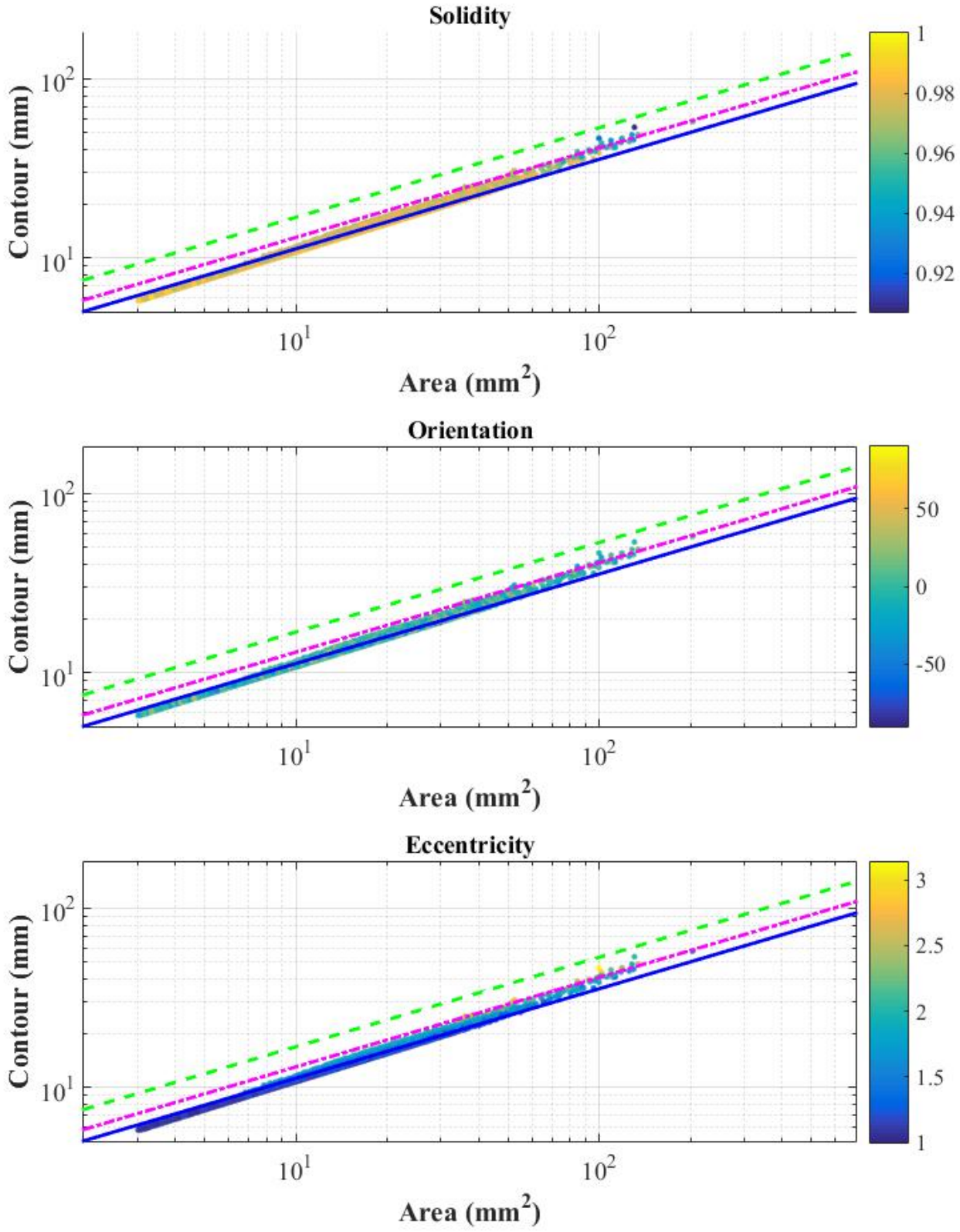

Figure II.13: Solidity, Orientation and Eccentricity as a function of Raw Area and Contour for WIB (in Water and 50 lph)

of the lower limit. The second error source is the length calculation of a curved line (here contour) on a square grid as it is the case for our shadography pictures. Therefore, the chain code is used, which were first proposed by (Freeman, 1961) and improved by (Groen & Verbeek, 1978). To calculate the length of a random line, the authors suggested to use probabaility density functions applied to the Freeman code in order to better estimate the exact length. This is done to take into account the position of two pixels to eachother (hoizontal/vertical or diagonal) since the distances are not the same(1 or $\sqrt{2}$). Furthermore, a decreasing error with increasing segment number was shown. In the following, (Proffitt & Rosen, 1979) investigated errors and coding efficiency for the representation of lines and edges. They projected a straight line at different angles on a square grid and studied the generated errors and standard deviations for several encoding schemes. These authors as well reported a decreasing behavior of the average error with increasing segment number. Finally, (Vossepoel & Smeulders, 1982) further improved the method and used a least-square fit. The authors also presented a more sophisticated quantization method, called Vossepoel-Smeulders Algorithm, which is implemented in Matlab and used for the present investigation. This method underestimates slightly, but systematically the length of horizontal and vertical pixel connections. Since the segment number (here image resolution) play an important role in error generation, this underestimation is more pronounced at lower bubble size values. However, with increasing bubble size, data points come closer to the dash dotted line meaning that bubbles are getting more and more flattened or deformed. This result is quit convincing, especially if one remebers that thousands of bubbles are presented.

Let us now check the considered filter parameters. As expected, solidity is rather constant at high values confirming the correct functioning of our first filter. Even at higher bubble size values, solidity is not varying much. The second parameter, eccentricity, is mainly around a value of 1.5 being in agreement with the literature for the considered bubble size in water. This proves also the good performance of our treatment to isolate WIBs. Furthermore, bubbles rotate and can be registered in all kinds of positions or angles to the horizontal axis. This is the reason why orientation is checked as well. Once again, the results seems to be consistent because determined angles are centered around 0°, or in other words in horizontal position. This is the best position to characterize bubbles properly, which is another advantage of our data treatment.

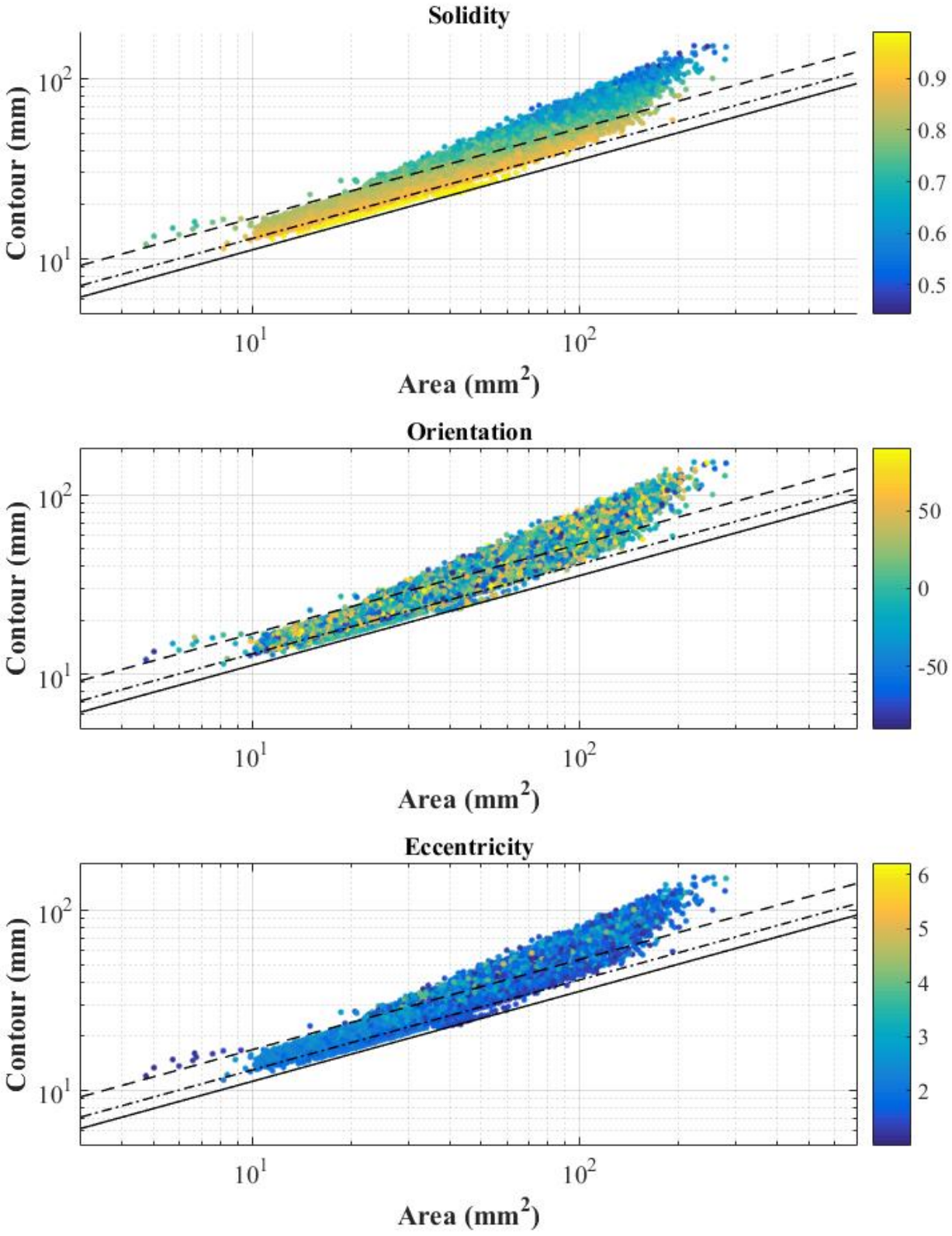

Figure II.14: Solidity, Orientation and Eccentricity as a function of Raw Area and Contour for Complex Situations (in Water and 50 lph)

In figure II.14 the same kind of data with the already mentioned geometrical lines is presented for COSIs. The first observation is the low number of small bubbles, which is coherent, since they are almost not deformable and the probability of very small overlapping bubbles is low. The region characterizing elipsoidal bubbles (between solid and dash dotted line) is almost empty as well indicating that objects from this region are already categorized as WIBs. On the other hand, large objects are detected being loutside of the defined borders. Remembering the simple test case conditions whithout coalescence, break-ups or large deformed bubbles, one can easily conclude that these objects can not be single, but must be multiple overlapping bubbles. A large number is even located in regions where shadow shapes must be very complex and therefore composed of a large number of bubbles. To further investigate COSIs, the above mentionned parameters can serve to get additional information. For example, a strong relation between solidity and the contour for a given area is found. Solidity decreases lineraly with increasing contour values in orthongonal direction to the geometrical lines illustrating the importance of this paramter to get information about deformation in the case of bubbles. But the deformation is not enough, to identify correctly object's nature, which is why orientation is checked as well. Obviously, no clear relation between orientation and contour/area could be found, independantly of object's size. The large dispersion becomes even clearer by comparing COSI's orientation distribution with the one of WIBs from figure II.13. Indeed, bubble overlapping is a random event and no prefered direction exists. However, if the parameter is used in combination with others, bubble overlapping could be seperated from other COSIs. The third parameter, eccentricity, does not evolve much and increases only slightly with increasing contour, but small values can be found in every region of the figure showing that the parameter is not suffisant to identify objects. Besides, large values until six are also obtained corresponding to overlapping of multiple bubbles. Again, limiting values could be defined and used in combination with other parameters in order to distinguish overlapping from COSIs. After validating our shadowgraphy image treatment, two main informations can be deducted. The first objective was to characterize bubble shapes properly. Therefore, eccentricity is plotted as a function of the equivalent diameter as illustrated in figure II.15. To take into account only trustable data, the statistically relevant bubble size range from figure II.12 should be considered. The interval from $3.5mm$ to $6.5mm$ is a reasonable choice to determine bubble shapes here.

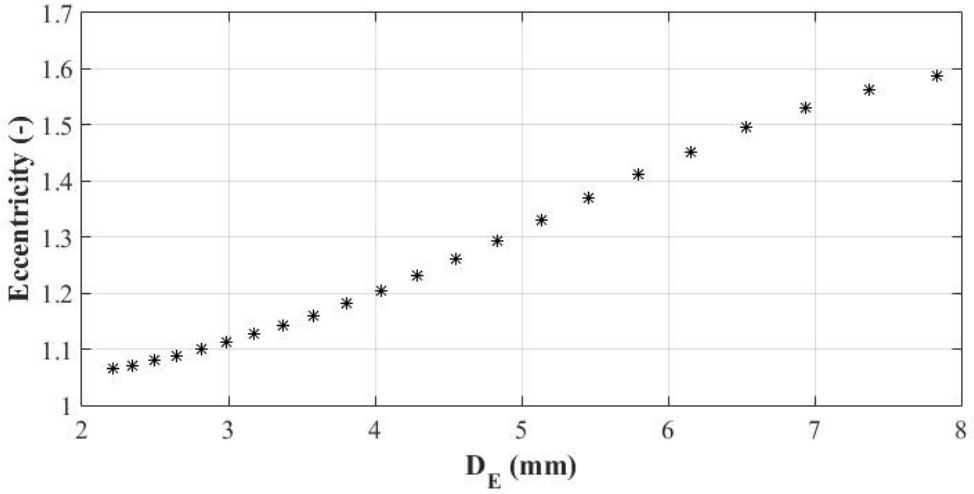

Figure II.15: Eccentricity as a function of the Equivalent Bubble Diameter in the case of WIBs

The second objective was to obtain the void fraction profile as plotted in figure II.16. The dash-dotted, the dotted and the solid line represent the overall, the COSI and the WIB void fraction, respectively. Both WIBs and COSIs represent approximately half of the global void fraction. At this point, one has to remember our choice of volume calculation of COSIs (see section II.1.3.3). Since the corresponding void fraction represents half of the total void fraction, the way of volume calculation is very important. The presented choice is keept, but it should be mentioned that the underestimation is larger than expected. The truth is certainly in between the two presented volume calculation possibilities. However, it is interesting to note that in the case of COSIs, dispersion is smaller and the two peaks are more pronounced. This result shows the connection between the local gas hold-up and the frequency of bubble interactions. In the center and at the edges of the total void fraction profil, it is easier to extract information concerning bubble characterization.

Test Case 2: $50\frac{l}{h}$**, Breox** (24%)**, CAPS**

For the second test case, spherical cap bubbles are injected in Breox 24% (of mass concentration corresponding to 100 times the viscosity of water) through a $1m$ long tube. In such viscous fluids, well shaped and especially stable caps are formed. In this way, statistical data can be extracted for the considered bubble type as shown in the following paragraph. In figure II.17 bubble size distributions for WIBs and COSIs are presented. The first observation is that way more WIBs than COSIs are identified. In this case,

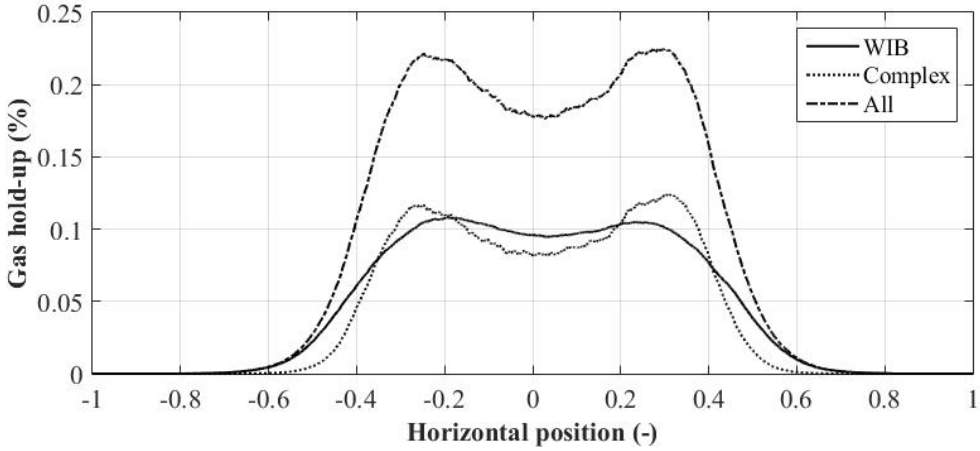

Figure II.16: Void Fraction Profil in Horizontal Direction in the case of Water, Membrane Injection and a Flow Rate of $50\frac{l}{h}$

bubbles are mainly isolated while rising towards the free surface and the only bubble interaction appearing is coalescence. This phenomenen was explained by (Bouche *et al.*, 2012) already mentioned in section I.1.3.4. The first bubble induces liquid agitation, which modifies the viscous dissipation and the local pressure distribution. Bubbles are aspirated in the wake and accelerated provoking coalescence with the first bubble after a certain distance. Since our interrogation window is in the column middle (only $70cm$ from the bottom), the probability to register such phenomena is rather small.

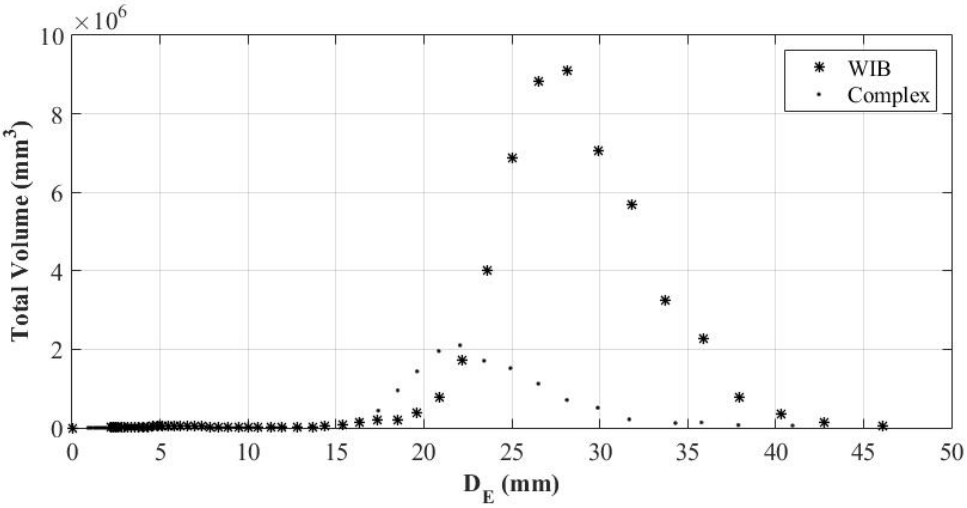

Figure II.17: Total Volume as a function of Equivalent Diameter for WIB and Complex Situations

However, shapes of the correspondng size distributions can already give us some information. The curve of WIBs is rather Gaussian like giving a statistical equivalent diameter.

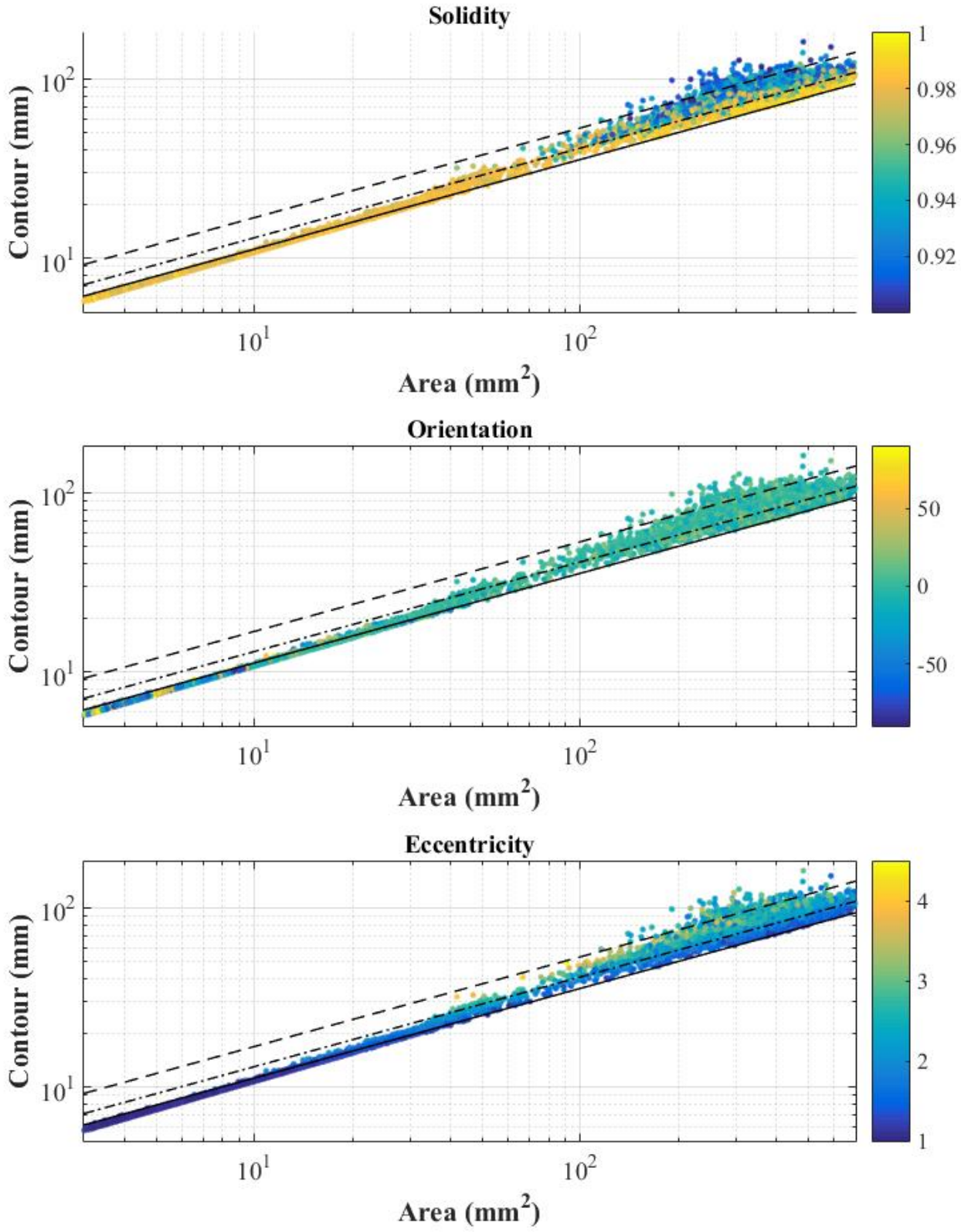

Figure II.18: Solidity, Orientation and Eccentricity as a function of Raw Area and Contour for WIB (in Water and 50 lph)

Only at high values, the shape is slightly asymmetric compared to the left half. These high values come from coalescing bubbles, which could not be filtered by our treatment. On the other hand, COSIs are centered at smaller equivalent diameter values than WIBs. One can assume that COSI volumes are underestimated since two bubbles should have a larger volume than a single one. This underestimation results from the way of volume calculation (see section II.1.3.3). Furthermore, the curve representing the size distribution of COSIs has a similar shape than COSI's size dictribution of the first test case. This may help to interpret the shape of such distributions, even without filtering of WIBs. In the present case a statistical object size could have been identified anyway.

In the same way than for the previous test case, solidity, orientation and eccentricity are plotted for both object types. Figure II.18 shows all three parameters in the case of WIBs. Axis and geometrical lines are the same as in figure II.13. First, the position of all bubbles compared to the defined geometrical lines must be analysed. Once again the majority of WIBs is located inside the defined limits. Small bubbles are generated by the slugflow sparger (used here) at the injection, at the free surface and during coalescence. This phenomenon is furthered by the decreased surface tension compared to water. With increasing size more and more bubbles are located close to the dashed line and even further, which can be explained by fluid properties. High viscosity induces higher dissipation, vorticity is damped and caps are more stable enabeling eccentricity values larger than 4. At the top of the figure, solidity is projected and shows high values for small (almost not deformed) bubbles and decreases with increasing size. Lower, but still reasonable large values approaching 0.9 can be explained by the moon liked shape of spherical caps in such viscous media. Very large bubbles with high solidtiy (close to 1) are probably coalescing bubbles, which could not have been removed by our algorithm due to their spherical shape as already mentioned above. This argument is confirmed by the eccentricity being close to 1 (to a circle) for the considered data points. Furthermore, a linear evolution of the eccentricity with increasing contour values in orthogonal direction to our geometrical lines is observed. Hence, there is a coupling between eccentricity and bubble's size and contour for the considered conditions. Finally, the orientation is mostly centered around $0°$ as for WIBs in the first test case, which is in agreement with the straight trajectory of such large acsending caps. High values for small areas correspond to overlapping bubbles of very small bubbles.

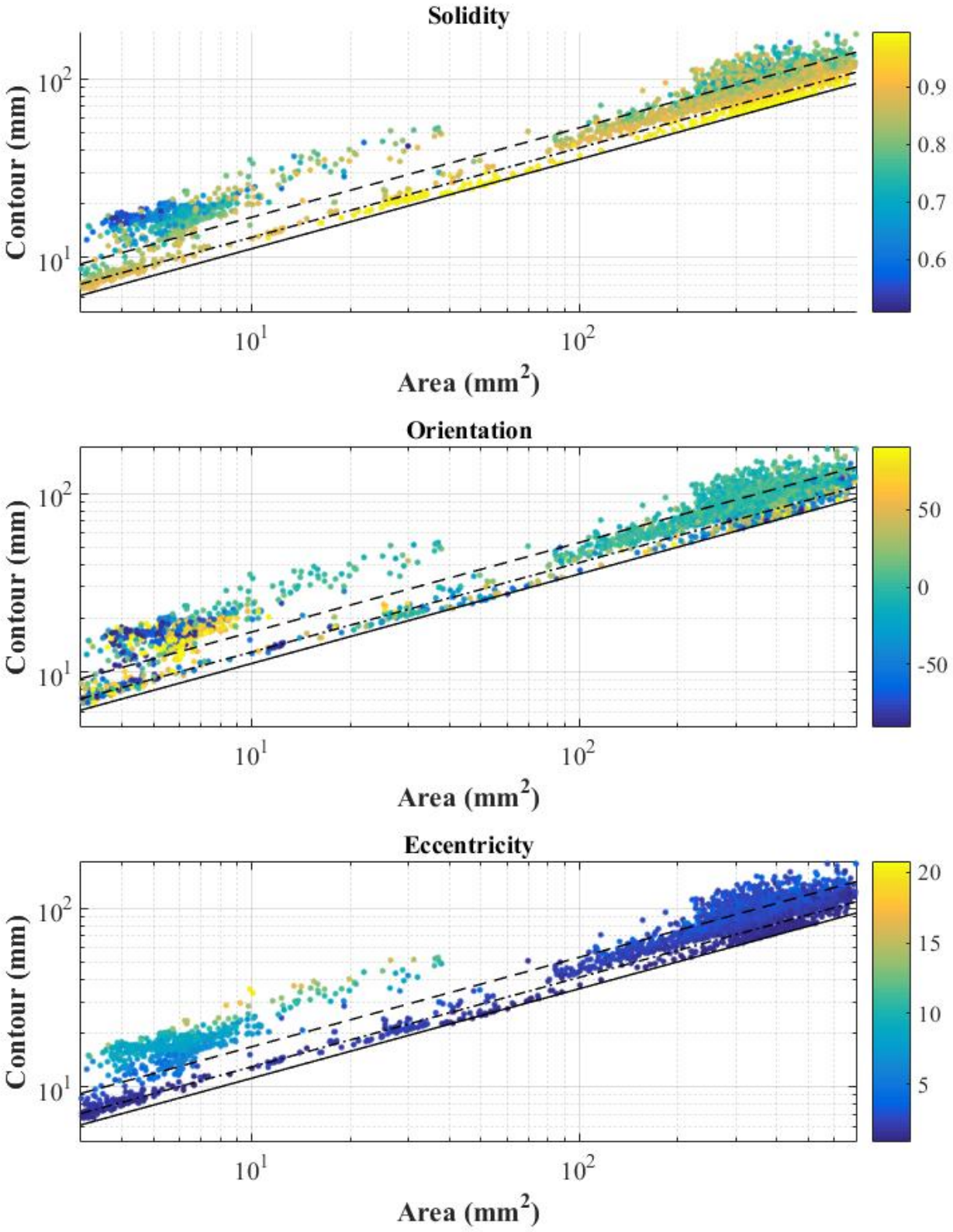

Figure II.19: Solidity, Orientation and Eccentricity as a function of Raw Area and Contour for Complex Situations (Breox (24%) and 50 lph)

Figure II.19 shows solidity, orietation and eccentricity for COSIs of the second test case to further validate our image treatment. As previously, point locations are compared to geometrical relations first. Most of the objects are located ouside the defined borders indicating that they do not correspond to single bubbles. For small sizes, spaces between the three lines are almost empty. To understand where the small COSIs are coming from, one must consider our three control parameters. Their solidity is very small standing generally for overlays. This thought is confirmed by the orientations, which are far away from 0°. Plus, all these objects show very large eccentricity values revealing overlays of more than two bubbles. Larger objects, located between the solid and the dash dotted line, show high solidity values for COSIs. These objects were filtered because of the very low and high angles. In combination with the rather low eccentricity (almost circle shaped), it can be assumed that theses are large almost coalesced bubbles.
Our analysis becomes more difficult for large objects with higher contour values. Solidity is low, but all angles are located around 0°, which is a little surprising if one remembers our filter of 30°. Eccentricity is high with values around 5 or even higher suggesting that these COSIs do not involve two or more large coalescing bubbles. But during coalescence in such viscous media, two phenomena were observed. When it comes to coalescence between a large bubble followed by a small one, the first contact appears most of the time at the edges of the large bubbles. This phenomenon is illustrated in figure II.20.

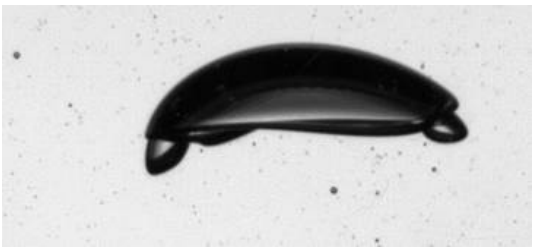

Figure II.20: Coalescence of a large and small bubbles in Breox (24%)

But why are that many bubbles registered by our image treatment if coalescence is as rare as one said in the column middle? This can be explained by the second phenomenon, which is illustrated in figure II.21. After the first contact, bubbles form some kinds of clusters. They stay attached while rising together for a certain time before coalescing. This can be explained by the high viscosity and therefore the high bubble stability. Depending on the size differences of the involved bubbles, either a bouncing (for similar sizes) or a

rotative movement of the small bubble around the big one (for large size difference) was observed. In both cases solidity decreases and eccentricity increases while keeping a horizontal position. These phenomena should be investigated in detail, but are not subject of the current work.

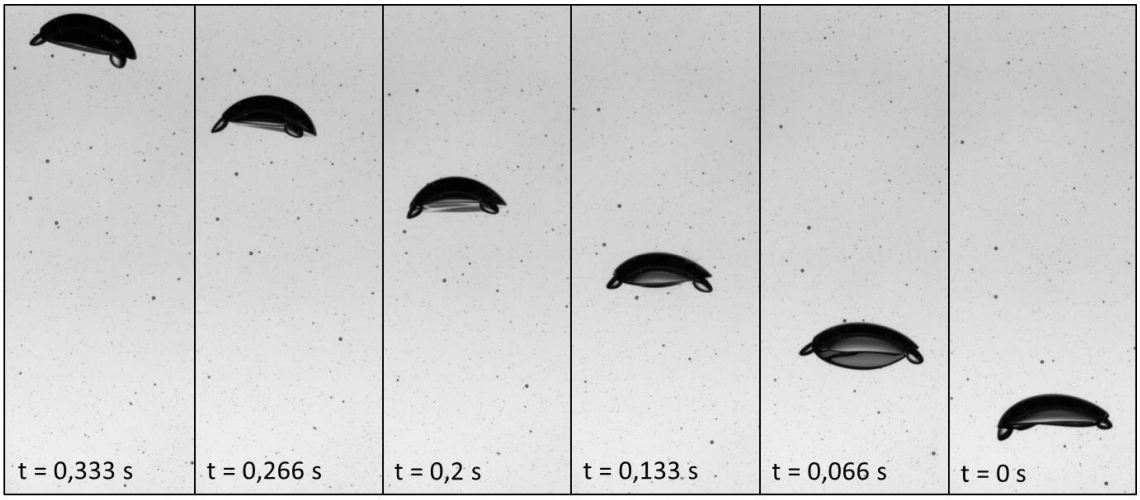

Figure II.21: Time Evolution of Coalescence of small and large Bubbles in Breox (24%)

It was shown that our algorithm is able to separate isolated bubbles (WIBs) from complex situations (COSIs) like coalescence, cluster, bouncing and overlapping. Hence, WIBs shape can be analysed as a function of the equivalent bubble diameter in a statistically coherent range as illutrated in figure II.22. In the size range $25mm < D_E < 35mm$, an eccentricity between 2.1 and 2.2 is found, which is in agreement with the theoretical value of 2.12 for a spherical cap with an opening angle of 100°.

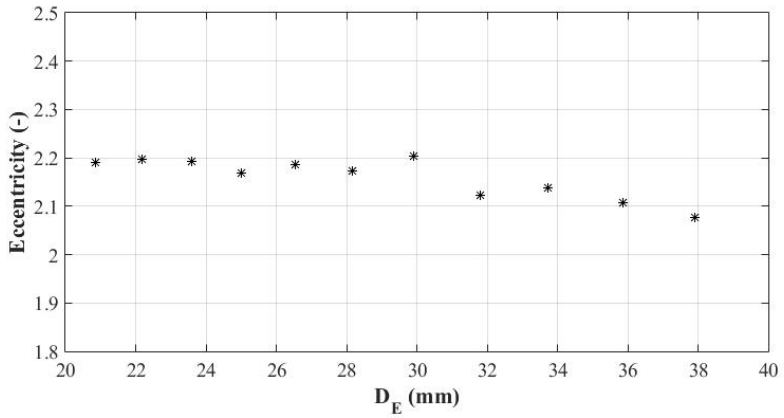

Figure II.22: Eccentricity as a function of the Equivalent Bubble Diameter in the case of WIBs

Furthermore, the void fraction profile can be plotted as shown in figure II.23. It is worth to mention that way more WIBs are identified than COSIs indicating the efficency of our image treatment. A very small dispersion of the considered bubble plume can be recognized, resulting from the high viscosity, which is damping transverse movements. One can conclude that bubbles rise on a almost straight line. The only oscillating trajectory behaviour results from coalescing phenomena and is therefore rare.

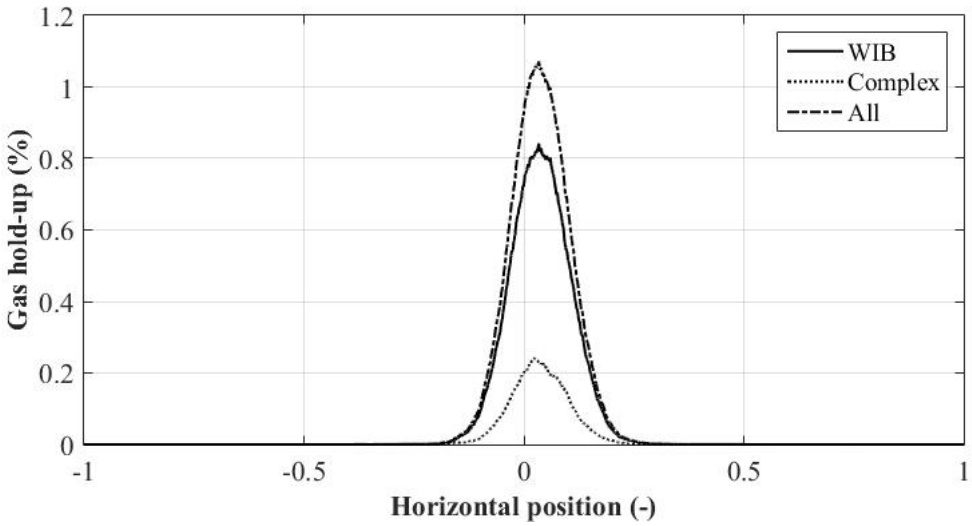

Figure II.23: Void Fraction Profil in Horizontal Direction in the case of Breox (24%), Slugflow Injection and a Flow Rate of $50\frac{l}{h}$

II.1.3.4 Bubble Image Velocimetry (BIV)

To characterize bubbles completely, the rise velocity must be determined as well. Therefore, an other algorithm was developped. As in the case of PIV, image pairs are registered with a time interval of $2ms$. This interval is imposed by the PIV or in other words by the liquid velocity since both techniques are perfectly synchronized. In order to get a sufficient velocity field resolution with high accuracy, which means with enough seeding particles in the interrogation matrix for spatial intercorrelation, $2ms$ could not be exceeded. This makes BIV complicated because bubble velocities are smaller and higher at the same time. Hence, another type of spatial intercorrelation must be applied to bubble image pairs.

First, a flat is applied to every image in the exact same way than for object identification to remove possible heterogeneities in the background. Besides, light gradients (contrasts) are slightly intensified improving image treatment. Then obejects are detected and a interrogation matrix of the same length and height is defined.
The first step after the flattening is the object detection on the first image of every pair. Then, every object is isolated and labeled. The rectangular interrogation matrix around the object plus its position is defined and then transported to the second image. This is illustrated in figure II.24 for two different objects of the same image. Around the matrix (drawn in red) a layer of 14 pixels in every direction is added to define the final interrogation matrix (whole image on the right handside of figure II.24) on the second image. The size of the layer must be large enough to detect the whole object shift to the second image, but small enough to not induce error sources by taking into account too many other objects on the interrogation matrix.

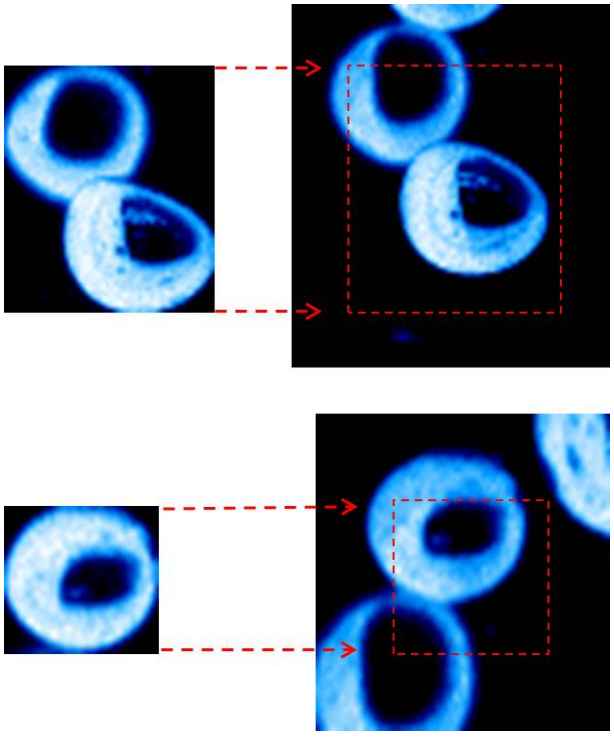

Figure II.24: Two Examples of detected Objects + Matrix Projection from the First to the Second Image

This strategy is applied to every single detected object on every image pair. Now, spatial intercorrelation can be applied between the two defined matrices. It is important

to point out that BIV should be applied to non-binarized images in order to improve spatial intercorrelations. In this way, the light intensity gradient is taken into account and even subpixel intercorrelation can be performed. Such kind of spatial intercorrelations were developped for solar observations in order to stabilize image acquisition by (Gelly *et al.*, 2008).

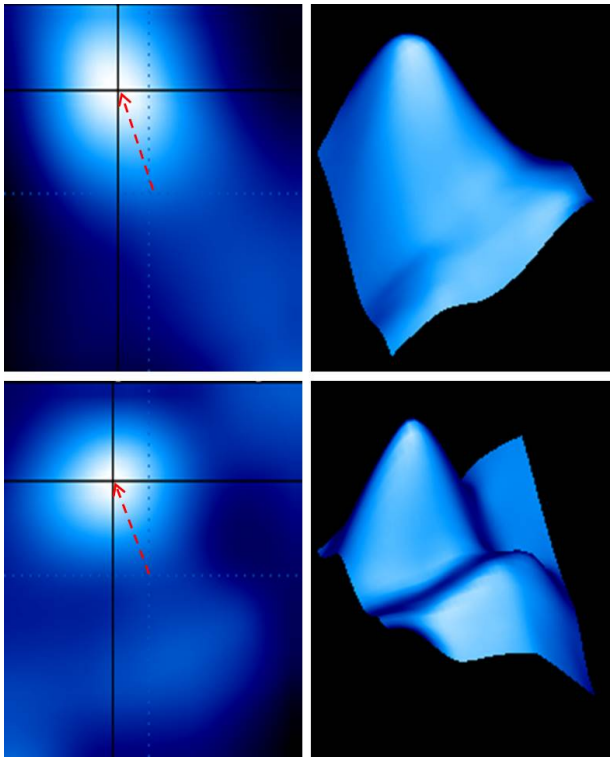

Figure II.25: Example of Spatial Correlation Maps in 2D (left) and 3D (right)

In figure II.25 the correlation maps in two and three dimensions are plotted for the two detected objects shown in figure II.24. A clear global maximum can be observed in both cases. In the first case only one global and no local maximum is found. This is because almost no other object is present on the second interrogation matrix. In the second case two other objects can be observed in the second interrogation matrix. Here, it is particulary important to treat "raw" and not binarized images. Therefore, even in the presence of two other objects generating two local maximums, a global one can be found. This example illustrates the good performance of our algorithm. By calculating the distance between the matrix center and the global intercorrelation maximum, one can determine the velocity of the considered object since the time delay of $2ms$ is fixed and known. In order to decrease calculation times the SAD method was applied. (Löfdahl,

2010) published a review paper on calculation methods of intercorrelations and compared them. The SAD method turned out to be the fastest one.

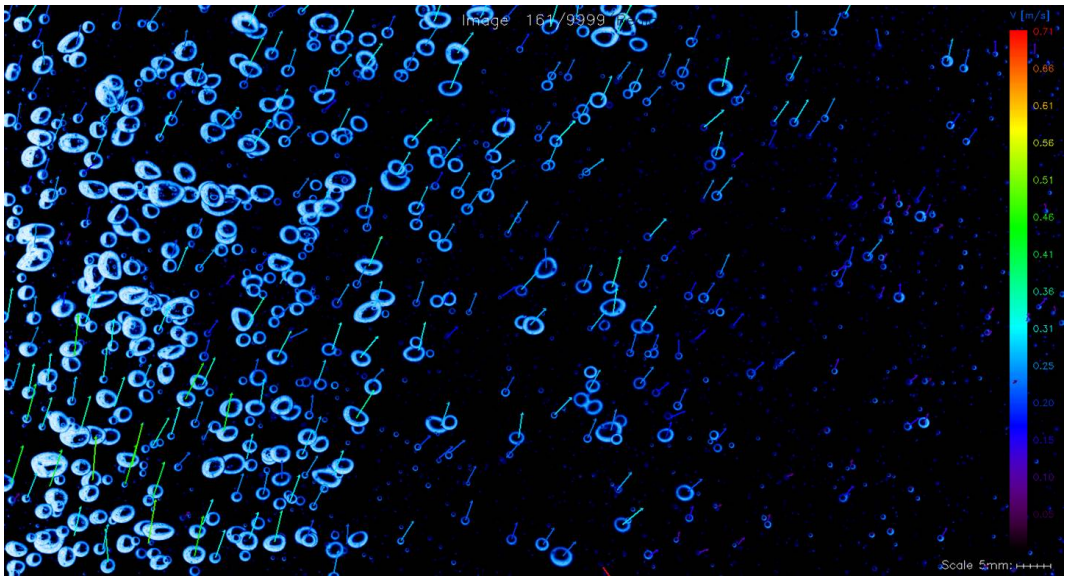

Figure II.26: Resulting Bubble Velocity Map for one image pair

Finally, the strategy can be applied to every object on all image pairs. An example of the resulting "velocity map" can be seen in figure II.26. Every detected object (WIB or COSI) shows a dedicated velocity vector. This information can be coupled with the previous object detection algorithm. Hence, velocities can also be calculated for all WIBs and COSIs.

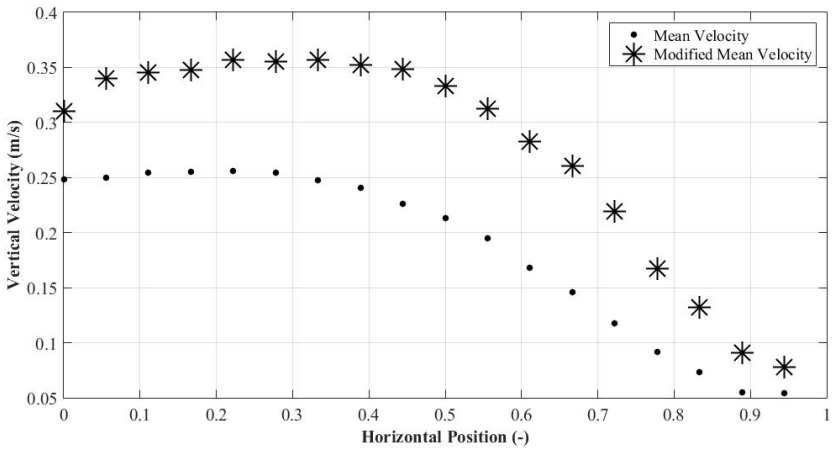

Figure II.27: Mean Rising Swarm Velocity in the case of CAPS and $100\frac{l}{h}$

However, in the present study, the swarm velocity of all objects is important. Therefore, all objects are taken into account for mean value calculations (see figure II.27). The dots are indicating the considered curve. The problem of this strategy is that all bubbles independently of their size have the same importance. Logically, this can cause problems in the case of polydispersed size distribution. For example a spherical cap bubble moves way more liquid around itself than a small one and has therefore another impact on hydrodynamic structures. Hence, the raw two dimensional surface is taken into account for every bubble to resolve the problem. This is done for every objects in all spatial intervals on the horizontal axis, which can be expressed by:

$$\overline{U_b} = \frac{\sum_{i=1}^{N} A_{raw_i} U_{b_i}}{\sum_{i=1}^{N} A_{raw_i}} \tag{II.19}$$

where $\overline{U_b}$ is the resulting mean velocity of every interval. The new modified velocity profil is plotted with stars in figure II.27. A clear increase can be seen in comparison with the standart mean velocity (dots). This is coherent since larger objects showing higher velocities are getting more importance. These larger objects are supposed to "control" swarm velocity and must be treated differently.

II.1.3.5 Mixing Time

Since this work is dealing with hydrodynamics and mixing, one has to talk about time scales characterizing column mixing. Therefore, additional experiments were performed where blue methylen dissolved in water is injected at the column side close to the bottom. In this region, close to the sparger, plume oscillation is not developped. Hence, the initial injection moment is independent of the bubble plume position. Light absorption of the considered media is used to determine the moment when the steady state is reached and the continuous phase and the dye in the column are perfectly mixed. Two white LED panels and two cameras (Basler) are used to define two interrogation windows of the same size ($5cm \times 5cm$)(see figure II.28).

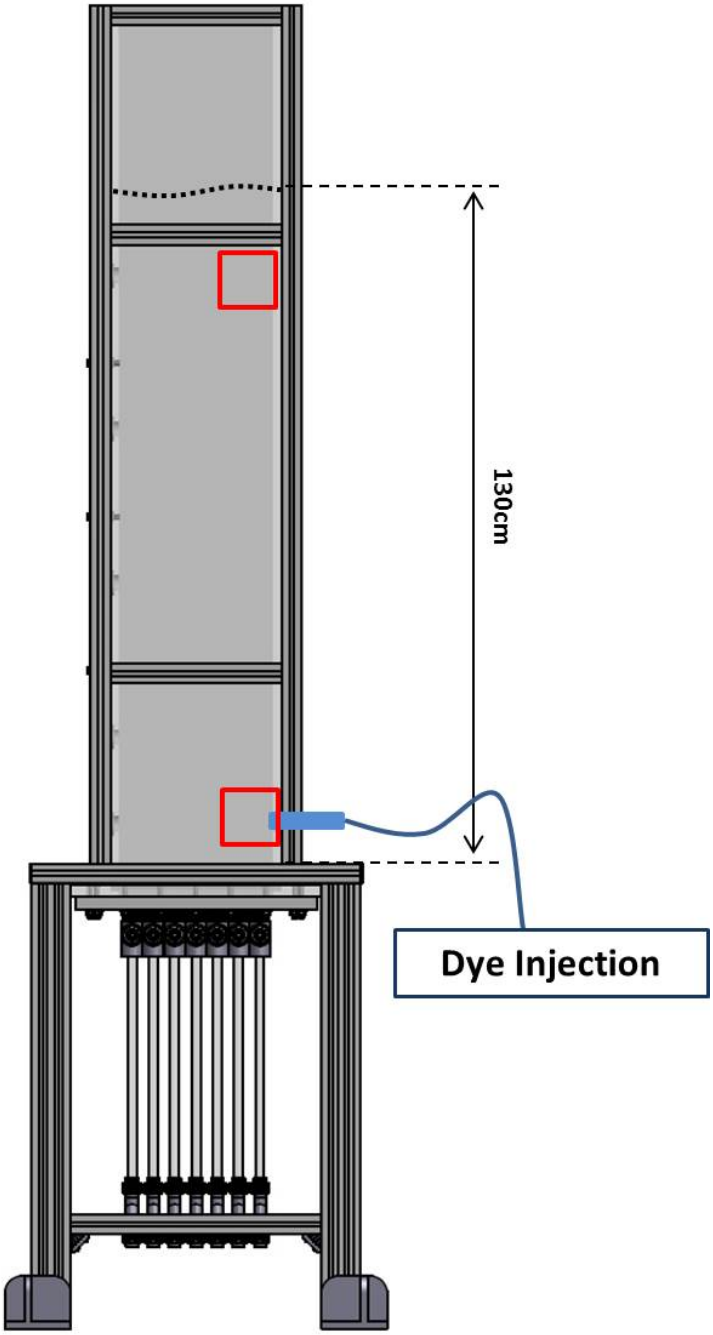

Figure II.28: Experimental Setup for Mixing Times Measurements - Column

Besides, blue methylen has the highest absorbance in the red color range at $\approx 650nm$. In our experiments, only $1ml$ is injected in a reactor of $40l$, which means that the dye is strongly diluted. Due to this very low concentration the absorbance is low as well. To register variations anyway, one has to focus on the color range with the highest absorbance, or in other words the red range. Therefore, high pass filters are added to each camera to focus only on wavelengths greater than $590\mu m$ (see II.29). However, in order to get clean results, pictures without dye are aquired to get the light intensity reference. Then, $1ml$ of dye is injected during $2s$ for all experiments. By adding blue methylen dye to the liquid phase, light absorption is increased and the transmitted light intensity captured by the cameras decreases. Plus, bubbles can appear in the interrogation window, which is why image treatment is applied to detect every object in order to reject it. Hence, errors due to bubble presence could be avoided. Finally, the light intensity or gray level is integrated over the whole window where only liquid is present.

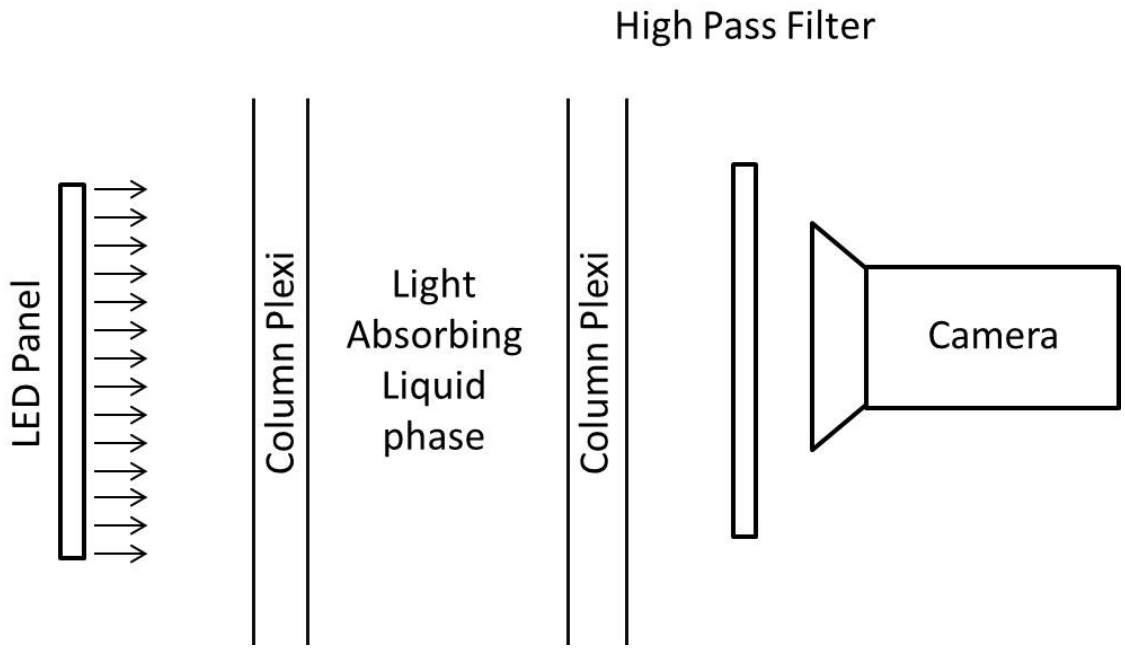

Figure II.29: Experimental Setup for Mixing Time Measurements - Absorbance

Both cameras have separate tasks. The resulting signal from the camera at the bottom is sued to define the initial moment t_0 corresponding to the moment when dye injection is beginning (see figure II.30 (top)). The second camera located close to the

free surface is used to define the final moment t_{final} when the continuous phase can be considered as perfectly mixed (see figure II.30 (bottom)).

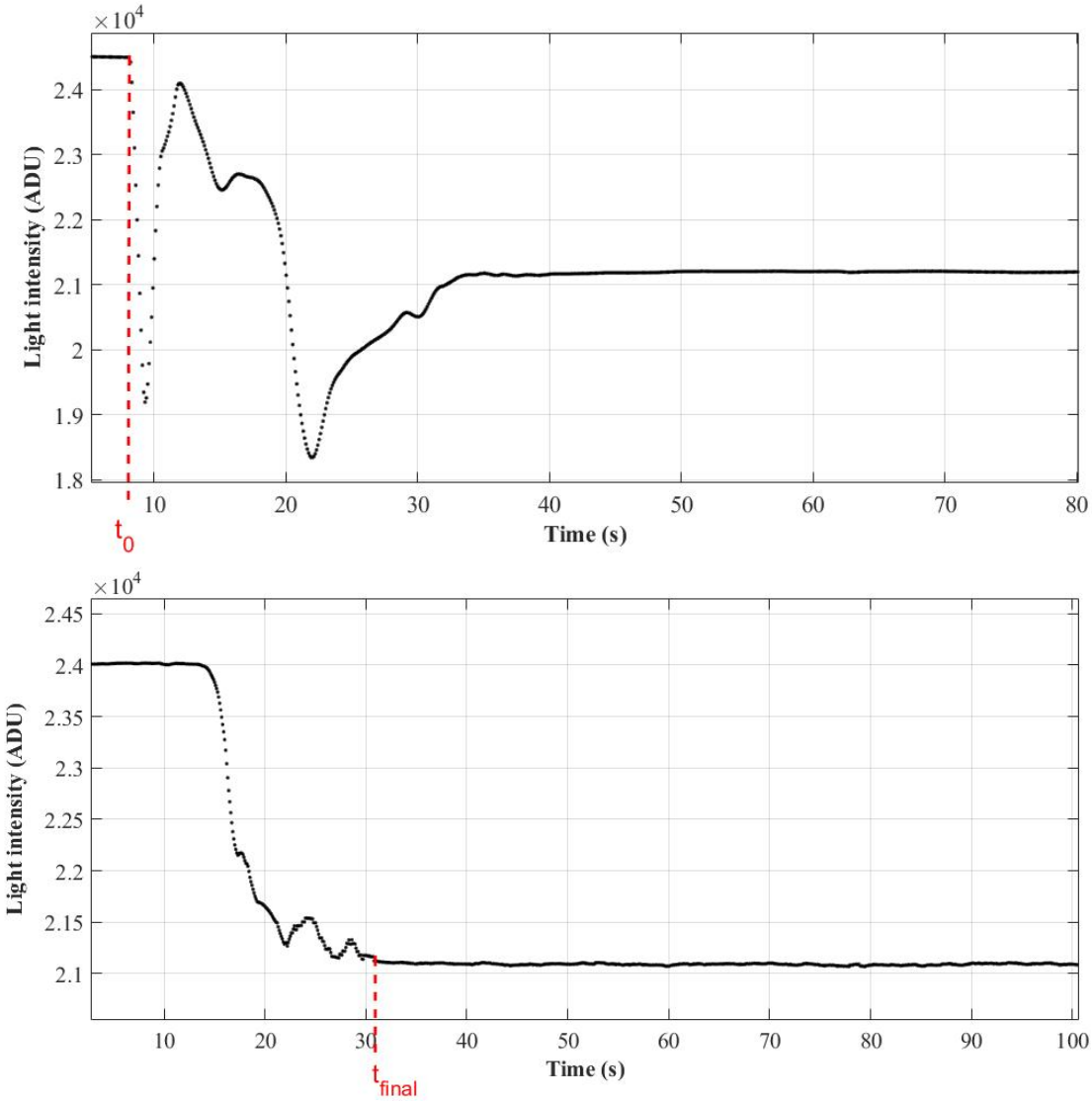

Figure II.30: Light Intensity followed in time in the case of Membrane Injection in Water with $100\frac{l}{h}$ from the Camera at a) the Bottom b) the Top

Finally, the mixing time in the present investigation is defined as the difference of both moments:

$$T_M = t_{final} - t_0 \tag{II.20}$$

II.1.3.6 Pressure & Oxygen sensors

Pressure sensors

Four pressure sensors (PR41X from Keller) are installed at column edges. On the left handside three sensors are distributed over the whole column height at $30cm$, $55cm$ and $80cm$ from the free surface, plus a fourth one on the rigth handside at $55cm$. The acquisition frequency is $1000Hz$. Hence, one is able to observe pressure fluctuations in the liquid phase at different positions of the column. All sensors are synchronized enabling a joint analysis of all pressure signals. Intercorrelations between the different signals can be performed, but will not be discussed in the present investigation.

Oxygen probes

Furthermore, two oxygen probes (OX25 Fast from Unisense), at the right colum side near top and bottom of the column are available permitting local measurements of the dissolved oxygen concentration in the liquid phase. Thus, the thermodynamic equilibrium of oxygen and nitrogen is used to get knowledge about mass transfer through the bubble interface. To provoke such a mass transfer, compressed air and nitrogen injection is used to oxygenate and deoxygenate the liquid phase, respectively. During these processes, fluctuations in dissolved oxygen concentration representing characteristic time scales similar to bubble swarm oscillations, could be recorded. One should mention that the response time of $0.5s$ causes higher filtering than for the other metrological methods. Plus, characteristic mass transfer time scales describing the global mass flux through the bubble interface can be studied. First, nitrogen is injected to deoxgenate the liquid phase completely. Then the gas injection can be changed from nitrogen to oxygen while keeping the exact same flow rate to not disturb the hydrodynamic structure. By following the oxygen concentration in time, the k_La can be determined (see figure II.31):

$$C(t) = C_0 + (C^\star - C_0)\exp(-k_La t) \tag{II.21}$$

where C correspond to the instantaneous, C_0 to the initial (close to 0) and $C^\star$ to the final (satured) oxygen concentration. The following equation can be deduced:

$$ln\Big(\frac{C^\star - C(t)}{C^\star - C_0}\Big) = k_La t \tag{II.22}$$

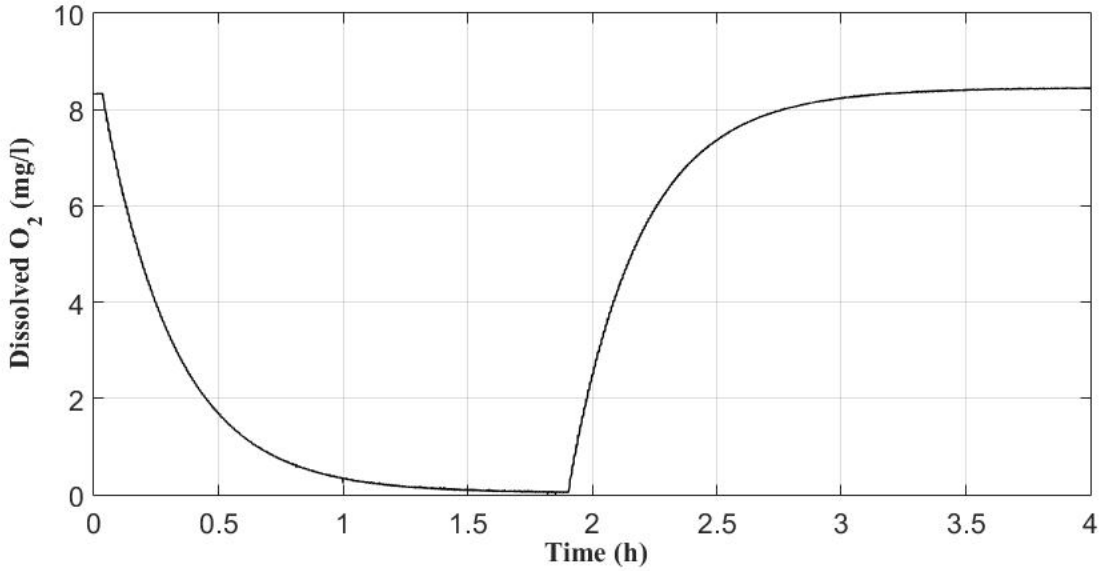

Figure II.31: Deoxygenation and Reoxygenation followed in time in the case of Membrane Injection in Water and $50\frac{l}{h}$

In this way the exponential curve is tranformed into a linear one making an interpolation much easier. The slope of the curve represents then the k_La. Finally, a characteristic transfer time scale τ_c can be deducted by calculating the inverse of the k_La value:

$$\tau_c = \frac{1}{k_La} \tag{II.23}$$

II.1.4 3D Bubble Plume (3D-BP)

This section is dedicated to three dimensional cylindrical bubble columns for the simple reason that such configurations are closer to industrical applications. The main idea of our work is the understanding of macro-mixing in large tanks, which are of course three dimensional as well. Therefore, during this project, complementary experiments were performed at the Helmholtz-Zentrum Dresden Rossendorf.

II.1.4.1 Setup

A three dimensional cylindrical bubble column with an inner diameter of $392mm$ and a height of $1.8m$ is made out of large PVC tubes as it can be seen in figure II.32. In the same way than for the 2D configuration, four pressure sensors (PR41X from Keller) are

installed at column walls. Three of them are located at a height of $0,78m$ separated by an angle of 120° and a fourth one at a height of $1.22m$ vertically aligned with one of the first three ones. In this way spatial intercorrelations between the different sensors can be done. Furthermore, the Wire-Mesh system, which will be presented in the next section, is installed at a height of $1,38m$ with a spatial resolution of $64 * 64$. The mesh size is $6.125mm * 6.125mm$. At the column bottom, a single orifice located in the center of the injection plate is used for bubble injection. In order to compare easily the results from 2D and 3D configurations, the exact same gas sparger system is installed. In this way one is able to choose between a membrane and slugflow injection like it is the case for the experiments in Toulouse at the LISBP (see section II.1). To control the injection flow rate a mass flowmeter (FMA-2608A-BAR) from Omega is used.

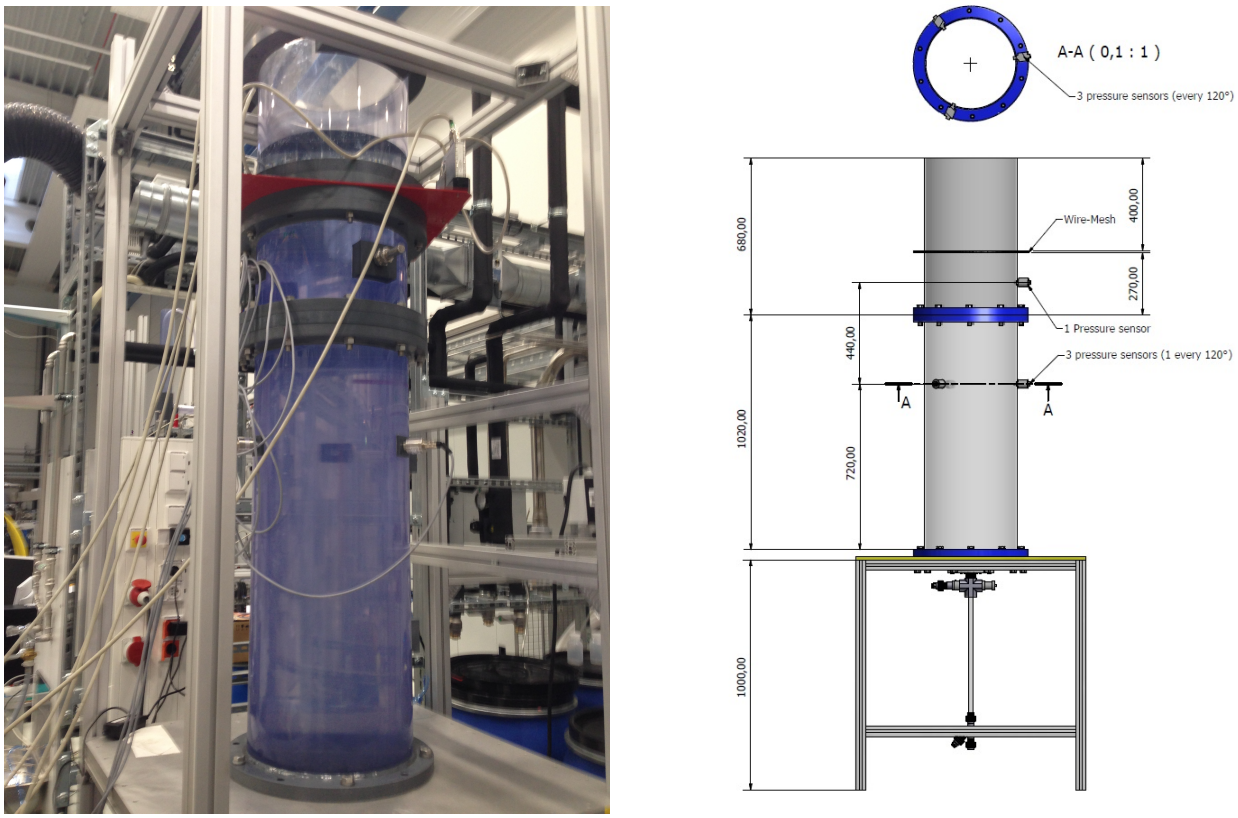

Figure II.32: Experimental Setup at HZDR a) Picture b) Sketch

II.1.4.2 Wire-Mesh

The Wire-Mesh system recently developped by the Helmholtz-Zentrum Dresden-Rossendorf (HZDR) is a metrological device permitting the measurement of local gas holdups. The system is made of two gride layers. Each layer is composed of 16, 32, 64

or 128 wires parallel to each other. Both layer directions are orthogonal to each other and $4mm$ spaced in vertical direction. In the first layer, wires are used as emitters and in the second one as receivers. In this way an electric potential between both layers is created. Since this potential is constant, the resulting electric current is proportionnal to the electric resistance and therefore to the conductivity of the fluid. For additional information on the system we refer the reader to (Silva *et al.*, 2007). Finally, fluid conductivity is modified by the presence of gas bubbles. After calibration one can go the other way around and is able to deduce the local gas hold up from the measured conductivity at each crossing point.

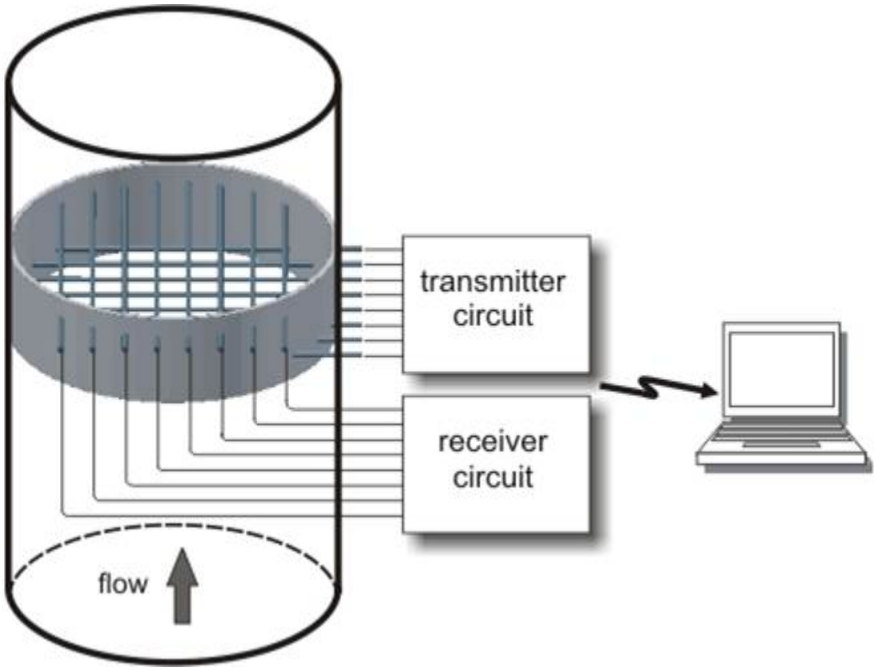

Figure II.33: Sketch of Wire-Mesh System

Dimensions and geometry can be adapted to experimental conditions. In our case, the grid of $64 * 64$ is covering the whole horizontal cross section of the cylindrical bubble column (see section I). In this way, the local time resolved gas hold up in the total horizontal cross section can be obtained. The mesh size was $6.125mm * 6.125mm$ and wires are made of $200\mu m$ thick steel to be as less intrusive as possible.

II.2 Time Series Analysis

The aim of the present investigation is to find periodic behaviours, which could either further or hinder bubble column mixing. Therefore, different strategies can be applied, such as spectral analysis from the so called power spectrum (Fourier Transformation (FT)), the autocorrelation function or the proper orthogonal decomposition (POD). First two ones can be used to obtain characteristic time scales while the POD can give additional information concerning eddy structures and energy dissipation from PIV images. All methods can be applied to any time resolved signal, which will be expressed by $x(t)$, in order to find at least one characteristic frequency. Depending on the order of magnitude, frequencies can be related to different kind of phenomena of different spatial scales. (Drahoš *et al.*, 1991) investigated for characteristic pressure fluctuations in bubble columns. The authors were able to categorize frequency ranges corresponding to phenomena like bubble formation, passages, coalescence, liquid-level fluctuations as well as large and medium-scale eddies. For this reason frequencies of order $10^{-2}Hz$ corresponding to large eddies are of special interest for this work since one wants to know if they further bubble column mixing. In our case, large eddies correspond to the oscillating bubble plume motion. An example of a pressure signal in the case of membrane injection in water with a flow rate of $50\frac{l}{h}$ is presented in figure II.34. The top image corresponds to a non-centered pressure signal. By considering the hydrostatic pressure, which is close to $30mBar$, one deduces a water depth close to $30cm$ from the free surface. In order to get clean results, one should subtract the mean value to analyse only signal fluctuations via the methods being presented in this section.

II.2.1 Spectral Analysis

A classical way to extract characteristic time scales, or frequencies, from time series is the Fourier Transformation (FT) as expressed by the following equation:

$$P_s(w) = |F(w)^2| = |\frac{1}{2\pi}\int_{-\infty}^{\infty} x(t)exp(-iwt)dt|^2 \tag{II.24}$$

where

$$w = 2\pi f \tag{II.25}$$

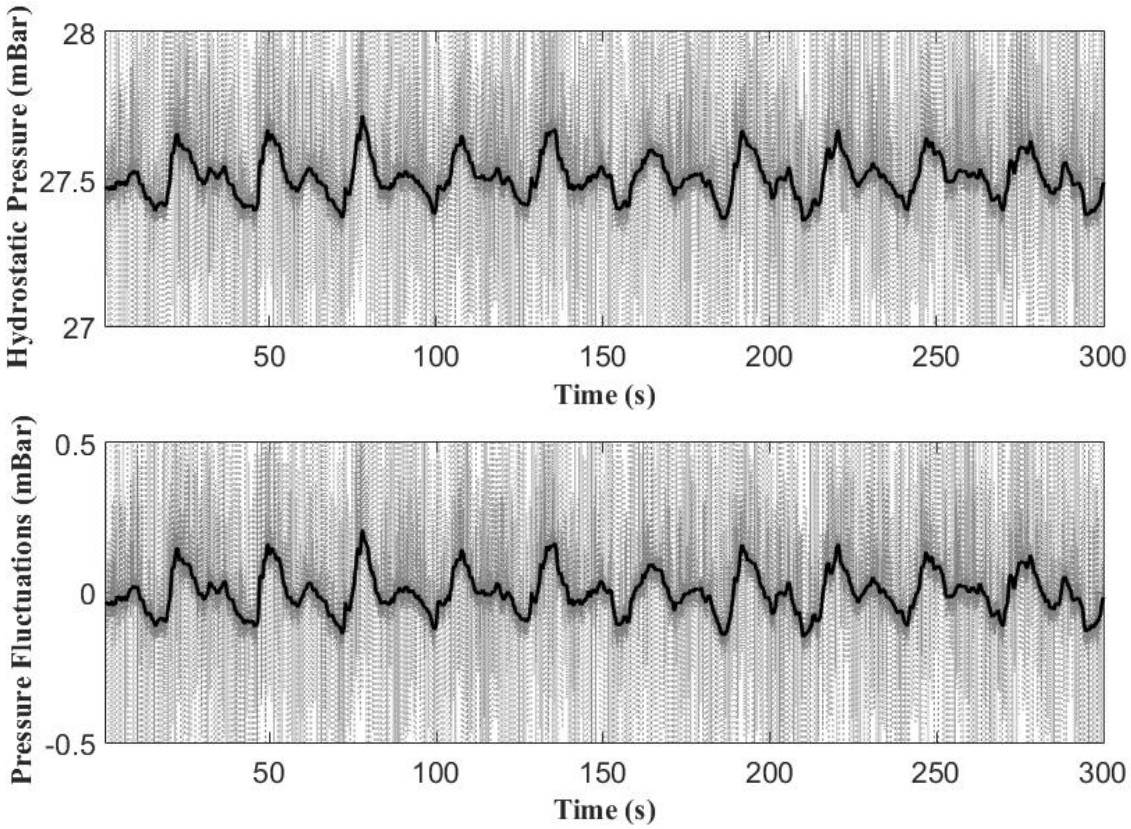

Figure II.34: Example of pressure signal in the case of membrane injection in water and $50\frac{l}{h}$; dotted line = raw signal ; solid line = filtered signal; a) pressures signal b) pressure fluctuations

The basic idea of Fourier Transformation is to decompose time series functions into their frequencies, or in other words, to represent time functions in the frequency domain. The power spectra as a function of frequencies can be plotted as in figure II.35. More often a frequency is registered, larger its energy amplitude will be. For more detailed informations, we refer the reader to the book from (Chatfield, C., 1984). At this point, the decision was made to rather show a concrete example instead of explaining the mathematical background. In figure II.35 the FT of the fluctuation signal shown in figure II.34 is plotted where two clear peaks can be identified. The peaks are situated at $0.0354Hz$ and $0.0709Hz$ meaning that the second peak indicates exactly half the period of the first one. This result is in total agreement with time signal observations. A first characteristic frequency of $0.0354Hz$ resulting from large peaks could be determined. In addition, smaller peaks of the signal from figure II.34 generate in combination with the large ones a second characteristic frequency of $0.0709Hz$. Since the oscillating behaviour does not change during the whole measurement, two clear peaks of similar amplitude appear.

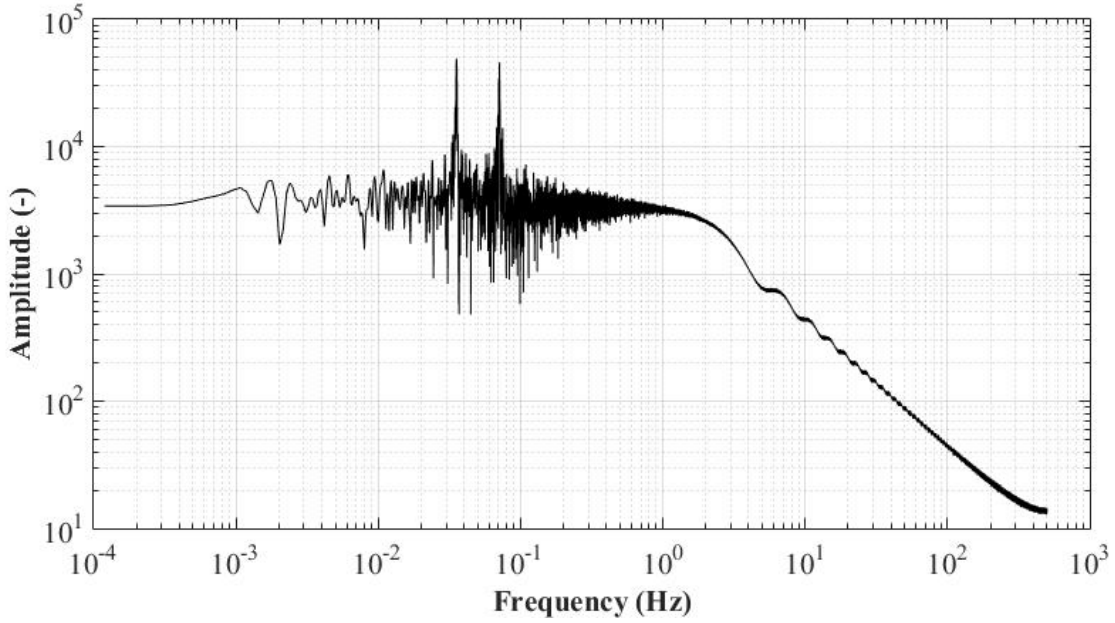

Figure II.35: Example of FT from a pressure signal in the case of membrane injection in water and $50\frac{l}{h}$

II.2.2 Autocorrelation

An other efficient way to extract periodic time scales from any temporal signal (or measurement with N points) is the autocorrelation coefficient, which can be expressed as follows:

$$a_{correlation}(\tau) = \frac{\sum_{t=1}^{N-1}(x(t)-\overline{x})(x(t+\tau)-\overline{x})}{\sum_{t=1}^{N}(x(t)-\overline{x})^2} \tag{II.26}$$

where $x(t)$ can be any signal at time t, $\overline{x}$ is the corresponding time averaged value and τ the time lag. The autocorrelation scalar can be plotted as a function of any possible time lag τ. The coefficients corresponding to the statistically most important lag shows peaks as it can be seen in figure II.36. Again, instead of describing in detail the mathematical background, the decision was made to rather show a concrete example. For more information, we refer the reader again to the book from (Chatfield, C., 1984). Similar to the FT, two different characteristic time scales can be determined. The lag between the origin and the first peak indicates a periodic time scale of $14.1s$. The difference between the origin and the second one shows exactly two times this value, which means $28.2s$. By

regarding the signal from figure II.34, one can say that small and large peaks correspond to the first and second autocorrelation peak, respectively. These two timescales coincide perfectly with the results from the FT. But in contrast to the FT, the autocorrelation gives additional information via the amplitudes, which are similar to those from the original time series signal. In conclusion, it does worth it to apply the autocorrelation function in addition to the FT for two reasons. First, a comparison can validate FT results and secondly, complementary information in terms of amplitudes can be extracted.

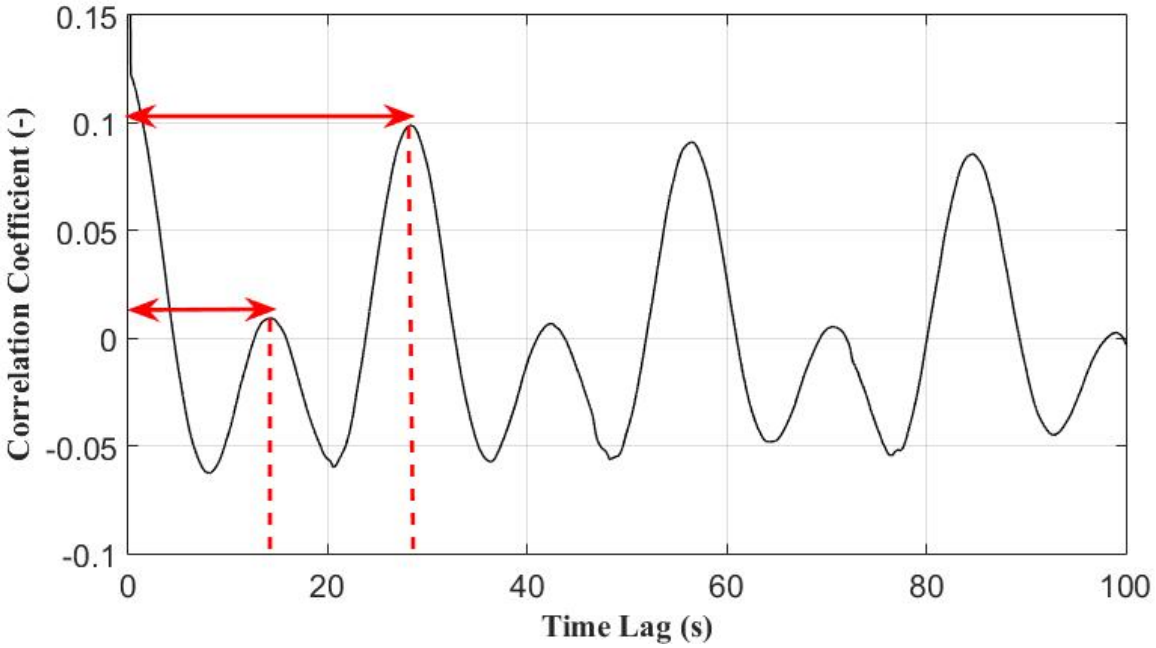

Figure II.36: Example of Autocorrelation function from a pressure signal in the case of membrane injection in water and $50\frac{l}{h}$

II.2.3 Proper Orthogonal Decomposition

The proper orthogonal decomposition (POD) is a powerfull tool to extract different scales in time and space from experimental or numerical data to get more information, especially concerning spatial fields. The technique gives orthogonal bases for the modal decomposition of an ensemble of functions. These functions can be data from experimental acquisitions like PIV measurements or from direct numerical simulations (DNS) or 1D signals from pressure sensors for example. In the current project, POD is applied to PIV fields in the case of 2D-BP only.

The main advantage is the extraction of supplementary informations in space and time via a linear procedure out of a set of instantaneous fields. At this moment one must mention that the POD technique does not serve in every case. Only hydrodynamic structures (mean flow, meso-scale eddies, turbulence) of significant energy differences can be distinguished and then analysed in detail to understand their contribution to the overall flow regime. Multiscaling phenomena depending on the kinetic energy level of each decomposed mode can so be studied. (Lumley, 1967) proposed that coherent structures like mean flow or large eddies in turbulent flow should be those with the largest mean square projection on the velocity field. (Berkooz *et al.*, 1993) illustrated the decomposition of instantaneous velocity fields. In the two dimensional case, the decomposition on the above mentioned orthogonal bases can be written as follows:

$$\vec{V_k}(x,y,t) = \sum_{n=1}^{\infty} \vec{V_k^{(n)}}(x,y,t) = \sum_{n=1}^{\infty} a_k^{(n)}(t)\vec{\phi^{(n)}}(x,y) \tag{II.27}$$

where $\vec{V_k}$ is the k-th instantaneous velocity field and $\vec{V_k^n}$ the n-th component of the POD decomposition. Every velocity field component can further be decomposed into temporal scalars $a_k^n(t)$ and time independent spatial modes $\vec{\phi^n}(x,y)$. In this way, time and spatial information are separated and decomposed depending on their energy level. Furthermore, (Sirovich, 1987) adapted the Fredholm eigenvalue integral equation to:

$$\int\int\int R_{ij}(x,y,x',v',t,t')\phi^n(x',y')dx'dy'dt' = \lambda^{(n)}(t)\vec{\phi^{(n)}}(x,y) \tag{II.28}$$

where R_{ij}, λ^n and $\vec{\phi^n}$ correspond to the cross-correlation tensor, the eigenvalues and the eigenfunctions, respectively. The tensor R_{ij} contains all spatial and temporal informations and is build in the following manner. First a velocity field is considered:

$$\vec{V_k} = \begin{pmatrix} \vec{V_k}(x_1,y_1) & \vec{V_k}(x_1,y_2) & \cdots & \vec{V_k}(x_1,y_C) \\ \vec{V_k}(x_2,y_1) & \vec{V_k}(x_2,y_2) & \cdots & \vec{V_k}(x_2,y_C) \\ \vdots & \vdots & \vdots & \\ \vec{V_k}(x_L,y_1) & \vec{V_k}(x_L,y_2) & \cdots & \vec{V_k}(x_L,y_C) \end{pmatrix} \tag{II.29}$$

where k is the index on the instantaneous measurement. C and L are the numbers of

measurement points (of the considered data field) in horizontal (columns) and vertical (lines) directions, respectively. This instantanious field can be reshaped to a column vector presenting $2*LC$ lines:

$$\vec{V_k} = \begin{pmatrix} u_k(x_1, y_1) \\ u_k(x_2, y_2) \\ \vdots \\ u_k(x_L, y_C) \\ \vdots \\ w_k(x_1, y_1) \\ w_k(x_2, y_2) \\ \vdots \\ w_k(x_L, y_C) \end{pmatrix} \tag{II.30}$$

where u corresponds to the horizontal and w to the vertical velocity component. If one considers every measurement event (or snapshot (Sirovich, 1987)), the corresponding matrix M containing all informations in space (linewise) and time (columnwise) can be written as:

$$M = \begin{pmatrix} u_1(x_1, y_1) & u_2(x_1, y_2) & \cdots & u_N(x_1, y_C) \\ u_1(x_2, y_1) & u_2(x_2, y_2) & \cdots & u_N(x_2, y_C) \\ \vdots & \vdots & & \vdots \\ u_1(x_L, y_1) & u_2(x_L, y_2) & \cdots & u_N(x_L, y_C) \\ \vdots & \vdots & & \vdots \\ w_1(x_1, y_1) & w_2(x_1, y_2) & \cdots & w_N(x_1, y_C) \\ w_1(x_2, y_1) & w_2(x_2, y_2) & \cdots & w_N(x_2, y_C) \\ \vdots & \vdots & & \vdots \\ w_1(x_L, y_1) & w_2(x_L, y_2) & \cdots & w_N(x_L, y_C) \end{pmatrix} \tag{II.31}$$

Then, the auto-covariance tensor R can be determined:

$$R = \frac{1}{N} M \cdot M^T = \begin{pmatrix} \overline{u^2(x_1, y_1)} & & \\ & \cdots & \\ & & \overline{w^2(x_L, y_C)} \end{pmatrix} \tag{II.32}$$

By using equation II.28 the resulting eigenvalue problem can now be solved. One must mention that the eigenvectors of equation II.28 have no dimension. Only the eigenvalues show the dimension ($\frac{m^4}{s^2}$). Once they are multiplied to the considered surface ($dxdy$), the eigenvalues are proportional to the kinetic energy corresponding to the dimension ($\frac{m^2}{s^2}$). Anyway, by organizing all eigenvalues depending on their kinetic energy in decreasing order, flow structures can be identified. Most of the time the first eigenvalue shows much higher energy distribution and corresponds to the mean flow. Eigenvalues with lower energy correspond to coherent structures like large eddies. If they are close in terms of energy, they correspond in general to the same flow structure. (Liné *et al.*, 2013) showed a nice flow structure decomposition in water and in shearthinning fluids. The authors were able to identify mean flow, secondary structures, ternary structures until turbulence. Plus, relations between different modes in terms of time and energy scales are presented. Once eigenvalues and eigenvectors are properly determined, instantaneous velocity fields can be projected on the obtained eigenfunctions $\vec{\phi^n}$ giving us the POD coefficients a_k^n:

$$a_k^n = \vec{V_k} \vec{\phi^n} \tag{II.33}$$

In the other way around, the instantaneous fields can be reconstructed corresponding to the n-th POD component:

$$\vec{V_k^n} = a_k^n \vec{\phi^n} \tag{II.34}$$

Hence, it is easier to understand the contribution of every flow component by reconstructing the corresponding velocity field or fluctuations.

Chapter III

Experimental Results

The beginning of this chapter deals with the oscillating behaviour of bubble plumes, including influences of injection conditions and liquid properties. Afterwards, the two different phases are analyzed separately in detail. The gas phase is studied via bubble's shape, size and velocity to determine void fractions. Concerning the liquid, besides average values, special attention is given to fluctuations. Characteristic time scales for mass transfer and mixing are shown and a comparison between two and three dimensional low frequency oscillations is done using the results from the Wire-Mesh system of the HZDR.

III.1 Oscillation Frequency

III.1.1 Water

Our first step was to make sure that bubble swarm's oscillating motion can be captured by different measurement techniques in both phases showing same periodic time scales for same injection conditions and fluid properties. For this reason, a certain number of experiments are realised in water for three different injection flow rates and two different spargers. Both parameters and associated superficial gas velocities can be seen in table III.1. The superficial gas velocity is defined by the expression:

$$U_{GS} = \frac{Q_{inlet}}{A_{section}} \tag{III.1}$$

where Q_{inlet} is the gas flow rate and $A_{section}$ the surface of the horizontal bubble column cross section.

Bubble type	Ellipsoidal bubbles , Caps
Injection flow rate (l/h)	[50 ; 100 ; 200]
Superficial gas velocity (mm/s)	[0.66 ; 1.32 ; 2.65]

TABLEAU III.1: Parameters of experiments

Spectral analysis is applied to acquired data from pressure and dissolved oxygen concentration measurements as well as from velocity to time signals obtained by PIV measurements in one point. The aim is to quantify low frequency oscillations of the wandering bubble plume in the liquid phase. To confirm our results shadowgraphy is applied on the gas phase in order to follow the gravity center position in time. Figure III.1 shows signals from the above mentioned metrological methods in the case of membrane sparger injection in water with a gas flow rate of $50\frac{L}{h}$ corresponding to a superficial gas velocity of $0.66\frac{mm}{s}$. Dotted lines correspond to raw data, solid lines to filtered signals. In case of figure III.1 a) two filtered signals are drawn. The dash-dotted line corresponds to the horizontal velocity component U and the solid line to the vertical velocity one V. All signals show the same periodic time scale even if the signal shape can differ. Small peaks in figure III.1 a), b) and d) result from vortex cell passages. In table III.2 all characteristic periodic time scales from all metrological methods for different experimental conditions are listed.

Flow rate (l/h)	Bubble type	Pressure	O_2 probe	PIV	Shadowgraphy
50	EB	28.1	25.3	28.0	28.2
50	CAPS	26.1	24.4	25.9	25.7
100	EB	21.7	21.7	21.9	21.6
100	CAPS	20.0	20.0	20.6	20.5
200	EB	15.3	13.7	15.4	15.3
200	CAPS	15.0	14.1	15.1	15.1

TABLEAU III.2: Characteristic periodic time scales in seconds measured by different metrological methods in water for different injection flow rates and both spargers/bubble types; EB = Ellipsoidal bubbles; CAPS = Spherical caps

Our first observation is the good agreement between all measurement techniques. Indeed, the wandering bubble plume transfer its momentum to the liquid phase creating

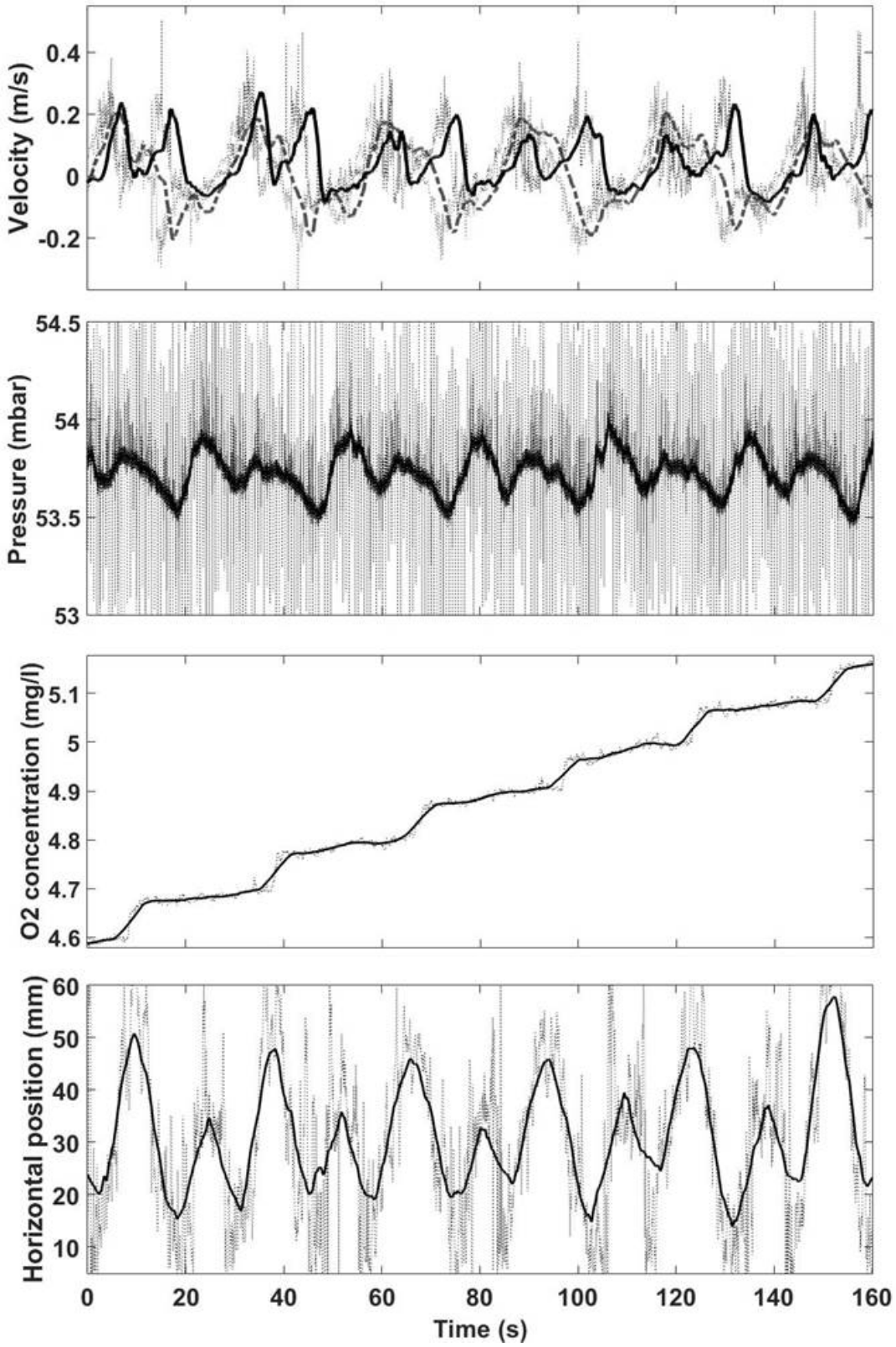

Figure III.1: Signal-to-time comparison between all metrological methods; Dotted line = raw data; Solid line = filtered signal; a) PIV: Solid line = vertical velocity component; Dot-dashed line = horizontal velocity component; b) Pressure (from the sensor in the middle (left) of the column); c) Dissolved oxygen concentration (from the sensor at the bottom); d) Gravity center position in horizontal direction

hydrodynamic structures with similar time scales. Besides, small fluctuations of the dissolved oxygen concentration could be measured by the two oxygen probes. This is particulary interesting for the current investigation if one takes a closer look to the signal from the probe at column bottom. As already mentioned, these fluctuations result from vortex cells, which are created at column top, descend along column edges before dissipating at the bottom. These vortex cells contain more or less oxygen, depending on the injected gas inducing the observed fluctuations. One should mention the corresponding signals require a more important data treatment generating less precise results. Plus, the response time of the oxygen sensors is much higher than for pressure sensors as mentioned in section II.1.3.6. However, our results prove that the same low frequency can be verified by four different metrological methods. This information can be usefull for industrial applications to get knowledge of meso and macroscopic structures contributing to mixing inside bioreactors. Furthermore, close, but slightly different characteristic time scales are measured for the two different spargers. Both show the same decreasing time scale evolution with increasing gas injection rate. Differences, especially for low gas flow rates, can be explained by bubble size and the resulting terminal bubble velocity (see (Clift *et al.*, 1978)). This velocity seems to play an important role in bubble plume oscillations. At the highest considered injection flow rate, the appearance of larger bubbles due to coalescence in the case of the membrane sparger and the appearance of smaller bubbles created at the outlet of the slugflow sparger, generates similar polydisperse bubble size distributions. Therefore, almost identical time scales for both spargers are measured.

III.1.2 Liquid Property Influences

In the following section, influences of viscosity and surface tension are analyzed. A copolymer, called Breox from BASF, is used to create different fluid properties. By adding a small quantity of Breox (0.5 % of mass concentration) to deionized water, one is able to produce a fluid with same viscosity as water, but a decreased surface tension by 25%. With increasing mass concentration, surface tension remains constant, but a large range of different viscosities can be obtained. The exact fluid properties are shown in table II.1.

Flow rate (l/h)	Bubble type	Water	B (0.5%)	B (8.7%)	B (13.6%)	B (18.5%)
50	EB	28.2	25.9	22.6	21.4	22.4
50	CAPS	25.7	26.5	25.9	26.3	-
100	EB	21.6	21.3	17.4	16.2	17.3
100	CAPS	20.5	20.0	20.2	20.3	-
200	EB	15.3	14.5	13.2	13.4	17.9
200	CAPS	15.1	14.3	13.7	14.1	-

TABLEAU III.3: Characteristic periodic time scales in seconds measured in different liquids for different injection flow rates and both spargers/bubble types; EB = Ellipsoidal bubbles; CAPS = Spherical caps

III.1.2.1 Surface tension

A comparison between two liquids with same viscosity and density, but different surface tensions is done for both spargers and three gas flow rates. The characteristic time scales for all 12 measurements can be seen in table III.3. One can recognize that the influence of surface tension on flow pattern is almost negligible in case of large spherical caps and low injection flow rate. At the highest considered gas flow rate, the impact of surface tension on bubble plume oscillation becomes more important. This result can be explained by more frequent bubble interactions being in agreement with (Cachaza *et al.*, 2011) (see section I.4).

In case of the membrane sparger the impact of surface tension is different. At the lowest gas flow rate, time scale difference is important because bubble interaction is already frequent without appearance of coalescence or breakups. Plus, the modified bubble size due to surface tension decrease involves a modification of the terminal bubble velocity. At the highest flow rate, large bubbles appear and bubble size distribution becomes polydisperse and similar to slugflow sparger conditions at high flow rate. Only in the case of an injection rate of $100l/h$, the characteristic time scale is not modified. Probably, two different phenomena appear and compensate themself. First one is the modified bubble size distribution and therefore modified terminal velocities. The second one is bubble interaction including coalescence. However, surface tension shows the highest influence in situations where bubble interactions are frequent, but without coalescence.

III.1.2.2 Viscosity

In the following section, the viscosity effect is in focus. Therefore, comparisons are done between the different Breox fluids since surface tension and density are constant for all of them. Like in the previous section, all characteristic time scales can be seen in table III.3. Furthermore, results are presented in graphical form in figure III.2. In case of membrane sparger injection, a clear tendency is recognized. For all injection flow rates characteristic time scales are decreasing with increasing viscosity in a range from $1mPa.s$ to $20mPa.s$. If viscosity further increases up to $52mPa.s$ time scales increase again for all considered injection flow rates.

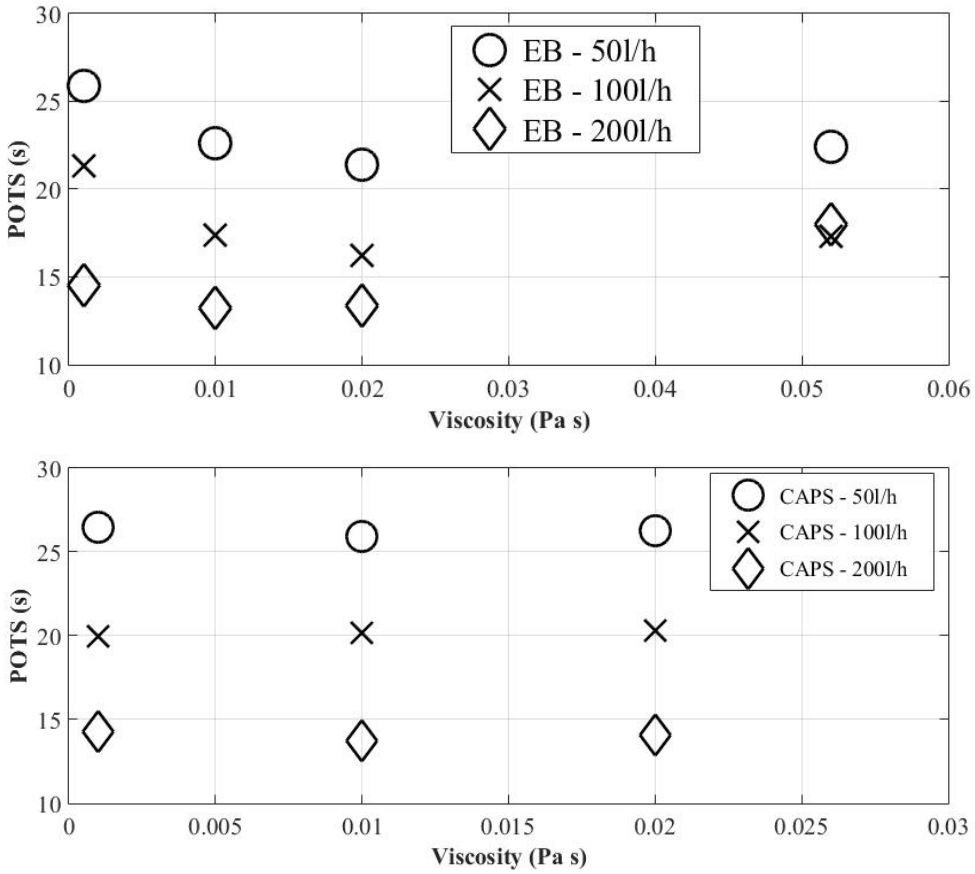

Figure III.2: Characteristic time scales in function of viscosity for three different injection flow rates in case of a) membrane sparger and b) slugflow sparger

This observation results from the appearance of larger bubbles. Indeed, the high viscosity provokes bubble coalescence generating large spherical caps. This phenomenon has also been observed in case of homogeneously aerated 3D bubble columns (Olivieri *et al.*, 2013), (Besagni *et al.*, 2017). For a better understanding, raw images from shadowgraphy are shown in figure III.3. Projected bubble shadows in Breox with

mass concentrations of 8.7% and 18.5% at low and high gas injection rate through the membrane sparger can be seen. At low gas injection rate (figure III.3 a) and c)) bubble size distribution is almost monodisperse. At higher gas flow rates, larger bubbles are formed at the sparger and bubble size distribution becomes polydisperse. Therefore, an attenuation of the decreasing time scales was observed at higher viscosities. The bubbles formed by coalescence become larger with increasing viscosity, which also increases characteristic time scales. This fact illustrates the coupling between bubble size, the associated terminal bubble velocity and the wandering plume motion.

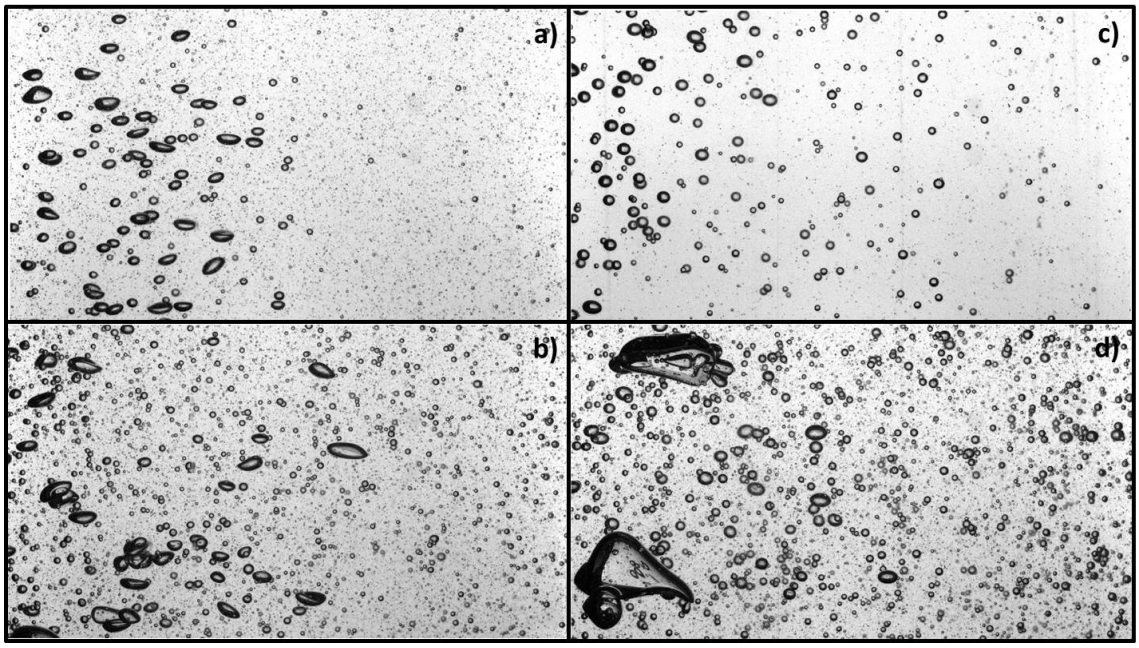

Figure III.3: Images from shadowgraphy in case of membrane sparger, a) Breox(8,7%) and 50 l/h b) Breox(8,7%) and 200 l/h c) Breox(18,5%) and 50 l/h d) Breox(18,5%) and 200 l/h

A remarkable result is the insensitivity of the oscillating motion to viscosity in case of spherical caps. For the considered viscosity range characteristic time scales remain unchanged. This can be explained by low bubble interaction rates as well as by bubble size and therefore bubble's terminal velocity, which do not change much. This is another indication of the strong coupling between the low frequency oscillation and the terminal bubble velocity. Indeed, the vertical void fraction gradient, which is directly dependent on the rising velocity and the dispersion, seems to have great impact on the wandering motion. This argumentation is in line with the Brunt-Väisälä frequency, which is an

unstability oscillation due to density stratification.
In the case of Breox (18.5%) and the slugflow sparger no clear frequency could be identified any more. Both spargers show transition from VF to DCTF for the highest considered viscosity of $100mPa.s$ and all injection flow rates. Furthermore, dispersion decreases with increasing viscosity for both spargers and all considered gas flow rates. In other words, the increasing viscosity amortizes the amplitude of the oscillating bubble swarm wave. This information can be usefull to determine distances between spargers in large tanks depending on viscosity and the sparger.
A last aspect, which should at least be mentioned is the appearance of microbubbles due to the low surface tension. During certain experiments, bubble coalescence, break-ups and injection generate microbubbles. The phenomen goes on until saturation, which takes place after some minutes. This may change the effective mixture viscosity but because of the difficulties to measure last one, the parameter is not investigated in detail.

III.1.3 Dimensionless numbers

In this section dimensionless numbers are used to compare our work to others. In literature, (Caballina *et al.*, 2003) suggested to take the following Grashof number expression:

$$Gr = \frac{gL_i^3 U_{GS}}{\nu^2 U_{b_\infty}} \tag{III.2}$$

where g is the gravity constant, L_i the inlet length, U_{GS} the superficial gas velocity, ν the kinematic viscosity and U_{b_∞} the terminal bubble velocity. The Grashof number was first introduced for thermally induced plumes, but works also for other two dimensional bubble plums in case of water. The second number generally used for bubble plume characterization is the Strouhal number:

$$St = \frac{fL_i}{U_{GS}} \tag{III.3}$$

where f is the oscillating plume frequency, L_i the inlet length and U_{GS} the superficial gas velocity. (Rensen & Roig, 2001) used this number in order to categorize bubble plume oscillations in heterogeneously aerated bubble columns. They defined it as normalized frequency.

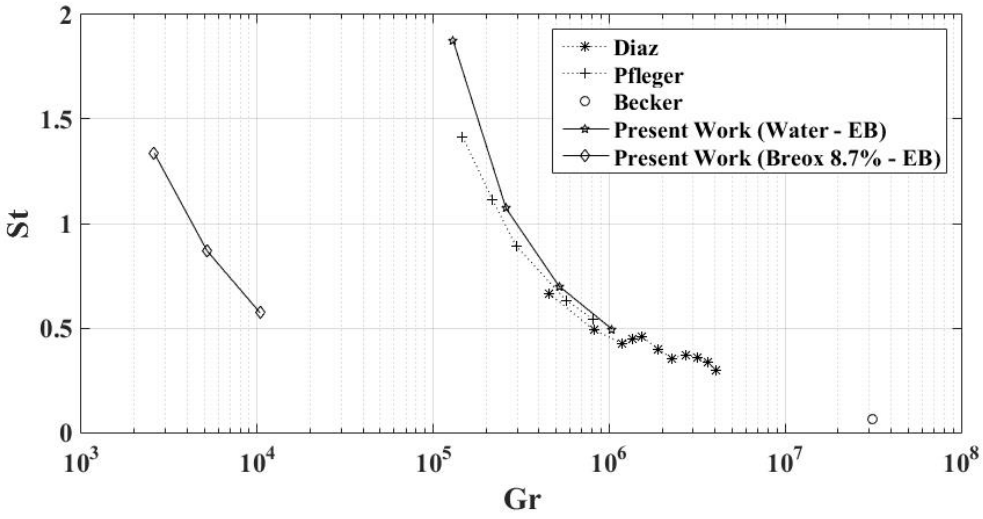

Figure III.4: Strouhal number in function of Grashof number

In figure III.4 a good agreement between our results in water and the results from (Diaz *et al.*, 2006), (Pfleger *et al.*, 1999) and (Becker *et al.*, 1994) can be seen. Unfortunately, these two numbers do not seem to take into account the viscosity in the right way. In case of Breox (8.7%) having a viscosity 10 times higher than the other experiments performed in water, a difference of two decades is observed. Because of the power two in the Grashof expression, viscosity influence is much more important than in the Strouhal number expression. This is also the case for the Rayleigh number, which is often used as well (Rensen & Roig, 2001).

It can be concluded that at least one of these numbers must be modified to take into account viscosity in a different way. We noticed that both dimensionless numbers are mainly based on bubble column characteristics, but during our experiments one observed that bubble size and shape have also large influence on bubble plume oscillations. Therefore, bubble properties like size and shape and thus indirectly fluid properties like surface tension and viscosity (Clift *et al.*, 1978) should be taken into consideration. To our mind one of the dimensionless numbers should be directly based on bubble characteristics. Our suggestion is to use the Froude number, which is comparing flow inertia and gravity effects, defined as follows:

$$Fr = \frac{U_{GS}}{\sqrt{gD_E}} \tag{III.4}$$

where D_E is the equivalent bubble diameter and g the gravity constant.

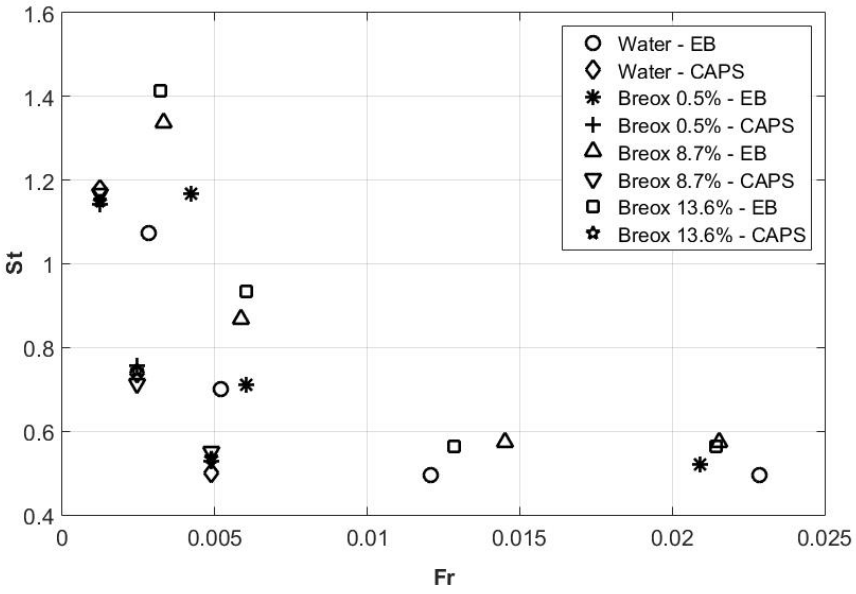

Figure III.5: Strouhal number as a function of Froude number

In figure III.5 the Strouhal as a function of the Froude number is plotted. A decreasing asymptotic evolution of the Strouhal number with increasing Froude number can be observed. One has to mention that in case of high viscosity and/or high injection flow rate, bubble size distribution becomes bimodal. For this reason, two Froude numbers based on different equivalent bubble diameters are calculated for one single experiment, or in other words for one single Strouhal number. Our results suggest that large bubbles, corresponding to low Froude numbers and presenting the highest terminal velocity, are predominantly influencing low frequency oscillations. Finally, we have to admit that our suggestion still needs improvements, but the strategy to base at least one dimensionless number on bubble size and shape to take into account fluid properties seems to make sense. Additionally, the choice of the considered velocity describing the phenomenon should be discussed. In literature, it is generally admitted to use U_{GS} considering bubble column dimensions and gas injection flow rate. However, the sliding or terminal bubble velocity could eventually provide better results.

III.2 Bubble Characterisation

The importance of accurate bubble characterization was already pointed out in the last section. Hence, experimental results from our image treatment (section II.1.3.3) are presented in table III.4.

Fluid	Sparger	Flow Rate (l/h)	D_E (WIB)(mm)	D_E (COSI)(mm)
Water	Membrane	50	4.8	8.9
Water	Membrane	100	6.6	16.3
Water	Membrane	200	5.8	31.8
Water	Slugflow	50	28	30
Water	Slugflow	100	31.8	33.9
Water	Slugflow	200	43.3	45.8
Breox (0.5%)	Membrane	50	3.3	6.4
Breox (0.5%)	Slugflow	50	26.1	26.2
Breox (13.6%)	Membrane	50	3.2	7.9
Breox (13.6%)	Slugflow	50	28.2	26.5
Breox (18.5%)	Membrane	50	3.4	7.4
Breox (18.5%)	Slugflow	50	28.2	22.1
Breox (24%)	Membrane	50	3.8	15.3
Breox (24%)	Slugflow	50	28.2	22.1

TABLEAU III.4: Bubble Characterization for a large range of experimental conditions

In table III.4, the convergent equivalent diameters of WIBs and COSIs are listed. Characteristic sizes are shown for different injection conditions and in different fluids. As expected with membrane injection, all COSIs show larger mean bubble diameter than WIBs. Last ones are identified as single bubbles while COSIs consist of multiple overlapping bubbles, which are consequently larger. Even the different ways of volume calculation between WIBs and COSIs do not change this tendency. The same observation is done for the slugflow sparger in water and Breox (0.5%). While WIBs correspond to well defined spherical caps, COSIs represent mostly up breaking or coalescing bubbles creating very large and complex object shapes. Considering the slugflow sparger in more viscous fluids, COSIs show lower diameter values than WIBs. In these experimental conditions, object's shapes are less complex implying that WIBs and COSIs are more similar. Hence,

the manner of volume calculation (see section II.1.3.3) becomes important, which is why smaller diameter values are found for COSIs. However, WIBs are used to determine eccentricity as a function of the equivalent bubble diameter in different fluids. An increase factor of 1.2 is chosen to define size intervals depending on the equivalent bubble diameter. After image treatment, the median eccentricity value is calculated for all of them.

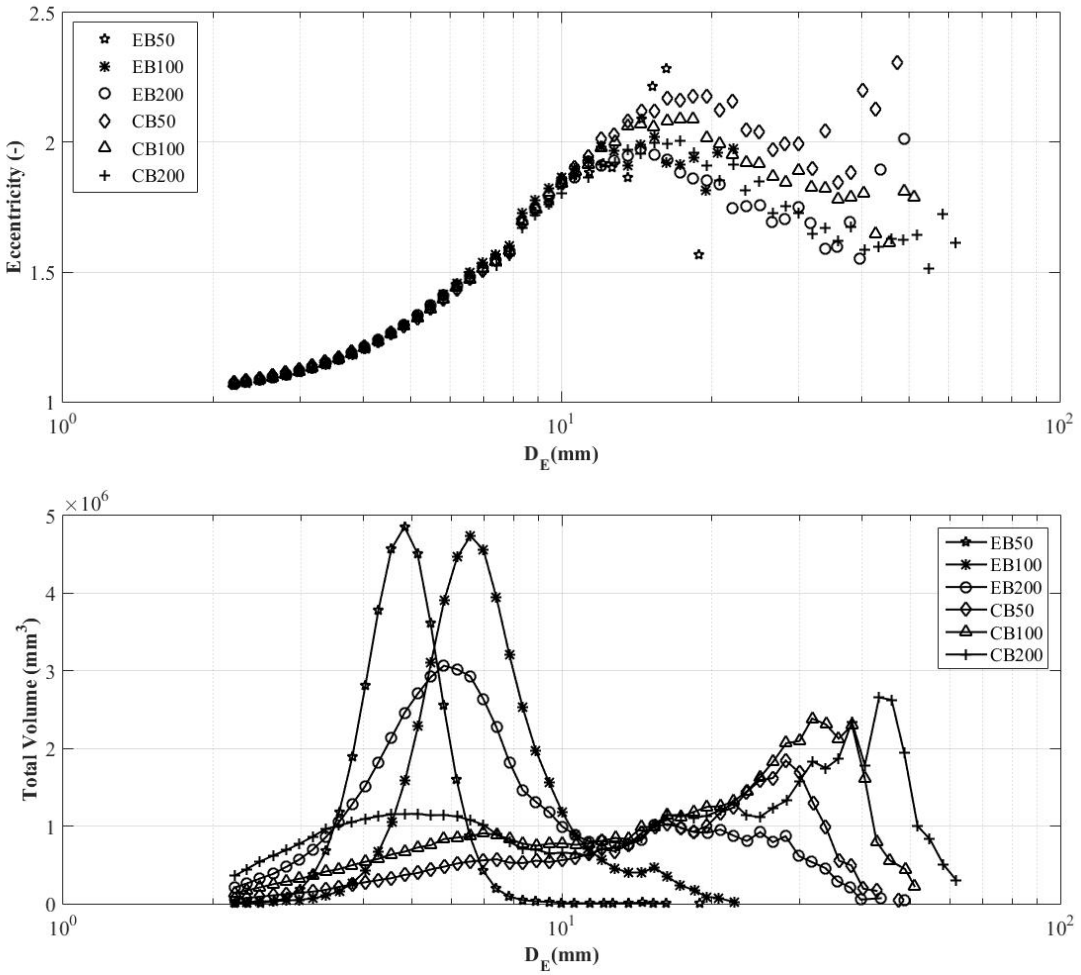

Figure III.6: Eccentricity and Bubble Size Distribution as a function of the Equivalent Diameter in Water

In figure III.6 eccentricity values for six different injection conditions are plotted. In the range between $2mm$ and $10mm$ all measurements fit very well. The six curves merge perfectly. The small gap around $8mm$ results from a filter of our image treatment and is present on all figures. Anyway, at higher diameter values, results begin to disperse. Therefore, bubble size distributions, illustrated at the bottom of the figure, must be taken into account to chose data points at best. For example, the most accurate results for

larger bubbles are determined in the case of slugflow injection at $50\frac{l}{h}$ and $100\frac{l}{h}$. In this way, one makes sure to not take into acount WIB results from too dense bubbly flows, being eventually influenced by COSIs, which could not be filtered by our treatment. However, the two mentioned injection conditions give statistically valuable results in a coherent size domain. Diamonds and Triangles (as marker) should be considered for eccentricity determination in the case of such large bubbles. Values around 2 are found in the corresponding size range. Surprisingly, at even higher bubble sizes, eccentricity decreases again. These results may be influenced by COSIs, which could not be filtered, because of the rather low number of very large objects. Indeed, very large objects are most of the time coalescing or collapsing since no stable shape exist any more.

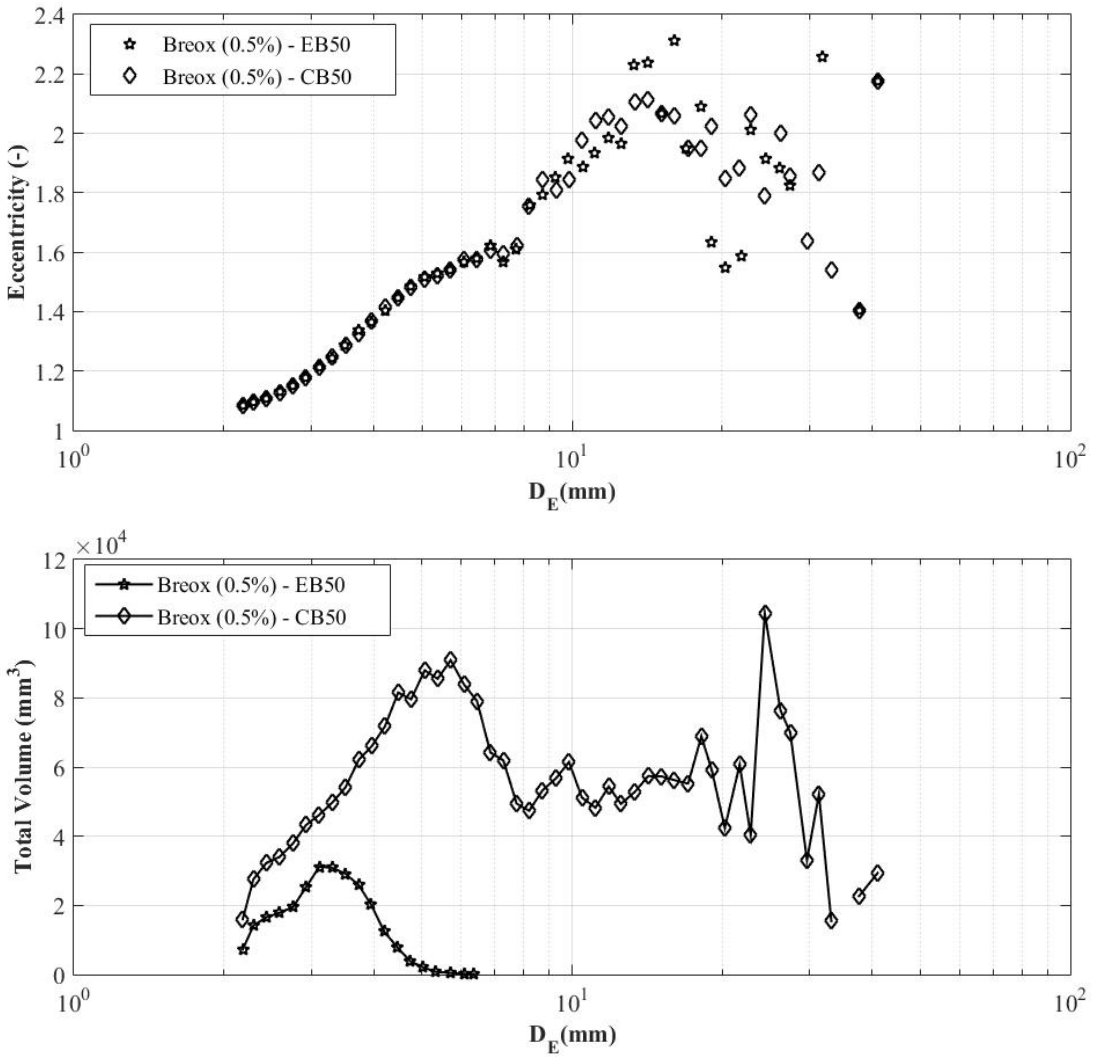

Figure III.7: Eccentricity and Bubble Size Distribution in function of the Equivalent Diameter in Breox (0.5%)

In water the most coherent results are found for rather low injection flow rates. Hence, the smallest one is chosen to investigate eccentricity for the other fluids. In figure III.7 eccentricity (top) and bubble size distribution (bottom) are plotted for Breox (0.5%) at $50\frac{l}{h}$. As in water, image processing seems to furnish good results in the lower size range. With increasing size, results begin to disperse again, which another time can be explained by the unstable behaviour of large bubbles. This phenomenon is even furthered by the decreased surface tension because of the destabilizing effect on the interface. This is also the reason why the equivalent diameter for both, WIBs and COSIs, are smaller than in water.

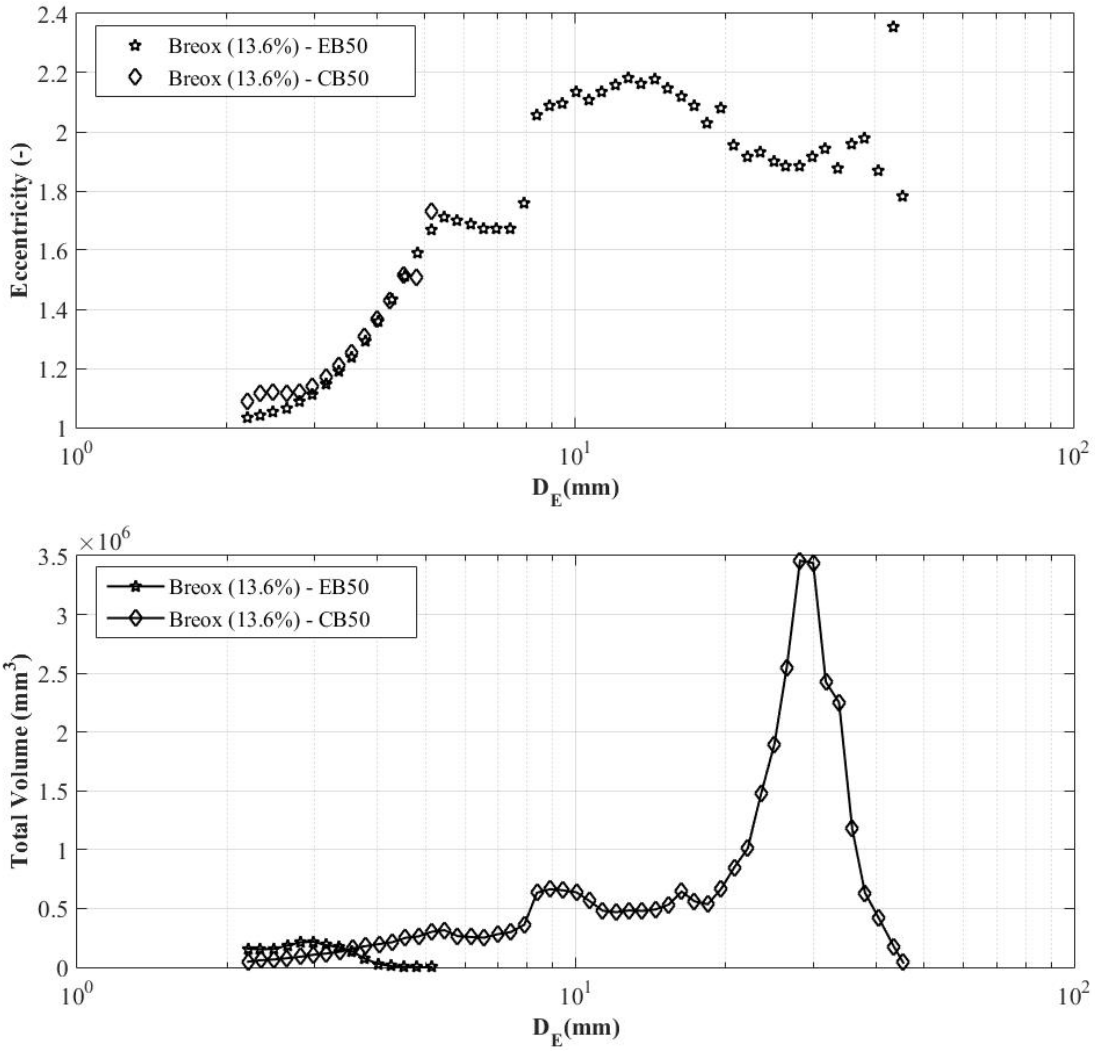

Figure III.8: Eccentricity and Bubble Size Distribution as a function of the Equivalent Diameter in Breox (13.6%)

In figure III.8 bubble shapes in Breox (13.6%) are studied. Again, eccentricity and size distribution are shown. In contrast to the last two cases, more attention must be

given to the size distribution. Only in the range of very small bubbles around $3-4mm$ and very large ones around $30mm$, eccentricity should be considered. In membrane sparger conditions, most of the detected objects correspond to COSIs. Hence, the discontinuous evolution of the eccentricity between $5mm$ and $8mm$ is not physical. However, eccentricity increases between $10mm$ and $15mm$, reaches a maximum value of 2.2 and decreases for larger sizes. This evolution is quit similar to the results in water. Besides, points are less dispersed indicating a more stable bubble interface.

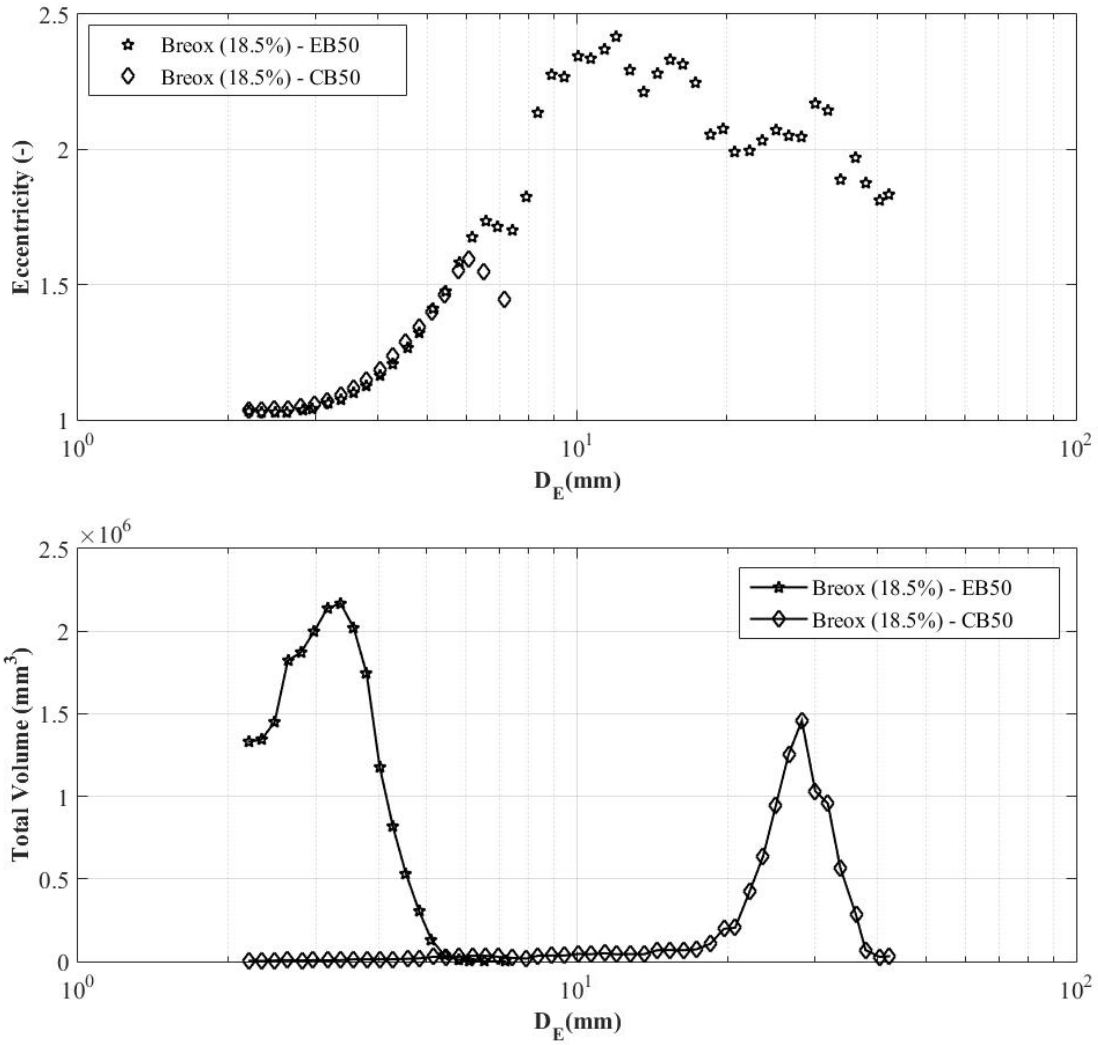

Figure III.9: Eccentricity and Bubble Size Distribution as a function of the Equivalent Diameter in Breox (18.5%)

The same data is also shown in figure III.9 and analyzed for Breox (18.5%). Regarding the bubble size distribution, a bi-modal shape can be recognized. This means that in the case of the membrane sparger, ellipsoidal bubbles are mainly taken into account while

the slugflow sparger generates only spherical caps. Both bubble types show rather stable interface behaviour. In the statistically relevant size range a clear eccentricity evolution can be seen. With increasing size, eccentricity increases, but less than in the above considered fluids. For very large bubbles, a decreasing slope can be recognized as in the case of Breox (13.6%).

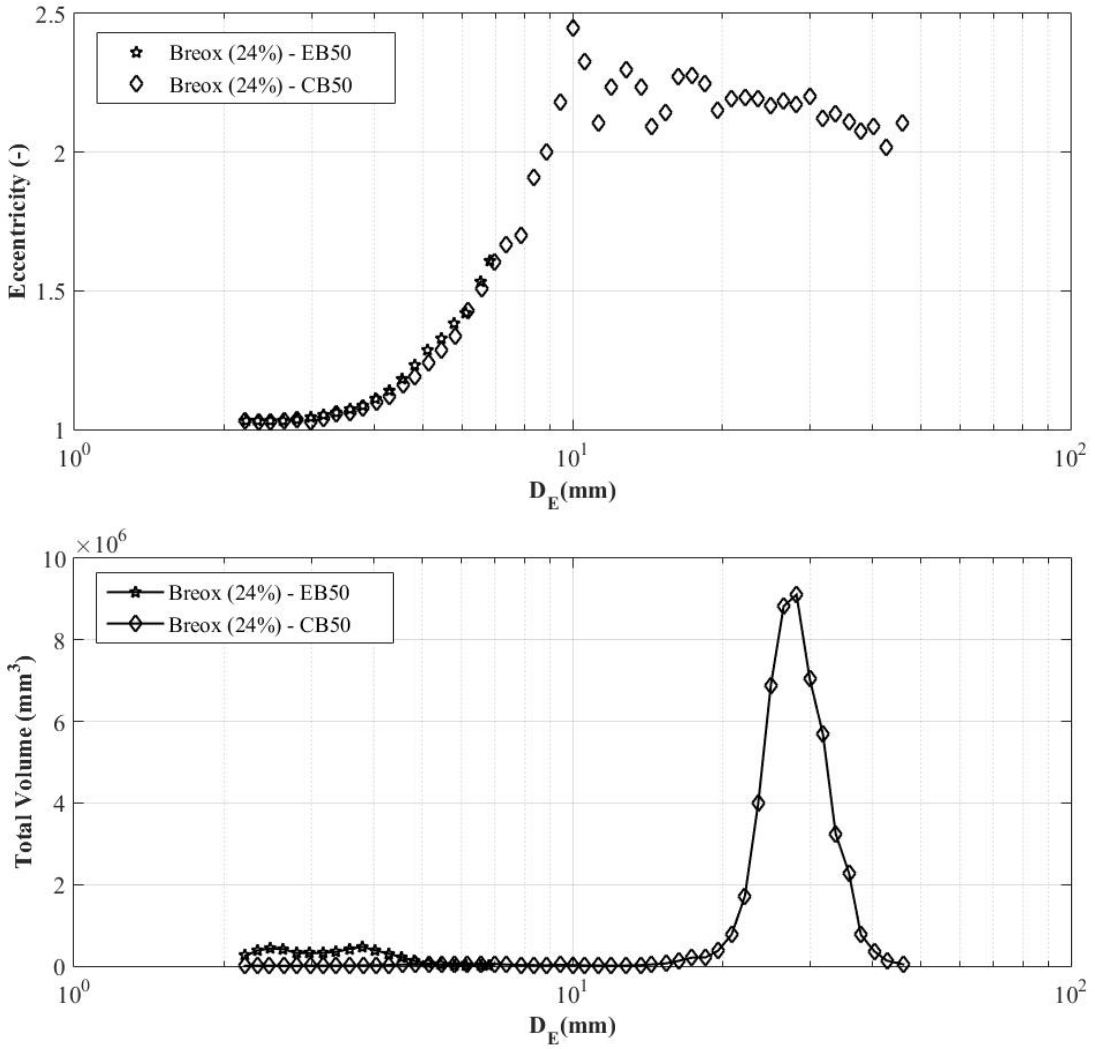

Figure III.10: Eccentricity and Bubble Size Distribution as a function of the Equivalent Diameter in Breox (24%)

Last but not least, eccentricity is also investigated in the most viscous of our fluids. The slope of the curve in the lower size range increases slightly less compared to the other fluids. At this point, one can already conclude that with increasing viscosity, more stable and therefore less flattened ellipsoidal bubbles are formed. In the case of spherical caps, similar values than in the other fluids are found, but decrease less with increasing

size. Well shaped and stable bubbles could be observed during the experiments. The dispersion of the results is very slow and the quantity of WIB very high. Hence, these results are particularly trustable.

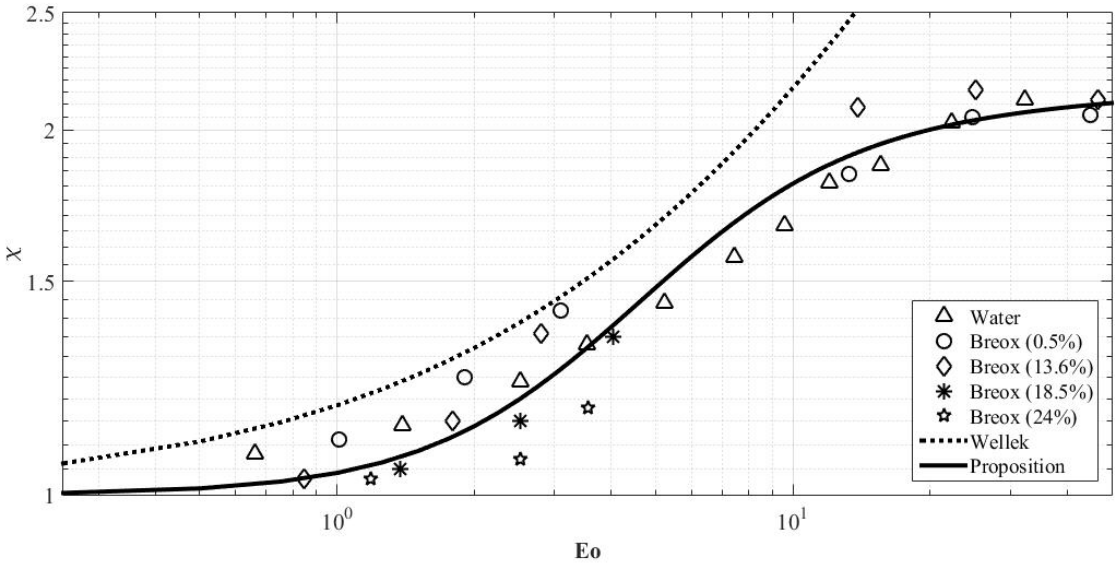

Figure III.11: Statistical Eccentricity as a function of the Eötvös Number

Anyhow, the Eötvös number is used to plot eccentricity of all considered fluids on a single graphe as shown in figure III.11. Our results are compared to equation I.20 from (Wellek *et al.*, 1966). It can be seen that the agreement with our experimental data is acceptable for low Eötvös numbers, but not for high ones. One must point out that III.11 is valid for an isolated object and not for an ensemble as in the present case. This is also the main argument to explain the gap, especially at high Eötvös numbers. Bubbles interact with eachother and instability wakes are generated, which influence the pressure distribution around the bubbles making the shape very unstable. This means that bubbles do not rise in a stagnant flow where the pressure distribution would be symmetric around the axis of revolution (from bubble top to its tail). Here, they experience disturbances from liquid agitation making them oscillate. Therefore, bubbles deform from flattened spheroids to spheres and back again, reducing the statistical eccentrcity. A second reason for the observed gap is a small overestimation of the short axis and implying a small underestimation of the eccentricity. This error results from the fact that bubbles are observed in different positions, even after applying our "orientation"

filter limiting the range to $[-30° \; ; \; 30°]$. Anyway, WIB could be separated from COSIs and used for bubble characterization in bubble swarms. Clear tendencies with increasing size could be identified and viscosity as well as surface tension show effects on bubble size and shape. While surface tension generates smaller bubbles and destabilizes the interface, viscosity has a stabilizing effect on last one.

Finally, we suggest equation III.5 for the eccentrcitiy as a function of the Eötvös number in order to summarize our experimental results. To our knowledge, no work investigating the statistical shape of bubbles inside a swarm, exists in literature. In this way, our bubble characterization can be compared to future results. The equation is obtained by using the nonlienear last squares (NLLS) Marquardt-Levenberg algorithm.

$$\chi = 1 + \frac{0.044 Eo^{1.87}}{1 + 0.044 Eo^{1.84}} \tag{III.5}$$

III.3 Bubble Dispersion

After this bubble characterization, bubble swarm dispersion is investigated, because injection conditions as well as liquid properties have not only an impact on the oscillation frequency, but also on the plume width, which is an important point when it comes to reactor scale-up including sparger distances. Turbulent interactions between bubbles, but also large eddies at the mesoscale play an important role in plume dispersion. One wants to find out, which one is the driving phenomenon. Again sparger types, surface tension and viscosity are investigated. Both liquid properties can significantly modify bubble interactions like collisions with and without coalescence, but also the dynamic of large eddies. Hence, void fraction profiles in different fluids and for both spargers are studied. To better understand these averaged void fraction profiles a time resolved example is show in figure III.12. The mean void fraction at different moments corresponding to multiples of the semi-period, is plotted ($t = [0.5P, 1P, 2P, 3.5P]$). At $t = 0$ the profile is an instantaneousus one. The other profiles are averaged on more and more periods, which makes them more and more flattened in time. After several periods the two characteristic peaks for the present case can be observed. In the following, the void fraction profile do not vary much any more.

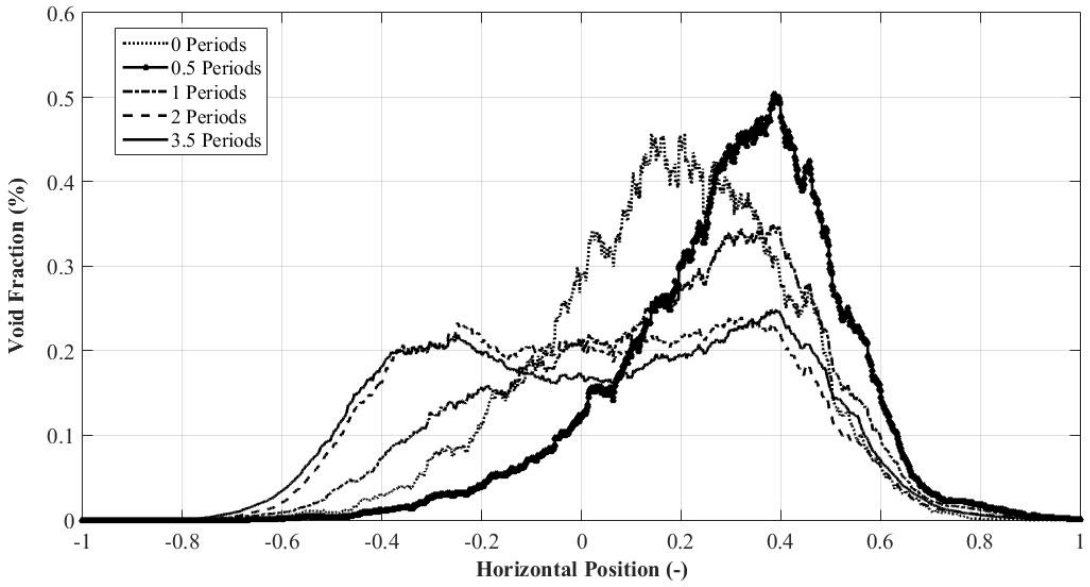

Figure III.12: Evolution of the mean void fraction profile in time in the case of Water membrane sparger and $50\frac{l}{h}$

III.3.1 Water

The following void fraction profiles are averaged over the whole measurement time meaning that at least 25 periods are taken into account. In figure III.13 the profiles in the case of the membrane sparger in water for three different gas flow rates are presented. Our first observations are the two characteristic peaks being well defined at flow rates of $50\frac{l}{h}$ and $100\frac{l}{h}$. These are the regions where bubble interactions are frequent indicating the importance of turbulent interactions on dispersion. Regarding the highest flow rate no double peak can be observed any more. In this case, bubble interactions are as frequent in the column center as in the "peak regions" of the void fraction profiles at lower gas flow rates. Plus, larger bubbles appear due to coalescence changing the nature of interactions. However, a general evolution with increasing gas flow rate can be identified. By increasing the gas injection by a factor of 2, the gas hold-up is approximately doubled as well.

In figure III.14 the same kind of data is plotted in the case of the slugflow sparger. In comparison to figure III.13, the mean bubble dispersion induced by the slugflow sparger is smaller. This difference is becoming less obvious with increasing gas flow rate indicating again an important role of turbulent dispersion. Indeed, at low flow rate

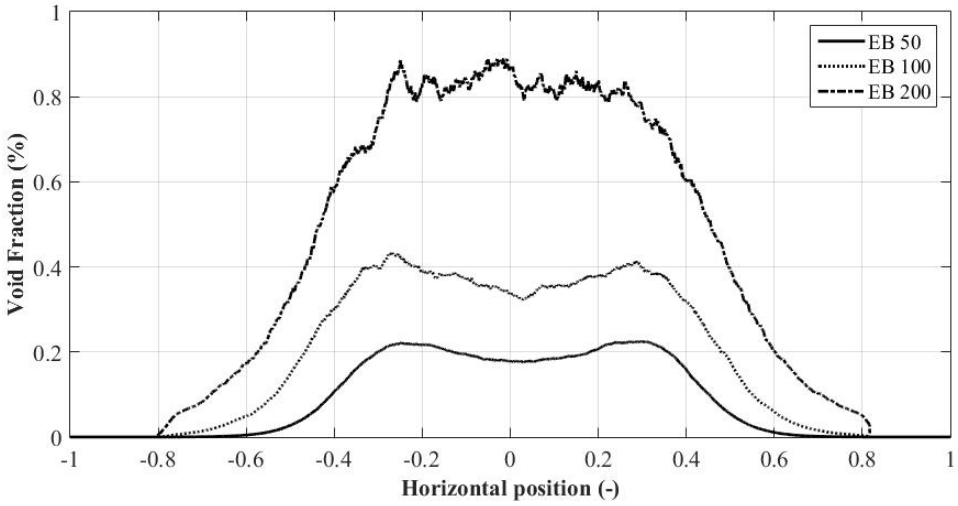

Figure III.13: Void Fraction Profiles in the case of Membrane Injection in Water at different Flow Rates

bubble interaction frequencies between both spargers are very different inducing different plume widths. Ellipsoidal bubbles interact a lot while spherical caps rise rather isolatedly. This means that in the case of spherical cap bubbles, bubble dispersion is driven by the unstable trajectory behaviour and especially by recirculating liquid or mesoscale eddies. At the highest flow rate bubble interaction is frequent for both sparger and becomes the driving phenomenon in bubble dispersion generating similar void fraction profiles.

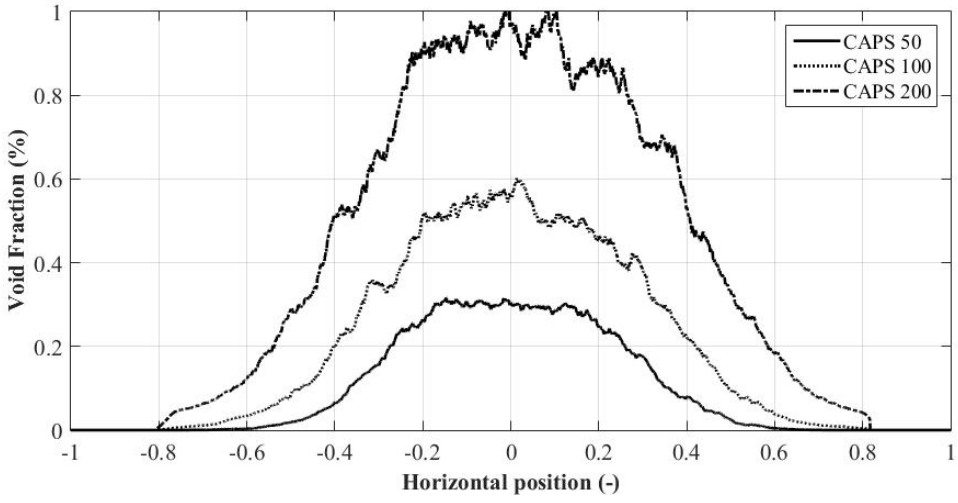

Figure III.14: Void Fraction Profils in the case of Slugflow Injection in Water at different Flow Rates

III.3.2 Liquid Properties

The same void fraction profiles are also plotted for the other fluids at the lowest gas injection flow rate of $50\frac{l}{h}$ and both sparger types. In figure III.15 results from all fluids in the case of the membrane sparger are illustrated. A clear effect of the surface tension can be seen. It was already pointed out that surface tension is mainly influencing bubble interactions without coalescence or break-ups. These interactions are frequent in case of Breox (0.5%) and impact strongly turbulent bubble dispersion. Hence, a larger void fraction profile compared to water can be seen. Plus, due to the decreased bubble sizes, more bubbles are captured in liquid recirculation resulting in a higher averaged gas hold-up.

The viscosity shows a damping effect on bubble dispersion. Bubbles are more and more located in the center and the double peaks disappears. The plume is becoming more confined and takes even a jet-like shape at the highest viscosity.

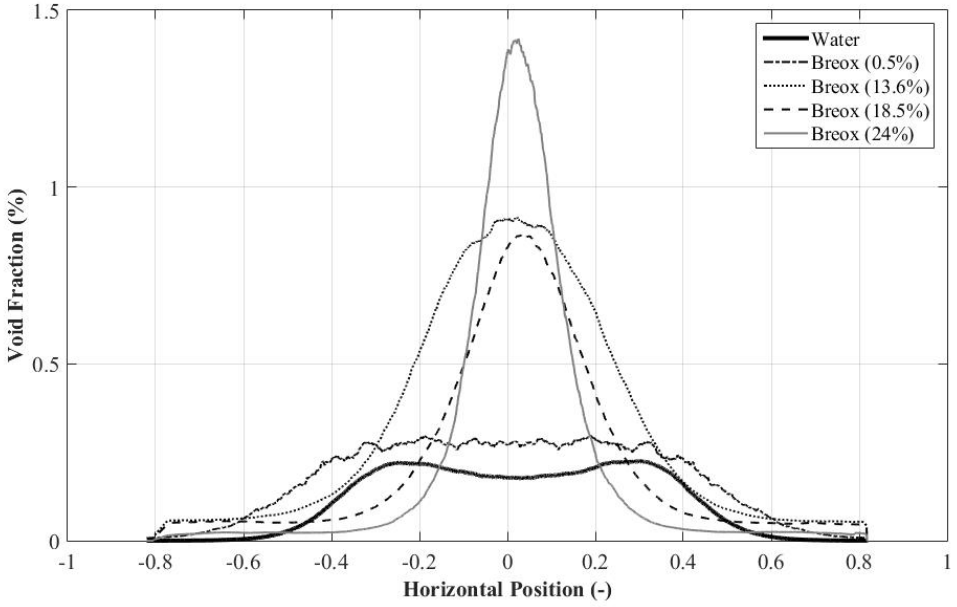

Figure III.15: Void Fraction Profiles in case of Membrane Sparger with $50\frac{l}{h}$ in Different Fluids

Figure III.16 shows bubble dispersion in different fluids in the case of the slugflow sparger. An unexpected result is the higher gas hold-up in Water compared to Breox (0.5%). This could derive from our image treatment or more precisely from the different

ways of volume calculation of WIBs and COSIs. Indeed, in fluids with decreased surface tension, bubbles are less stable and show lower solidity. Consequently, in Breox (0.5%) more COSIs are identified than in Water. Since COSIs volume is calculated differently, the mean gas hold-up is probably underestimated. Normally, it was presumed that surface tension modifcation will not influnce much spherical cap rising, which is why one rather expects a similar void fraction profile than in water.

Anyway, a comparable behavior between the two spargers is observed with increasing viscosity. Here as well, bubble dispersion decreases until taking a jet-like profile at the highest viscosity.

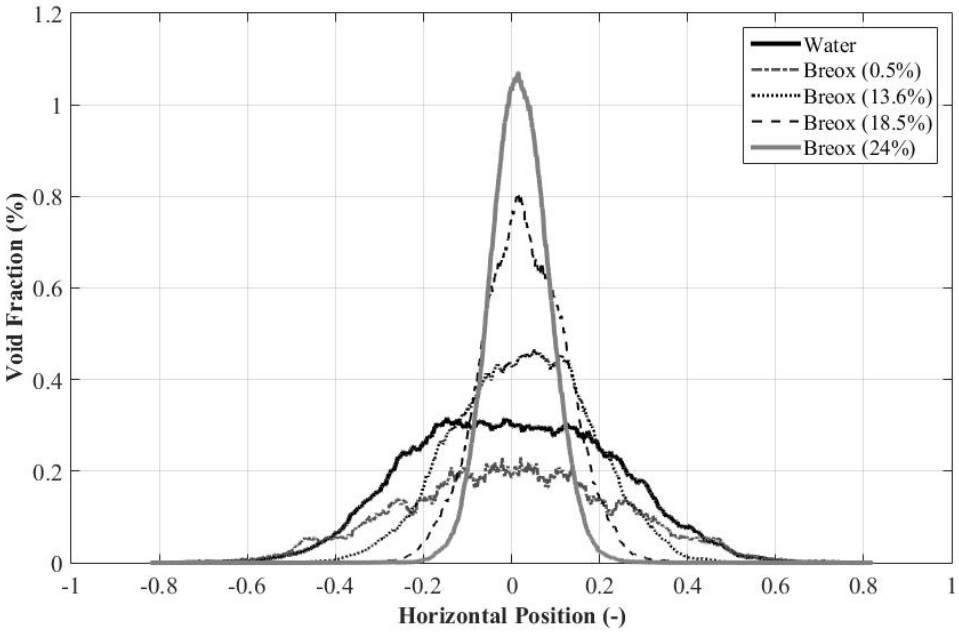

Figure III.16: Void Fraction Profiles in case of Slugflow Sparger with $50\frac{l}{h}$ in Different Fluids

In conclusion, liquid properties influence greatly the dispersion of bubble plumes. Surface tension plays only a role in the case of the membrane sparger by modifying bubble size and interactions. In contrast, viscosity impacts bubble dispersion strongly sparger independently. It shows a damping effect on rising instability, liquid recirculation and bubble-wake interaction.

III.4 Liquid Velocity

To further investigate hydrodynamics, the liquid velocity induced by bubble plumes and its sensitivity to experimental conditions are studied. At this point, a citation from the book (Chatfield, C., 1984) seems appropriate:

Anyone who tries to analyse a time series, without plotting it first, is asking for trouble.

III.4.1 Water

This comment is very important in non stationnary flows, especially when averaged values may lead to misunderstandings. Hence, the liquid velocity in time for both sparger types at the flow rate of $50\frac{l}{h}$ is plotted in figure III.17.

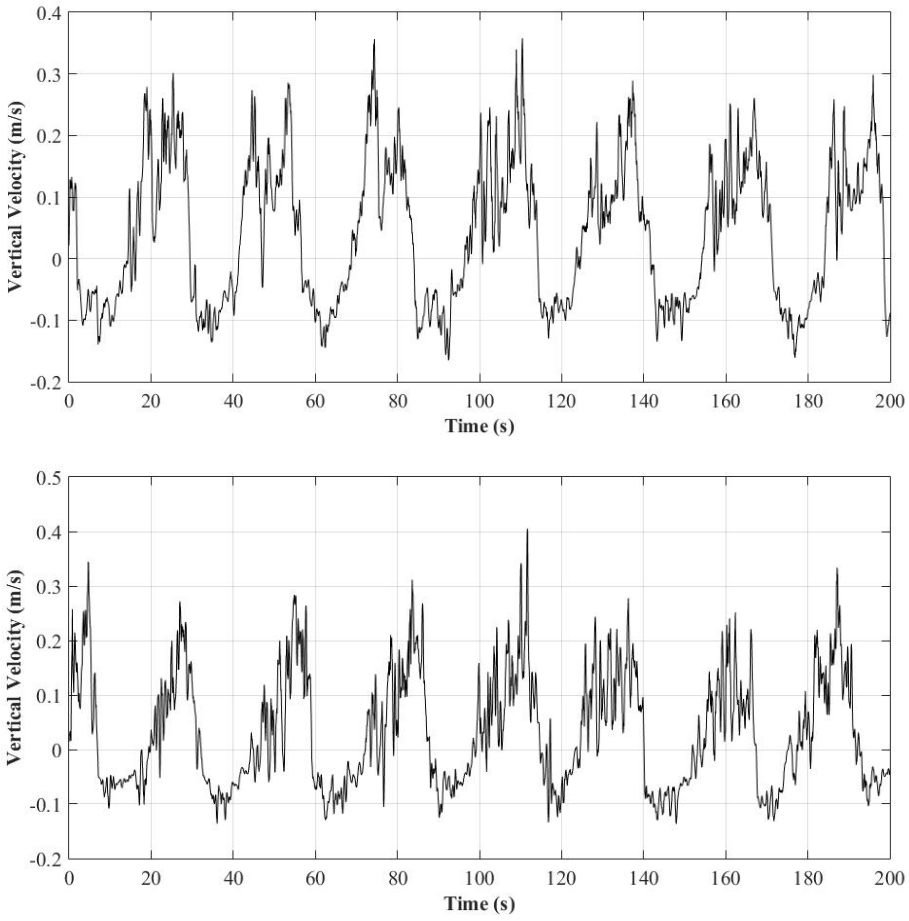

Figure III.17: Vertical Liquid Velocity in Time in Water and $50\frac{l}{h}$ for a) Membrane Sparger and b) Slugflow Sparger

The periodic behaviour of both signals is very similar. Like already presented in section III.1, time scales characterizing bubble plume oscillations for both spargers at the same gas flow rate are close to each other. Anyway, attention should rather be given to the signal itself and to corresponding scales. It is worth to mention that even in vertical direction velocity fluctuations are centered around a value, which is close to zero. This gives a first idea that fluctuations may be more important than the mean flow in bubble plume motion.

III.4.1.1 Vertical Direction

Mean Values

However, averaged values must be investigated anyway. Once again, sparger and injection flow rates are studied in water, first. In figure III.18 averaged liquid velocities in case of the membrane sparger for three different flow rates are presented. The first observation are the relatively weak values compared to the raw signal confirming that fluctuations are at least as important as the mean flow. Secondly, all curves pass through the point (0.5,0) validating in a certain manner our two dimensional measurements. Two zones can be distinguished. On the left hand side of the point located at $x = 0.5$ an upstream flow can be recognized while on the right hand side a downstream flow is present. By integrating the velocity along the whole horizontal axis one obtains a result close to zero. This means that mass balance is met in the considered two dimensional interrogation field. Hence, our assumption that the considered hydrodynamic structure is two dimensional is checked and validated.

The sensitivity to the injection flow rate is clear. Maximum and minimum values increases and decreases with increasing gas flow rate, respectively. For a given time, at higher flow rates more fluid quantity is pushed upwards and then downwards. Between the highest and the lowest flow rate a velocity difference of factor 2 is found. One must also mention that measurements are only performed until a certain distance of some millimeters to the wall. Therefore, the curves do not reach a velocity of zero in the wall region.

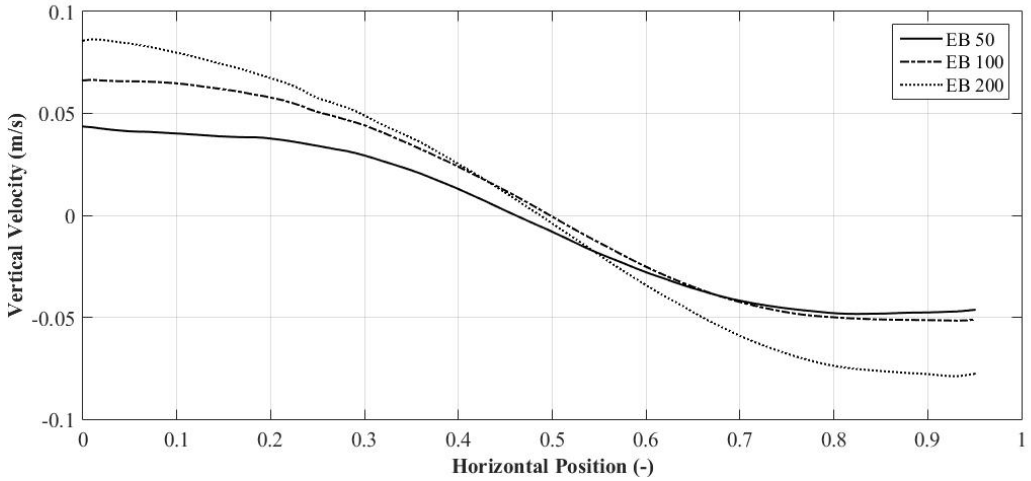

Figure III.18: Vertical Mean Liquid Velocity in the case of Membrane Sparger in Water

In figure III.19 the same information is plotted in the case of the slugflow sparger. Again with increasing gas flow rate, liquid velocity increases in the column center and decreases at column edges. In comparison to figure III.18 all maximum values are closer to each other, which can be explained by similar bubble rising velocities due to similar size distributions. Regarding the flow rate of $50\frac{l}{h}$, mass conservation is not met indicating the presence of three dimensional effects. Last may be provoked by the unstable rising behavior of rather isolated spherical caps.

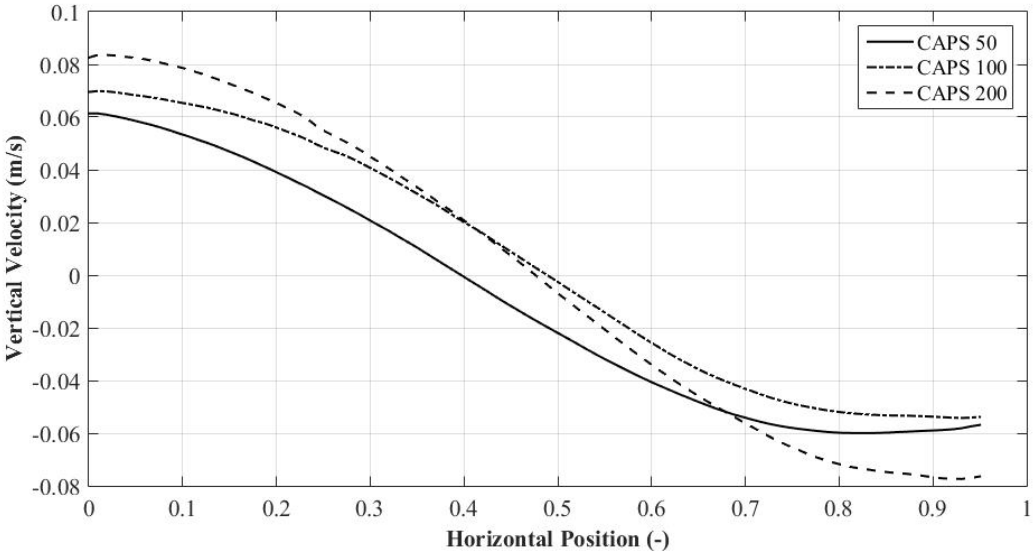

Figure III.19: Vertical Mean Liquid Velocity in the case of Slugflow Sparger in Water

Fluctuations

It is clear that studying averaged values in order to analyze a non stationnary phenomenon is not enough. To go deeper in the analysis, velocity standard deviations (RMS) are plotted for both spargers in water and with a flow rate of $50\frac{l}{h}$ (see figure III.20 (top)). Both curves show higher fluctuations close to the center where more bubbles are present and lower values close to the edges. Velocities in the very center should be considered carefully. Because of the truncation, erroneous values appear. The most interesting part of figure III.20 (top) are the scales, which are high compared to averaged velocities. Strong upstream as well as downstream flows and large eddies induce strong fluctuations. It should also be noted that a maximum is located close to $x = 0.25$ in figure III.20 (top left) corresponding to the position of the peaks in the void fraction profiles in figure III.13 indicating a strong relation between both. This result is confirmed by figure III.20 (top right) and figure III.14 where these peaks are absent. To better understand these values, two points on the horizontal axis were chosen to plot mean velocity histograms for both spargers (figure III.20 (middle and bottom)).
The first point located at the "peak position" $x = 0.25$ is chosen to compare the impact of the bubble type in the column center. Histograms of the vertical velocity can be seen in figure III.20 (middle). Regarding the membrane sparger (left) a bi-modal distribution with almost sinusoidal shape can be recognized. By also taking into account the scales, it is rather easy to understand that these fluctuations are well organized and must correspond to bubble plume motion. In the case of the slugflow sparger, the histogram at $x = 0.25$ is not that clear. An overlay of a sinusoidal and a Gaussian distribution can be observed. Again, the bi-modal one results from the low frequency bubble plume motion. The Gaussian distribution is induced by the unstable trajectory behavior (Ryskin & Leal, 1984b) of spherical cap bubbles provoking chaotic flow structures. The second point close to the edge at $x = 0.9$ was chosen to further analyze bubble type influences (see figure III.20 (bottom)) in wall region. This time both histograms show clearly a combination of sinusoidal and Gaussian distribution. The sinusidal one results from the organized bubble plume motion, which is still present in the considered zone. The Gaussian distribution indicates chaotic or random motion. Considering the small velocity values of these fluctuations one can conclude that they must correspond to wall effects or wall induced turbulence.

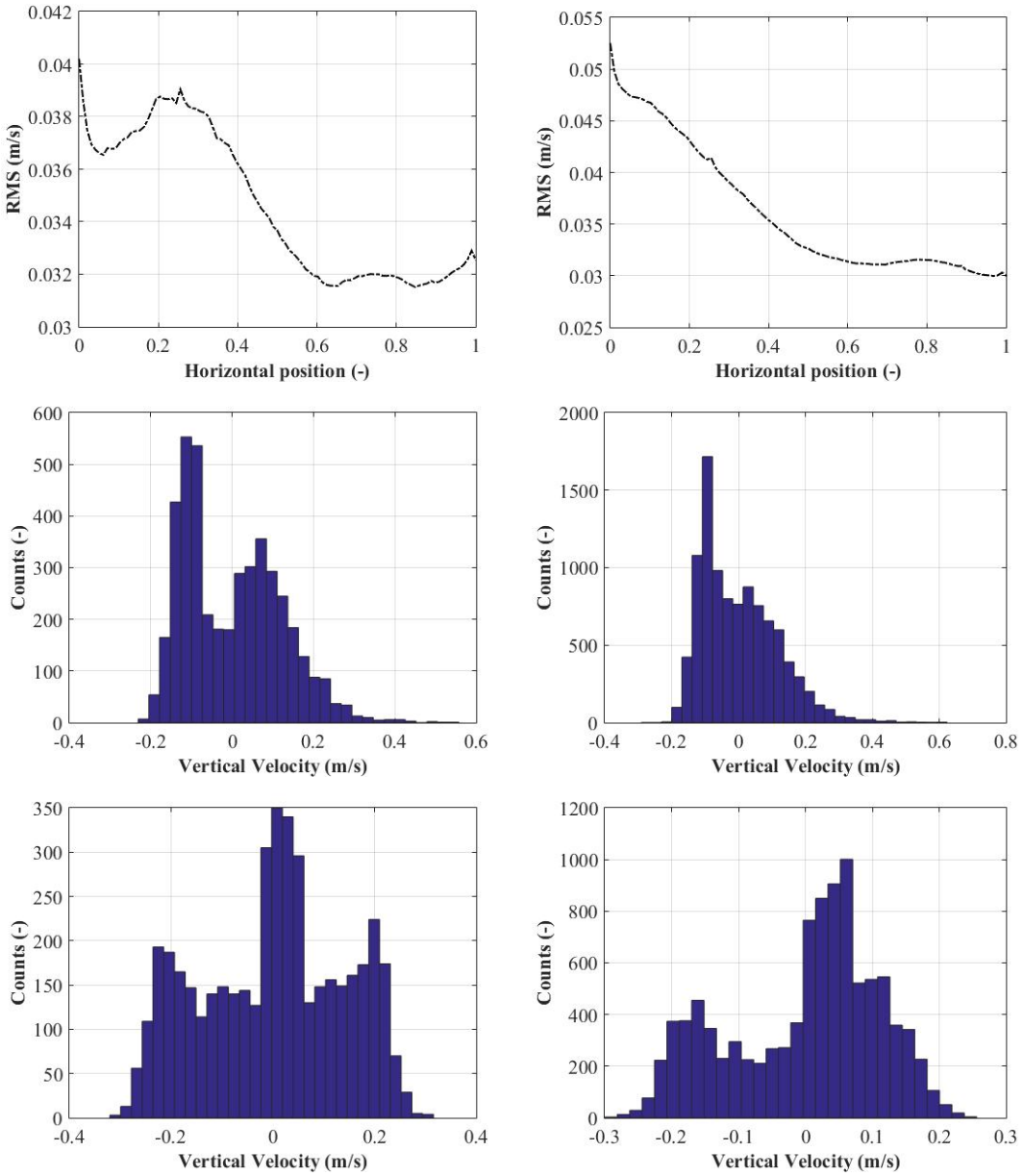

Figure III.20: RMS and Histograms in Vertical Direction at $X = 0.25$ (middle) and $X = 0.9$ (bottom) in Water and $50\frac{l}{h}$ for Membrane Sparger (left) and Slugflow Sparger (right)

It was shown that both bubble types induce organized motion over the whole column cross section. This organized motion is easier to quantify in the wall region than in column midle where bubble induced agitation is also present. Besides, spherical cap bubbles provoke way more randon motion than ellipsoidal bubbles due to their unstable rising behavior.

POD

POD is applied to velocity fields to understand the contribution of every flow structure to the global regime in terms of energy. For a better understanding only velocity profiles including fluctuations are analyzed. But first, the spectrum from the eigenvalue solution of equation II.28 is presented in figure III.21 (left).

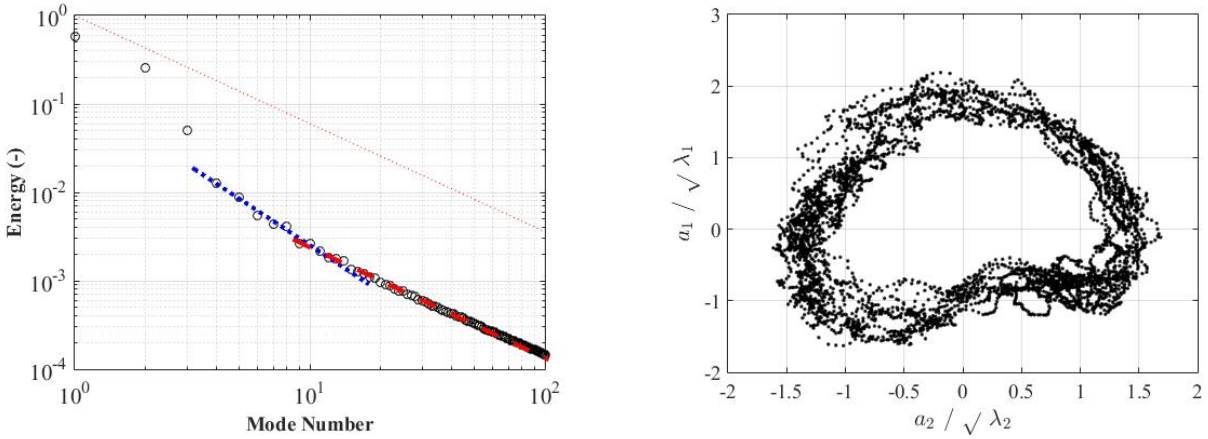

Figure III.21: POD Energy Spectrum (left) and Mode Dependency between Mode 1 and 2 (right)

All energy distributions are plotted as a function of their mode number. The two first modes show a way higher energy contribution than all the others. In our case the highest energy is induced by large fluctuations corresponding to organized bubble plume motion. Plus, the similar energy level of the first two modes can indicate that both are related to eachother. This is the reason why dependency between the first modes $(1-4)$ is checked. It turned out that the first and the second mode are strongly related as illustrated in figure III.21 (right) where the corresponding phase portrait is plotted. The almost circle like shape of the curve indicates that both modes belong to the same hydrodynamic structure. The third mode is rather separated from all other modes in terms of energy. It is assumed that this one could be a transition mode between organized and ramdon motion. But if one had to decide where this mode belongs to, the response would rather be organized motion. Furthermore, the modes $4-10$ follow a line with a slope of $-\frac{5}{3}$ that is presented by a dotted blue line in the figure. The origin of this value will be discussed at the end of the chapter. Finally, the modes $11-100$ follows a line with a slope of $-\frac{11}{9}$, which is drawn by the red dashed line. (Sirovich, 1987) related this value to inertial turbulence. With respect to the results mentioned

above, the vertical velocity in a single point at $x = 0.25$ is reconstructed for different mode combinations. In the present case, even time resolved reconstruction is possible:

$$w_t^n = \sum_n a_t^n \phi_z^n \tag{III.6}$$

Three defined mode combinations ($n \in [1,2]$, $n = [3]$ and $n \in [4,7]$) are chosen to estimate the contribution of bubble plume motion and bubble induced liquid fluctuations. In figure III.22 the reconstructed velocities in time and the corresponding fluctuation histograms can be seen. The first two modes show a strong coupling and represent clearly the oscillating bubble plume motion, which could be separated from the rest of the flow structure. The signal is sinusoidal and the frequency coincides perfectly with low frequency time scales from section III.1. The third mode (III.21 (middle)) representing an intermediate energy, shows indeed a transition between organized and chaotic flow. Quasi periodic fluctuations can still be recognized, but noise corresponding to random motion becomes important as well. This interpretation becomes even more obvious by looking at the attached histogram. As in the fluctuation analysis a combination of a sinusoidal and a Gaussian distribution can be identified. But in figure III.20 the Gaussian one is slightly more dominant than here suggesting again that the third mode belongs rather to organized motion. Finally, the same reconstruction is done for modes $4-7$. The signal is completly disorganized, which is confirmed by the histogram. The distribution shows Gaussian shape indicating chaotic flow. By taking into account the small energy values, one can assume that these fluctuations correspond completly to bubble induced fluctuations.

In figure III.23 the RMS as a function of the horizontal position are reconstructed, on the left handside for low mode numbers and at the right handside for higher ones. The RMS profile for the first two modes resulting from the bubble plume motion indicates their domination on the flow structure in the wall region where bubble passages are rare. With increasing modes the RMS increases in the center. This illustrates the contribution of bubble induced liquid fluctuations. On the right figure higher modes are plotted. Over a mode number of ≈ 10 fluctuations are rather related to turbulence, which was already suggested by the slope of the energy spectrum.

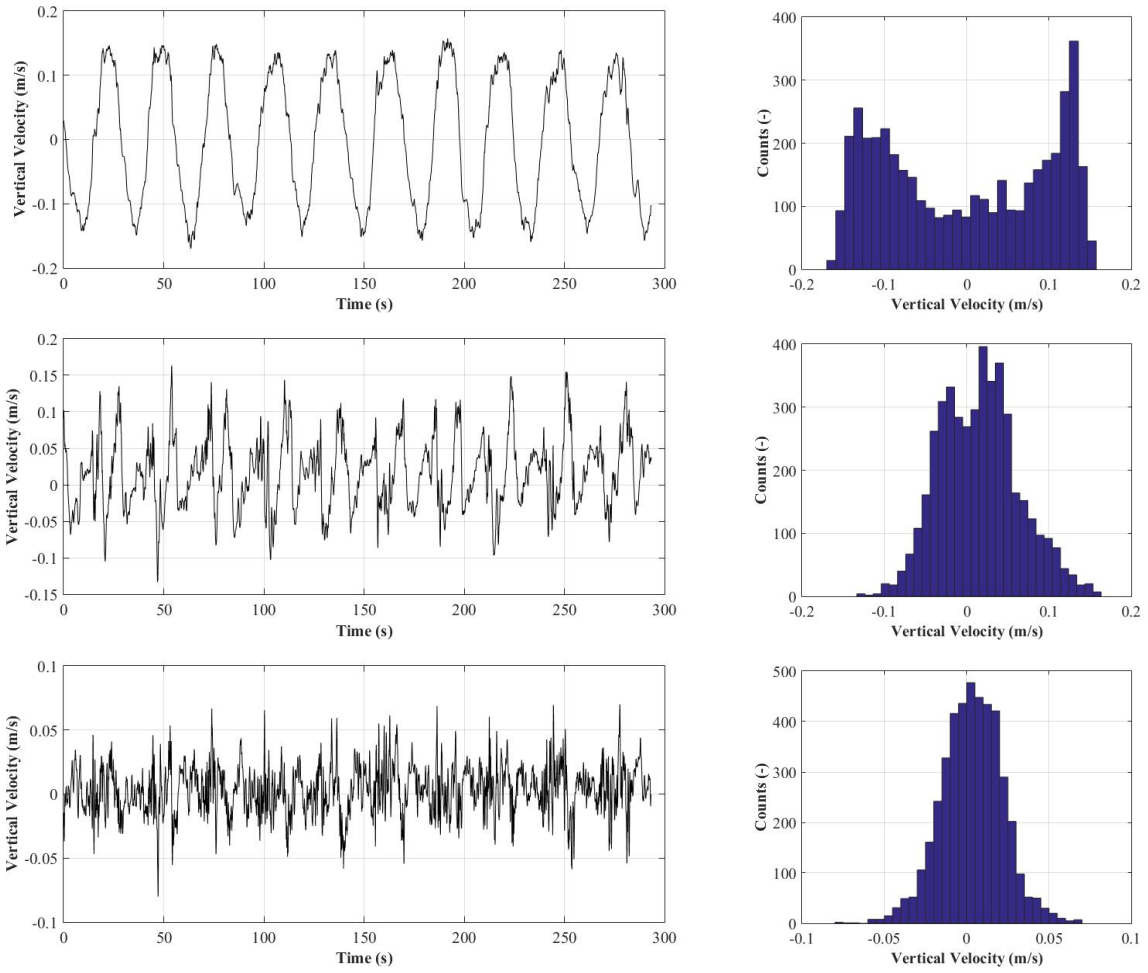

Figure III.22: POD Time Signals and Histograms in Water and $50\frac{l}{h}$ for Modes 1 & 2 (top), 3 (middle) and 4 to 7 (bottom) for Membrane Sparger

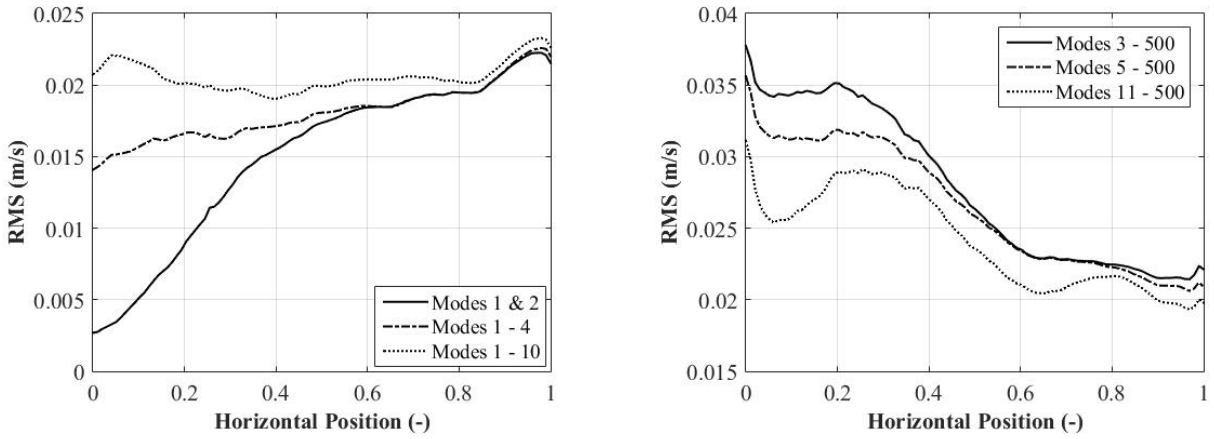

Figure III.23: Reconstructed RMS from POD Treatment for Membrane Sparger

In figure III.24 contributions from disorganized motion (bubble induced fluctuations and turbulence) and organized plume induced fluctuations are compared to the total RMS. As it could be expected, organzied motion is present over the whole column cross section, but becomes more important towards the walls. Disorganized motion (bubble induced agitation and turbulence) is increasing towards the column center.

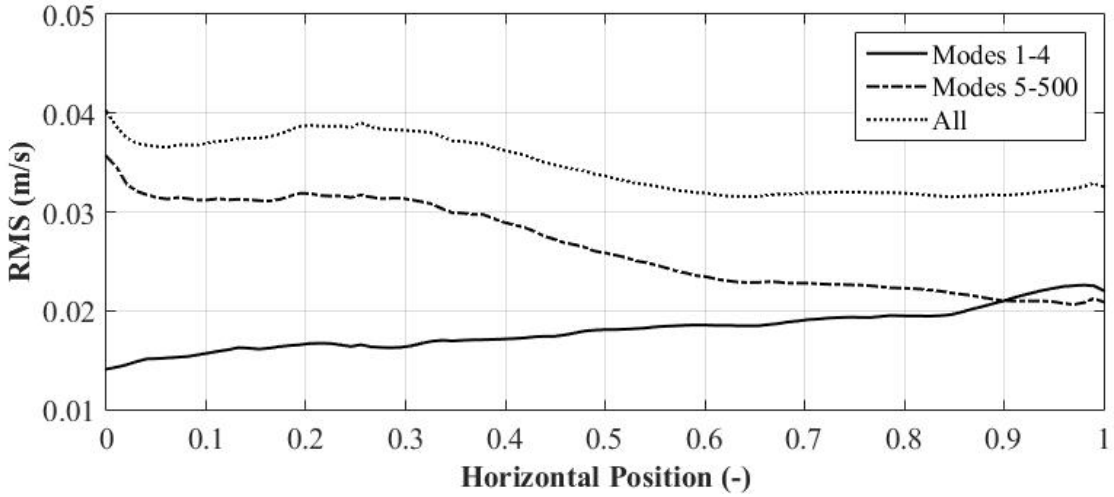

Figure III.24: Reconstructed and Raw RMS in the case of Water, $50\frac{l}{h}$ and Slugflow Sparger

The same POD analysis is done for the case of the slugflow sparger. In figure III.25, the energy spectrum and the dependency of the first modes are plotted for spherical caps. As previously, the same energy ditribution and the same mode dependency than for the membrane sparger is found. Modes 1 and 2 correspond to organized motion, mode 3 to transition and higher modes to chaotic or random motion. The two different mentioned slopes are observed here as well. Hence, one is able to distinguish bubble induced fluctuations and turbulence. This result could be expected since comparable low frequency oscillations were determined in section III.1. Therefore, one comes directly to the reconstructed velocity signals from the point $x = 0.25$. Because of the similar results of eigenvalues, the exact same mode separation than for the membrane sparger ia shown in figure III.26.

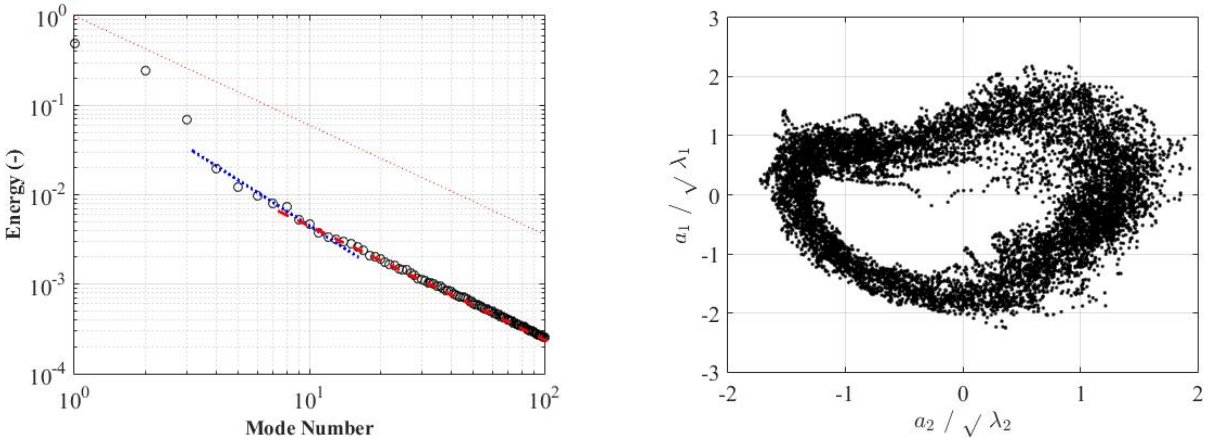

Figure III.25: POD Energy Spectrum (left) and Mode Dependency between Mode 1 and 2 (right)

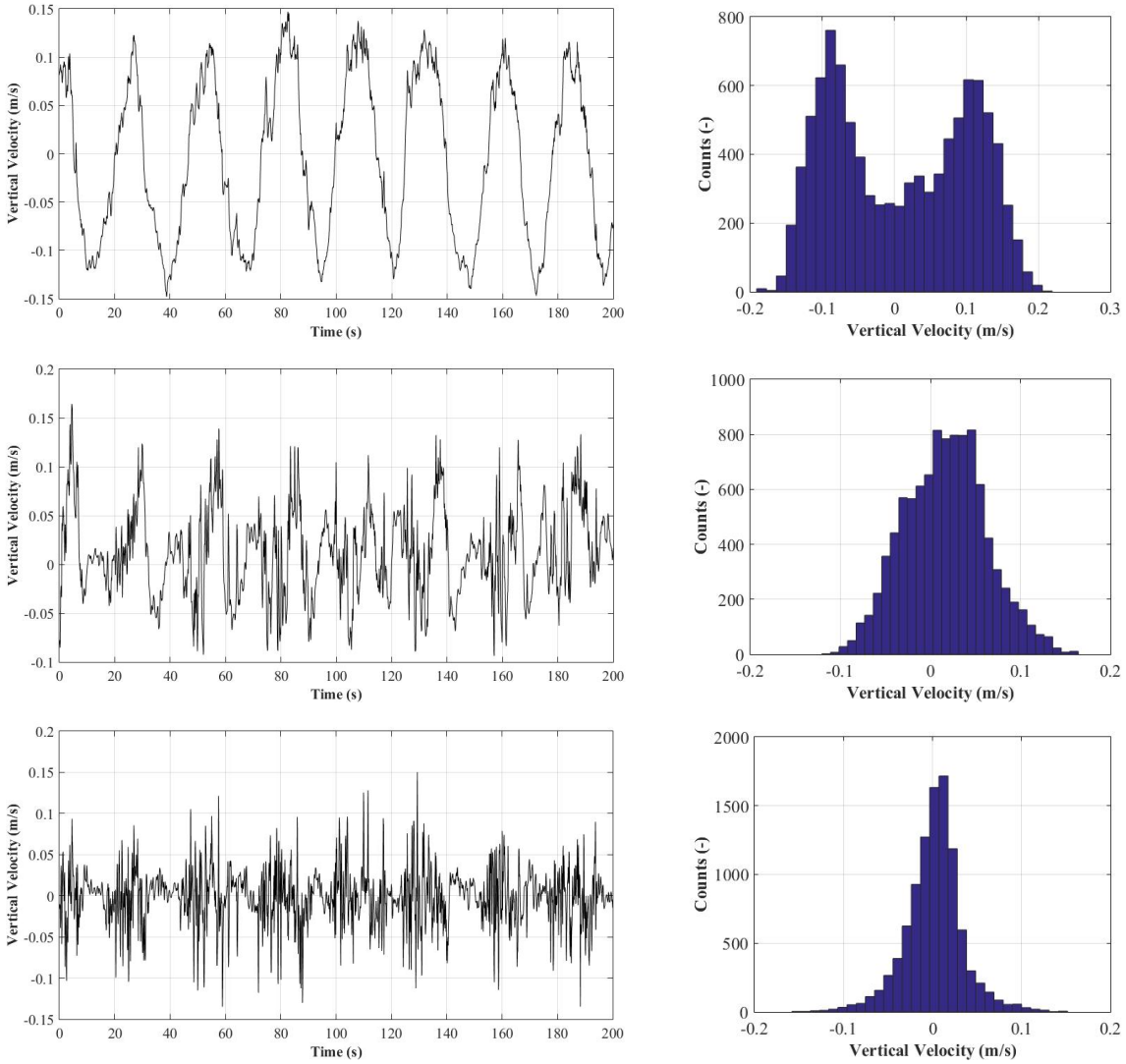

Figure III.26: POD Time Signals and Histograms in Water and $50\frac{l}{h}$ for Modes 1 & 2 (top), 3 (middle) and 4 to 7 (bottom) for Slugflow Sparger

Again, the first two modes belong to the oscillating bubble plume motion. The chaotic bubble induced motion of the spherical caps could be filtered. Hence, a clear sinusoidal ditribution can be seen for the reconstructed signal of these first two modes. In the middle of figure III.26 the third mode is used separately for reconstruction since it is believed to be a transition mode as for the membrane sparger. Indeed, the histograms are similar, but a small difference between both spargers can be recognized anyway. The sinusoidal distribution, seen in the case of the membrane sparger, is not as clear anymore indicating that the third mode is less organized in the case of spherical caps. The bubble plume motion is less structured because of the unstable trajectory behaviour and more bubble induced fluctuations are measured. Lastly, modes $4-7$ show a chaotic behaviour creating a well shaped Gaussian distribution. These fluctuations are believed to derive from bubble induced agitation.

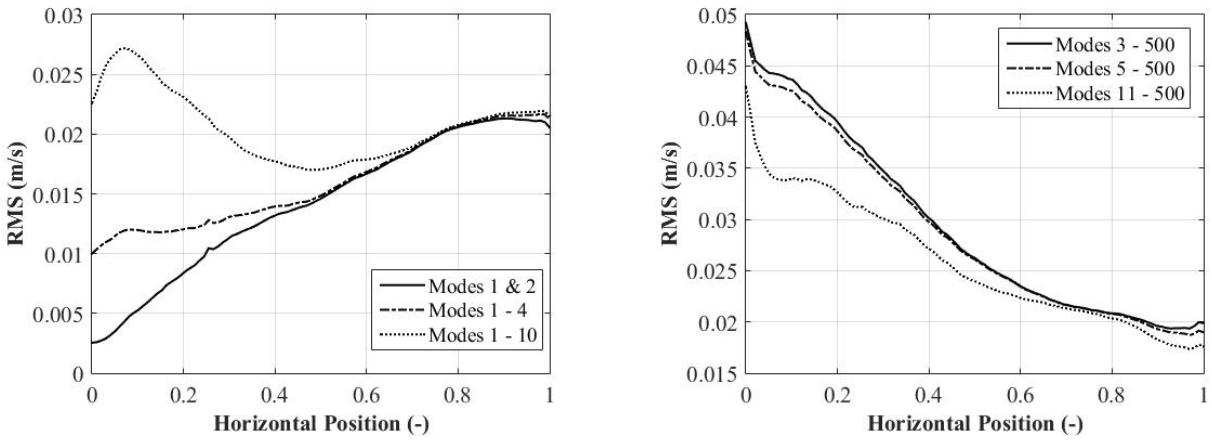

Figure III.27: Reconstructed RMS from POD Treatment for Slugflow Sparger

In figure III.27 the RMS are reconstructed for different mode combinations. First two modes corresponding to organized motion related to the bubble plume movement show the highest contribution in the region next to the walls. With increasing mode numbers, the contribution of bubble induced fluctuations increases as well in the column center. On the right figure RMS is plotted for higher modes. The contribution of bubble induced fluctuations can be recognized by the gap between the dotted and the dash dotted line. Turbulence on the other hand is rather distributed over the whole column width.

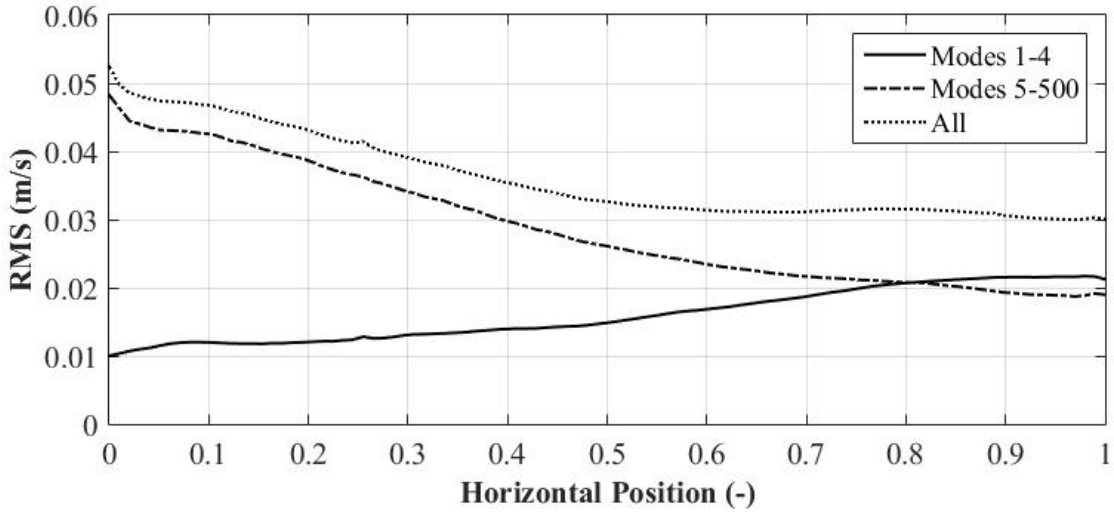

Figure III.28: Reconstructed and Raw RMS in the case of Water, $50\frac{l}{h}$ and Slugflow Sparger

In figure III.28 contributions of organized and random motion to the total RMS are shown. Similar to the membrane sparger, organized motion contributes more at the edges and random structures in the column center. In conclusion, the studied flow structure is mainly constituted by organized fluctuations in the case of both spargers. The RMS of fluctuations are of similar amplitude compared to averaged velocity values. Therefore, it make sense to apply the POD in order to understand the contribution of organized fluctuating and chaotic motion. Last one could be further investigated in order to estimate the contribution of bubble induced and turbulence influences.

III.4.1.2 Horizontal Direction

Here as well velocity signals are plotted before any analysis for the same reasons than in vertical direction. In figure III.29 the horizontal velocity component in a single point is shown in time. Both signals from the different spargers show the same oscillating behaviour. Even the amplitudes are very close.

Mean Values

Let us begin by analyzing averaged velocity profiles that are plotted in figure III.30 for the membrane (left) and the slugflow sparger (right).

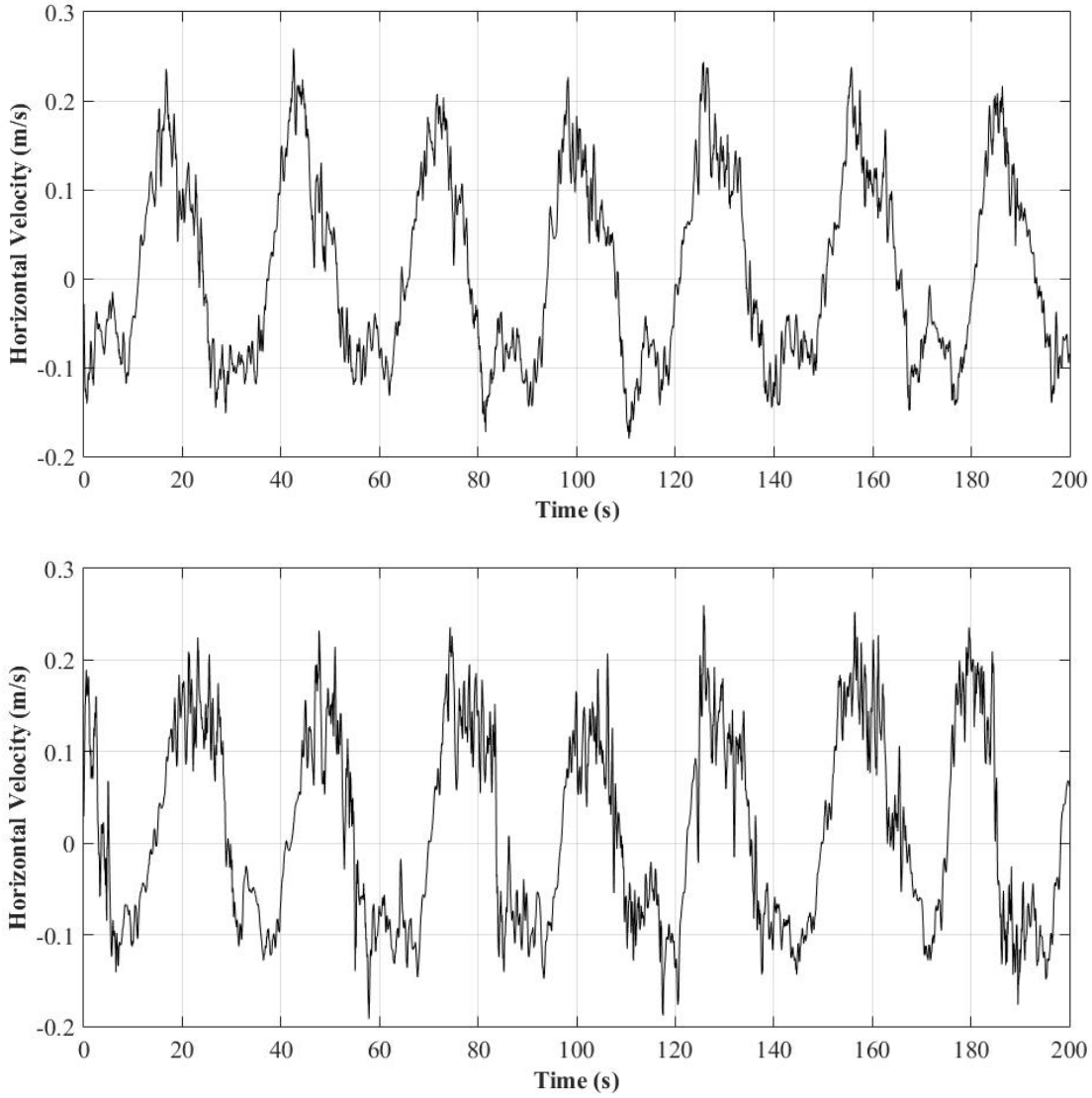

Figure III.29: Liquid Velocity Signals in Time in Water and $50\frac{l}{h}$ for Membrane Sparger (top) and Slugflow Sparger (bottom)

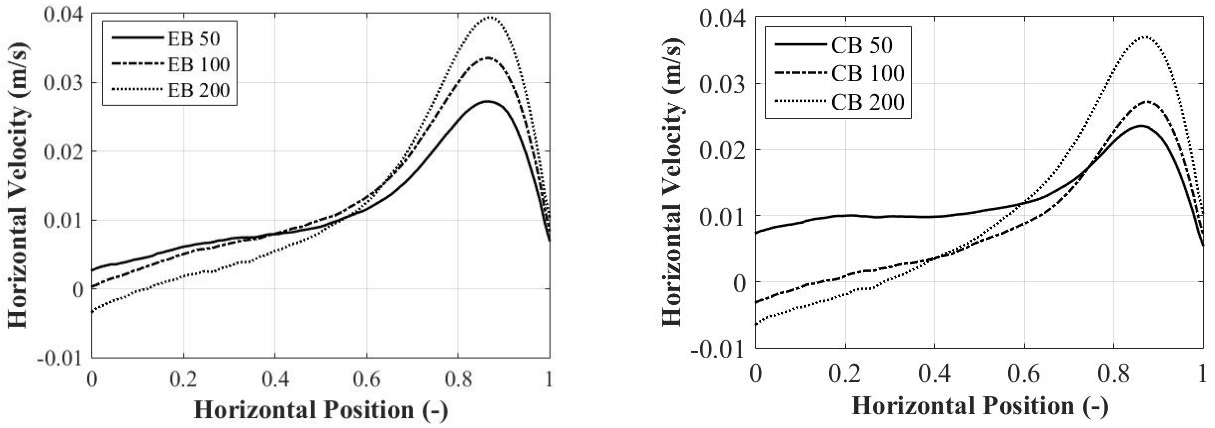

Figure III.30: Time Averaged Horizontal Liquid Velocity in Water for Membrane Sparger (left) and Slugflow Sparger (right)

Both sparger types produce very similar horizontal velocity distributions. In the column center the averaged transverse velocity is very small. It is worth to mention that with increasing gas flow rate liquid velocities become even negative, but only slightly. The highest velocities in horizontal direction are detected close to the walls and increases with increasing gas flow rate. It is a little difficult to interpret such mean values in non stationnary flows. But one can estimate that more liquid moves towards the wall than towards the center. The explanation can be given in form of residence time. First the vortical cells passes through the acquisition window. Since the velocity of these vortices is constant they should not have great impact on averaged values. The second situation is when bubbles are pushed towards the walls through the interrogation window. Then liquid is pushed against the walls generating higher horizontal mean velocities close to the walls.

Fluctuations

Anyway, to investigate horizontal velocity in detail, fluctuations must be considered. As in the case of the vertical direction, horizontal fluctuations in form of RMS are plotted in figure III.31 (top) for both spargers. The highest horizontal velocity fluctuations are registered in the column center while the lowest ones are close to walls. The wall damps the horizontal movement creating lower values. The same evolution can be observed for both spargers. Even the scales are very similar.

To go further in our analysis, velocity fluctuations are plotted in the same positions than for the vertical velocity ($x = 0.25$ and $x = 0.9$). In horizontal direction both spargers show the exact same behaviour. In the column middle a rather sinusoidal distribution can be observed. These bi-modal fluctuations belong to the bubble plume oscillating motion. It seems that both bubble types induce equally organized motion in horizontal direction in the center. Close to the walls at $x = 0.9$ horizontal fluctuations are more chaotic, which can be recognized by the Gaussian distribution of the RMS. Indeed, bubble induced fluctuations are higher in horizontal direction. Hence, they contribute more to liquid fluctuations than the organized motion in the considered zone.

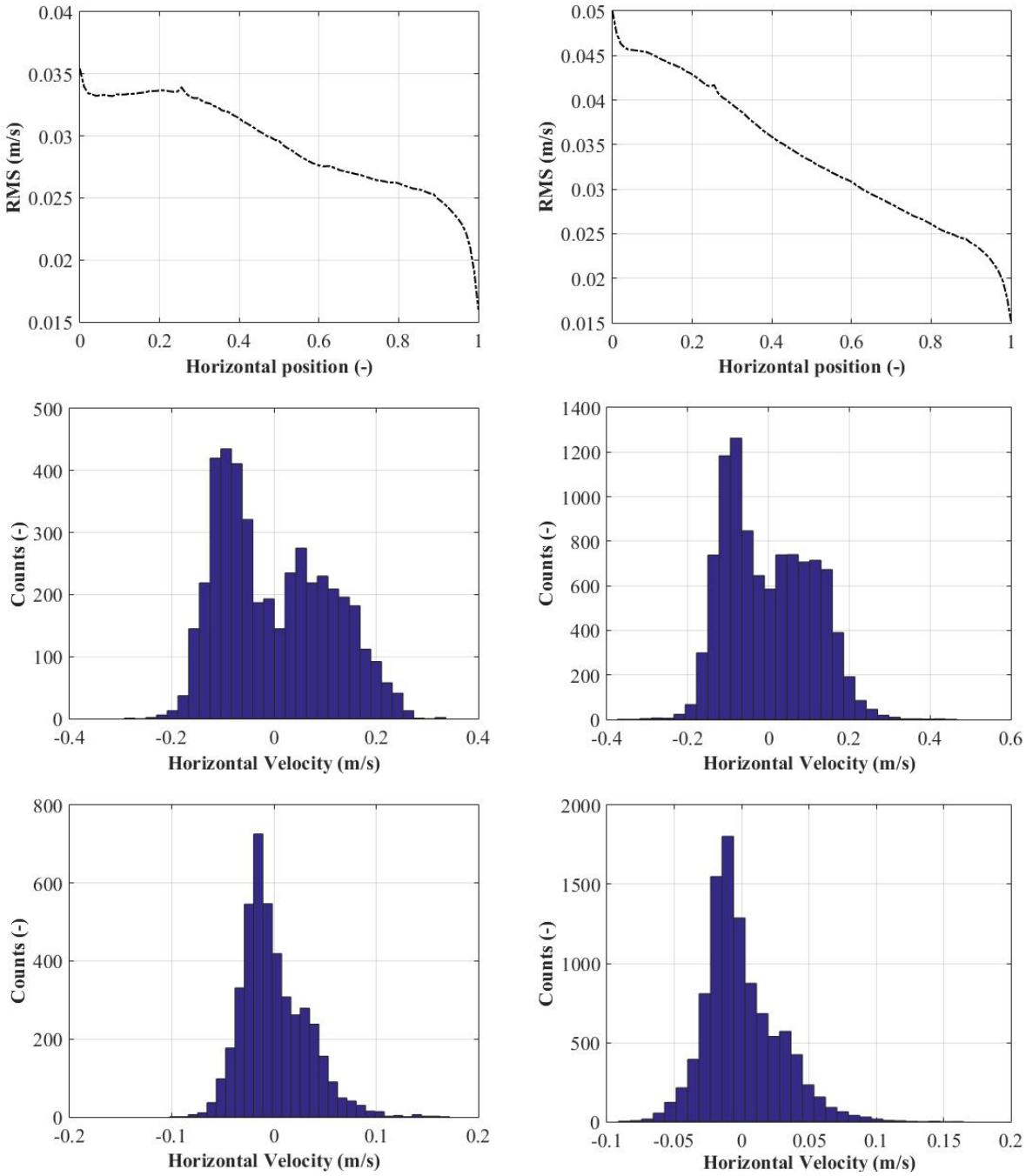

Figure III.31: RMS and Histograms in horizontal direction at $X = 0.25$ (middle) and $X = 0.9$ (bottom) in Water and $50\frac{l}{h}$ for Membrane Sparger (left) and Slugflow Sparger (right)

III.4.2 Liquid Properties

The influences of fluid properties on liquid hydrodynamics induced by bubbles is studied as well. Therefore, vertical velocities in different fluids and for both spargers are plotted.

III.4.2.1 Vertical Direction

Mean Values

In figure III.32 and figure III.33 averaged vertical velocities at a gas flow rate of $50\frac{l}{h}$ are plotted for the membrane and the slugflow sparger, respectively. First the membrane sparger is studied. In figure III.32 the same curve shapes with ascending and descending part than in water are recognized. A first comparison is done between water and Breox (0.5%) to investigate surface tension modifications.

A surprising observation is the velocity increase in Breox (0.5%) having a lower surface tension than water. This difference is larger in the upstream than in the donwstream part indicating slightly stronger three dimensional effects. Indeed, it was already mentioned that surface tension shows high influence when bubble interaction is frequent, but without coalescence.

To further investigate liquid propertries, all Breox fluids are compared between eachother to study viscosity impact. The same decreasing behaviour from the center to the edges until reaching negative values close to the wall is observed. Hence, a mean recirculation zone can be identified. Maximum values in the center increases significantly with increasing viscosity. At this point one can make the connection with airlift configurations. It is possible to consider the upstream and the downstream part as two different columns. The middle part would be the riser and the external parts the downcomers. In such airlift configuration, liquid velocities are driven by the weight difference between these two parts. This argument can be used here as well. With increasing gas flow rate, the gas hold-up and therefore the mixture density difference becomes larger and liquid velocity is increased. Furthermore, the ascending zone is becoming smaller while the descending zone is becoming more important. This can be related to the dispersion, which is decreasing as well with increasing viscosity. Also, it seems that wall effects are becoming important damping the descending liquid motion. This is particularly evident in the case of Breox (24%) where the velocity close to the wall approaches zero.

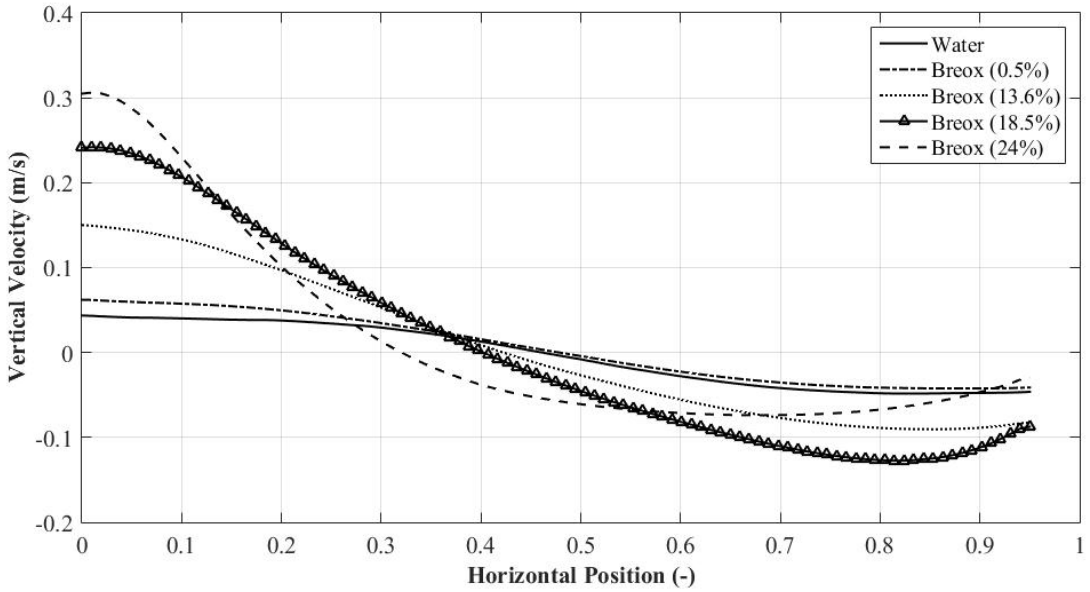

Figure III.32: Vertical Mean Liquid Velocity in the case of Membrane Sparger in different Fluids

The same analysis is performed in the case of the slugflow sparger (see figure III.33). As expected, surface tension shows only a minor effect on liquid hydrodynamics. This is because surface tension is mainly influencing bubble interactions, which are not frequent here. With increasing viscosity the same tendencies than in figure III.32 are observed. Maximum values in the center increase and the ascending zone becomes smaller. Once again, the connection with the airlift configuration can give an explanation for this observation. Plus, the same non linear relation between velocities close to the wall and viscosity can be seen. Again, wall effects become more important with increasing viscosity. Figure III.33 shows that spherical caps generate lower velocity than ellipsoidal bubbles in fluids with higher viscosity than water. This indicates a difference of the momentum transfers from the gas to the liquid phase between both bubble types.
In conclusion, both spargers show a quite similar evolution concerning liquid velocity with increasing viscosity. The main differences are the maximums and minimums being higher in the case of the membrane sparger for all fluids. At the same flow rate, ellipsoidal bubbles seem to better transfer their momentum to the liquid phase than spherical cap bubbles. This can be explained by a larger interfacial area of smaller objects for a given volume (here injection flow rate).

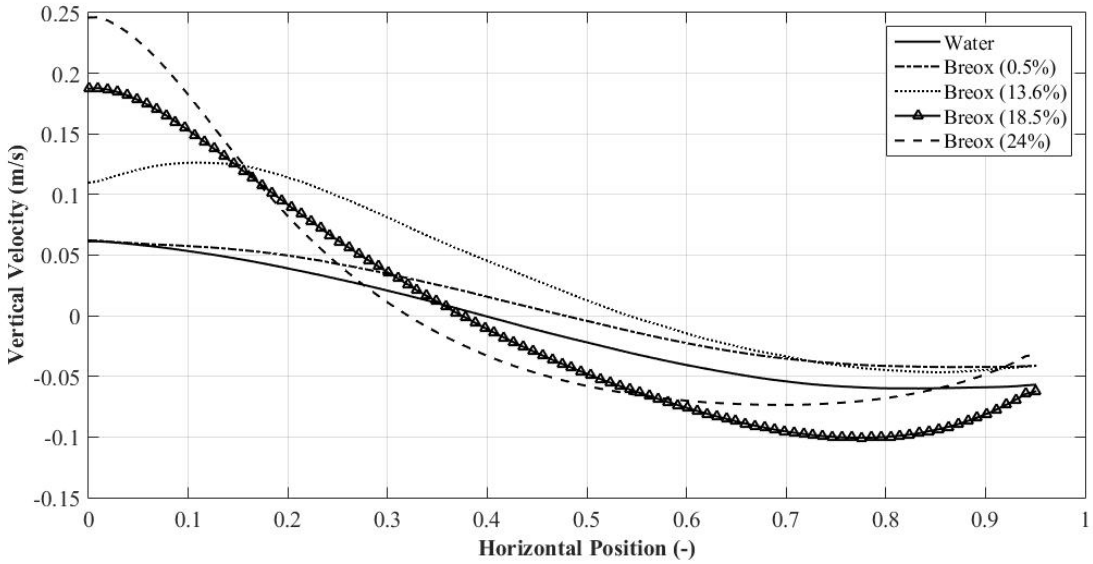

Figure III.33: Vertical Mean Liquid Velocity in the case of Slugflow Sparger in different Fluids

Fluctuations

The case of Breox (13.6%) with a gas flow rate of $50\frac{l}{h}$ through both spargers was chosen to analyze fluctuations in viscous media in the same way than in water. Similarly to water, fluctuations are at least of the same order of magnitude than the mean flow. This illustrates that they must be considered again. In figure III.34 fluctuations for both spargers and the corresponding histograms in two different points are plotted. The general evolution from the column center to the edges is similar in both cases. Fluctuations are maximum in the center and minimum values are registered close to the wall. The main difference concerns the scales. Indeed, spherical cap bubbles induce higher velocity fluctuations. To get more inside, histograms are considered as well. In the case of the membrane sparger (left) both histograms are very comparable. At both column positions, a combination of a sinusoidal and a Gaussian distribution can be observed. Following the same argumentation than previously, the fluctuations are strongly influenced by the organized motion and by bubble induced fluctuations. It seems that compared to water, the flow is more chaotic since the Gaussian distribution predominates. This observation suggests that organized motion is more damped by viscous effects than bubble agitation indicating that the energy contribution of the

different flow structures is not the same than in water. In the case of the slugflow sparger, only fully Gaussian distributions are found. It seems that no organized motion is present anymore in that case. The chaotic bubble induced motion from spherical caps dominates compared to swarm effects like bubble plume wandering confirming that last one is more damped by the viscosity.

POD

The study of the considered fluctuations showed that the case of the membrane sparger is better adapted for further analyzes since plume motion can still be recognized. In the slugflow sparger case, no traces of organized motion were found as illustrated above. For an easy understanding the same figures than for the POD in water are plotted. In figure III.35 the energy spectrum and the phase portrait are shown. The energy spectrum is slightly different than in water. The first mode contains more energy ($\approx 60\%$) than all the other ones and is not related as it was the case in water. In Breox the second and the third modes are very close to each other in terms of energy (each mode $\approx 10\%$). Hence, one supposed a mode dependancy between these two ones. But the relation between these modes is not as clear as in water (see figure III.35 (right)). Nevertheless, for further treatments one supposed that both, the second and the third, are transition modes. Besides, the same two slopes corresponding to bubble induced liquid fluctuations and turbulence are observed.

In figure III.36 reconstructed velocity signals in time in one point and the corresponding histograms are plotted. In contrast to the case of water, the first mode is plotted as single one, then modes two and three together and finally modes $4-7$ again. By considering the signal of the first mode it is pretty clear that bubble plume motion is represented. This is also confirmed by the sinusoidal shaped histogram. The reconstructed signal from the second and third mode are plotted in the middle. As in the case of water the transition signal shows disorganized oscillating behaviour. Indeed, the histogram is mainly Gaussian, but shows also a slightly bi-modal distribution. Hence, organized and chaotic motion is present. Finally, the last signal of figure III.36 represents only disorganized or random motion. No oscillation period is found and the histogram shows Gaussian shape.

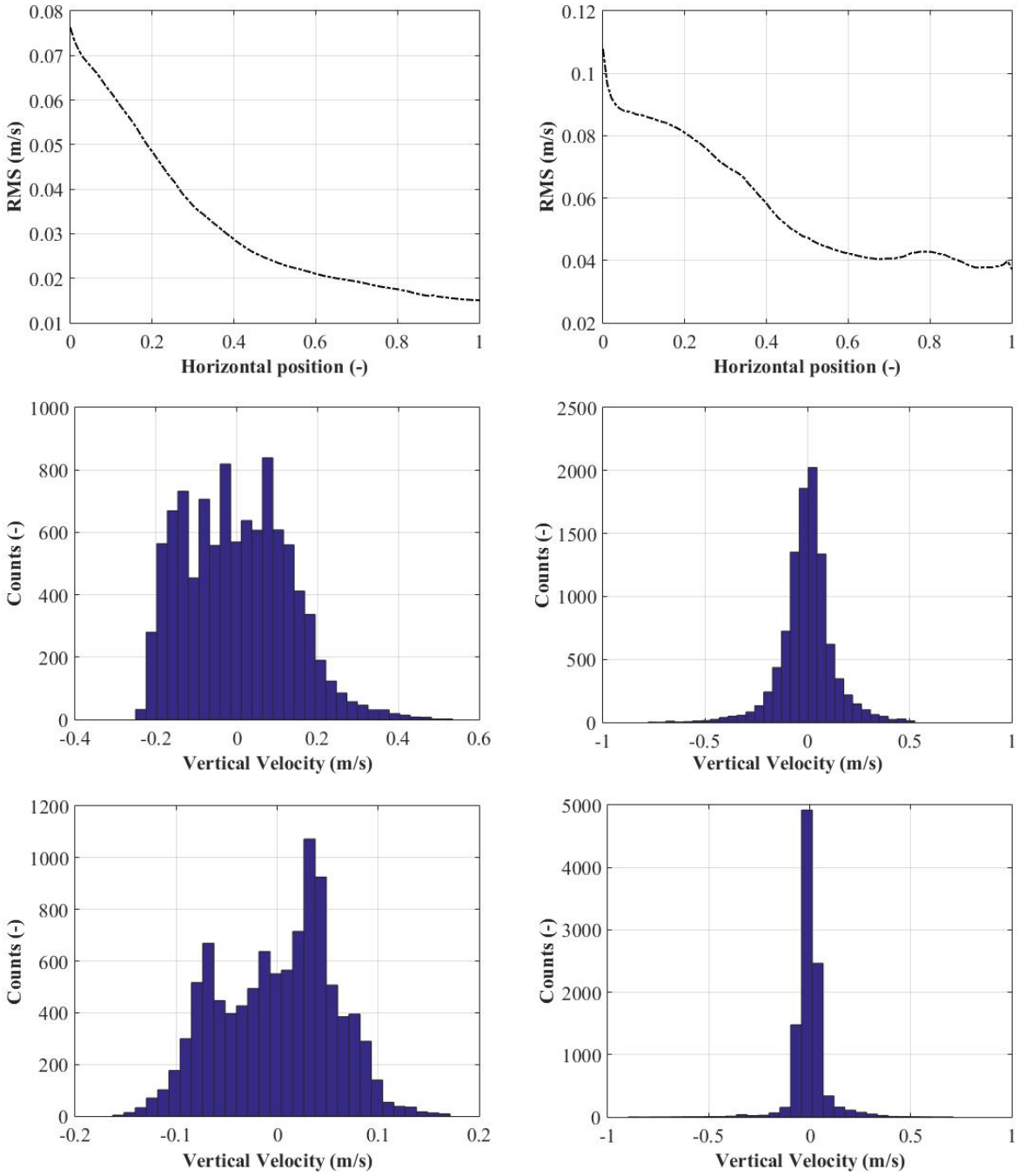

Figure III.34: RMS and Histograms of Velocity in Vertical Direction at $X = 0.25$ (middle) and $X = 0.9$ (bottom) in Breox (13.6%) and $50\frac{l}{h}$ for Membrane Sparger (left) and Slugflow Sparger (right)

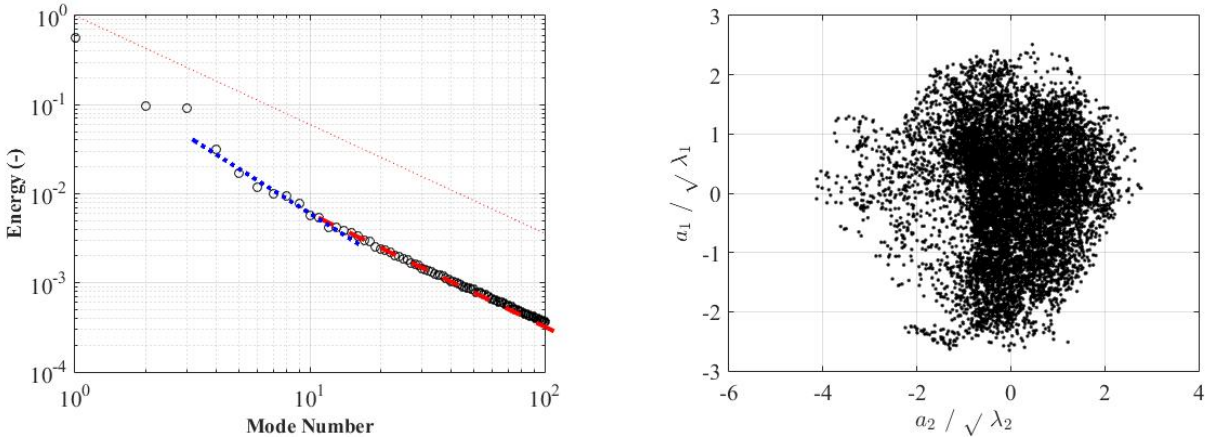

Figure III.35: POD a) Energy Spectrum and b) Mode Dependency between Mode 2 and 3

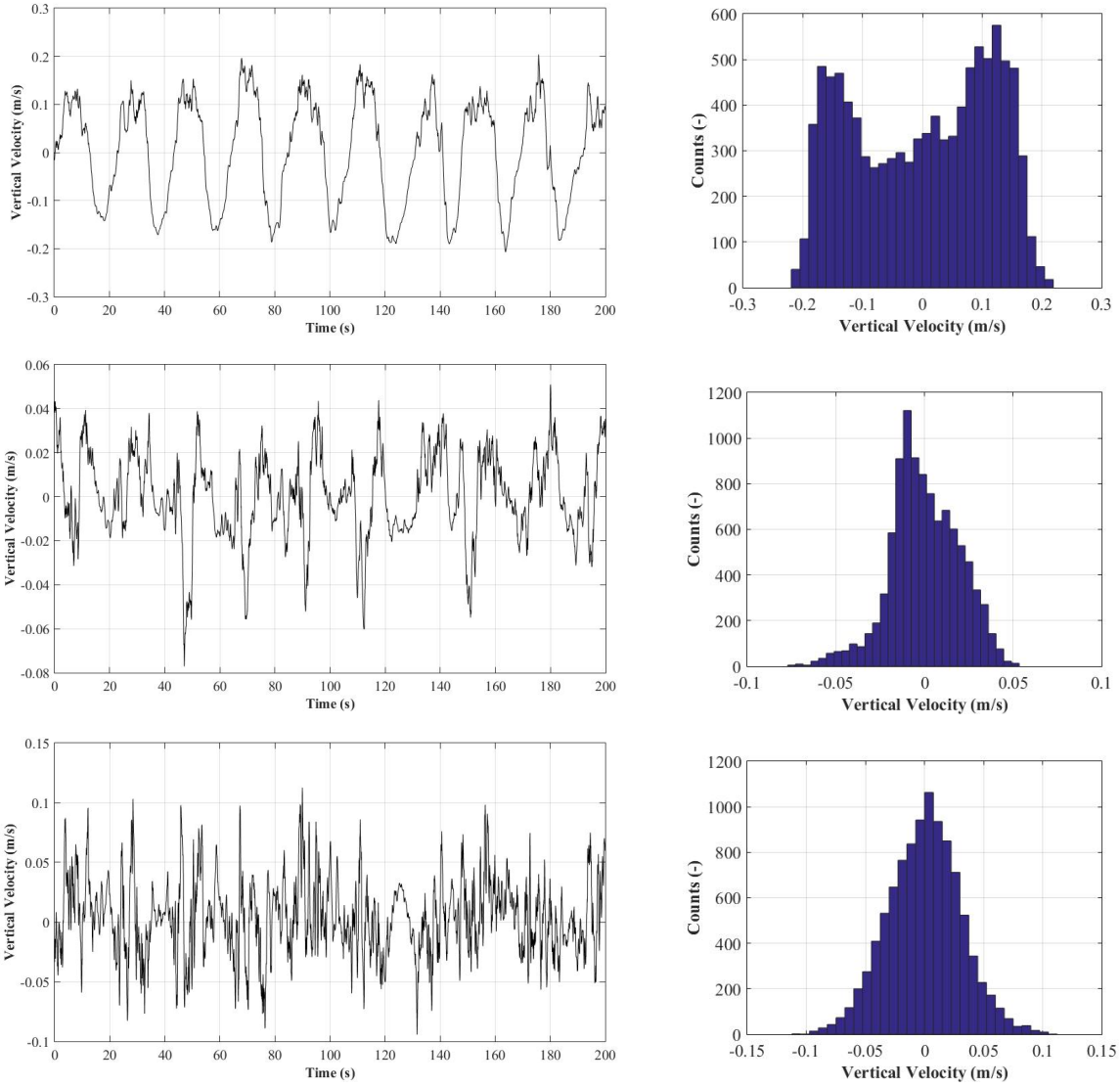

Figure III.36: POD Time Signals and Histograms in Water and $50\frac{l}{h}$ for Modes 1 (top) ,2 & 3 (middle) and 4 to 7 (bottom) for Membrane Sparger

In figure III.37 reconstructed RMS are plotted. For lower modes (left) clear tendencies can be seen. The first mode related to plume oscillation is more or less constant along the horizontal axis. With increasing number of modes taken into account, RMS is increasing in the column center. This evolution can again be related to bubble induced chaotic motion. On the right handside of figure III.37 the same information for higher modes is plotted. The small gaps between the curves indicate less important contribution of chaotic motion, which is certainly damped by viscous effects.

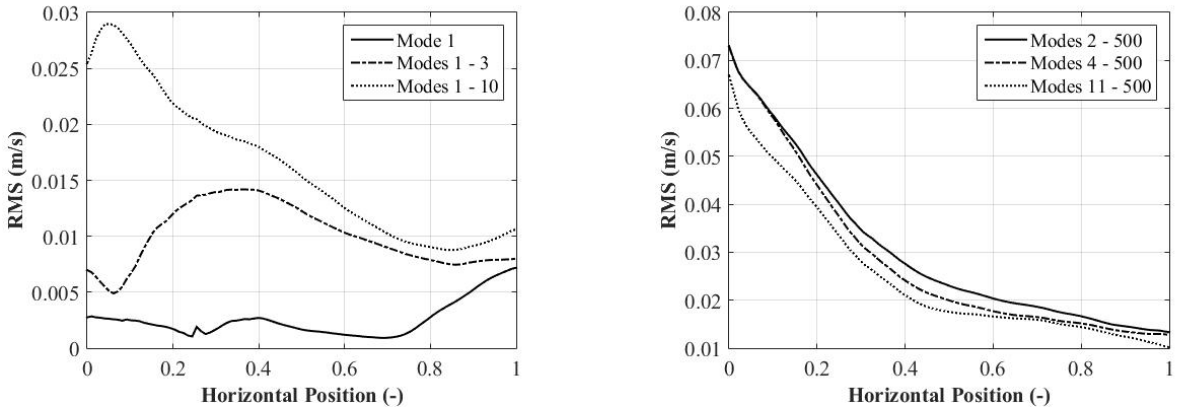

Figure III.37: Reconstructed RMS of Velocity from POD Treatment for Membrane Sparger in Breox (13.6%)

Finally, figure III.38 compares all contributions to the total RMS. Bubble plume motion induced fluctuations are rather homogeneous along the horizontal axis. Chaotic motion contributes clearly more in the center and becomes less important by approaching the walls.

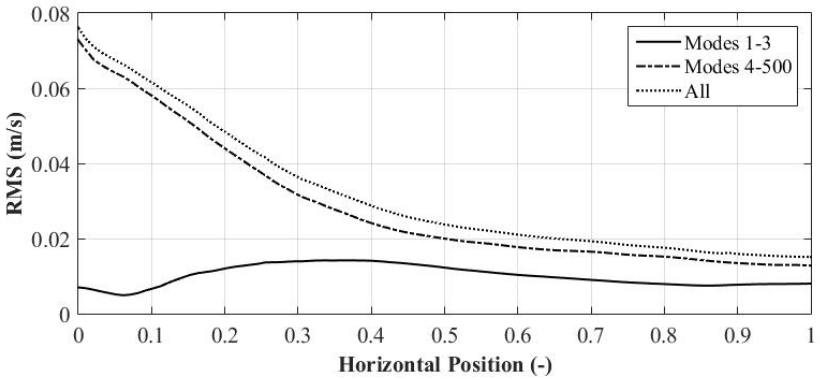

Figure III.38: Reconstructed and Raw RMS of Velocity in the case of Breox (13.6%), $50\frac{l}{h}$ and Membrane Sparger

To further investigate viscous effects the energy spectrum in the case of membrane injection in Breox (18.5%) is show in figure III.39. In such viscous media no oscillation frequency or other organized motion can be identified any more. Also the slope of $-\frac{11}{9}$ indicating classical turbulence is not observed. The slope $-\frac{5}{3}$ (blue dashed line) suggests that only random bubble induced liquid fluctuations are present.

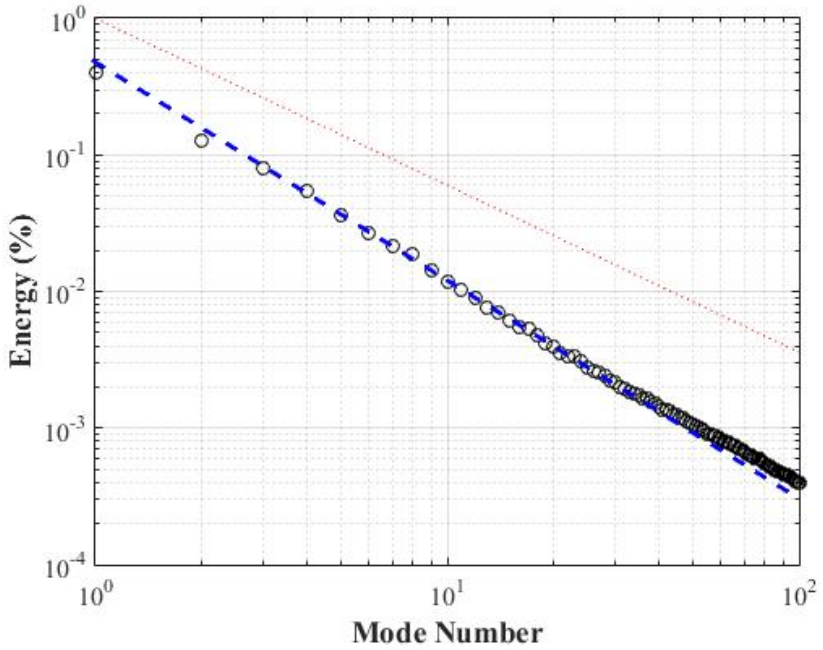

Figure III.39: Energy Spectrum in the case of Breox (18.5%), $50\frac{l}{h}$ and Membrane Sparger

In turbulent flow, the eigenvalue spectrum exhibits a $-\frac{11}{9}$ slope in log–log plot of eigenvalue λ as a function of eigenvalue number N. This result was explained by (Knight & Sirovich, 1990) arguing that it is a characteristic of the inertial range of turbulence. As exposed by these authors, in turbulent flows, the turbulent kinetic energy (tke) can be related to the energy density spectrum of velocity $E_V(K)$, per vector wave number K, as follows:

$$tke = \frac{1}{V}\int\int\int u'^2 dv = \int\int\int E_V(K)dK \tag{III.7}$$

Clearly, the dimension of the energy density spectrum of velocity $E_V(K)$ is $\frac{L^5}{T^2}$. In the inertial range of turbulence, one can express the energy density spectrum of velocity $E_V(K)$ per vector wave number in terms of the energy density spectrum of velocity $E_S(\kappa)$ per scalar wave number κ: $E_V(K) = E_S\frac{(\kappa)}{(4\pi\kappa^2)}$. The trend of the energy density spectrum

of velocity $E_S(\kappa)$ per scalar wave number is well known $E_S(\kappa) \propto \epsilon^{(\frac{2}{3})}\kappa^{(-\frac{5}{3})}$. One can thus derive the energy density spectrum of velocity $E_V(K)$ per vector wave number as $E_V(K) \propto \kappa^{(-\frac{11}{3})}$. (Knight & Sirovich, 1990) considered that each eigenvalue is a generalisation of the energy density spectrum of velocity $E_V(K)$, carrying the same physical dimensions. In addition, (Knight & Sirovich, 1990) stipulated that the wave number may be related to the eigenvalue number as $\kappa = N^{\frac{1}{3}}$. Hence, they obtained the $\frac{-11}{9}$ trend $\lambda(N) \propto N^{\frac{-11}{9}}$, which is observed in our data processing for large values of N. Surprisingly, for intermediate values of eigenvalue number N (between 5 and $10 - 15$), the slope of the log–log plot of eigenvalue λ as a function of the eigenvalue number N is different. This may be due to bubble-induced turbulence. Indeed, (Risso, 2018) explained the -3 trend observed in the energy density spectrum of velocity $E_S(\kappa)$ per scalar wave number in bubbly flow for intermediate wave numbers. Following the previous analysis, given density spectrum of velocity $E_S(\kappa) \propto \kappa^{(-3)}$, the energy density spectrum of velocity $E_V(K)$ per vector wave number becomes $E_V(K) \propto \kappa^{-5}$ and thus, $E_V(K) \propto N^{-\frac{5}{3}}$. This trend is observed in our data processing for intermediate values of N when the flow is fully-turbulent (cases water and Breox (13.6%)) and it is observed for the whole range of eigenvalues in the case Breox (18.5%). The difference between fully-developed turbulent flow, transitional and laminar ones is tricky. One can refer to a recent paper of (Abdelsamie & Thévenin, 2017) on "spectral entropy as a flow state indicator". Following these authors, one can estimate the relative energy $P(N)$ related to the Nth eigenvalue as:

$$P_N = \frac{\lambda_N}{\sum_{M=1}^{Max} \lambda_M} \tag{III.8}$$

where Max is the mode number. The authors define the spectral entropy S as:

$$S = -\sum_{M=1}^{Max} P_M log(P_M) \tag{III.9}$$

Then, the authors propose to use the spectral entropy as a flow state indicator:

- if $S > 1.25$: fully-turbulent flow
- if S close to unity: transitional flow
- if $S < 1$: laminar flow

In our case, the values of spectral entropy can be deduced from eigenvalue data. The results are listed in table III.5. Following this approach, the last case is laminar.

Fluid	Sparger Type	Entropy
Water	Membrane	1.52
Water	Slugflow	1.92
Breox (13.6%)	Membrane	1.41
Breox (13.6%)	Slugflow	1.41
Breox (18.5%)	Membrane	0.86

TABLEAU III.5: Entropy Values for Different Experimental Conditions

In conclusion, one is able to separate different flow structures like organized motion, bubble induced fluctuations and turbulence in terms of energy. The ratio of the energy contribution is changing with increasing viscosity. Organized motion as well as turbulence are damped by viscous effects. Furthermore, in all studied liquids, the membrane sparger produces more coherent flow structures than spherical caps, which can be explained by the unstable behaviour of these bubbles.

III.4.2.2 Horizontal Direction

Mean Values

The influence of liquid properties on the horizontal velocity component is also investigated, but only averaged values are studied. In figure III.40 the mean horizontal velocity in different fluids is plotted for the membrane (left) and the slugflow sparger (right).

The averaged horizontal velocity is not very sensitive to sparger types since similar behaviour can be seen for all fluids. Once again, surface tension has only a minor effect on the velocity. Values close to zero are found in the column center and maximums close to the walls. With increasing viscosity the horizontal averaged movement is clearly damped, which is in agreement with results from section III.3 concerning dispersion. Breox (13.6%) is the only case where a difference between both sparger can be seen. In the case of the membrane sparger no transverse movement between the column center and the point $x = 0.5$ can be identified. The only horizontal positive velocity is registered close to the walls with a maximum at $x \approx 0.9$. This maximum value is three times lower than in water. On the other hand, in the case of the slugflow sparger a more or less

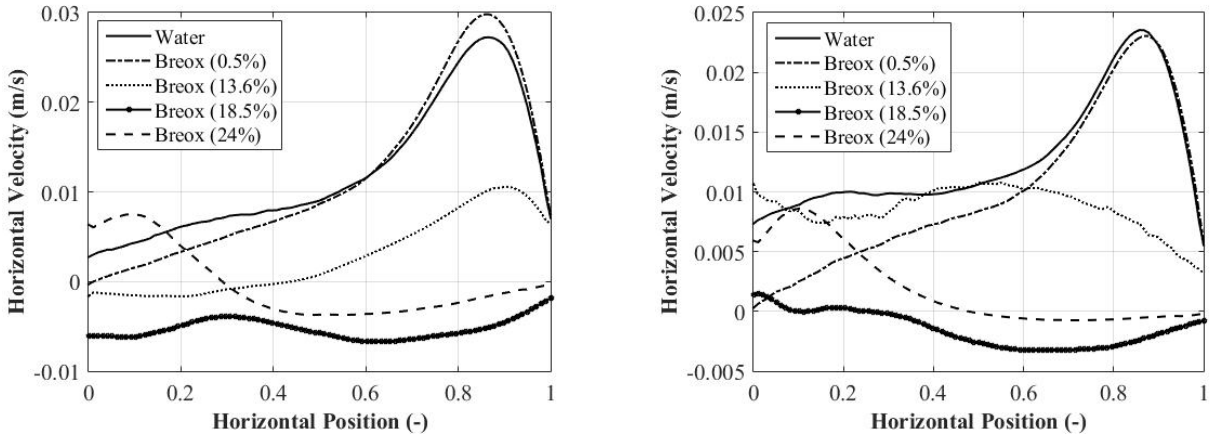

Figure III.40: Horizontal Liquid Velocity in Time in Water for a) Membrane Sparger and b) Slugflow Sparger

constant averaged velocity along the horizontal axis is found. Regarding Breox (18.5%), almost no horizontal mean movement is observed. Only a weak averaged velocity towards the column center is determined, which is slightly higher for the membrane sparger. At even higher viscosity (Breox (24%)) both spargers induce comparable profiles again being in agreement with their similar flow structure. The hydrodynamics are jet-like and mostly large bubbles are generated. In the region between $x = 0.5$ and $x = 1$ no mean velocity is seen. But in the center region a clear horizontal mean velocity towards the walls is indicated. At this moment one has to point out that fluctuations in horizontal direction are not studied. One assumes that similar behaviour than in vertical direction would be found as it is the case in water. Instead, the results of this short paragraph will be used in the next section in combination with horizontal BIV results to investigate bubble dispersion.

III.5 Bubble Swarm Velocity

It was already mentioned in section III.1 that the bubble rise velocity seems to play an important role in bubble plume oscillations. Indeed, the unstable behaviour of the oscillating plume is generated by the vertical density gradient, which is directly related to the local gas fraction and hence to the bubble rise velocity. Therefore, an algoritm was developped to determine the velocity in vertical and horizontal direction (see section II.1.3.4). Since the resulting swarm velocity seems to be more important than velocities

of isolated or well characterized bubbles, all objects are taken into account for mean velocity calculations here. The first part of this section is dedicated to the influence of injection conditions on bubble velocities. Both spargers and three different injection flow rates are considered. In the second part, fluid properties are investigated via the already presented fluids from section II.1.2.

III.5.1 Water

The vertical bubble swarm rising velocity is studied in the case of membrane and slugflow injection in water as presented in figure III.45 and III.46, respectively.

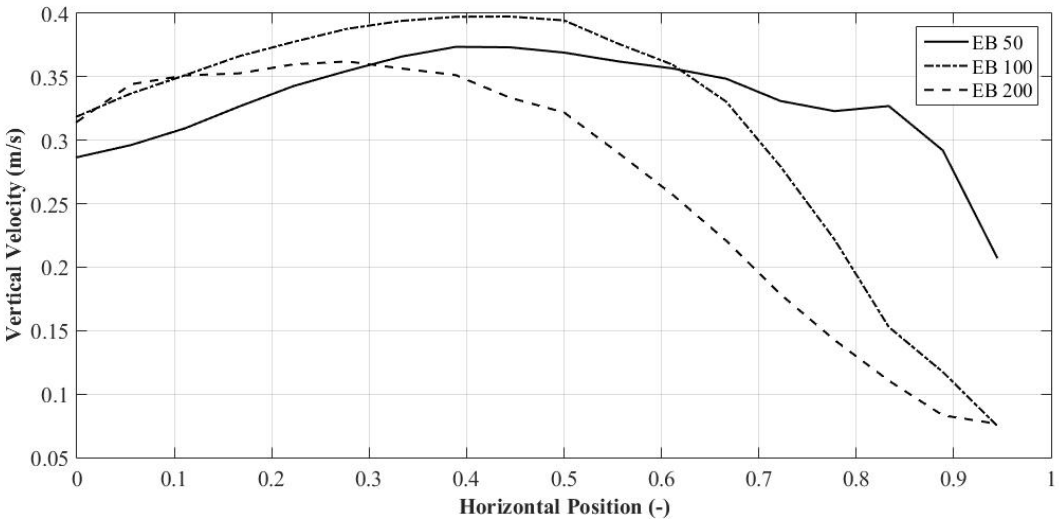

Figure III.41: Vertical Mean Bubble Velocity in the case of Membrane Sparger in Water

Regarding membrane injection (III.41), it is interesting to note that maximum velocities are located at the same horizontal position with a value close to 0.4 for gas flow rates of $50\frac{l}{h}$ and $100\frac{l}{h}$. In the case of the highest flow rate the maximum velocity is slightly closer to the center. This result is in agreement with the corresponding void fraction profiles showing double peaks only for the lowest and the medium flow rate. By approaching the wall a decreasing evolution can be seen for all curves. This can be explained by bubbles trapped in liquid recirculation. Indeed, with increasing flow rate, liquid recirculation become stronger (see section III.4). More bubbles get entrained and are taken into account in mean value calculations decreasing the resulting velocity. To

complete our analysis, velocity values in the center should be compared as well. In the case of the lowest gas flow rate a value of $\approx 0.28\frac{m}{s}$ is obtained. At higher flow rates the same velocity of $\approx 0.32\frac{m}{s}$ is found indicating an ensemble effect inside the bubble swarm. In line with the discussion of section I.1.3.2, the drag coefficient seems to be decreased by swarm effects like coalescence generating higher velocities. This effect is limited in the considered void fraction range, which is the reason why at the highest flow rate the same value in the column center is found.

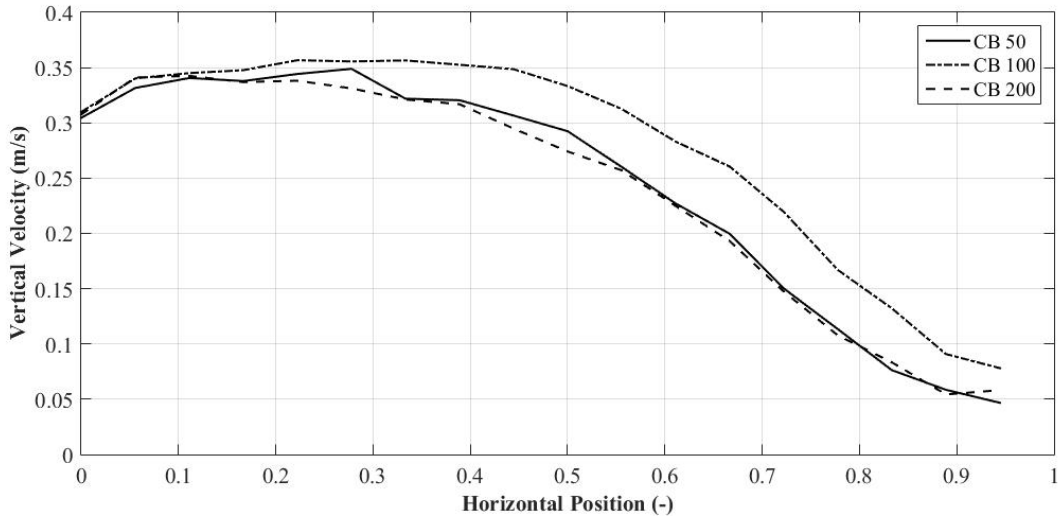

Figure III.42: Vertical Mean Bubble Velocity in the case of Slugflow Sparger in Water

In figure III.42 the same kind of data is presented for slugflow injection. In contrast to the membrane sparger, the slugflow sparger generates very similar curve shapes at all considered flow rates. All three curves show the same evolution from the center to the column edges than the membrane sparger at the highest flow rate of $200\frac{l}{h}$. This result is consistent with bubble size distributions. The membrane sparger shows large objects due to coalescence with size ranges close to spherical cap ones. Since in water, no stable bubble shape is possible for such large objects, a limit of $D_E = 28mm$ is found. The corresponding saturation swarm velocity seems to be $\approx 0.32\frac{m}{s}$. This means that spherical cap induced hydrodynamics are similar to each other, which is in agreement with the constant low frequency oscillation for all flow rates (similar density gradient).
Let us now consider the horizontal swarm velocity that can give further information about bubble dispersion. In figure III.43 horizontal mean velocities are show for membrane

sparger injection. It is not surprising to observe almost exclusively positive mean values indicating bubble movement towards the wall, which can also be understood as dispersion. Only at the lowest flow rate negative values are registered close to the wall. This movement in column center direction results from bubble trapped in vortex cells created by recirculation.

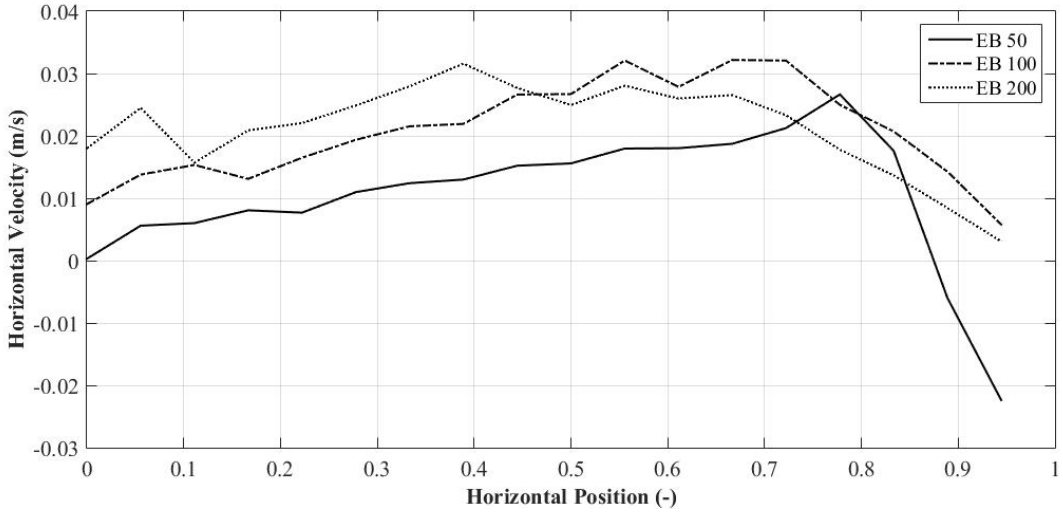

Figure III.43: Horizontal Mean Bubble Velocity in the case of Membrane Sparger in Water

A similar observation is found for the slugflow injection in figure III.44. In this case all horizontal mean swarm velocities show positive values, even at the lowest flow rate. The difference to the membrane sparger can be found in the bubble size distribution. There are not enough small bubbles trapped in the vortex cells to create negative mean values. Finally, these results are perfectly consistent with visual observations and the natural bubble dispersion.

III.5.2 Liquid Properties

In this section, influences of liquid properties on bubble swarm velocities are investigated. Therefore, only the lowest gas flow rate of $50\frac{l}{h}$ is chosen again to illustrate vertical swarm rise velocities for all fluids (III.45). For the analyse results are compared to the reference liquid in literature, water. The mean bubble size in water for the considered case is around $5mm$. The measured rise velocity near the center where bubbles are exclusively rising is around $0.28\frac{m}{s}$, which is in agreement with literature.

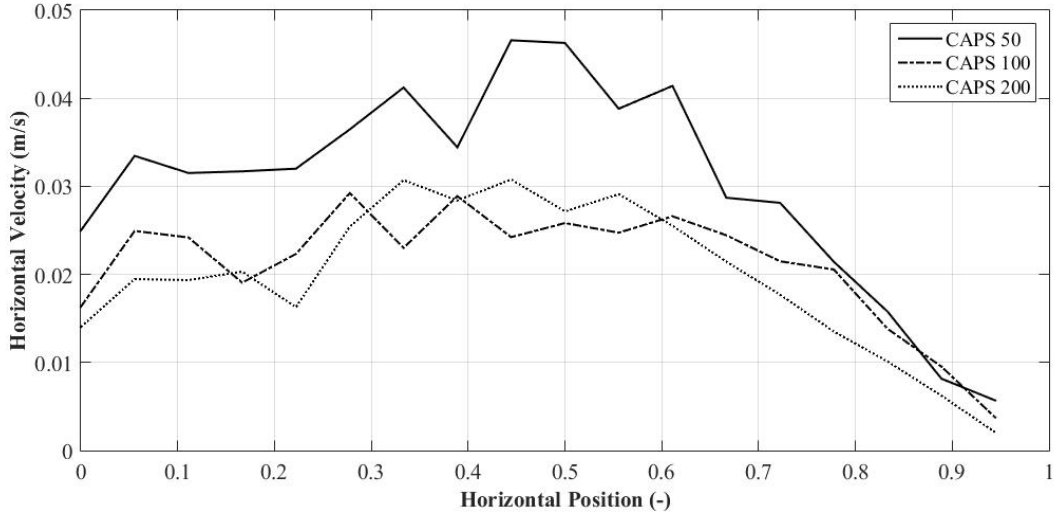

Figure III.44: Horizontal Mean Bubble Velocity in the case of Slugflow Sparger in Water

As first liquid property, surface tension is studied. A comparison is done between water and Breox (0.5%). Both curves show the same evolution along the horizontal column section, except that in the case of Breox (0.5%) the velocity is significantly decreased. Visual oberservations revealed two main reasons, the generation of microbubbles and a general decrease of the mean bubble size distribution. In other words, for approximatly the same void fraction, way more bubbles are present in the column. Bubble interactions are frequent and can have influence on the effective viscosity of the mixture. In general all kinds of inclusions, including bubbles, increase the viscosity. Plus, the rise velocity of every single bubble decreases with decreasing bubble size, which is the case here.
Furthermore, the viscosity impact is studied. The Breox fluids with 0.5%, 8.7%, 13.6%, 18.5% and 24% of mass concentration show viscosities of $1mPas$, $10mPas$, $20mPas$, $50mPas$ and $100mPas$, respectively. By comparing all Breox fluids, increasing velocities in the column center with increasing viscosity can be seen. The slighlty lower value at $x = 0$ in the case of Breox (24%, $100mPas$) is assumed to result from our image treatment and more precisely from the image border truncation. However, the velocity increase can be explained by at least two phenomena. The first one is the trajectory modification from zigzag to straight line. In this way the traveled paths become shorter and the resulting rising velocity higher. Furthermore, the bubble size distribution plays again an important role. With increasing viscosity, bubble shapes become more stable. Break-ups do not appear any more, but coalescence does. Hence, the mean size is

increasing, which is the reason why the rise velocity increases as well. Secondly, bubble induced liquid agitation is damped by the viscosity. The momentum transfer from gas to liquid is less disturbed and higher velocity values can be generated. This is in agreement with III.32 showing higher maximum and minimum values with increasing viscosity revealing strong liquid convection. This convection also provokes higher recirculation entraining more bubbles, which is the reason why negative mean bubble velocities are found close to the edges for all Breox fluids except Breox (0.5%). All these fluids with higher viscosities than water converge to more or less the same value close to the egdes.

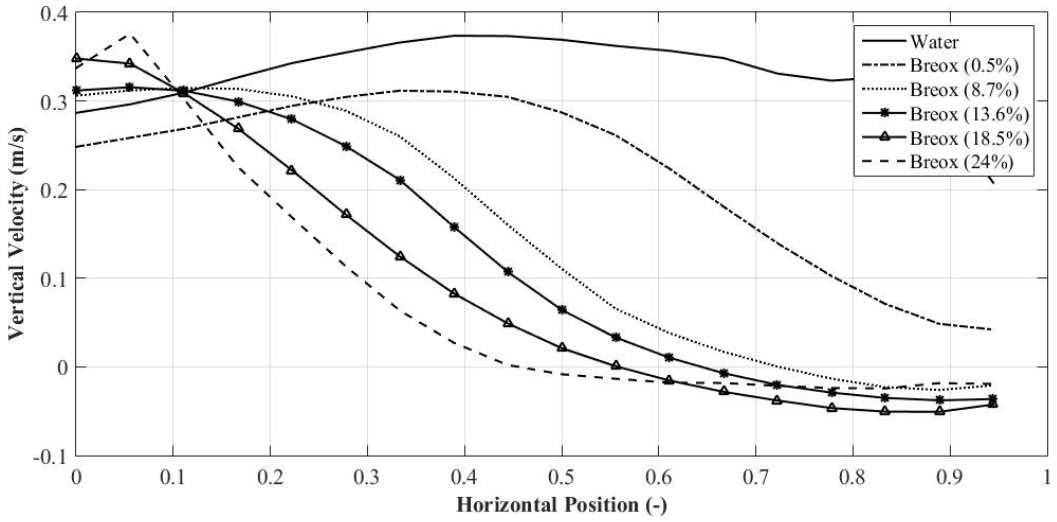

Figure III.45: Vertical Mean Bubble Velocity in the case of Membrane Sparger in different Fluids at $50\frac{l}{h}$

The effect of liquid properties is also studied in the case of spherical cap injection through the slugflow sparger (see figure III.46). Again, effects of surface tension are discussed by comparing water and Breox (0.5%). It is not surprising that both curves are practically merged confirming that surface tension has almost no influence on the rising of spherical cap bubbles. The only difference is the slightly decreased velocity in the column center, which can be explained by the appearance of microbubbles increasing the effective viscosity. This confirms equation I.1.3.1 predicting a more or less constant terminal bubble velocity in the considered size range. Plus, the void fraction is rather small meaning that correlations for single bubbles are still valid in water, especially in the case of spherical caps.

Once again all Breox fluids are used to study viscosity influences on rise velocities in the case of spherical cap bubbles. A clear tendancy can easily be observed. With increasing viscosity, the maximum velocity in the column center and the minimum one close to the edges increases and decreases, respectively. This velocity evolution combined with liquid circulation generates less dispersed bubble swarms. At this point one should remember that low frequency oscillations are insensitive to liquid properties in the case of spherical cap bubbles. Maximum velocities are changing significantly while low frequency oscillations are not modified illustrating that it is more complicated to determine the driving parameters. It seems that the whole velocity profile and not only maximum values determine swarm oscillations, which is in agreement with the assumption of an instability wave du to a vertical density gradient.

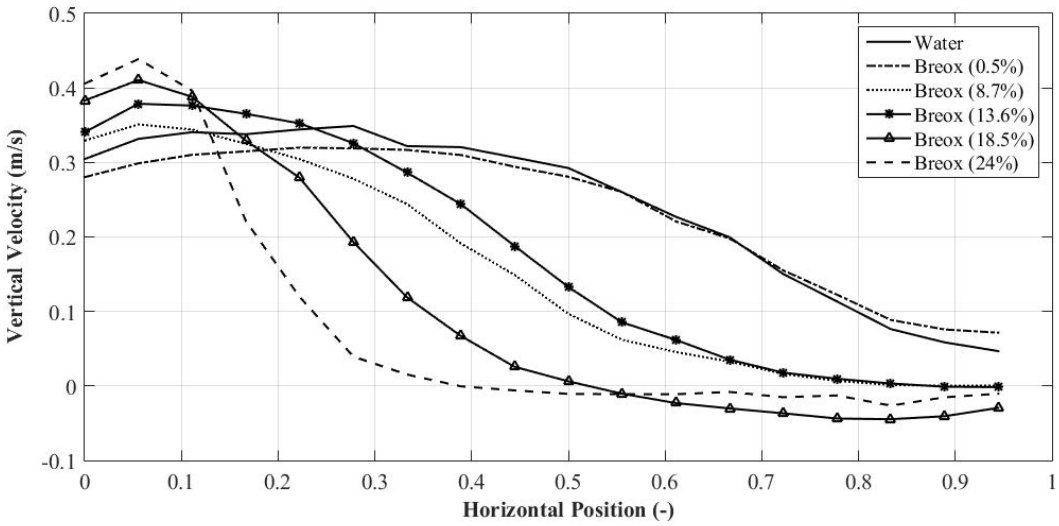

Figure III.46: Vertical Mean Bubble Velocity in the case of Slugflow Sparger in different Fluids at $50\frac{l}{h}$

Anyway, horizontal velocities are also plotted in figure III.47 and III.48 in the same way as in the case of water. Again, all curves show mainly positive values indicating bubble dispersion towards the walls. Plus, for both sparger types surface tension has a minor effect. It seems that both curves in the case of Breox (0.5%) are flattened due to the high number of small bubbles giving a more homogeneous velocity map.

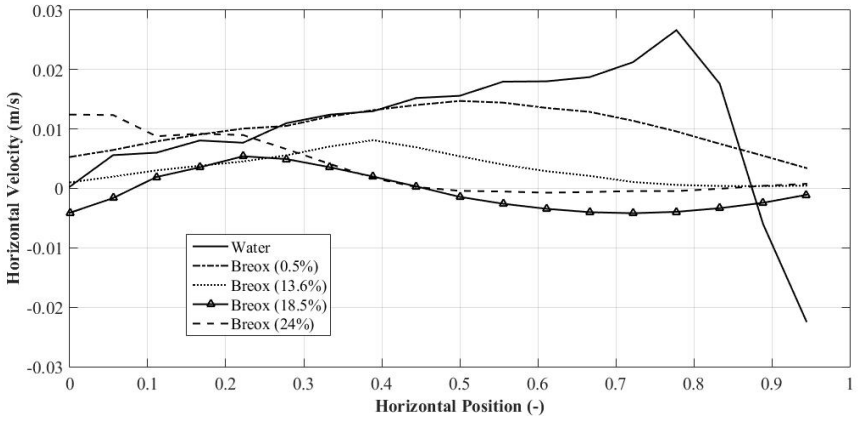

Figure III.47: Horizontal Mean Bubble Velocity in the case of Membrane Sparger in different Fluids at $50\frac{l}{h}$

Furthermore, viscosity influence is investigated. Again, for both spargers, the horizontal velocity decreases with increasing viscosity, confirming the decreasing bubble dispersion. In the case of membrane injection, viscosity shows smaller impact on the horizontal mean velocity than with the slugflow injection. This can be explained by bubble interactions, which are frequent for ellipsoidal bubbles. Hence, turbulent dispersion is damped, but not completly removed. Besides, the maximum velocity located initially close to the wall ($x = 0.75$) in water approaches the column center with increasing viscosity. In the case of spherical caps, viscosity shows much more influence on the velocity range. While at low viscosity, values of $0.04\frac{m}{s}$ are registered, at high viscosity the mean velocity is close to zero. Plus, maximums are located close to $x = 0.45$ except for the highest viscosities.

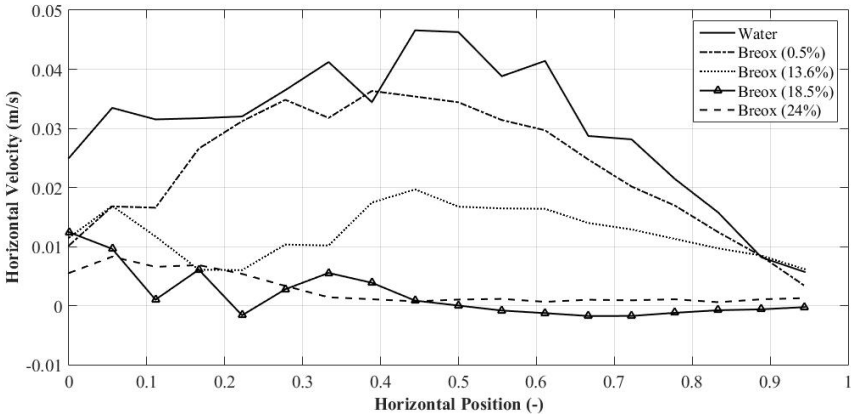

Figure III.48: Horizontal Mean Bubble Velocity in the case of Slugflow Sparger in different Fluids at $50\frac{l}{h}$

III.6 Mean Velocity Difference

The difference between the mean bubble swarm and the mean liquid velocity in vertical direction is calculated by the following equation:

$$\overline{U_r} = \overline{U_b} - \overline{U_l} \tag{III.10}$$

where $\overline{U_b}$ and $\overline{U_l}$ correspond to time averaged velocity profiles from BIV and PIV measurements, respectively. The resulting profiles can be seen in figure III.49. At the top of the figure three different flow rates are presented for the membrane sparger and at the bottom for the slugflow sparger. Because of the significant difference between the mean velocities of both phases, bubble swarm velocities are clearly dominant. The substraction of the liquid velocity can be considered as correction in order to approach the slip velocity in the case of isolated bubbles.

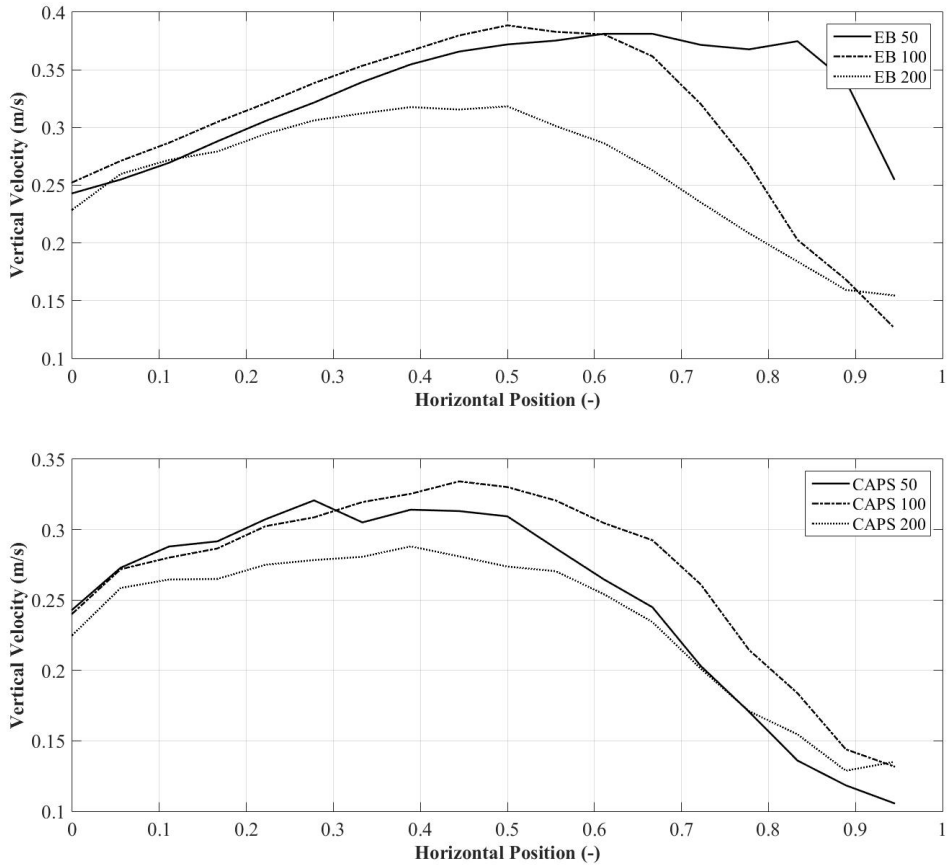

Figure III.49: Averaged Slip Velocity in Water for three different injection flow rates in case of Membrane sparger (top) and slugflow sparger (bottom)

However, these results must be treated carefully because the whole column depth is used for BIV while only a two dimensional plane is measured in the case of PIV. Besides, no filter in terms of bubble characteristics is applied to BIV results. In figure III.49 similar evolutions than in figure III.41 and III.42 are recognized. In the case of the membrane sparger maximum velocity values seem to migrate slowly towards the column center with increasing flow rate. While the highest velocity is registered around $x \approx 0.65$ for $50\frac{l}{h}$, the maximum velocity for $200\frac{l}{h}$ is found around $x \approx 0.4$. If one integrates the three curves, a decreasing evolution of the realtive velocity $\overline{U_r}$ with increasing gas flow rate is observed. This trend can not be seen in the case of the slugflow sparger where the highest integrated velocity value is obtained for the intermediate gas flow rate of $100\frac{l}{h}$. Also the position of the local velocity maximum does not vary much for different flow rates and stays around $x = 0.4$. This may help to understand why the low frequency oscillations remain constant in the case of spherical cap bubbles.

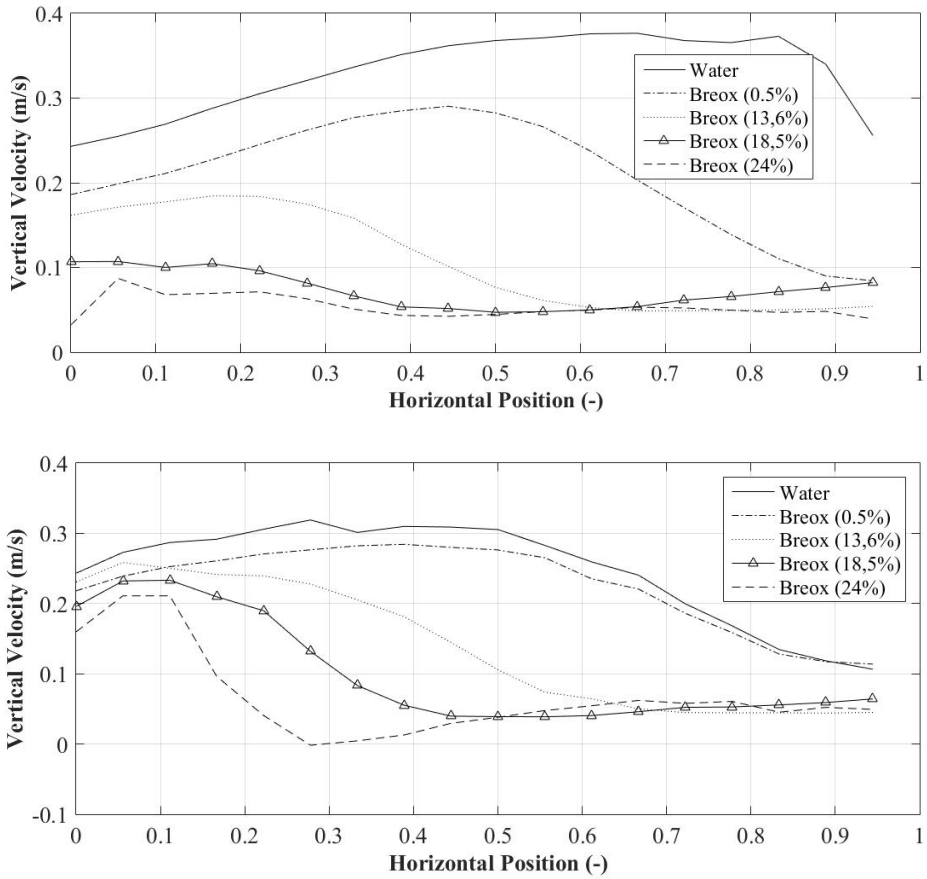

Figure III.50: Averaged Slip Velocity in Breox for three different injection flow rates in case of Membrane sparger (top) and slugflow sparger (bottom)

In figure III.50 the same information is plotted for different fluids and both spargers. Again, results must be treated carefully, especially in the case of spherical cap bubbles. This becomes obvious by regarding the velocities close to the edges. Values of $0.05\frac{m}{s}$ are found, which can clearly not correspond to spherical caps. Indeed, all objects, independently of their size, are taken into account for BIV measurements. Considering the dispersion, it becomes obvious that these weak velocities are related to small bubbles that can be easily trapped in liquid recirculations. Nevertheless, these figures can give important information about swarm velocities, especially in the center of the column.
In figure III.50 (top) coherent values around $0.25\frac{m}{s}$ for ellipsoidal bubbles are found being in agreement with literature. Only in the case of Breox (0.5%) a clear difference can be seen. Again, smaller bubble size and higher effective viscosity are the main reasons. In the case of the slugflow sparger, the last point is a little different. As previously presented, spherical cap dynamics are not very sensitive neither to surface tension, neither to viscosity. Hence, no large variation are observed. Nevertheless, comparable maximum velocities are determined for all fluids.

III.7 Mixing Time

Bubble plume injection is generally used for mixing in large tanks. This is the reason why some mixing times are investigated even if they are not comparable with three dimensional configurations. Nevertheless, the mixing ability of our pseudo two dimensional bubble column is studied. Therefore, dye injection is used as described in section II.1.3.5. It should be mentioned that the mixing time analyzed here corresponds to the time needed to homogenize the liquid in the considered interrogation windows close to the right wall. All determined mixing times in water and for both sparger types are presented in table III.6 and in graphical form in figure III.52.

Flow Rate (l/h)	50	100	200
Membrane injection (s)	50	25	25
Slugflow injection (s)	120	70	25

TABLEAU III.6: Mixing Times in Water

The first observation is the large difference of mixing times between both spargers at the lowest flow rate. With the slugflow sparger 2.5 times more time is needed to homogenize the column after dye injection. This result can partially be explained by the different bubble dispersions and induced agitation. Indeed, in the case of ellipsoidal bubbles the dispersion is slightly larger and bubbles interact more leading to a wider plume. Anyway, with increasing injection flow rate through both spargers mixing times decreases. In the case of the slugflow sparger the main reason is bubble interaction becoming frequent only at higher gas flow rates. At the highest injection flow rate the exact same time scale is found for both spargers suggesting that a minimum mixing time for the given bubble column geometry exists.

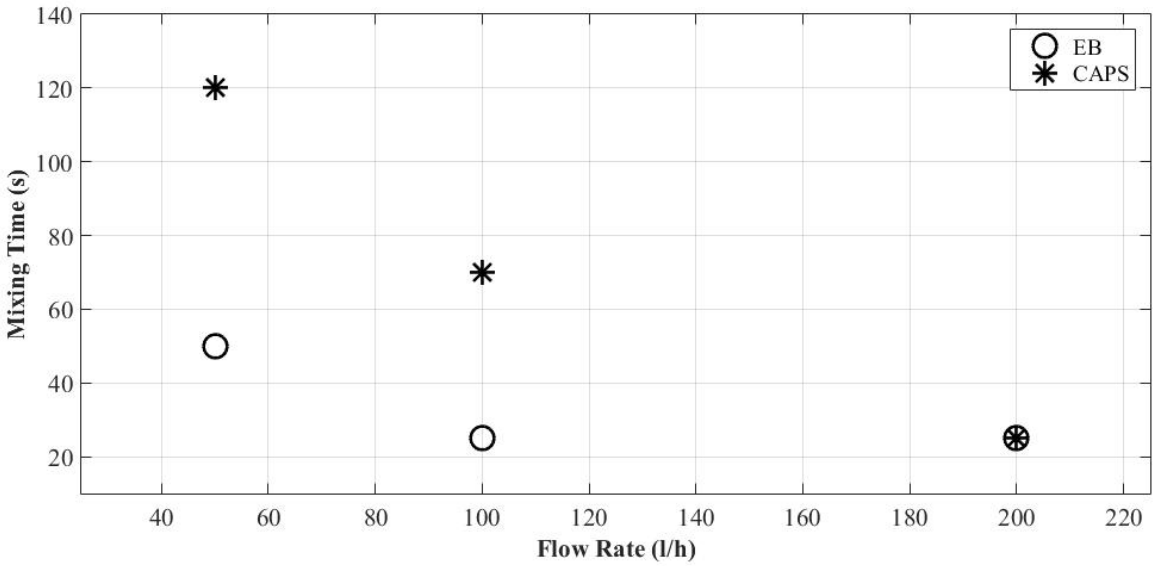

Figure III.51: Mixing Times in Water as a function of Injection Flow Rate for both Spargers

Mixing time scales are also investigated in more viscous fluids. Therefore, the Breox fluids at 20, 50 and 100 times the viscosity of water are chosen. Determined time scales are listed in table III.7 and plotted in figure III.52.

Fluids	Water	Breox (13.6 %)	Breox (18.5 %)	Breox (24 %)
Membrane injection (s)	50	65	170	150
Slugflow injection (s)	120	40	200	95

TABLEAU III.7: Mixing Times in different Fluids for $50\frac{l}{h}$

To our surprise, at a viscosity of $20mPas$ the slugflow sparger shows lower mixing times than the membrane sparger. This observation can be explained, at least partially, by the vertical averaged liquid velocity shown in figure III.45 and III.46. At the considered viscosity the ascending part is larger by $\approx 15\%$. It is difficult to clarify why in this particular case, more momentum seems to be transfered from the gas to the liquid phase via the spherical bubbles than for the ellipsoidal ones. One argument could be the higher maximum swarm velocity, but this is also the case for other fluids.

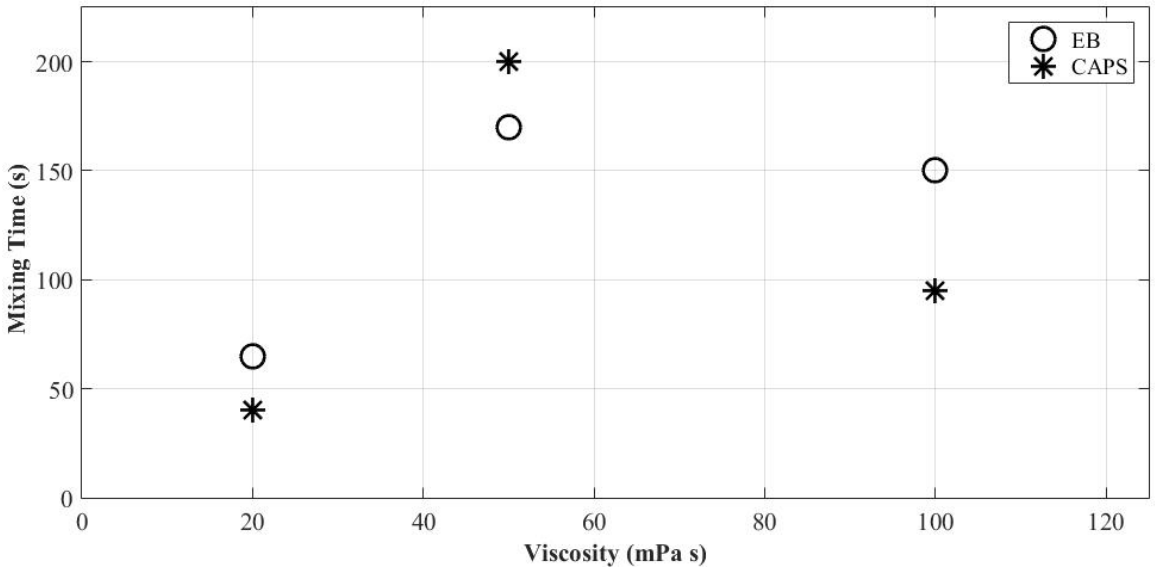

Figure III.52: Mixing Time as a function of Viscosity for both Spargers

With further increasing viscosity, mixing time is increasing as expected. This time ellipsoidal bubbles generated by the membrane sparger shows a lower time scale. Again, a relation between the mixing time and the vertical averaged velocity can be done. The ascending zones are of same size, but ellipsoidal bubbles show higher values, especially in the center. At the highest viscosity value, mixing time decreases again. This evolution can be justified by a flow transition from vortical flow to double cell transition flow as described in section I.3. In this case, it is assumed that mixing is driven by the averaged swarm velocity that is significantly higher in the case of the membrane sparger. Besides, bubble dispersion of both spargers is very similar in such viscous fluids. Hence, mixing is more efficient in the case of the slugflow sparger in the considered flow regime.

III.8 Mass Transfer

It was already mentioned that oxygen probes are used to measure the dissolved oxygen concentration in the liquid phase. In section III.1.1 results showed that low frequency oscillations could be measured by this way. Now, one wants to go a little further and determine characteristic mass transfer time scales. Therefore, the K_La value was determined like illustrated in section II.1.3.6. Then the inverse is taken to obtain time scales as shown in table III.8 for water and in table III.9 for the other fluids.

Flow Rate (l/h)	50	100	200
Membrane injection (s)	950	780	380
Slugflow injection (s)	1950	810	460

TABLEAU III.8: Mass Transfer Time Scales in Water

In figure III.53 all time scales from table III.8 are illustrated in graphical form. Circles and stars indicate ellipsodial bubbles (membrane sparger) and spherical caps (slugflow sparger), respectively. Both sparger types show decreasing time scales with increasing flow rate. At the lowest flow rate the time scale difference is large, which can be explained by different interfacial areas of the considered bubble types. Indeed, with decreasing size, the surface of any object is becoming larger compared to its volume. With increasing flow rate, time scales of both spargers are coming closer to each other, which can another time be explained by the interfacial area. Last one is controled by the bubble size distribution becoming more and more similar with increasing flow rate. At higher rates the membrane sparger generates large bubbles due to coalescence while the slugflow sparger produces small bubbles near the injection, the free surface and during break-ups. Plus, dissolved oxygen measurements are very long (of order of some hours). This is enough time to induce enough small bubbles to establish regimes, which are close to each other.

Fluids	Water	Breox (0.5 %)	Breox (8.7 %)	Breox (18.5 %)
Membrane injection (s)	950	510	880	985
Slugflow injection (s)	1950	940	1515	2280

TABLEAU III.9: Mass Transfer Time Scales in different Fluids for $50\frac{l}{h}$

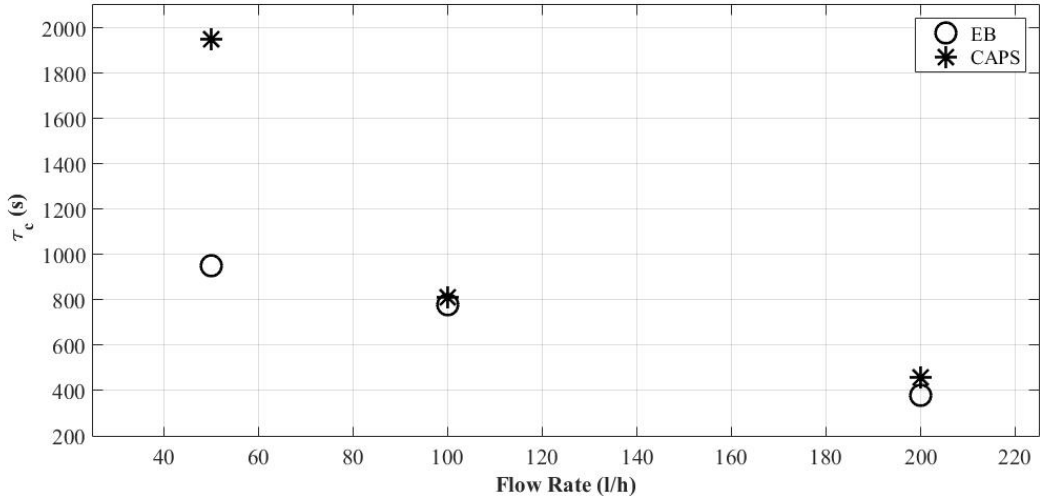

Figure III.53: Mass Transfer Time Scales as a function of the Flow Rate in Water for both Spargers

In figure III.54 the same type of time scales (from table III.9) are presented as a function of the viscosity for both spargers and a gas flow rate of $50\frac{l}{h}$. One must mention that Water and Breox (0.5%) show different surface tensions, which is constant for all Breox fluids. Since mass transfer is very sensitive to the bubble size distribution, only Breox (0.5%) is used for comparisons.

In line with the rest of our investigation, viscosity influences are studied again. Mass transfer is influenced by many different parameters like residence time, interface contamination or shear forces to name only a few. Plus, all of them are coupled, which illustrates how challenging it is to estimate mass transfer properly in such complex situations. Nevertheless, the parameter is investigated to get at least an idea about mass flux inside the reactor. It is not surprising that with increasing viscosity mass transfer time scales increases as well. This evolution is observed for both sparger types. Plus, at every viscosity, a clear difference between the spargers can be seen. This difference is becoming even larger with increasing viscosity, which can be explained by stabilizing effects on the interface. In the case of the membrane sparger bubble size distribution is not changing significantly. But for the slugflow sparger less and less small bubbles are detected with increasing viscosity. Since this modification decreases the mass transfer, one assumes that the interfacial area is the driving term here as well.

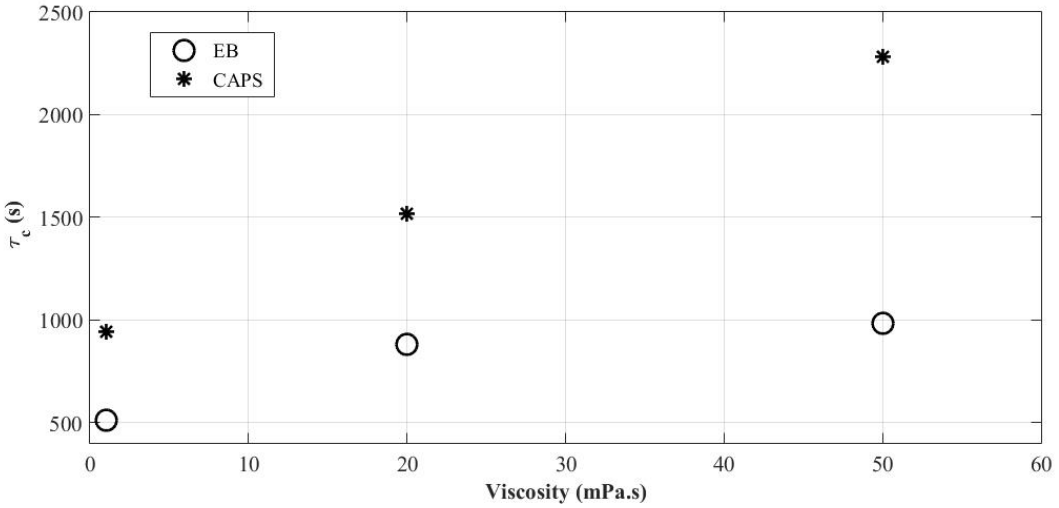

Figure III.54: Mass Transfer Time Scales in function of the Viscosity in the case of $50\frac{l}{h}$

In conclusion, it is difficult to estimate the impact of hydrodynamic structures on mass transfer in comparable flow situations. The bubble size distribution is clearly the driving term. To further investigate hydrodynamic influences, the bubble size should be better controled.

III.9 Comparisons with 3D-BP

Instabilities like bubble plumes occur normaly in non confined 3D situations such as large tanks. Hence, it makes only sense to compare two and three dimensional ones in order to approach real industrial conditions. Therefore, as mentioned in section II.1.4, measurements on 3D-BP were performed. It is assumed that in both geometries similar phenomena are acting and controling hydrodynamic structures involving that low frequency oscillations should be of the same order. On the continuity of thought, six gas injection flow rates are chosen as it can be seen in table III.10.

Injection Flow Rate ($\frac{l}{h}$)	50	100	200	287	574	1149
Superficial Gas Velocity ($\frac{mm}{s}$)	0.12	0.23	0.46	0.66	1.32	2.65

TABLEAU III.10: Experimental Conditions

The first three ones represent the exact same gas flow rate while the three last ones correspond to the same superficial gas velocities than for the 2D-BP. In this way, one wants to figure out, which one of these two parameters is more important for bubble plume oscillation characterization.

III.9.1 Oscillation Frequency

Measurements are performed in a cylindrical BC in order to analyse three dimensional oscillations. One is looking for similarities between both configurations since physical mechanisms should be the same. To follow such 3D oscillations, no visual metrological methods can be applied, which is the reason for our research of another technique. It is quit complex to follow bubble plume movements and to trust results if no look inside the reactor is possible. First, analyzes of pressure signals were performed. This was possible for simple cases in water, with membrane injection and moderate injection flow rates. But once large bubbles appear, the bubble plume is getting unstable. Different frequencies resulting from bubble coalescence and break-ups interfere with plume oscillations frequencies making the extraction of a characteristic frequency impossible. For this reason, one had to rethink the experimental setup, which brang us to the HZDR and the Wire-Mesh-system. This metrological method allows us to measure instantaneous void fraction maps in a complet column cross section over time.

Wire-Mesh Wire-Mesh data was acquired for a large range of experimental conditions in order to see if bubble plume motion occurs. The aim is still to follow the bubble plume position in time. Therefore, the gravity center of the total gas holdup in the cross section of the Wire-Mesh system, comparable to the gravity center from shadowgraphy images in section II.1.3.2, is determined.

$$(x_{gc}, y_{gc}) = \frac{\sum_{i=1}^{n}(x_i, y_i)\alpha_i}{\sum_{i=1}^{n}\alpha_i} \tag{III.11}$$

where (x_i, y_i) are the coordinates from every measuring point and α_i its local gas fraction. Furthermore, because of the circular cross section, cartesian coordinates are changed to polar ones by using the following equations:

$$R_{gc} = \sqrt{x_{gc}^2 + y_{gc}^2} \tag{III.12}$$

$$\theta_{gc} = \tan^{-1} \frac{x_{gc}}{y_{gc}} \tag{III.13}$$

Since it is our goal to identify low frequency oscillations, movements of the gravity center are followed in time. Intuitively, the choice of following θ_{gc} in time is coherent since the helicoidal trajectory of the ascending bubbles is supposed to turn around the column center.

	Flow Rate (l/h)	50	100	200	286.8	574.2	1149
Fluid	Bubble Type						
Water	EB	77	69	61	45	29	30
Water	CAPS		73	71	50	40	25
Breox (0.5%)	EB	97	94		72	67	
Breox (0.5%)	CAPS	262	105	94	77	67	43
Breox (8.7%)	EB		85	71	55	50	38
Breox (8.7%)	CAPS	202	114		67	50	25
Breox (13.6%)	EB	97	94		73	67	48
Breox (13.6%)	CAPS	262	105	94	77	62	43
Breox (18.5%)	EB	109	94	69	49		46
Breox (18.5%)	CAPS	154	94	82	94	69	54

TABLEAU III.11: Period Time Scales in Seconds

In table III.11 all periodic time scales from three dimensional measurements are listed. In some cases, no characteristic frequency could be identified. However, for all measurements a decreasing behaviour with increasing flow rate is recognized. Theses results are plotted in figure III.55. Full markers correspond to membrane and empty ones to the slugflow sparger. All curves of figure III.55 show more or less the same decreasing behaviour with increasing flow rate. At this point no clear differences depending on injection conditions or fluid properties could be identified. Therefore, further treatments must be performed. On the other hand, it is already possible to prove that low frequency oscillations occur in three dimensional situations. Plus, the measured time scales are of the same order of magnitude than in the case of 2D-BP. This means that the same hydrodynamic mechanisms appear in both configurations.

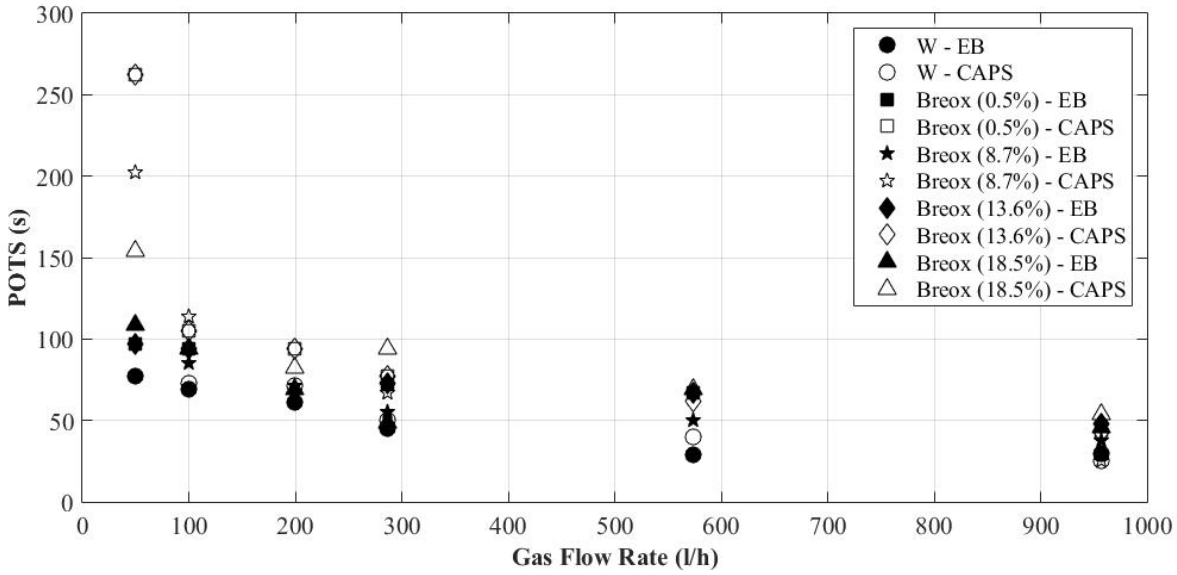

Figure III.55: Characteristic Time Scales of Low Frequency Oscillations in different Fluids

III.9.2 Dimensionless Numbers

Dimensionless numbers are used to further compare the two and the three dimensional case. At the beginning of this chapter different possibilities are presented including our proposition to use the Froude number. The application of our proposition is not possible here because no detailed information about bubble size, shape and velocity is available. Hence, it is impossible to base one dimensionless number directly on bubble characteristics. This is why the classical numbers suggested by literature are used, involving that only comparisons in water can be performed. The Strouhal and the Grashof number being both based on column characteristics are chosen. In figure III.56 both numbers as a function of each other are plotted.

In the figure results from different investigations are plotted. Two dimensional measurements from (Diaz *et al.*, 2006), (Pfleger & Becker, 2001), (Becker *et al.*, 1994) and ours are compared to our three dimensional ones and those from (Rensen & Roig, 2001). In the three dimensional case, frequencies are smaller for the same Grashof number, which is mainly influenced by the injection flow rate. The difference can be explained by the confinement of the two dimensional bubble column hindering the generation of 3D-BPs. This is not the case in cylindrical bubble columns where 3D-BP can develop. These three dimensional instability waves show longer bubble trajectories that could be an explanation for higher time scales. However, we were expecting our results to be rather in scale

with those from (Rensen & Roig, 2001) who used a three dimensional column as well. But in contrast to ours, their column has a squared cross section. This geometry can hinder meso scale phenomena like large eddies influencing bubble plume oscillations.

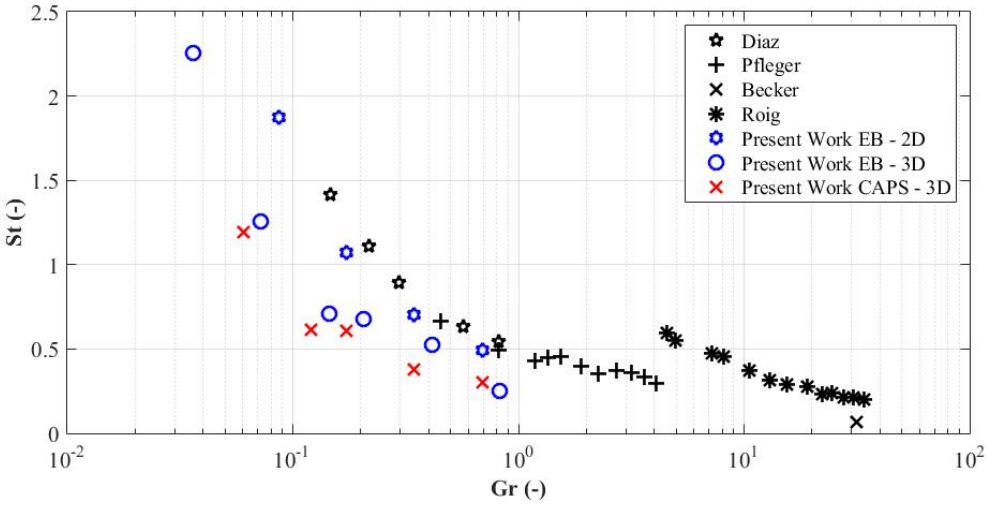

Figure III.56: Strouhal as a function of Grashof in Water

III.9.3 Bubble Dispersion

A last comparison is done by regarding gas hold-up profiles. In figure III.57 time averaged void fractions of a single slice of the WIre-Mesh system are plotted in different liquids and for different injection conditions. Membrane (left) and slugflow sparger (right) are presented in water (top), Breox (13.6%) (middle) and Breox (18.5%) (bottom). To our surprise the characteristic double peaks are identified in the case of the slugflow and not for the membrane sparger. Since only one slide of the Wire-Mesh measurements is used it is difficult to estimate if the 3D-BP prefers one direction or if these double-peaks really exist. Anyway, conclusions can be done concerning dispersion which increases with increasing flow rate being in agreement with 2D-BP measurements. It is interesting that in the case of the membrane sparger for three intermediate flow rates similar maximum values in the center are found. In these conditions the bubble plume becomes only wider. Furthermore, a clear decrease of the bubble width with increasing viscosity is observed. This result is more obvious in the case of the slugflow sparger which is in agreement with 2D-BP. Besides, at the highest viscosity, maximum values remain constant with increasing flow rate, but plume dispersion is increasing.

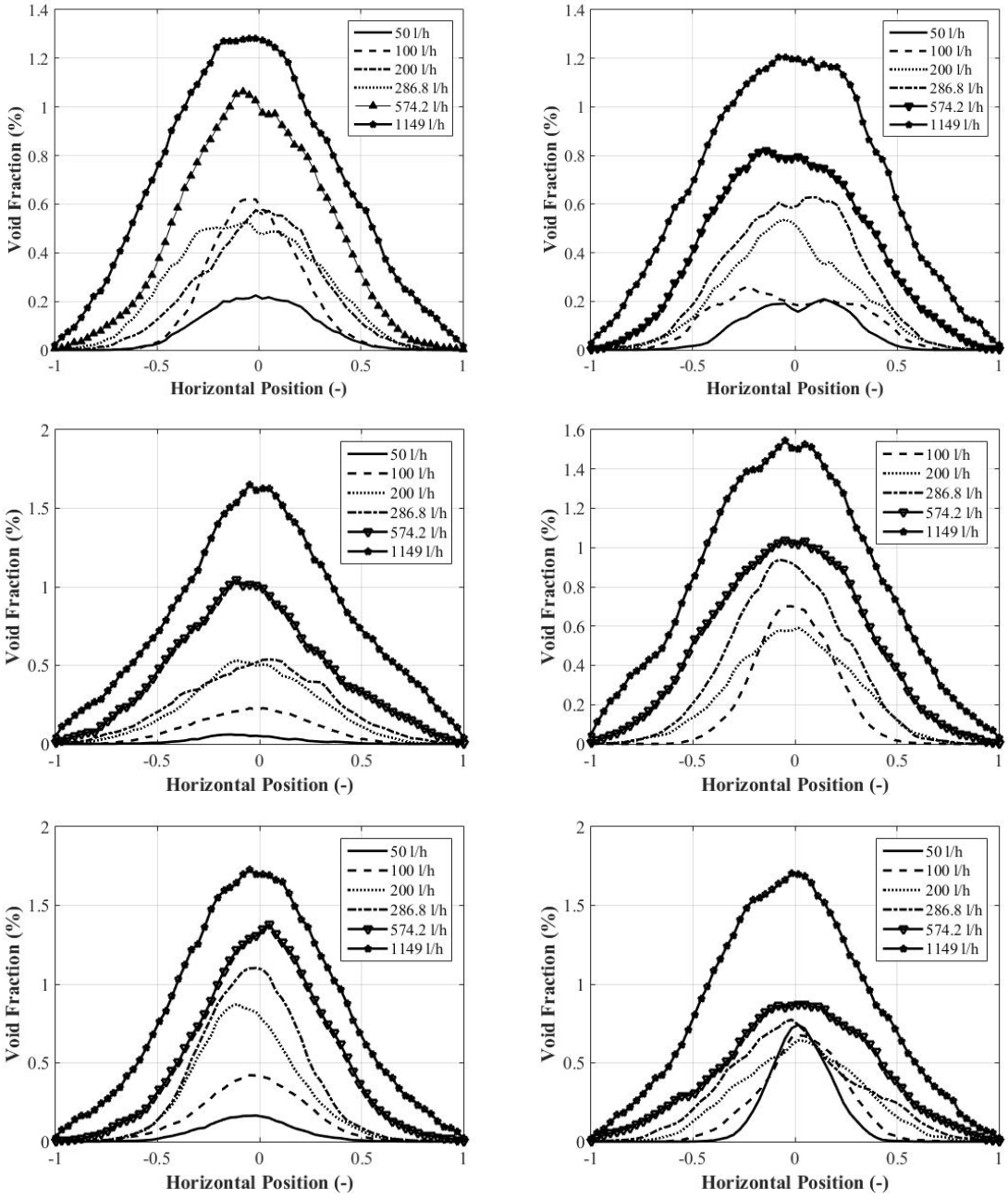

Figure III.57: 3D Dispersion in different Fluids: Water (top), Breox (13.6%) (middle), Breox (18.5%) (bottom) in case of the Membrane (left) and the Slugflow Sparger (right)

III.9.4 Conclusion

Different similarities between the 2D-DP and the 3D-BP could be observed. Concerning bubble plume wandering, comparable time scales of the same order of magnitude could be measured. It is worth mentioning that 3D-BP are less organized. The less confined cylindrical column, but also the Wire-Mesh intrusivity can be the reasons. Concerning last one, vortex cells being created at column top close to the free surface before descending to the bottom, could be hindered by the mesh. Finally, similar evolutions of void fraction profiles concerning flow rate and viscosity influences, are observed. Only the choice of the sparger type seems to be less important. This must be further investigated.

Chapter IV

CFD

The aim of the present study, as in most chemical engineering investigations, is to develop predictiv tools in order to effectuate correct scale-ups and to find optimum operation conditions. All the experiments presented in the last chapters can serve to validate CFD simulations, which will be the subject of this chapter. Therefore, a test case in water is chosen to evaluate generally used closure terms between both phases such as drag, lift, virtual mass and turbulent interactions.

IV.1 Modelling

The NEPTUNE CFD CODE is chosen to perfom CFD simulations. Several models are available and those used for our case are presented in the following section. At this point one wants to make clear that eventually better or more recent models are accessible in literature. Anyway, the focus of this investigation is to try those models already implemented in NEPTUNE CFD code.

IV.1.1 Two Fluid Model

The chosen CFD code works with an Euler-Euler approach to decrease calculation time compared to tracking strategies like Lagrangian simulations. In this approach the media is considered to be continous. Every cell of the mesh contains a certain percentage of gas and liquid and only mixture momentum equations are solved.

Continuty Equations Naturally, conservation equations for mass and momentum must be respected. Equations IV.1 and IV.4 illustrate these conservations for every phase k. Relation IV.2 and IV.3 describe exchange terms between both phases.

$$\frac{\partial}{\partial t}\alpha_k\rho_k + \frac{\partial}{\partial x_j}(\alpha_k\rho_k\overline{U_{k,i}}) = \overline{\Gamma_k} \tag{IV.1}$$

where

$$\overline{\Gamma_k} = \overline{\rho_k(\vec{U_I} - \vec{U_k})n_k\vec{\delta_I}} \tag{IV.2}$$

Equation IV.2 describes the mass transport if a normal component of the velocity difference $(\vec{U_I} - \vec{U_k})$ between the two phases exists. Then the mass transfer can be expressed by $\overline{\Gamma_k}$. The momentum transfer is more delicate, as it can be seen in the following equation:

$$\frac{\partial}{\partial t}(\alpha_k\rho_k\overline{U_{k,i}})+\frac{\partial}{\partial x_j}(\alpha_k\rho_k\overline{U_{k,i}U_{k,j}}) = \frac{\partial}{\partial x_j}\alpha_k(\overline{\tau_{k_{i,j}}}+\rho_k\overline{u'_{k,i}u'_{k,j}})-\alpha_k\frac{\partial\overline{P_k}}{\partial x_i}+\alpha_k\rho_k g_i+\overline{U_{k,I}\Gamma_k}+\overline{L_{I,k}} \tag{IV.3}$$

with

$$\overline{L_{I,k}} = -\overline{p_k n_{iIK}\delta_I} + \overline{\tau_{ijk}n_{jIK}\delta_I} \tag{IV.4}$$

The term $\overline{U_{k,I}\Gamma_k}$ expresses momentum transfer associated to the mass transfer $\overline{\Gamma_k}$. The closure terms $\overline{L_{I,k}}$ represent diffusive momentum transfers between both phases resulting from pressure and strain gradients. To establish a correct modeling of two phase flow, depending on the considered flow regime, different closure terms must be taken into account as shown in section IV.1.2.

$k-\epsilon$ Model

In chemical engineering it is generally admitted to use the $k-\epsilon$ model to describ turbulence in the continous phase. The idea is to relate velocity fluctuations in the liquid phase to the difference of the kinetic energy and viscous dissipation. This is expressed by

equation IV.5:

$$-\overline{u'_{L,i}u'_{L,j}} = \nu_t\left(\frac{\partial\overline{U_i}}{\partial x_j} + \frac{\overline{U_j}}{\partial x_i}\right) - \frac{2}{3}k\delta_{ij} \tag{IV.5}$$

It should be mentioned that the $k-\epsilon$ model is isotropic, which can lead to uncertainties. However, the turbulent viscosity can also be defined in terms of kinetic energy and energy dissipation:

$$\nu_t = C_\mu\frac{k^2}{\epsilon} \tag{IV.6}$$

Turbulent Interactions

In order to simulate turbulent interactions between the bubbles, the Tchen model is available. The basic idea of this model is to relate both phases by their velocity fluctuations as follows:

$$\overline{u'_{g,i}u'_{g,j}} = C_{Tchen}\overline{u'_{l,i}u'_{l,j}} \tag{IV.7}$$

where the coefficient is defined as:

$$C_{Tchen} = \frac{b^2+\eta_r}{1+\eta_r} \tag{IV.8}$$

η_r expresses a comparison between two time scales, the turbulent τ_t and the relaxation one τ_d:

$$\eta_r = \frac{\tau_t}{\tau_d} \tag{IV.9}$$

Bubbles show a short relaxation time since their inertia is rather small. This can also be described by the following equation:

$$\tau_d = \frac{2}{3}\frac{D_E}{\parallel \vec{U_r} \parallel} \tag{IV.10}$$

which is smaller than one in our case. The second characteristic time scale, the turbulent one, is expressed as a function of the kinetic energy and its dissipation:

$$\tau_t = \frac{k_l}{\epsilon_g} \tag{IV.11}$$

The second coefficient is written in the following way:

$$b = \frac{1 + C_{AM}}{\frac{\rho_g}{\rho_l} + C_{AM}} \tag{IV.12}$$

where C_{AM} corresponds to the added mass coefficient. This expression can be simplified in the case of bubbles to:

$$b = \frac{1 + C_{AM}}{C_{AM}} \tag{IV.13}$$

Finally, one can come back to the Tchen coefficient. Two asymptotic cases can be distinguished. For solid particles $\eta < 1$ implying $\tau_t < \tau_d$, one obtains:

$$C_{Tchen} = b^2 \tag{IV.14}$$

For deformable particles $\eta_r > 1$ implying $\tau_t > \tau_d$, one obtains:

$$C_{Tchen} \approx 1 \tag{IV.15}$$

Bubbles correspond naturally to the second case since they are deformable.

IV.1.2 Closing Terms

Drag

In section I.1.3.2, a discussion about drag coefficients depending on bubble shape size was already given. In the applied CFD code, the following drag model is available:

$$\vec{L_g^D} = -\frac{1}{8} A_i \rho_l C_D |U_g - U_l| (\vec{U_g} - \vec{U_l}) \tag{IV.16}$$

The drag coefficient is calcutated automatically based on the local regime. The empirical solution was given by (Ishii & Zuber, 1979):

$$C_D = \frac{2}{3} D_E \sqrt{\frac{g|\rho_g - \rho_l|}{\sigma}} \left(\frac{1 + 17.67 f(\alpha_g)^{\frac{6}{7}}}{18.67 f(\alpha_g)} \right) \tag{IV.17}$$

with

$$f(\alpha) = (1 - \alpha_g)^{1.5} \tag{IV.18}$$

To take into account the so called turbulent dispersion the drift flux model already mentioned in section I.1.3.4 can be implemented in the drag force. Instead of $\vec{U_g} - \vec{U_l}$, the term $\vec{U_g} - \vec{U_l} - \vec{U_D}$ is taken, where:

$$\vec{U_D} = D \frac{\vec{\nabla} \alpha_g}{\alpha_g} \tag{IV.19}$$

As described in equation IV.19, the local void fraction α_g is taken into account to calculate the real bubble velocity. Since void fraction gradients are mainly present in horizontal direction, transverse velocities are generated by this correction. The final drag force can be written as:

$$\vec{L_g^d} = -\frac{1}{8} A_i \rho_l C_D |U_g - U_l - U_D| (\vec{U_g} - \vec{U_l} - \vec{U_D}) \tag{IV.20}$$

The coefficient of equation IV.19 was further defined in the following way:

$$D = \nu_t \frac{b - \eta_r}{1 + \eta_r} \tag{IV.21}$$

where b and η_r correspond to equation IV.13 and IV.9, respectively.

Lift

$$L_g^L = -L_l^L = -C_L \alpha_g \rho_l (\vec{U_g} - \vec{U_l}) \wedge (\vec{\Delta} \wedge \vec{U_l}) \tag{IV.22}$$

The lift coefficient C_L is generally expressed as a function of the Eötvös number.

Therefore, the number was slightly changed:

$$E_H = \frac{g\Delta\rho D_H^2}{\sigma} \tag{IV.23}$$

where the maximal horizontal expansion is taken instead of the equivalent bubble diameter. Both can be related by the following equation as proposed by (Wellek *et al.*, 1966):

$$D_H = D_E\sqrt[3]{1 + 0.163Eo^{0.757}} \tag{IV.24}$$

where Eo, the Eötvös number is calculated with the equivalent bubble diameter. Furthermore, three different regimes depending on the modified Eötvös number can be identified:

if $E_H < 4$

$$C_L = min(0.288\tanh(0.121Re), 0.00105E_H^3 - 0.0159E_H^2 - 0.0204E_H + 0.474) \tag{IV.25}$$

if $4 \leq E_H \leq 10$

$$C_L = 0.00105E_H^3 - 0.0159E_H^2 - 0.0204E_H + 0.474 \tag{IV.26}$$

if $E_H \geq 10$

$$C_L = -0.27 \tag{IV.27}$$

The lift coefficient evolution depending on the modified Eötvös number is presented in figure IV.1. In the chosen case a uniform bubble size of $5mm$ is set involving a constant lift coefficient of 0.27.

Added Mass

In this manuscript, it was pointed out that bubble motion is non stationary. This means, since light particles like bubbles are considered, that the added mass force must be taken into consideration. The force can be expressed by the following equation:

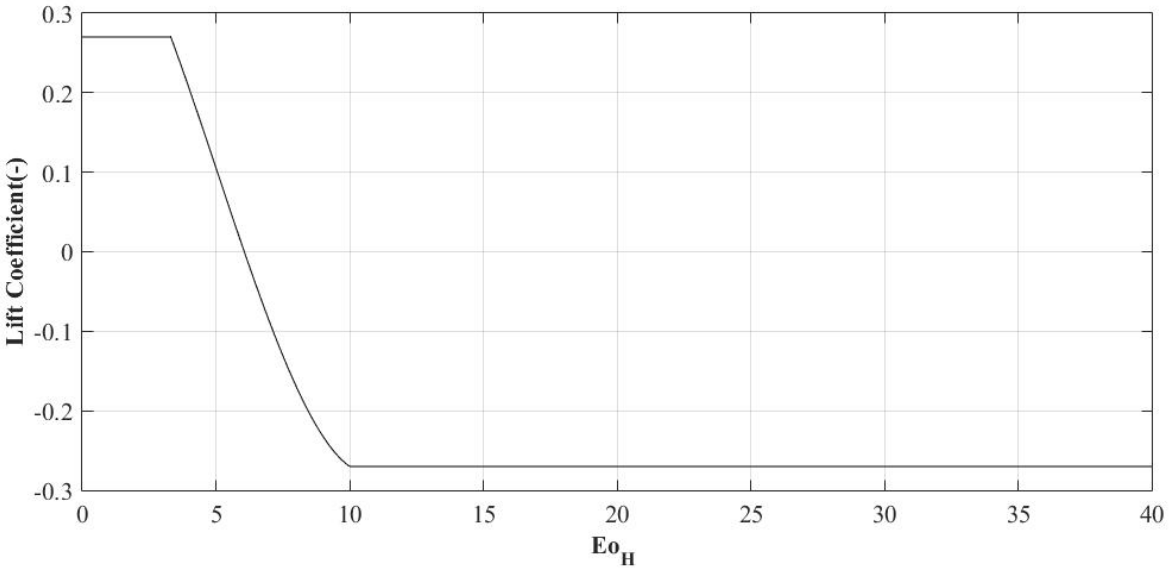

Figure IV.1: Lift Coefficient as a function of E_H

$$L_g^{AM} = -C_{AM}\frac{1+2\alpha_g}{1-\alpha_g}\alpha_g\rho_l\Big[\Big(\frac{\partial\vec{U_g}}{\partial t}+\vec{U_g}\cdot\vec{\nabla}\vec{U_g}\Big)-\Big(\frac{\partial\vec{U_l}}{\partial t}+\vec{U_l}\cdot\vec{\nabla}\vec{U_l}\Big)\Big] \tag{IV.28}$$

where C_{AM} is set to 0.5 for spherical bubbles and the fraction $\frac{1+2\alpha_g}{1-\alpha_g}$ takes into account bubble concentration.

IV.2 Test Case

A membrane sparger injection producing ellipsoidal bubbles at the lowest flow rate of $50\frac{l}{h}$ is chosen as test case for several reasons. First, bubble distribution is almost monodispersed making calculations easier. Second, all experimental methods are rather easy to apply generating very trustable results. And finally, water is considered to be the most current fluid in CFD simulations. By choosing this fluid, potential errors due to liquid properties can be avoided.

IV.2.1 Mesh

The studied hydrodynamic structure can be considered as low frequency instability wave being non stationary. In numerics an oscillating movement can be provoked easily by irregularities of the mesh. In order to make sure that asymmetries in the mesh do not generate any transverse movement, a mesh containing only quadrangles is chosen. Two different meshes were used to check the refinement sensibility. The first one contains 218400 cells corresponding to a cell mean size of $5^3 mm^3$ and the second contains 2134080 cells with a mean size of $2.3^3 mm^3$. In both cases, special attention is given to the injection area. One wanted to reproduce exactly the round injection orifice of an inner diameter of $2cm$. To solve this problem a square is projected in the middle of the injection area as shown in figure IV.2. In this way a perfectly symmetric mesh was generated for both resolutions.

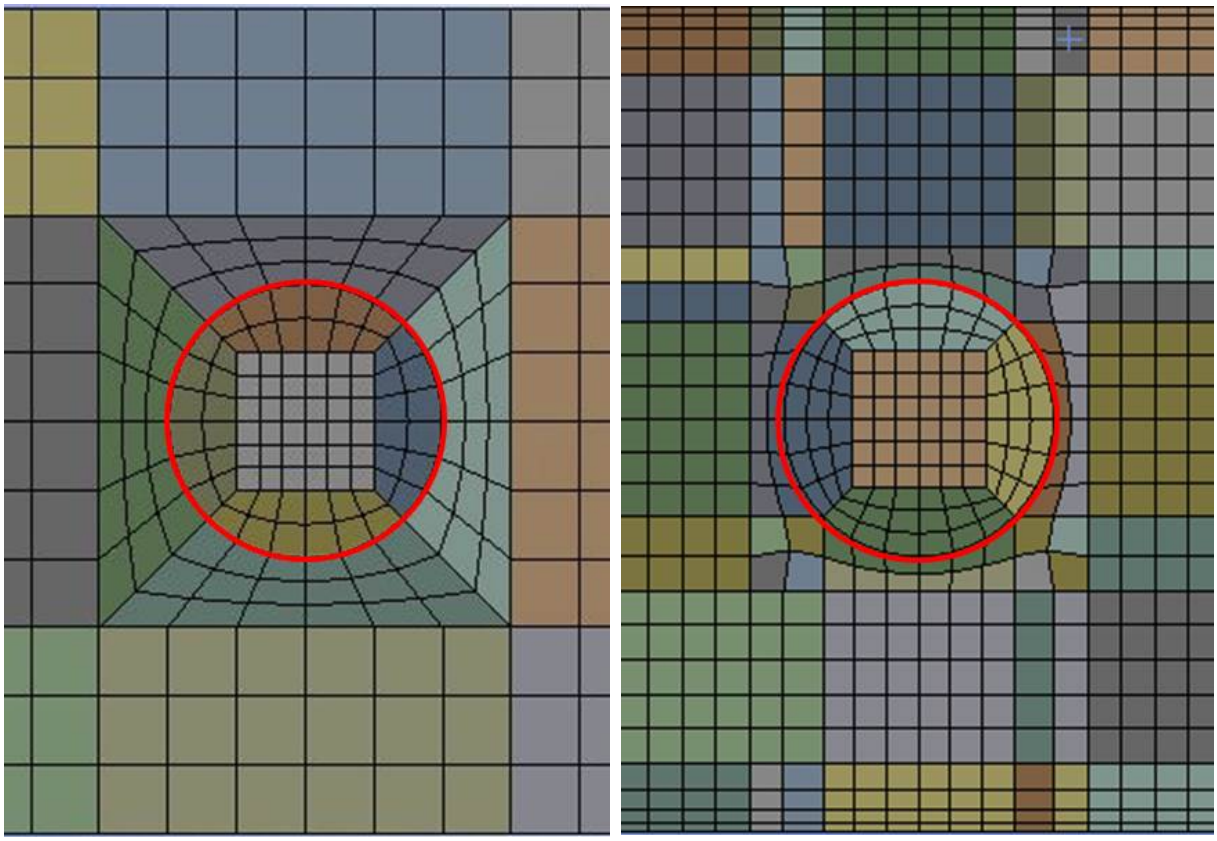

Figure IV.2: Mesh of the Sparger Zone seen from the bottom with low (left) and high (right) Resolution

It turned out that the two meshes produce the exact same results concerning the global structure as well as local analyzes. Hence, only the mesh with the lower resolution is used in the following in order to economize calculation time. Anyway, a friction

condition with a logorithmic low for velocity calculations is used as boundary condition at the wall. At the inlet, only gas is injected and at column top a degassing condition is set. This means only gas can go through the outlet.

IV.2.2 Simulated Conditions

As already mentioned, a simple test case in water with membrane injection and a flow rate of $50\frac{l}{h}$ was chosen. The convergent experimental diameter is $5mm$. For the CFD simulations a uniform equivalent diameter of the same size is taken. The associated measured low frequency oscillation time scale is $28.2s$.

IV.3 Results

The first objective was to check if the global hydrodynamic structure of our CFD simulation corresponds to the experiments. Therefore, only the drag force is chosen as closure term. A comparison between a shadowgraphy image (of $\approx 0.7m$ of the column height) and the gas fraction from simulations is shown in figure IV.3. It is clear that the marcoscopic bubble plume shape is well reproduced by the CFD.
The second step is the verification if the oscillating bubble plume behavior can be simulated in the right frequnecy range. Hence, fluctuations must be considered, no matter in which phase. In the current case the vertical velocity of the gas phase is used and recorded during $350s$ at several positions of the bubble column. The exact heights are $0.3m$, $0.6m$, $0.9m$ and $1.2m$. But before treating the data signals, stationarity must be studied. The overall averaged gas hold-up can serve to determine the moment when quasi-stationarity is achieved. The exact gas hold-up evolution in time from the numerical data is shown in figure IV.4. After $50s$ no large fluctuations can be seen anymore, which is why this moment is chosen to begin time series analyzes.

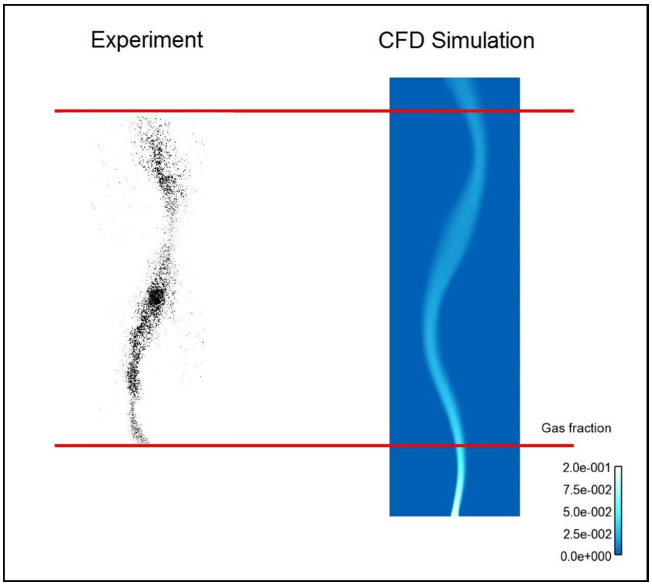

Figure IV.3: Averaged Gas Hold-up from CFD simulations in Water compared to the experiment; Membrane Sparger and $50\frac{l}{h}$

Typical raw bubble velocity signals with an acquisition frequency of $10Hz$ can be seen in figure IV.5 at the top. The corresponding autocorrelation functions from the different signals are illustrated in figure IV.5 (bottom).

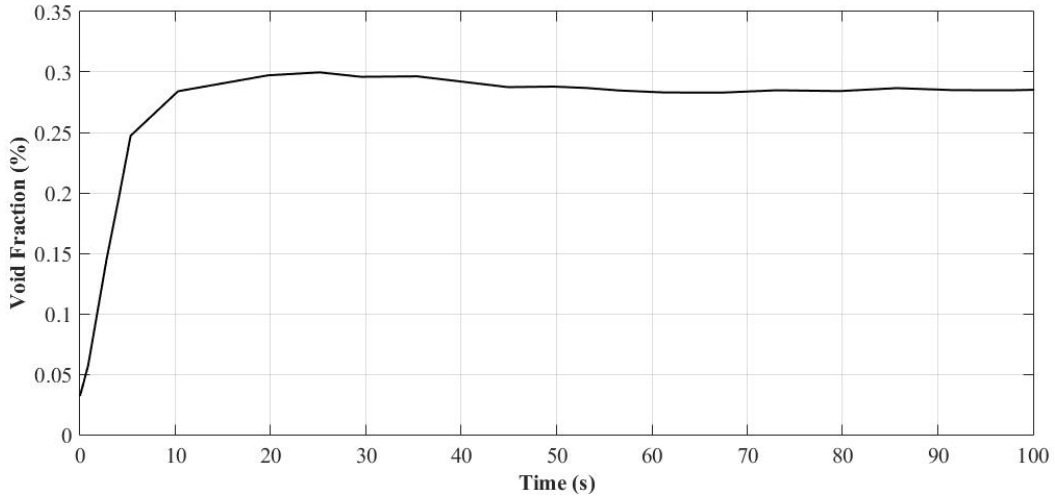

Figure IV.4: Averaged Gas Hold-up in Time from CFD simulations in Water, Membrane Sparger and $50\frac{l}{h}$

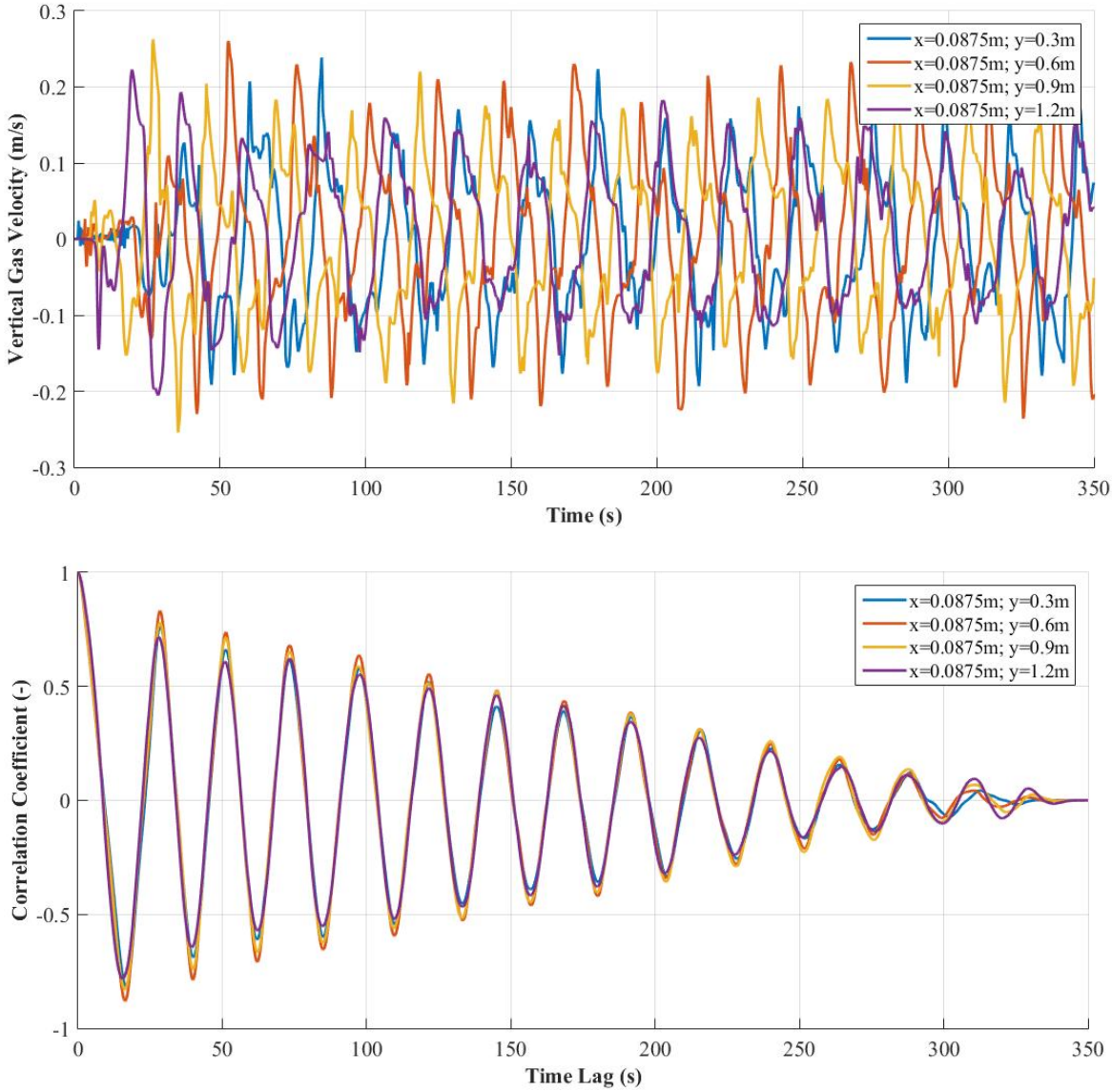

Figure IV.5: a) Raw Vertical Gas Velocities; b) Autocorrelation Functions; from four different Measurement Points

Time scales measured by all virtual sensors are identical, indicating that the low frequency oscillation is consistent over the whole column height. This result is in agreement with our measured pressure signals. Furthermore, all oscillation periods are in the right time scale range proving that, even in absence of lift and added mass forces, the oscillating behaviour can be reproduced. However, the bubble size of the considered case is in a range where bubbles are deformable and so where lift forces are acting. Plus, the flow regime is only quasi-stationary and bubbles show very low density compared to liquid. Hence, added mass forces should be considered as well. For this reason four different test cases in the sense of closure terms are defined and shown in table IV.1. The resulting

characteristic time scales are written in the last column. In all cases, the $k-\epsilon$ and the Tchen model are used to simulate turbulence in the liquid and gas phase, respectively.

Name	Drag	Added Mass	Lift	Period (s)
TC 1	Ishii	None	None	31.0
TC 2	Ishii	Standard	None	30.4
TC 3	Ishii	None	Tomiyama SMD	26.9
TC 4	Ishii	Standard	Tomiyama SMD	28.0

TABLEAU IV.1: Closure Terms and Models with resulting Time Scales

By comparing the different cases, one recognizes that the sensitivity to the closure terms is rather weak. Gravity, drag und turbulence seem to be the most important terms. Nevertheless, it is reassuring to see that the last case reproduces reality as best. It illustrates the importance to take into account all mentioned forces that are supposed to be involved in the current flow regime. After validation of the hydrodynamic structure, the analysis is conducted to more local comparisons. Therefore, void fraction profiles for different closure terms and experimental data are plotted in figure IV.6.

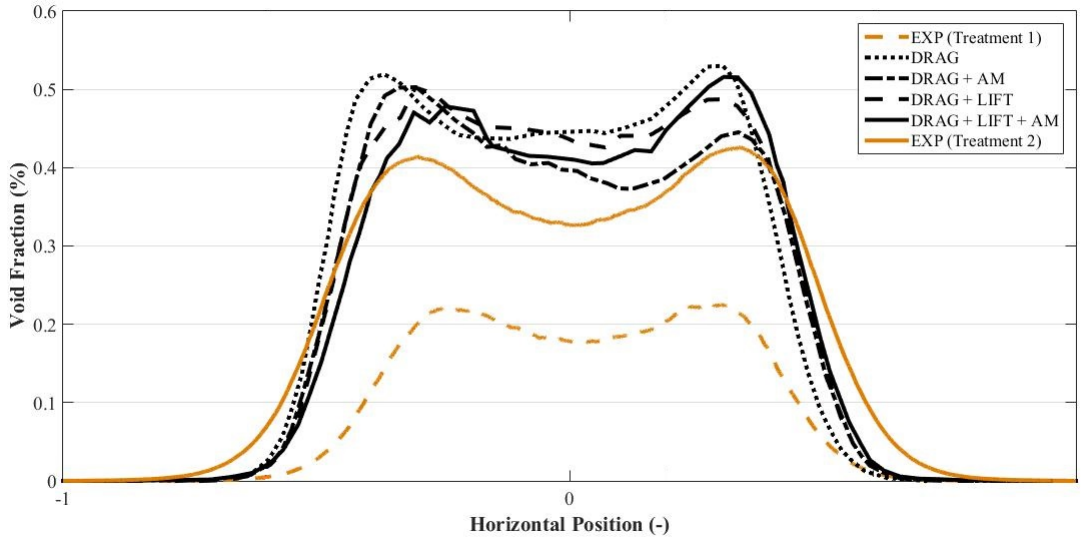

Figure IV.6: Void Fraction Profile Comparison between Experimental and Numerical Data for Different Closure Terms

In the considered figure four curves belonging to numerical data (black) and two curves from experimental data (orange) are shown. The difference between the orange profiles is the way of volume calculation concerning COSIs. The dashed line (Treament 1) corresponds to the choice taken in section II.1.3.3 (equation II.15, $V_{Ellipsoid} = \frac{4}{3}\pi m M^2$).

The solid line (Treament 2) represents the second possibility where the volume of COSIs and WIBs are calculated in the same way (equation I.5, $V_{Ellipsoid} = \frac{4}{3}\pi m^2 M$). However, two main conclusions can already be deduced from the obtained figure. First, one is able to reproduce numerically the charecteristic bubble peak in the time averaged void fraction of the considered case. Second, the profile shape is rather insensitive to different combinations of closure terms. Furthermore, the choice of Treatment 1 seems not being appropriate for the considered case. Indeed, half of the global void fraction results from COSIs, which is why the way of volume calculation for COSIs has significant importance for the averaged void fraction determination. Therefore, Treatment 2 is chosen to compare experimental and numerical data (both solid lines). Numerical simulations overestimates the time averaged void fraction and slightly underestimates bubble dispersion. The first point may be explained by the fact that numerical data is taken in the very center on a single slice where the gas hold-up may be higher than near the wall. Experimental data is integrated over the whole column depth and overlapping bubble are current. These two arguments may explain partially the observed gap. Nervertheless, the agreement between both data sets is rather good and the profile shape reproduced. To go further in our analysis vertical velocities of liquid U_l and gas phase U_g are studied. Figure IV.7 shows first one from the CFD simulation $TC4$ and from experimental measurements.

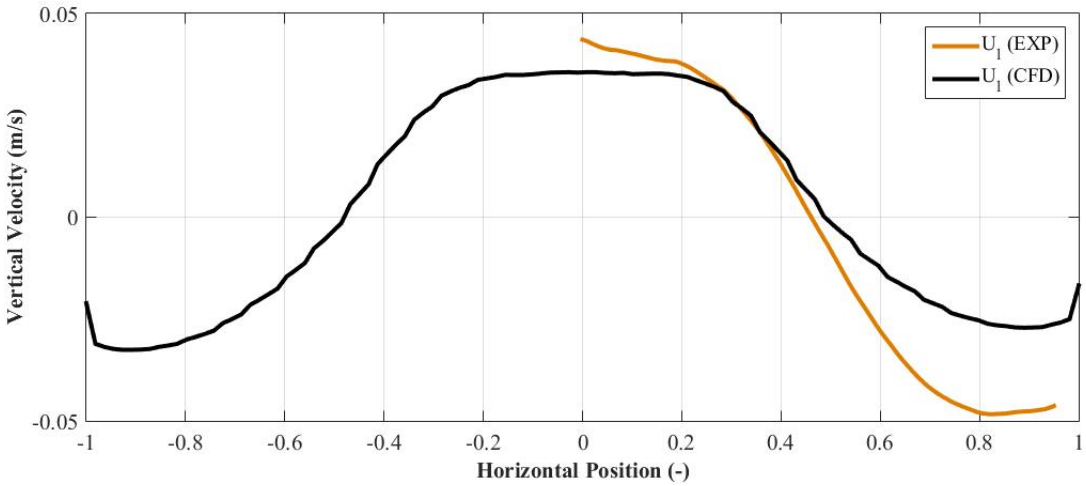

Figure IV.7: Liquid Velocity Profile Comparison between Experimental and Numerical Data

Regarding the liquid velocities, the agreement between CFD and experiments is rather good, even if the numerical one is slightly underestimated, especially in the donwcomer

part. The difference between the maximum velocity of the riser ($3.55\frac{cm}{s}$) and downcomer ($2.59\frac{cm}{s}$) indicates stronger three dimensional effects in the case of the simulated liquid velocity. Indeed, by integrating the velocity over the whole horizontal axis, one does not obtain zero meaning that mass balance is not met in the considered two dimensional plane as it is the case in our experiments.

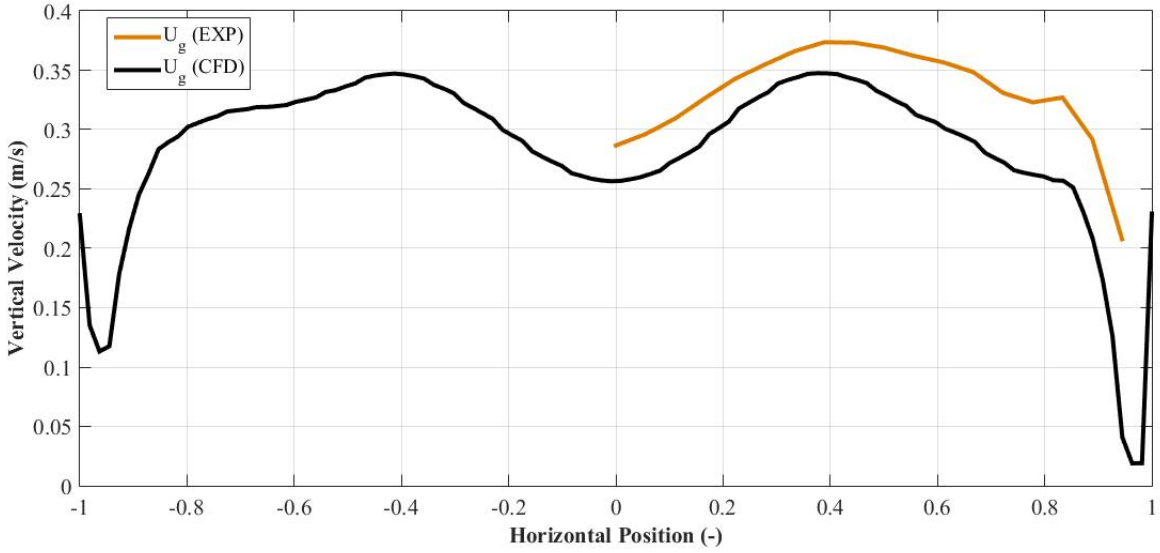

Figure IV.8: Gas Velocity Profile Comparison between Experimental and Numerical Data

Figure IV.8 shows the comparison of the rising gas velocity between numerical and experimental data. To achieve this correctly, the velocity must be calculated in a similar way than in equation II.19:

$$\overline{U_g} = \frac{\sum_{i=1}^{N} \alpha_{g_i} U_{b_i}}{\sum_{i=1}^{N} \alpha_{g_i}} \tag{IV.29}$$

Similar to section II.25 where the gas velocity is determined for every spatial interval, the numerical one is calculated for every mesh. However, the shape of the experimental curve could be well reproduced as it can be seen in figure IV.8. Maximums and minimums are located at same positions at ≈ 0.4 and ≈ 0.95, respectively, suggesting that hydrodynamics are simulated in a correct way. On the other hand, a gap between both data sets is observed. This result is in line with the overestimated void fraction shown in figure IV.6 and can be explained by at least two reasons. In section I.1.3.4 it was already shown that swarm effects can decrease the drag coefficient which necessarily results in

a veclocity increase. This effect is furtherd by a phenomenon, called bulk formation. It means that objects (here bubbles) agglomerate generating low pressure zones in its wake. Hence, bubbles rising behind the bulk, accelerate significantly. In smaller bubble columns such observations are called intermittencies. The second explanation is a little more abstract. In the moment when the bubble plume comes close to the wall changing the direction, a decceleration and a recceleration is observed. At this moment, the added mass force may generate a streamwise acceleration component meaning that at this typical moment an increase of the gas velocity can be observed.

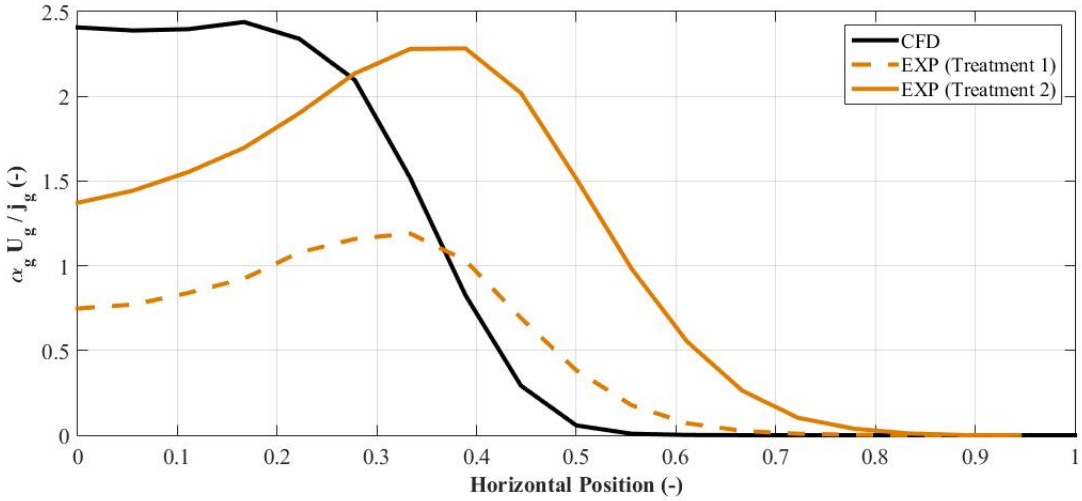

Figure IV.9: Flow Rate Profile Comparison between Experimental and Numerical Data

Finally, the flow rate calulated via U_g and α_g is compared to the injected one j_g as shown in figure IV.9. Again, the simulated case $TC4$ and experimental data from our two treatments are plotted in order to analyze bubble diffusion. Obviously, the CFD simulation is not capable to reproduce correctly the shape of the experimental flow rate profile. Furthermore, the qualitative shape of the considered profile is independent of our treatment to calculate volumes of COSI's. To understand which treatment is better adapted, one must integrate the considered curves over whole horizontal axis. At best the result should be equal or close to one, but this is only the case for our experimental data with treatment 2. In one way or another, one is able to recognize that the numerical profile shape does not match with the experimental one. This means that improvements concerning bubble diffusion must be done.

Anyway, the bubble plume flow regime of the considered test case could be well reproduced by CFD simulations. The hydrodynamic structure as well as the oscillation frequency matches almost perfectly. On the other hand, gaps between local numerical and experimental data indicate the need of model improvements. Drag and turbulent interaction seem to be the dominant terms, which is why other corresponding models, available in literature, should be checked. Furthermore, CFD simulations must be extended to other test cases. A first step could be the simulation of bubble plumes with large spherical caps in water. Then, the impact of liquid property modifications can be studied, which is even more usefull for industrial applications.

Conclusion and Perspectives

Conclusion

The present work investigated hydrodynamics, mass tranfer and mixing induced by quasi two dimensional bubble plumes. Especially, the oscillating behaviour was in focus. The deeper aim is to understand same phenomena induced by single spot spargers in large bioreactors. Hence, the acquisition of a large databank is reported. A large number of metrological methods was presented such as PIV, BIV, shadowgraphy, mixing time determination as well as time signals from pressure sensors and oxygen probes. In this way, different analyzes relating temporal and spatial scales could be performed. Several time scales for bubble plume oscillations, mass transfer and mixing are presented. Liquid and bubble velocities in function of fluid properties are reported as well, in terms of mean value, organized motion, bubble induced agitation and turbulence.
Different influences from spargers and liquid properties were studied. It turned out that in water sparger influence is rather small on bubbe plume oscillations, but large for mass transfer and mixing times. The same observation was done for surface tension influences. Furthermore, viscosity impact in the range of $1 - 100mPas$ on different time scales was analyzed. Results showed that the choice of the sparger becomes more important with increasing viscosity. Dispersion and oscilallation frequencies are dependent on sparger types. For example it was presented that viscosity has influence on the oscillation frequency in the case of membrane sparger, but not in the case of the slugflow sparger. Strong coupling between bubble size, velocity and the oscillating behaviour was presented. As expected, bubble dispersion decreases with increasing viscosity.

Besides, different evolutions of mass tranfer and mixing time scales with increasing viscosity are reported. While the mass transfer is decreasing, the analysis of mixing time scales as a function of viscosity remains tricky. This illustrates that different phenomena can dominate bubble plume flows depending on fluid properties. Finally, oscillation time scale comparisons were done with three dimensional measurements performed at the HZDR in Dresden. Similar frequencies in both geometries were found which shows the benefit of pseudo two dimensional analysis.
In the last chapter, preliminary three dimensional numerical results are presented for one test case using NEPTUNE CFD. Different closure terms between phases were tested in order to validate numerical results by comparison to oscillating time scales and void fraction profiles. It turned out that drag as well as lift and added mass terms must be taken into account to simulate bubble plume oscillation as close as possible to reality.

Perspectives

The last point of the conclusion should also be the starting point of future works. The large databank is giving the possibility to simulate a large range of several conditions and compare them to experimental results. First, injection conditions such as flow rates and sparger types should be investigated numerically. Therefore, the rather recent Large Interface Model (LIM) developped in NEPTUNE CFD could be used in order to simulate spherical cap bubbles. Then, liquid properties like surface tension and viscosity with the LIM must be investigated.
Liquid velocity fields should be used to go further in POD analyzes. For example, spatial intercorrelations could provide information about vortex size depending on their energy contribution. PIV measurements were also performed on small acquisition windows which could serve to investigate viscous dissipation.
A large analysis concerning bubble velocities can also be performed from Bubble Image Velocimetry (BIV) measurements. Velocity of each bubble can be related to other characteristics like eccentricity, solidity or size. In this way, bubble behaviour depending on their characteristics in bubble swarms can be investigated. With all the information about gas and liquid velocity, void fraction profiles as well as bubble shape and size, interfacial area and then mass tranfer should be studied in detail.

Appendix

Shadowgraphy Images in Different Fluids and for Both Spargers

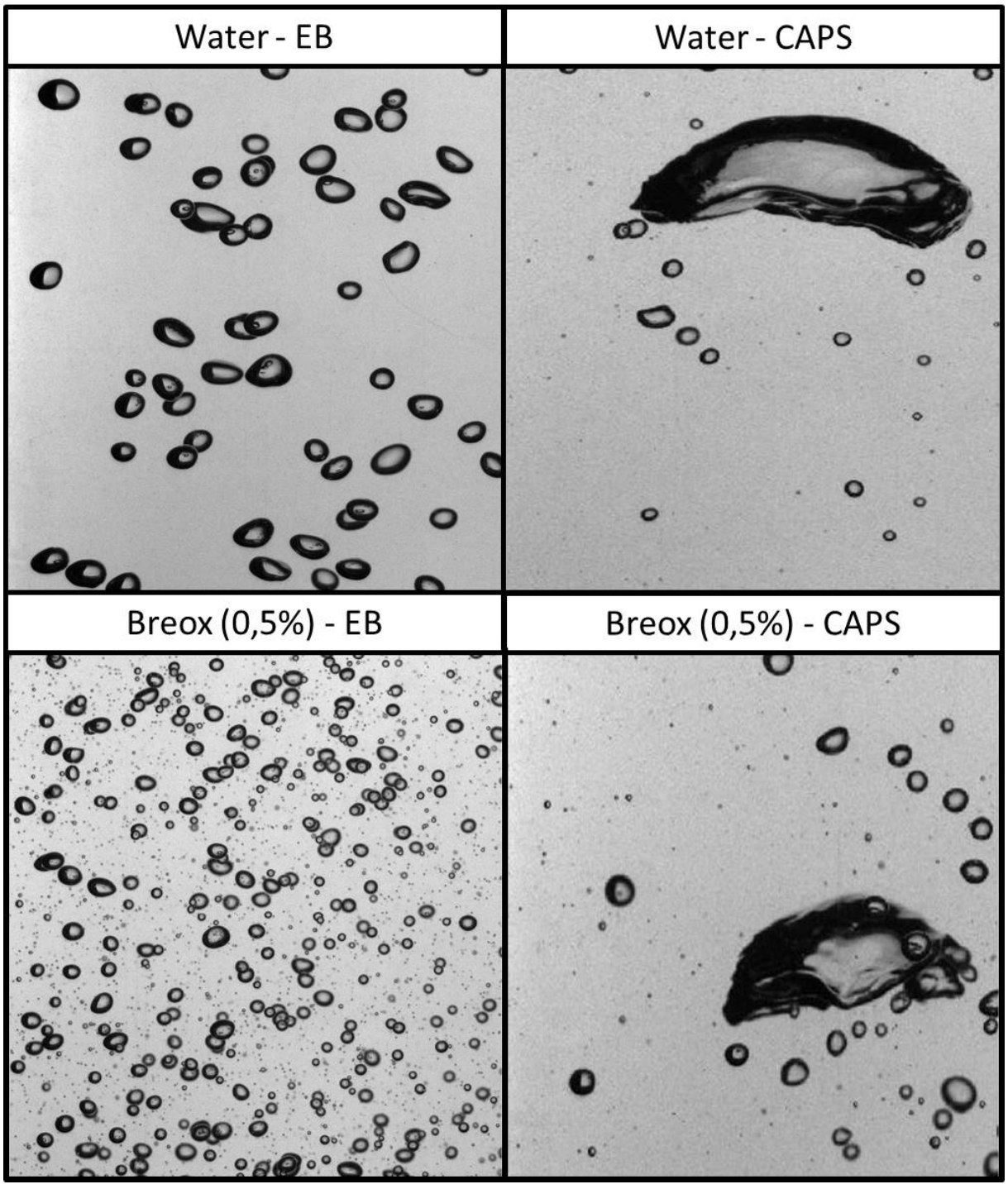

Figure 1: Raw Shadography Images for both Spargers in different Fluids

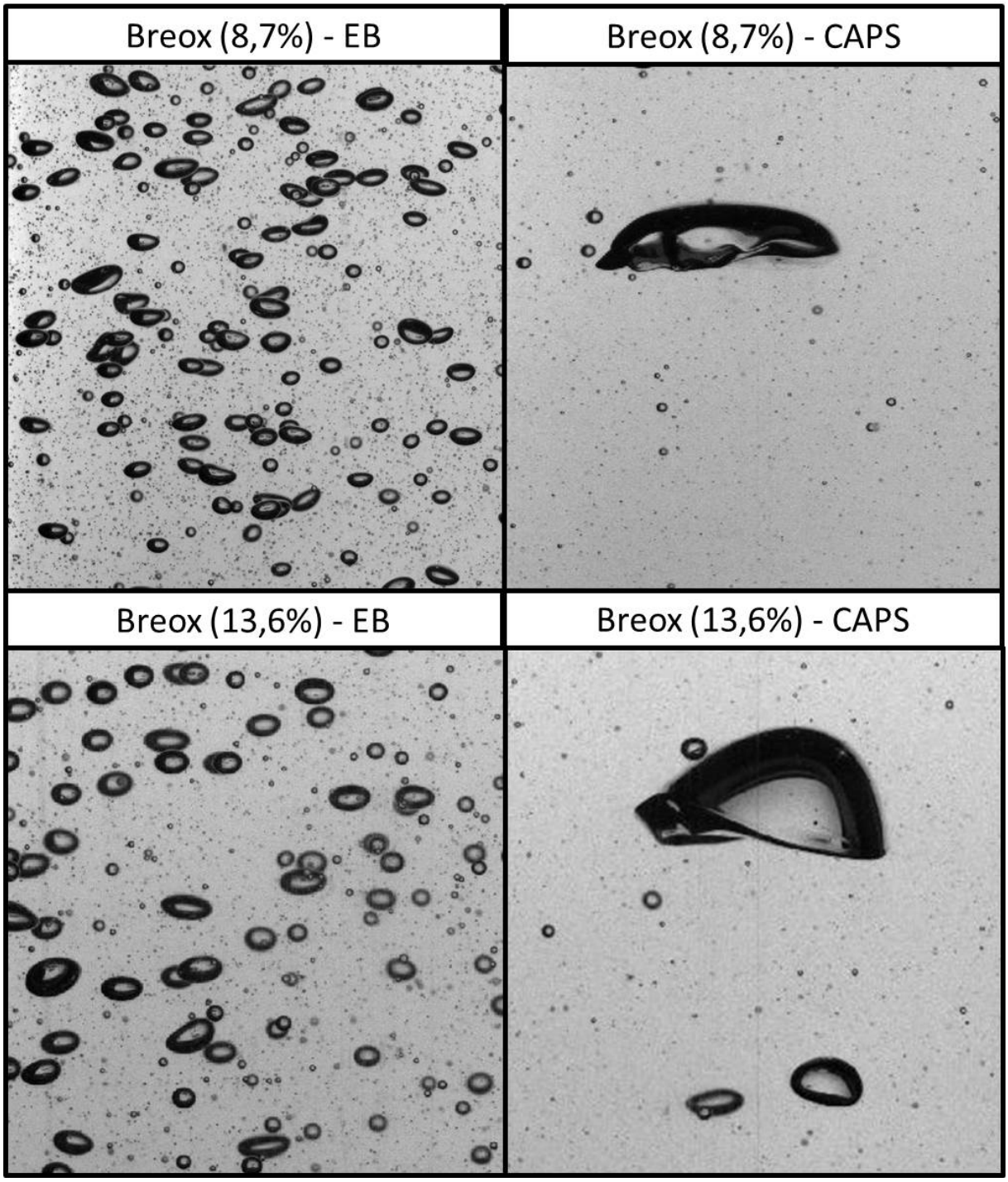

Figure 2: Raw Shadography Images for both Spargers in different Fluids

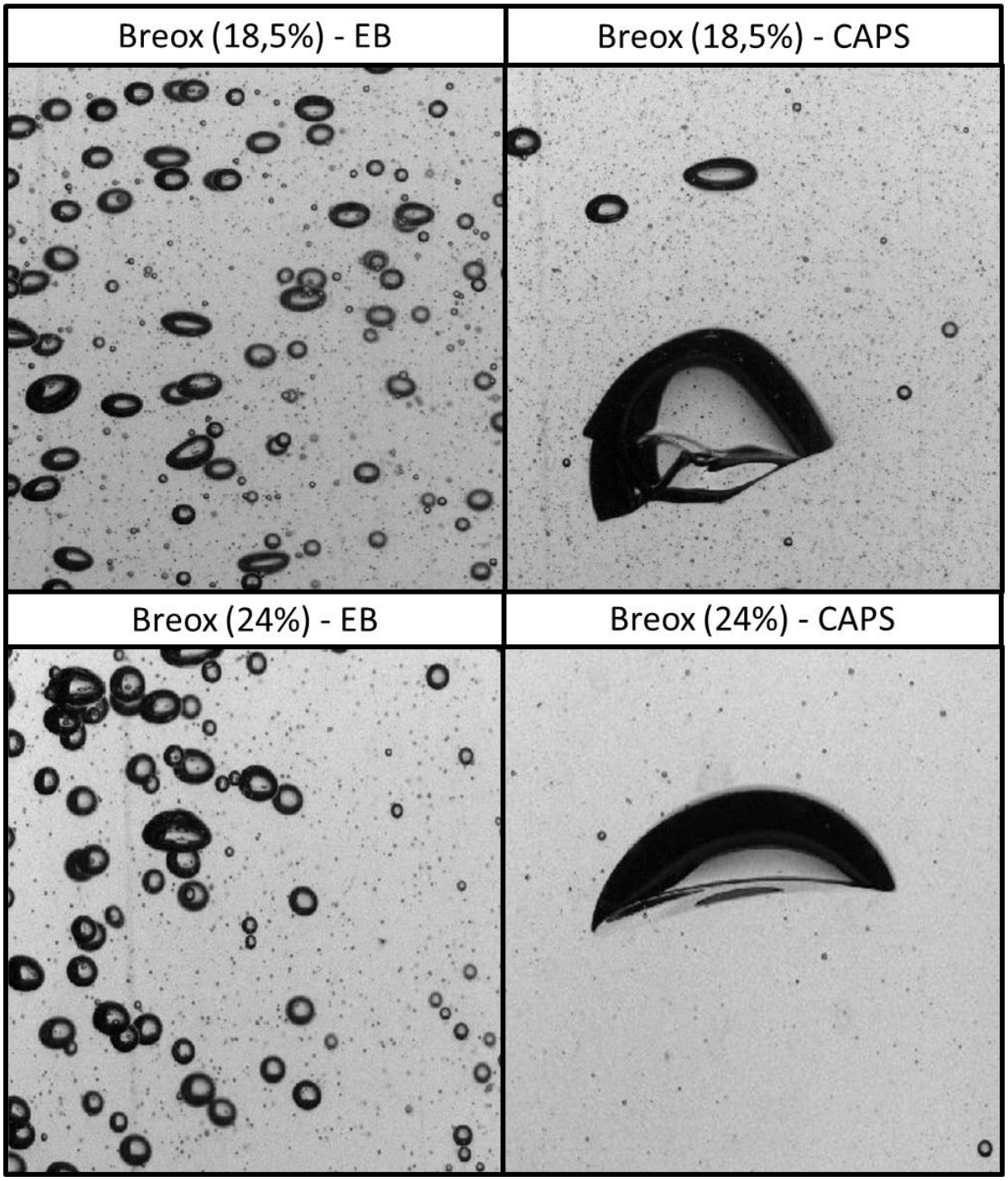

Figure 3: Raw Shadography Images for both Spargers in different Fluids

References

Abdelsamie, Abouelmagd, & Thévenin, Dominique. 2017. Direct numerical simulation of spray evaporation and autoignition in a temporally-evolving jet. *Proceedings of the Combustion Institute*, **36**(2), 2493–2502.

Akita, Kiyomi, & Yoshida, Fumitake. 1973. Gas Holdup and Volumetric Mass Transfer Coefficient in Bubble Columns. Effects of Liquid Properties. *Industrial & Engineering Chemistry Process Design and Development*, **12**(1), 76–80.

Aouinet, H. 2016. *Analyse experimental et modelisation de l'hydrodynamic induite par un panache de bulles dans des conditions d'aeration controle.*

Batchelor, G. K. 1972. Sedimentation in a dilute dispersion of spheres. *Journal of Fluid Mechanics*, **52**(2), 245–268.

Batchelor, G. K. 1987. The stability of a large gas bubble rising through liquid. *Journal of Fluid Mechanics*, **184**(Nov.), 399–422.

Becker, S., Sokolichin, A., & Eigenberger, G. 1994. Gas—liquid flow in bubble columns and loop reactors: Part II. Comparison of detailed experiments and flow simulations. *Chemical Engineering Science*, **49**(24, Part 2), 5747–5762.

Berkooz, G, Holmes, P, & Lumley, and J. L. 1993. The Proper Orthogonal Decomposition in the Analysis of Turbulent Flows. *Annual Review of Fluid Mechanics*, **25**(1), 539–575.

Besagni, Giorgio, Inzoli, Fabio, De Guido, Giorgia, & Pellegrini, Laura Annamaria. 2017. The dual effect of viscosity on bubble column hydrodynamics. *Chemical Engineering Science*, **158**(Feb.), 509–538.

Bouche, Emmanuella, Roig, Véronique, Risso, Frédéric, & Billet, Anne-Marie. 2012. Homogeneous swarm of high-Reynolds-number bubbles rising within a thin gap. Part 1. Bubble dynamics. *Journal of Fluid Mechanics*, **704**(Aug.), 211–231.

Buwa, Vivek V., & Ranade, Vivek V. 2003. Mixing in Bubble Column Reactors: Role of Unsteady Flow Structures. *The Canadian Journal of Chemical Engineering*, **81**(3-4), 402–411.

Caballina, Ophélie, Climent, Eric, & Dušek, Jan. 2003. Two-way coupling simulations of instabilities in a plane bubble plume. *Physics of Fluids (1994-present)*, **15**(6), 1535–1544.

Cachaza, Elena M., Elena Díaz, M., Montes, Francisco J., & Galán, Miguel A. 2011. Unified study of flow regimes and gas holdup in the presence of positive and negative surfactants in a non-uniformly aerated bubble column. *Chemical Engineering Science*, **66**(18), 4047–4058.

Cartellier, Alain, & Rivière, Nicolas. 2001. Bubble-induced agitation and microstructure in uniform bubbly flows at small to moderate particle Reynolds numbers. *Physics of Fluids*, **13**(8), 2165–2181.

Cartellier, Alain, Andreotti, Marcelo, & Sechet, Philippe. 2009. Induced agitation in homogeneous bubbly flows at moderate particle Reynolds number. *Physical Review E*, **80**(6), 065301.

Chatfield, C. 1984. The Analysis of Time Series: An Introduction, Sixth Edition. *In: The Analysis of Time Series*.

Clift, Roland, Grace, John R., & Weber, Martin E. 1978. *Bubbles, Drops, and Particles*. Academic Press. Google-Books-ID: n8gRAQAAIAAJ.

Comolet, Raymond. 1979. Sur le mouvement d'une bulle de gaz dans un liquide. *La Houille Blanche*, Jan., 31–42.

Cuenot, B., Magnaudet, J., & Spennato, B. 1997. The effects of slightly soluble surfactants on the flow around a spherical bubble. *Journal of Fluid Mechanics*, **339**(May), 25–53.

Danckwerts, P. V. 1951. Significance of Liquid-Film Coefficients in Gas Absorption. *Industrial & Engineering Chemistry*, **43**(6), 1460–1467.

Davies, R. M., Taylor, Sir Geoffrey, & S, F. R. 1950. Has a foldout - The mechanics of large bubbles rising through extended liquids and through liquids in tubes. *Proc. R. Soc. Lond. A*, **200**(1062), 375–390.

Deckwer, Wd. 1980. Access of Parameters Required in the Design and Scale up of Bubble Column Reactors. *Abstracts of Papers of the American Chemical Society*, **180**(AUG), 35–INDE. WOS:A1980LG43101800.

Delnoij, E., Kuipers, J. A. M., & van Swaaij, W. P. M. 1997. Dynamic simulation of gas-liquid two-phase flow: effect of column aspect ratio on the flow structure. *Chemical Engineering Science*, **52**(21–22), 3759–3772.

Diaz, M. Elena, Montes, Francisco J., & Galán, Miguel A. 2006. Influence of Aspect Ratio and Superficial Gas Velocity on the Evolution of Unsteady Flow Structures and Flow Transitions in a Rectangular Two-Dimensional Bubble Column. *Industrial & Engineering Chemistry Research*, **45**(21), 7301–7312.

Drahoš, J., Zahradník, J., Punčochář, M., Fialová, M., & Bradka, F. 1991. Effect of operating conditions on the characteristics of pressure fluctuations in a bubble column. *Chemical Engineering and Processing: Process Intensification*, **29**(2), 107–115.

Duineveld, P. C. 1995. Bouncing and coalescence of two bubbles in pure water. *Pages 151–160 of: IUTAM Symposium on Waves in Liquid/Gas and Liquid/Vapour Two-Phase Systems*. Fluid Mechanics and its Applications. Springer, Dordrecht.

F Richardson, J, & N. Zaki, W. 1954. Sedimentation and Fluidization: Part I. *Trans. Inst. Chem. Engrs*, **32**(Jan.), 35–53.

FAN, Liang-Shih, & Tsuchiya, Katsumi. 2013. *Bubble Wake Dynamics in Liquids and Liquid-Solid Suspensions*. Butterworth-Heinemann. Google-Books-ID: IQMhBQAAQBAJ.

Ferreira, A., Pereira, G., Teixeira, J. A., & Rocha, F. 2012. Statistical tool combined with image analysis to characterize hydrodynamics and mass transfer in a bubble column. *Chemical Engineering Journal*, **180**(Jan.), 216–228.

Fortescue, G., Pearson, J. 1967. On gas absorption into a turbulent liquid - ScienceDirect. *Chem. Eng. Sci.*

Freeman, H. 1961. On the Encoding of Arbitrary Geometric Configurations. *IRE Transactions on Electronic Computers*, **EC-10**(2), 260–268.

Garnier, C., Lance, M., & Marié, J. L. 2002. Measurement of local flow characteristics in buoyancy-driven bubbly flow at high void fraction. *Experimental Thermal and Fluid Science*, **6-7**(26), 811–815.

Gaudin, Antoine Marc. 1957. *Flotation*. McGraw-Hill. Google-Books-ID: cvYDAQAAIAAJ.

Gelly, Bernard, Men, Claude Le, Ariste, Arturo López, Delaigue, Cyril, & Perez, Ruyman Gónzalez. 2008. Design and implementation of an image stabilization device at the THEMIS solar telescope. *Experimental Astronomy*, **22**(1-2), 67–85.

Gourich, B., Vial, C., Essadki, A. H., Allam, F., Soulami, M. B., & Ziyad, M. 2006. Identification of flow regimes and transition points in a bubble column through analysis of differential pressure signal - Influence of the coalescence behavior of the liquid phase. *Chemical Engineering and Processing*, **45**(3), 214–223. WOS:000233508900008.

Groen, F. C. A., & Verbeek, P. W. 1978. Freeman-code probabilities of object boundary quantized contours. *Computer Graphics and Image Processing*, **7**(3), 391–402.

Hadamard, J. S., & Hadamard, J. 1911. Movement permanent lent d'une sphere liquide et visqueuse dans un liquide visqueux. Jan.

Hallez, Yannick, & Legendre, Dominique. 2011. Interaction between two spherical bubbles rising in a viscous liquid. *Journal of Fluid Mechanics*, **673**(Apr.), 406–431.

Higbie, Ralph. 1935. *The rate of absorption of a pure gas into still liquid during short periods of exposure*. Open Library ID: OL6329191M.

Hikita, H., Asai, S., Tanigawa, K., Segawa, K., & Kitao, M. 1980. Gas hold-up in bubble columns. *The Chemical Engineering Journal*, **20**(1), 59–67.

Ishii, Mamoru, & Zuber, Novak. 1979. Drag coefficient and relative velocity in bubbly, droplet or particulate flows. *AIChE Journal*, **25**(5), 843–855.

Knight, B, & Sirovich, Lawrence. 1990. Kolmogorov inertial range for inhomogeneous turbulent flows. *Physical review letters*, **65**(Oct.), 1356–1359.

Koch, Donald L. 1993. Hydrodynamic diffusion in dilute sedimenting suspensions at moderate Reynolds numbers. *Physics of Fluids A: Fluid Dynamics*, **5**(5), 1141–1155.

Krishna, R, Urseanu, M. I, van Baten, J. M, & Ellenberger, J. 1999. Rise velocity of a swarm of large gas bubbles in liquids. *Chemical Engineering Science*, **54**(2), 171–183.

Lamont and Scott. 1970. An eddy cell model of mass transfer into the surface of a turbulent liquid - Lamont - 1970 - AIChE Journal - Wiley Online Library. *AlCHe J.*

Legendre, Dominique, Magnaudet, Jacques, & Mougin, Guillaume. 2003. Hydrodynamic interactions between two spherical bubbles rising side by side in a viscous liquid. *Journal of Fluid Mechanics*, **497**(Dec.), 133–166.

Legendre, Dominique, Zenit, Roberto, & Velez-Cordero, J. Rodrigo. 2012. On the deformation of gas bubbles in liquids. *Physics of Fluids*, **24**(4), 043303.

León-Becerril, Elizebeth, Cockx, Arnaud, & Liné, Alain. 2002. Effect of bubble deformation on stability and mixing in bubble columns. *Chemical Engineering Science*, **57**(16), 3283–3297.

Löfdahl, Mats G. 2010. Evaluation of image-shift measurement algorithms for solar Shack-Hartmann wavefront sensors. *Astronomy & Astrophysics*, **524**(Dec.), A90. arXiv: 1009.3401.

Liné, A., Gabelle, J. C., Morchain, J., Anne-Archard, D., & Augier, F. 2013. On POD analysis of PIV measurements applied to mixing in a stirred vessel with a shear thinning fluid. *Chemical Engineering Research and Design*, **91**(11), 2073–2083.

Lindken, R., & Merzkirch, W. 2002. A novel PIV technique for measurements in multiphase flows and its application to two-phase bubbly flows. *Experiments in Fluids*, **33**(6), 814–825. WOS:000179986400010.

Lumley, JL. 1967. The Structure of Inhomogeneous Turbulent Flows. *Pages 166–178 of:* Yaglom, AM, & Tatarski, VI (eds), *Atmospheric turbulence and radio propagation*. Nauka.

Maruyama, T., Yoshida, S., & Mizushina, T. 1981. The Flow Transition in a Bubble Column. *Journal of Chemical Engineering of Japan*, **14**(5), 352–357. WOS:A1981MK57200002.

Maxworthy, T., Gnann, C., Kurten, M., & Durst, F. 1996. Experiments on the rise of air bubbles in clean viscous liquids. *Journal of Fluid Mechanics*, **321**(Aug.), 421–441. WOS:A1996VH37700017.

Mendelson, Harvey D. 1967. The prediction of bubble terminal velocities from wave theory. *AIChE Journal*, **13**(2), 250–253.

Mikaelian, David, Larcy, Aurélie, Cockx, Arnaud, Wylock, Christophe, & Haut, Benoit. 2015. Dynamics and morphology of single ellipsoidal bubbles in liquids. *Experimental Thermal and Fluid Science*, **64**(June), 1–12.

Milne Thomson L.N. 1962. *Theoretical Hydrodynamics Fourth Edition.* The Macmillan And Company.

Moore, D. M. 1959. Population Studies on Viola Lactea Sm. and Its Wild Hybrids. *Evolution*, **13**(3), 318–332.

Moore, D. W. 1965. The velocity of rise of distorted gas bubbles in a liquid of small viscosity. *Journal of Fluid Mechanics*, **23**(4), 749–766.

Mudde, Robert F., & Simonin, Oliver. 1999. Two- and three-dimensional simulations of a bubble plume using a two-fluid model. *Chemical Engineering Science*, **54**(21), 5061–5069.

Olivieri, Giuseppe, Grillo, Silvio, D'Errico, Gerardino, Marzocchella, Antonio, Ruzicka, Marek, & Salatino, Piero. 2013. Preliminary Assessments of Combined Effects of Surface Tension and Viscosity on Bubble Column Hydrodynamics. *Pages 1579–1584 of:* Pierucci, S., & Klemes, J. J. (eds), *Icheap-11: 11th International Conference on Chemical and Process Engineering, Pts 1-4*, vol. 32. Milano: Aidic Servizi Srl. WOS:000335952100264.

Peebles, FN & Garber, HJ. 1953. *Chemical Engineering Progress*, 88–97.

Pfleger, D., & Becker, S. 2001. Modelling and simulation of the dynamic flow behaviour in a bubble column. *Chemical Engineering Science*, **56**(4), 1737–1747.

Pfleger, D., Gomes, S., Gilbert, N., & Wagner, H. G. 1999. Hydrodynamic simulations of laboratory scale bubble columns fundamental studies of the Eulerian–Eulerian modelling approach. *Chemical Engineering Science*, **54**(21), 5091–5099.

Proffitt, D., & Rosen, D. 1979. Metrication errors and coding efficiency of chain-encoding schemes for the representation of lines and edges. *Computer Graphics and Image Processing*, **10**(4), 318–332.

Rensen, J, & Roig, V. 2001. Experimental study of the unsteady structure of a confined bubble plume. *International Journal of Multiphase Flow*, **27**(8), 1431–1449.

Riboux, Guillaume, Risso, Frédéric, & Legendre, Dominique. 2010. Experimental characterization of the agitation generated by bubbles rising at high Reynolds number. *Journal of Fluid Mechanics*, **643**(Jan.), 509–539.

Risso, Frédéric. 2018. Agitation, Mixing, and Transfers Induced by Bubbles. *Annual Review of Fluid Mechanics*, **50**(1), null.

Roghair, I., Lau, Y. M., Deen, N. G., Slagter, H. M., Baltussen, M. W., Van Sint Annaland, M., & Kuipers, J. A. M. 2011. On the drag force of bubbles in bubble swarms at intermediate and high Reynolds numbers. *Chemical Engineering Science*, **66**(14), 3204–3211.

Ruzicka, M., Drahoš, J., & Thomas, N.h. 2001. Effect of Bubble Column Dimensions on Flow Regime Transition. *Chemie Ingenieur Technik*, **73**(6), 755–755.

Ruzicka, M. C., Vecer, M. M., Orvalho, S., & Drahoš, J. 2008. Effect of surfactant on homogeneous regime stability in bubble column. *Chemical Engineering Science*, **63**(4), 951–967.

Rybczyński, Witold. 1911. *Über die fortschreitende Bewegung einer flüssigen Kugel in einen zähen Medium*. Akademia Umiejętności. Google-Books-ID: MYn2rQEACAAJ.

Ryskin, G., & Leal, Lg. 1984a. Numerical-Solution of Free-Boundary Problems in Fluid-Mechanics .2. Buoyancy-Driven Motion of a Gas Bubble Through a Quiescent Liquid. *Journal of Fluid Mechanics*, **148**(NOV), 19–35. WOS:A1984TY47500002.

Ryskin, G., & Leal, Lg. 1984b. Numerical-Solution of Free-Boundary Problems in Fluid-Mechanics .3. Bubble Deformation in an Axisymmetric Straining Flow. *Journal of Fluid Mechanics*, **148**(NOV), 37–43. WOS:A1984TY47500003.

Sadhal, S. S., & Johnson, Robert E. 1983. Stokes flow past bubbles and drops partially coated with thin films. Part 1. Stagnant cap of surfactant film – exact solution. *Journal of Fluid Mechanics*, **126**(Jan.), 237–250.

Schiller, L, & Naumann, AZ. 1933. {\"U}ber die grundlegenden {B}erechnungen bei der {S}chwerkraftaufbereitung. *Ver. Deut. Ing.*, **77**, 318–320.

Silva, M. J. Da, Schleicher, E., & Hampel, U. 2007. Capacitance wire-mesh sensor for fast measurement of phase fraction distributions. *Measurement Science and Technology*, **18**(7), 2245.

Simiano, M., Zboray, R., de Cachard, F., Lakehal, D., & Yadigaroglu, G. 2006. Comprehensive experimental investigation of the hydrodynamics of large-scale, 3D, oscillating bubble plumes. *International Journal of Multiphase Flow*, **32**(10), 1160–1181.

Sirovich, Lawrence. 1987. Turbulence and the dynamics of coherent structures. III. Dynamics and scaling. *Quarterly of Applied Mathematics*, **45**(3), 583–590.

Sokolichin, A., Eigenberger, G., Lapin, A., & Lübert, A. 1997. Dynamic numerical simulation of gas-liquid two-phase flows Euler/Euler versus Euler/Lagrange. *Chemical Engineering Science*, **52**(4), 611–626.

Stokes, George Gabriel, Larmor, Joseph, & Rayleigh, John William Strutt. 1880. *Mathematical and physical papers*. Cambridge : University Press.

Talaia, Mário A. R. Terminal Velocity of a Bubble Rise in a Liquid.

Tomiyama, Akio, Kataoka, Isao, Zun, Iztok, & Sakaguchi, Tadashi. 1998. Drag Coefficients of Single Bubbles under Normal and Micro Gravity Conditions. *JSME International Journal Series B*, **41**(2), 472–479.

Vial, C., Camarasa, E., Poncin, S., Wild, G., Midoux, N., & Bouillard, J. 2000. Study of hydrodynamic behaviour in bubble columns and external loop airlift reactors through analysis of pressure fluctuations. *Chemical Engineering Science*, **55**(15), 2957–2973. WOS:000087060100019.

Vossepoel, A. M., & Smeulders, A. W. M. 1982. Vector code probability and metrication error in the representation of straight lines of finite length. *Computer Graphics and Image Processing*, **20**(4), 347–364.

Wallis, Graham B. 1969. *One-dimensional two-phase flow.* McGraw-Hill. Google-Books-ID: xvFQAAAAMAAJ.

Wallis, Graham B. 1974. The terminal speed of single drops or bubbles in an infinite medium. *International Journal of Multiphase Flow*, **1**(4), 491–511.

Wellek, R. M., Agrawal, A. K., & Skelland, A. H. P. 1966. Shape of liquid drops moving in liquid media. *AIChE Journal*, **12**(5), 854–862.

Wijngaarden, L. van, & Kapteyn, C. 1990. Concentration waves in dilute bubble/liquid mixtures. *Journal of Fluid Mechanics*, **212**(Mar.), 111–137.

Zahradnik, J., Fialova, M., Ruzicka, M., Drahos, J., Kastanek, F., & Thomas, N. H. 1997. Duality of the gas-liquid flow regimes in bubble column reactors. *Chemical Engineering Science*, **52**(21-22), 3811–3826. WOS:A1997YL42800019.

Zuber, N., & Findlay, J. A. 1965. Average Volumetric Concentration in Two-Phase Flow Systems. *Journal of Heat Transfer*, **87**(4), 453–468.